FERMILAB-THESIS-1993-65

Accelerator Physics
Ph. D. program
(no eff. #)

A STUDY OF LONGITUDINAL INSTABILITIES AND EMITTANCE GROWTH IN THE FERMILAB BOOSTER SYNCHROTRON

A Thesis

Submitted to the Faculty

of

Purdue University

by

Katherine Cecelia Harkay

In Partial Fulfillment of the

Requirements for the Degree

of

Doctor of Philosophy

December 1993

kedves szüleimnek

ACKNOWLEDGEMENTS

Over the course of this research effort, I have enjoyed a productive collaboration with several physicists in the Accelerator Division at Fermilab*. Foremost, I wish to express my gratitude to Patrick Colestock, who served as my mentor. I am indebted to Pat especially for sharing his physical insights and rich experimental and analytical experience with me. The originator for the thesis topic is Vinod Bharadwaj, who, as head of the Booster during my first year, ensured that facilities and equipment were available to me as needed. David Wildman collaborated on the studies to identify the offending RF cavity HOMs, and designed and fabricated the dampers. David Wildman, David McGinnis, and James Crisp assisted with many technical details and shared their data with me on numerous occasions. I thank Barry Barnes and James Lackey for valuable discussions and good-natured assistance. Andrei Gerasimov also offered thought-provoking discussion. Gerald Jackson assisted with his ACNET GPIB program. Jean-François Ostiguy provided hours of logistical help implementing the UNIX version of ESME, while James MacLachlan assisted with my questions about the code and Alex Bogacz provided a skeleton Booster input data file. Carol Johnstone deserves my special thanks for introducing me to PAW, which proved invaluable in the data reduction and presentation, and Linda Klamp for her participation in the final beam studies "marathon." Without exception, the Booster staff was always ready beyond the call of duty to assist with my many requests. The Operations staff was also

* This work has been supported by Fermi National Accelerator Laboratory under the Joint University-Fermilab Doctoral Program in Accelerator Physics. Fermilab is operated by the Universities Research Association under contract with the United States Department of Energy.

supportive and helpful during the numerous beam studies. I would also like to recognize my former colleagues at ANSER for my initial exposure to beam physics, propelling my return to academia.

My advisor, Dr. Laszlo Gutay's persistent guidance and concern for my physics career has created many opportunities for me, including my participation in this Fermilab research program. My family's love and encouragement over the years has meant a great deal to me. With great sadness, I regret that my father did not live to see the fruit of his pride. The support of my dear friend François throughout is something I can perhaps never repay. I thank you all for not letting me give up.

TABLE OF CONTENTS

Page

LIST OF TABLES vii

LIST OF FIGURES ix

ABSTRACT xv

1. INTRODUCTION 1

    1.1 Motivation for Research 1
    1.2 Observations in the Booster 4
    1.2 Organization of Thesis 10

2. BOOSTER SYNCHROTRON 13

    2.1 Introduction 13
    2.2 RF Cavities 19
    2.3 Operational Considerations 28

3. THEORETICAL BASIS 32

    3.1 Introduction to Longitudinal Beam Physics 33
    3.2 Coupled-Bunch Modes 44
    3.3 Linear Coupled-Bunch Mode Instability Theory 58

4. MEASUREMENTS 68

    4.1 RF Cavity Impedance 68

Page

4.2 RF Cavity Spectra 100
4.3 Bunch Spectra and Emittance 103

5. EXPERIMENTAL STUDIES 110

5.1 Observations of the Coupled-Bunch Instability 111
5.2 RF Cavity Higher-Order Mode Damping 120
5.3 Anomalous Emittance Growth 133

6. CALCULATIONS 137

6.1 Calculation of Linear Instability Growth Rates 138
6.2 Comparison with Observations 145

7. SIMULATION 150

7.1 ESME: Longitudinal Particle Tracking Code 150
7.2 Booster Simulation Results 153

8. CONCLUSIONS 174

8.1 Conclusions 174
8.2 Recommendations 176

LIST OF REFERENCES 177

APPENDICES

Appendix A: Booster Kinematic and Operational Tables and Curves 182
Appendix B: RF Cavity Impedance Tables and Curves 190
Appendix C: ESME Input Data Files for Simulation of Booster 205

VITA 211

LIST OF TABLES

Table Page

2.1 Typical Booster Operating Parameters. 16

2.2 RF Cavity Parameters. 25

3.1 Criterion for Swept LRC Resonator in Booster. 62

4.1 Designations of Booster RF Cavity Resonant Modes. 81

4.2 Measurement Results for Power Dissipation Method. 90

5.1 Data Run Designations of Parametric Beam Studies. 112

6.1 Criterion for Microwave Instability Threshold in the Booster. 149

7.1 Final ESME Simulations 162

Appendix
Table

A.1 Standard Booster Kinematic Parameters: 200 MeV to 8 GeV. 183

A.2 Variation on Booster Kinematic Parameters: 200 MeV to 4 GeV. 184

A.3 Booster Kinematic Parameters after Linac Upgrade: 400 MeV to 8 GeV. 185

B.1 Single-Gap Stretched Wire Datasets. 191

B.2 Single-Gap Impedance, Single-Gap Stretched Wire, HOM Dampers Out. 192

B.3 Single-Gap Impedance, Single-Gap Stretched Wire, HOM Dampers In. 194

B.4 Phase Shift Results from Bead-Pull Method. 196

B.5 Comparison of Single-Gap Impedance Calculation Between Bead-Pull and Stretched-Wire Methods. 196

B.6 Frequency Spread in HOMs Among Booster RF Cavities. 197

Appendix
Table Page

B.7 Equivalent R, Q for Single-Cavity and Net Sum Impedance, HOM Dampers Out. 198

B.8 Equivalent R, Q for Single-Cavity and Net Sum Impedance, HOM Dampers In. 201

B.9 Comparison of Single-Gap Impedance due to Resonant Modes for Nominal and Damped RF Cavity at t=21 msec. 204

B.10 Effect of Cavity Shorts on Impedance vs. HOM Dampers. 204

LIST OF FIGURES

Figure		Page
1.1	Time Evolution of the Bunch Phase (Mountain Range Plots) Through a Portion of the Booster Cycle	5
1.2	Longitudinal Emittance Through the Booster Cycle for Several Beam Intensities	6
1.3	Longitudinal Emittance Through the Booster Cycle for Fixed Beam Intensity Before and After RF Cavity HOM Damping	8
1.4	Longitudinal Emittance at Extraction from the Booster as a Function of Beam Intensity Before and After RF Cavity HOM Damping	9
1.5	Approach Taken in Study of Booster Coupled-Bunch Instability to Compare Data with Analytical Results and Simulation.	12
2.1	Layout of the Booster Synchrotron Ring.	14
2.2	Standard Quadrupole Magnets.	18
2.3	Booster Combined-Function Magnets	18
2.4	Geometry, Equivalent Transmission Line, and Field Pattern for the Quarter-Wave Coaxial Cavity Resonator.	21
2.5	Geometry, Schematic, and Field Pattern for the Half-Wave Coaxial Cavity Resonator.	23
2.6	Cut-Away Drawing of Booster RF Cavity	24
2.7	Major Components of Booster RF System.	27
3.1	Longitudinal Phase Stability of Synchrotron Motion.	40
3.2	Contours of Particle Motion in Longitudinal Phase Space.	40
3.3	Phase Space Area and Charge Density Representations of Synchrotron Oscillation Modes	45

Figure Page

3.4 Phase Space Area and Charge Density Representations of a Combination of Dipole and Quadrupole Synchrotron Oscillation Modes. 46

3.5 Equilibrium Phase (n=0) Representation of Coupled-Bunch Modes for an Example Train of Six Bunches. 47

3.6 Phase Oscillation Representation for n=1 Coupled-Bunch Dipole Mode m=1 for Six-Bunch Example. 48

3.7 Phase Oscillation Representation for n=1 Coupled-Bunch Quadrupole Mode m=2 for Six-Bunch Example. 48

3.8 Phase Oscillation Representation for Higher-Order (n=2,3,4,5,6) Coupled-Bunch Modes in Example. 49

3.9 Frequency Spectrum Chart for Dipole Synchrotron Oscillation Mode. 57

3.10 Model Resonant LRC Circuits. 61

3.11 Resonant Response of Parallel LRC Circuit in Figure 3.10 (b). 61

4.1 Single-Gap Stretched Wire Measurement of RF Cavity Gap Impedance. 71

4.2 Network Analyzer Measurement Illustrating the S-Parameter Set. 72

4.3 Transmission S_{21} Data Through Gap Using Single-Gap Stretched-Wire Assembly. 74

4.4 Reference Transmission $S_{21\,REF}$ with Assembly Inside Beam Pipe. 75

4.5 Calibration Transmission $S_{21\,CAL}$ Through Optoelectronic System. 76

4.6 Equivalent Circuits for Single-Gap Stretched Wire RF Cavity Impedance Measurement. 77

4.7 Calculated Single-Gap Impedance of Booster RF Cavity De-embedded from Single-Gap Stretched Wire Measurement 80

4.8 Experimental Setup for Bead Pull Measurement of RF Cavity Single Gap Impedance. 84

4.9 Typical Scans in Bead Pull Measurement Showing Resulting Phase Shift 84

Figure Page

4.10 Gaussian Fits of (a) Calculated Gap Profile and (b) Measured Phase Shift Scan. 86

4.11 Correlation Between Stretched-Wire and Bead Pull Measurements of Single-Gap Impedance and Q. 88

4.12 Power Dissipation Measurement Setup to Determine RF Gap Impedance 90

4.13 Log Magnitude and Phase Measured with Monopole Probes Inserted into RF Cavity Gaps. 92

4.14 Intergap Mode Phase Angle Constructed for Analysis. 93

4.15 Single Cavity vs. Twice Single-Gap Impedance. 95

4.16 Representative Distributions in RF Cavity Higher-Order Modes. 97

4.17 Net Impedance With and Without Intercavity Spread. 98

4.18 RF Cavity Spectrum due to Beam. 102

4.19 Pulse-to-Pulse Variation of Coupled-Bunch Instability Amplitude. 105

4.20 Nominal Beam Momentum Spread. 105

4.21 Booster RF Sum and Charge Signals. 107

4.22 Typical Frequency Spectrum Showing the Coupled-Bunch Mode Signal. 109

4.23 Typical Charge Distribution Signal in the Booster. 109

5.1 Longitudinal Emittance Growth as a Function of Time in the Booster. 113

5.2 Effect on Emittance of Shorting vs. Removing RF Cavities. 114

5.3 Repeat of Longitudinal Emittance Growth Studies vs. Intensity. 114

5.4 Extraction of Bunch Charge Distributions from Spectrum. 117

5.5 Verification of Spectral Analysis of Charge Density. 117

5.6 Coupled-Bunch Mode Amplitude as a Function of Time in the Booster Cycle 118

Figure Page

5.7 Frequency Spectra Showing the Coupled-Bunch Mode Signal Before and After RF Cavity HOM Damping 120

5.8 Correspondance of RF Cavity HOM Impedance and Coupled-Bunch Mode Spectrum Before HOM Dampers. 122

5.9 Excitation of RF Cavity Mode f2 (82.0MHz). 123

5.10 Excitation of RF Cavity Mode f4 (168.8 MHz). 124

5.11 Excitation of RF Cavity Mode f6 (220.8 MHz). 125

5.12 RF Cavity Showing Installation of HOM Dampers. 127

5.13 Photographs of RF Cavity HOM Dampers 128

5.14 HOM Dampers Represented as Circuits. 129

5.15 Comparison of RF Cavity Single-Gap Impedance Before and After HOM Dampers. 130

5.16 Effect of the Cavity Short on the Impedance. 131

5.17 Correspondance of RF Cavity HOM Imedance and Coupled-Bunch Mode Spectrum After HOM Dampers. 134

5.18 Nominal and Increased Momentum Spread.. 135

5.19 Spectrum for Large Momentum Spread.. 135

5.20 Coupled-Bunch Mode Amplitudes and Emittance Growth for Large Momentum Spread.. 136

6.1 Form Factors for Coupled-Bunch Instability. 140

6.2 Form Factors Comparing the Dipole Coupled-Bunch Mode for Different Particle Distributions. 141

6.3 Linear Instability Growth Rates in Booster.. 141

6.4 Correspondence of Linear Instability Growth Rate and Perturbed Beam Spectrum. 142

6.5 Instability Curves Showing Graphical Solution of Growth Rate. 144

Figure Page

6.6 Comparison of Linear Instability Theory With the Data. 146

6.7 Coherent Instability Growth Time vs Decoherence Time. 147

6.8 Measured Impedance due to Booster D Magnets. 147

6.9 Microwave Instability Threshold for Booster. 149

7.1 Model Parallel LRC Fit of Net RF Cavity HOM Impedance (Dampers Out). 155

7.2 Model Parallel LRC Fit of Net RF Cavity HOM Impedance (Dampers In). 156

7.3 Effect of Tracking Step Size on Slewing Resonance in ESME. 157

7.4 ESME Phase Space Plots: HOM Dampers Out. 163

7.5 Mountain Range Plots in Simulation, HOM Dampers Out. 164

7.6 Emittance Growth in Simulation Compared with Data, HOM Dampers Out. 165

7.7 Mountain Range in Simulation Compared with Data, HOM Dampers In. 168

7.8 ESME Phase Space Plots: HOM Dampers In. 169

7.9 Emittance Growth in Simulation Compared with Data, HOM Dampers In. 170

7.10 Mountain Range Plots in Simulation for Both 400 MeV Upgrade and no HOM Impedance. 171

7.11 ESME Phase Space Plots: HOM Dampers In, 400 MeV Upgrade. 172

7.12 Emittance Growth Predicted by Simulation for 400 MeV Linac Upgrade. 173

Appendix
Figure

A.1 Moving RF Bucket Parameters. 186

A.2 Amplitude Dependence of Synchrotron Frequency. 186

Appendix
Figure Page

A.3 Beam Scaling Parameters 187

A.4 Standard Booster Kinematic Parameters. 188

A.5 Standard Booster Acceleration Parameters. 189

B.1 Single-Gap Impedance (ReZ, ImZ) De-embedded, HOM Dampers Out, Showing Detail (t=21 msec) 193

B.2 Single-Gap Impedance (ReZ, ImZ) De-embedded, HOM Dampers In, Showing Detail (t=21 msec) 195

B.3 Single Cavity Impedance (ReZ, ImZ) Calculated, HOM Dampers Out, Showing Detail (t=21 msec) 199

B.4 Net Impedance (ReZ, ImZ) Calculated, 15 Cavities, HOM Dampers Out, Showing Detail (t=21 msec) 200

B.5 Single Cavity Impedance (ReZ, ImZ) Calculated, HOM Dampers In, Showing Detail (t=21 msec) 202

B.6 Net Impedance (ReZ, ImZ) Calculated, 15 Cavities, HOM Dampers In, Showing Detail (t=21 msec) 203

ABSTRACT

Harkay, Katherine Cecelia. Ph.D., Purdue University, December 1993. A Study of Longitudinal Instabilities and Emittance Growth in the Fermilab Booster Synchrotron. Major Professor: Laszlo Gutay.

Attempts to measure and describe beam instabilities have been made ever since they were first observed in particle accelerators thirty years ago. Such collective, coherent effects arise due to the electromagnetic interaction of the beam with its environment, namely, the elements in the beamline. With sufficient intensity, the motion can become unstable, possibly leading to phase space dilution and beam loss. A coupled-bunch instability has long been observed in the Booster, an 8-GeV proton synchrotron at Fermi National Accelerator Laboratory. The accompanying longitudinal emittance growth is a major limit to beam brightness, limiting also the performance of subsequent accelerator stages. Previous studies have indicated that the coupled-bunch mode fluctuations are likely due to the influence of higher-order modes (HOM) in the radio-frequency (RF) accelerating cavities. However, the physics, especially that of the emittance growth, was only partially characterized.

It is my goal in this thesis to expand what we understand about coherent longitudinal phenomena and integrate it with a real machine which does not readily give up her secrets. Building upon prior observations and coupled with the advent of more sophisticated diagnostic and computational tools, this research seeks to characterize the unstable beam behavior in a rapidly cycling synchrotron. Experimental studies are designed to systematically vary parameters in order to establish functional dependencies. Bench measurements are made of the impedance due to RF cavity HOMs. These data are compared with analytic results derived from the standard linear perturbation treatment as well as with simulation.

The major finding of this research is that the theoretical predictions of linear growth rates of the longitudinal coupled-bunch instability based on the measured impedance show quantitative agreement with the data, but only when the beam momentum spread and nonlinearity of the RF potential are incorporated self-consistently. Development and installation in the cavities of passive HOM dampers proved to reduce the emittance by a factor of three and allowed, for the first time, an experimental test of instability thresholds. The linear theory is inadequate in describing the observed emittance growth, for which simulation results are invoked instead to provide a scaling rule.

1. INTRODUCTION

1.1 Motivation for Research

Modern particle accelerators and colliders find application in a wide range of physics, medical, and industrial fields. Efforts to improve designs are driven in part by the high-energy physics community. In colliders, for instance, a critical design parameter is luminosity, or the interaction rate per unit cross section. At Fermilab, a three-phase upgrade program is underway to increase the beam luminosity to 5.6×10^{31} cm^{-2} sec^{-1}, about an order of magnitude over that achieved during the 1992-1993 collider run (IA).[1] This is considered necessary for new discoveries in particle physics. After a number of simplifications, the luminosity in a synchrotron $p\bar{p}$ collider is given by[2]

$$L = 3\gamma\frac{\omega_0}{2\pi}\frac{BN_pN_{\bar{p}}}{\left(\varepsilon_{n_p}+\varepsilon_{n_{\bar{p}}}\right)\beta^*}F\left(\frac{\sigma_L}{\beta^*}\right) \qquad [\mathrm{cm}^{-2}\ \mathrm{sec}^{-1}] \qquad (1.1)$$

where ω_0 is the particle revolution frequency, B the number of bunches in each beam, N the number per bunch of each particle species, F a form factor dependent on the longitudinal bunch width σ_L and lattice parameter β^*, and $\varepsilon_n = \gamma\beta\varepsilon_x\varepsilon_y$ the normalized transverse emittance, where $\gamma\beta$ are the usual Lorentz factors. The total emittance is the area in six-dimensional phase space occupied by the beam. Maximizing luminosity, then, is a trade-off between maximum particles per bunch (intensity), maximum number of bunches, and the beam emittance. However, high brightness (N/ε) can permit large self-fields to develop which can then become amplified by structures in the beam pipe, leading to undesired forces coupling to the beam. Large amplitude perturbations can lead to beam loss during either acceleration, beam extraction, or transfer to subsequent accelerator stages. Nonlinearities in the system may stabilize the oscillations; however, they also dilute the phase space density. Hence, attempts to improve the intensity of machines are often accompanied, and in

some cases are hampered, by the appearance of beam instabilities. Fermilab is no exception, and part of the upgrade program is the control of beam instabilities in the three synchrotrons: the Booster, Main Ring and Tevatron.[1,3] All told, the study of beam instabilities, especially the development of diagnostic techniques and physical models, remains important and relevant at Fermilab and other accelerators. It was the goal of this thesis research to experimentally observe and analytically characterize the longitudinal coupled-bunch instability in the Booster and to implement improvements designed to control the resulting longitudinal emittance growth.

Beam instabilities are collective, coherent, intensity-dependent effects that arise due to the unavoidable electromagnetic interaction of the charged beam with its environment. The passage of the beam through discontinuities in the beam pipe like bellows, metal plates in detectors and kickers, and the radio-frequency (RF) accelerating cavities themselves can cause spurious electromagnetic fields to develop. These so-called wake fields can persist and act back on the beam, resulting in undesired forces. By convention and convenience, this effect of beamline structures is characterized in the frequency domain by a parameter known as the impedance $Z(\omega)$, which is the Fourier transform of the time-dependent wake field. The impedance relates the response $V(\omega)$ of the system to the perturbing beam current $I(\omega)$. It is normally the impedance rather than the wake field that can be readily measured.

Under appropriate resonance conditions and with sufficient intensity, beam fluctuations may evolve out of the noise and the motion can become unstable, possibly leading to emittance blow-up and beam loss. The collective interaction among different bunches in the beam due to the driving impedance gives rise to the coupled-bunch modes. These oscillations appear as phase-modulation sidebands at specific rotation harmonics in the frequency spectrum of the beam current. Internal bunch oscillation modes are also possible; if the interbunch phase is random, these are called microwave modes since the frequencies typically fall in the microwave region. The time evolution of the instability depends on the initial conditions in a multi-parameter space. In a system with large noise levels, there can be great pulse-to-pulse variation, as observed in the Booster, although the average behavior is repeatable. To be distinguished from instabilities are fluctuations in the beam current caused by phase errors as the particles are injected into the machine, or due to the discontinuous process of passing through transition energy (described later). Unless they are amplified by some

resonant structure, these oscillations decay, or decohere, through nonlinear processes in the beam.

Mitigation of beam instabilities takes three forms, and in some cases a combination is required. If the driving impedances and associated beamline structures can be positively identified, they can possibly be damped at the source. The procedure can involve both bench measurements of candidate beamline components and parametric beam studies in which individual structures are removed or shorted and the beam response noted. Pickups inside or near suspected structures can be monitored for beam-induced signals. The impedance due to individual beamline components may be measured on the bench, for example, by replacing the beam with a current-carrying wire. A combination of such data is important to demonstrate cause and effect, and not simply coincidence, of impedance sources in the ring and perturbation frequencies excited in the beam. Alternately, one may reduce the effect of the impedance by increasing the energy spread in the beam, providing in principle a damping mechanism through Landau damping. This involves manipulations with the RF acceleration system. Finally, one may introduce an equal but negative impedance such as with a beam feedback system by sampling the phase error in the beam and applying a correction voltage to kick the beam back towards its nominal trajectory. The kicker can be, for example, a wideband cavity with a single gap across which the correction signal is applied. The signal processing must precisely account for all delays through the electronics, for the delay between the pickup and the kicker, and for the particle transit time.

Several factors come into consideration when choosing the means for eliminating or at least reducing a particular instability in a particular machine. A number of difficulties present themselves. Isolating suspected impedance sources is often tricky due to limited diagnostics and the complexity of the parameter space. Bench measurements of the impedance due to individual beamline components must be interpreted properly to determine the correct sum effect on the beam. Tests in which beamline components are removed are obviously not possible for critical devices. Repeatability can be an issue if the studies require a shutdown for access into the beamline enclosure. Subsequent turn-on and re-tuning of the beam often leaves the machine in a new operating state, making it difficult to directly compare the data. The implementation of Landau damping, while conceptually straightforward, in practice

can be difficult to control. Of course, this method is beneficial only if one can tolerate the degraded luminosity: an increased energy spread leads to an increased bunch length, and luminosity is decreased as a consequence. The practical application of active beam damping may be exacerbated by poor signal-to-noise or large acceleration rates (large frequency sweeps).

1.2 Observations in the Booster

A longitudinal coupled-bunch mode instability has long been observed in the Booster, an 8 GeV (kinetic energy) fast-cycling proton synchrotron. The time development of large amplitude, predominantly dipole phase oscillations can be seen for one bunch (out of a total of 84) in Figure 1.1 in a series of what are known as mountain range plots. Each plot records a sequence of oscilloscope traces of the longitudinal charge density from a resistive-wall beam pickup signal. The horizontal scale is 2 nsec per division. The scope is triggered at a chosen interval, and each resulting trace is displayed offset vertically a small amount for clarity. In this setup, the time interval between traces is ten revolutions and each plot thus covers about 1 msec in different Booster cycles. The time sequence begins in the lower left corner, beginning immediately before transition. Higher-order structure is evident in the bunch around 24 msec. In this example from several years ago, the bunch intensity is 1.5×10^{10} protons per bunch. The effect is minimal at the lowest operating intensities. The longitudinal emittance, proportional to the square of the bunch length, may be computed as a function of time in the cycle. A family of curves showing the emittance growth over the acceleration cycle can be seen in Figure 1.2. The effect on the emittance of increasing the beam intensity is dramatic.

It was suspected that the bunch oscillations were likely due to the influence of higher-order parasitic modes (HOM) in the RF accelerating cavities. The driven, fundamental frequency of the cavities, given by $\omega_{RF} = h\omega_0$, is a multiple of the particle revolution frequency $\omega_0 = 2\pi$ 628 kHz (at extraction), with a harmonic number h=84. Because they are resonant structures, higher frequencies can also be supported in the cavities through parasitic excitation by the beam. Passive cavity mode damping in the past was known to successfully stabilize a coupled-bunch instability in the Main Ring. In the Booster, however, primarily because of limited diagnostics and additional

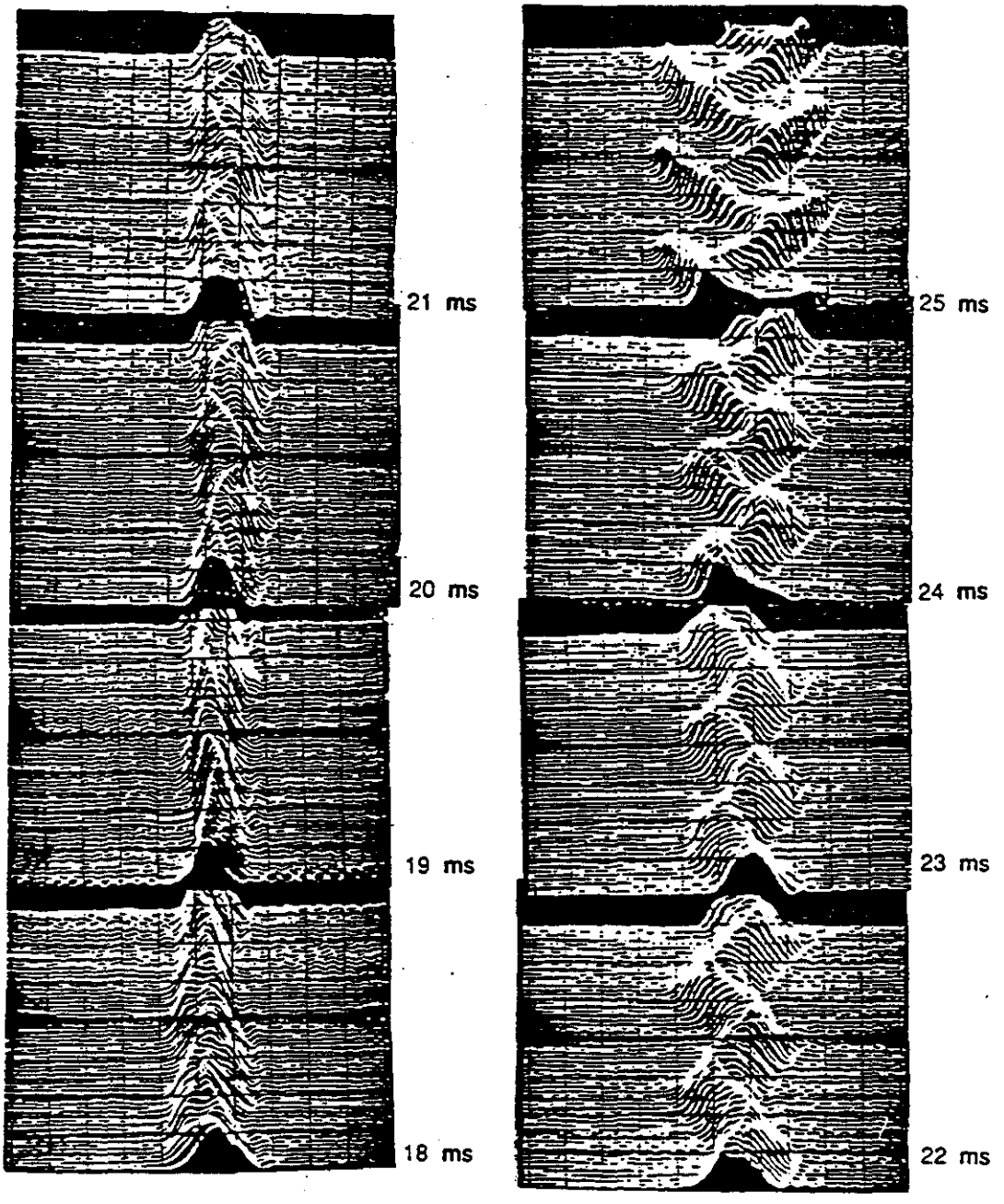

Figure 1.1 Time Evolution of the Bunch Phase (Mountain Range Plots) Through a Portion of the Booster Cycle. Growing dipole oscillations indicative of the coupled-bunch instability are clearly seen. The beam intensity is 1.5×10^{10} protons per bunch, the transition jump system is off, and the RF cavity dampers are out. The horizontal scale is 2 nsec per division. [Ref. 43]

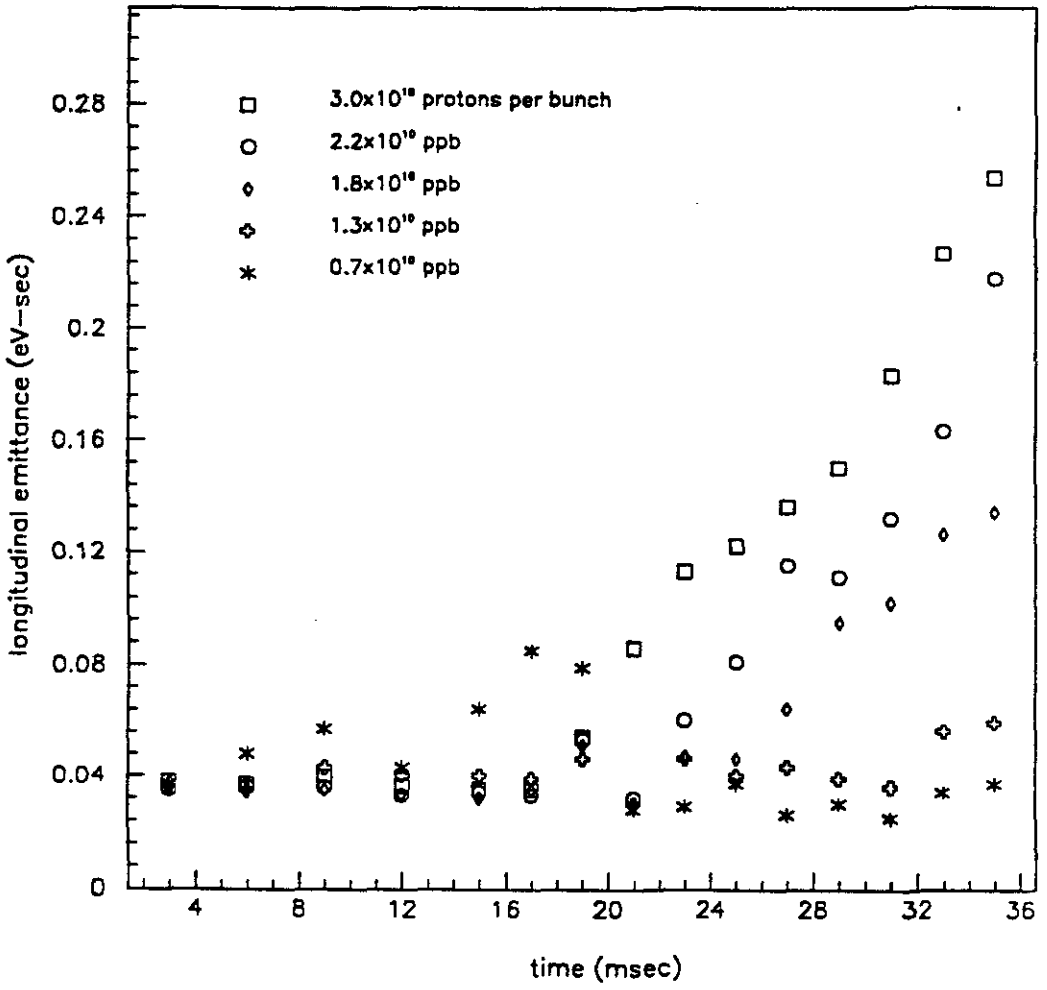

Figure 1.2 Longitudinal Emittance Through the Booster Cycle for Several Beam Intensities. The number of RF cavities turned on is fixed at 16. Emittance growth occurs mainly after transition (19 msec) and is most pronounced at the highest intensities.

complexities, there was disagreement as to which cavity modes drove the beam instability. The most serious issue is that high resolution spectral measurements are hampered by the short acceleration time (33.3 msec) coupled with a large sweep in the frequency of the RF drive (30 to 53 MHz.) For these reasons, prior efforts over the period between 1975 and 1989 concentrated instead on employing beam damping through Landau damping and active beam feedback. These improvements were met with limited success. Unfortunately, no reduction of the emittance growth was observed for either technique. In the one case, the frequencies of two RF cavities were changed to correspond to harmonic numbers h=83 and 85 in order to effect a synchrotron frequency spread in the beam. No obvious effect was seen on the beam with this modification. Also, a longitudinal bunch-by-bunch beam damper was installed using a broadband 800 volt cavity for feedback. Some reduction was seen in the coupled-bunch mode amplitudes for medium beam intensities, but the nominal, higher intensity beam remained as unstable as before. As of this writing, a separate effort is underway which is dedicated to upgrading this existing longitudinal feedback system. This work was begun after that described in this thesis, has not yet been implemented, and thus will not be discussed herein.

The emergence in recent years of improved diagnostics and computational tools has made it possible to re-examine the Booster coupled-bunch mode instability with greater sophistication. A systematic and concerted effort over two years combining experimental studies and calculation lead first to the identification of the offending HOMs, followed by the design and installation of passive dampers in the RF cavities. Our efforts have resulted in the reduction of the longitudinal emittance in the Booster by a factor of three, never before achieved. These data are plotted in Figure 1.3, which gives the emittance through the Booster cycle both before and after the dampers were installed. The comparison for the emittance at extraction plotted as a function of bunch intensity is shown in Figure 1.4. This graph illustrates the practical consequence of emittance growth, which is to define an intensity limit in the Booster due to momentum aperture constraints in the Main Ring. Linear extrapolation from the present data, while oversimplified, suggests that an increase in intensity of about a factor of two is allowed.

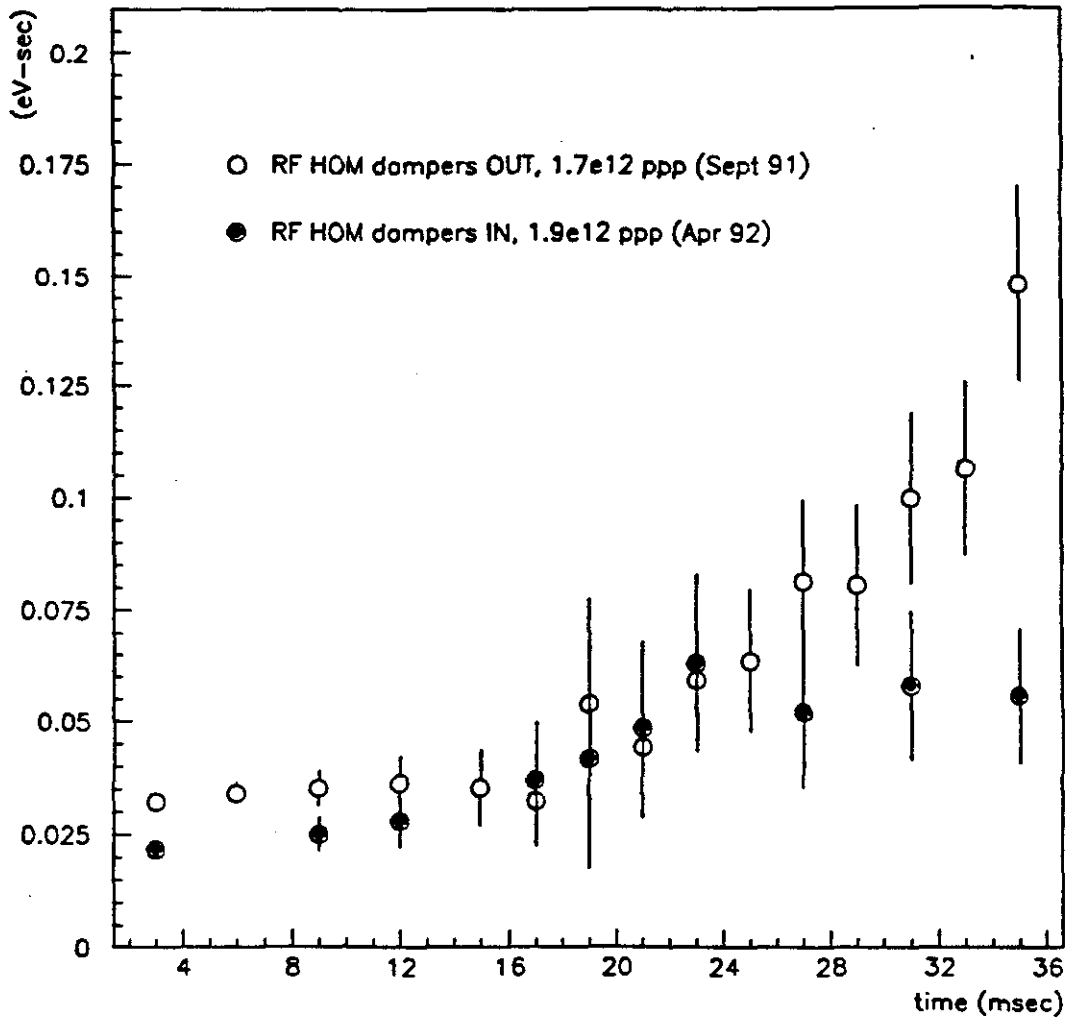

Figure 1.3 Longitudinal Emittance Through the Booster Cycle for Fixed Beam Intensity Before and After RF Cavity HOM Damping. The emittance at extraction has been reduced by about a factor of three. The beam intensity is actually somewhat larger in the measurement after the dampers were added.

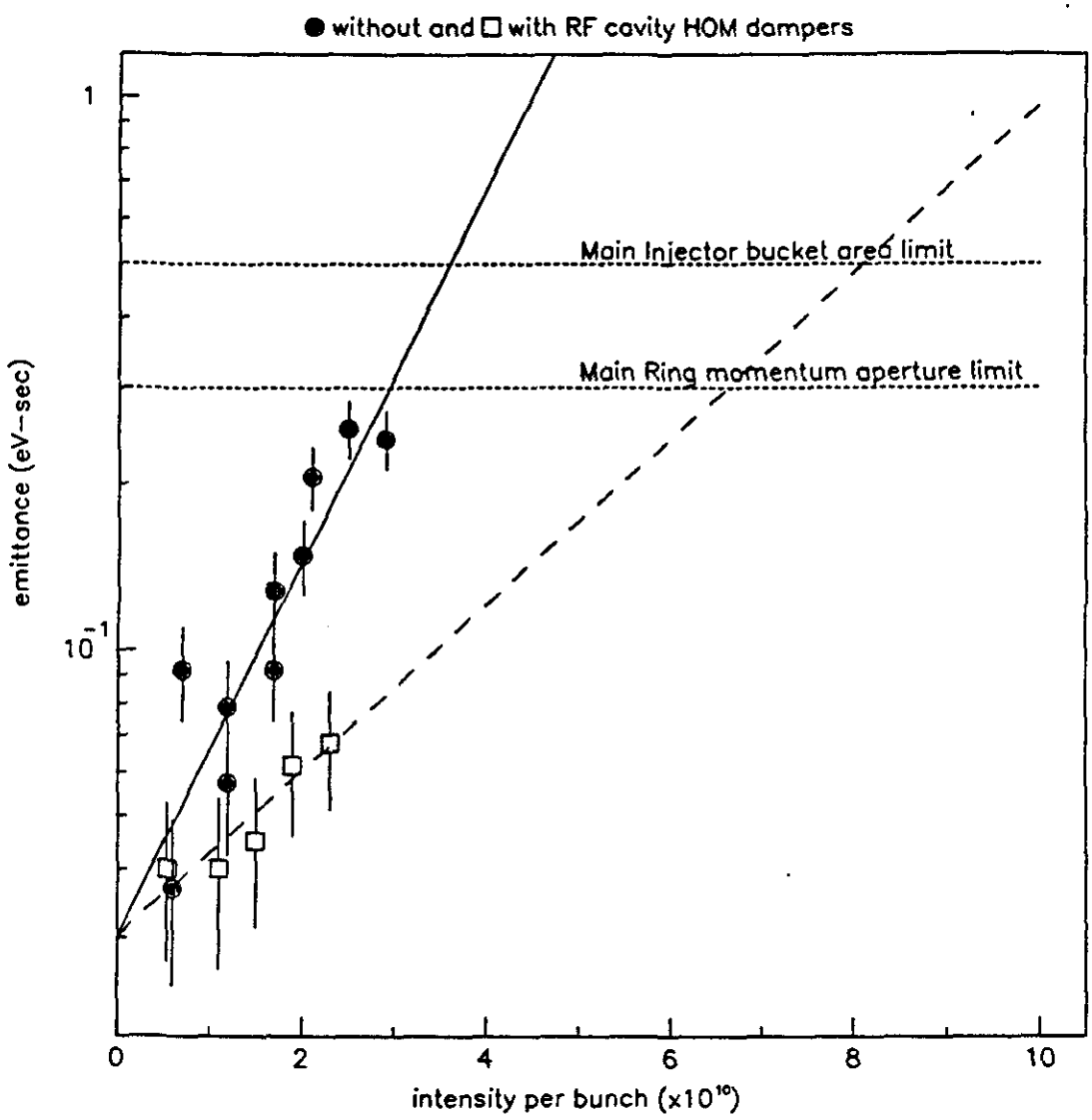

Figure 1.4 Longitudinal Emittance at Extraction from the Booster as a Function of Beam Intensity Before and After RF Cavity HOM Damping. Shown also are the momentum aperture limits for the Main Ring and the proposed Main Injector.

The second stage of this research involved the comprehensive comparison of the data with the predictions of the coupled-bunch mode theory. Even after installation of the RF cavity mode dampers, questions remained as to the mechanism for the emittance growth. The physics of beam instabilities was first described in detail twenty years ago by Sacherer[4] using a linear perturbation treatment. As new phenomena like the coupled-bunch instabilities were discovered, the basic theory was modified and refined. In general, simplifying assumptions are incorporated to allow analytical solutions for the coherent modes, giving the linear instability growth rates and frequency shifts. While there is strong evidence from the mountain range (Figure 1.1) that nonlinear effects may be important, our goal was to study the data quantitatively at least to determine the point at which the linear theory breaks down. But characterization of even the linear behavior in the Booster proved difficult. Initial comparisons of the measured instability growth with the theory showed only qualitative agreement. Furthermore, the linear theory was completely inadequate in explaining the observed emittance growth. What ensued was a rigorous test of and modification of some of the assumptions used in the literature for proper application to the Booster. Solutions were found numerically using standard algorithms. It was found that including self-consistently the effects of the beam momentum spread and nonlinear RF potential (Landau damping) was essential to accurately describe the unstable beam behavior. To study emittance growth, a fully nonlinear simulation was invoked. The particle tracking code ESME, developed at Fermilab, was implemented to observe the response of the longitudinal, or energy-phase, distribution of the beam in the presence of a high-Q resonant driving impedance. Subsequent analyses of the results produced a qualitative scaling of the emittance growth and a deepened understanding of the subtleties and sensitivities of the instability on various parameters.

1.3 Organization of Thesis

This dissertation is organized into eight chapters. The first three chapters provide the background for discussions in the later chapters. Chapters four and five describe the measurements and experiments, respectively, and Chapter seven the simulations designed to shed light on the cause-and-effect of the Booster coupled-bunch instability. The bulk of the data analysis is found in the sixth chapter. Conclusions and recommendations are offered in the last chapter.

This first chapter describes the motivation behind this research, including a general discussion of beam instability terminology. The second chapter describes the Booster synchrotron in some detail, focusing on the RF accelerating resonant cavities and operational properties relevant to our experimental studies. The basic theory of longitudinal beam motion is discussed in chapter three, defining parameters commonly used in accelerator physics. Also in chapter three, the coupled-bunch modes are described and expressions for their excitation and growth are derived. The model for a resonant impedance is introduced.

All the RF cavity and beam measurements, with the accompanying hardware, are described in chapter four. Chapter five gives the results of numerous experimental studies designed to characterize the coupled-bunch instability. First is a series of observations while varying beam conditions. Next is a discussion of the RF cavity HOM damper effort: how the offending modes were identified, the design of the dampers, and the effect on the beam. Finally, studies varying the beam momentum spread are described, showing anomalous emittance growth behavior seemingly inconsistent with the theory. Chapters three, four, and five present material in a logical sequence, but in a somewhat reversed chronological order. The experimental studies in fact preceded the bulk of the theoretical work.

The computational results for the linear coupled-bunch instability growth are compared with observations in Chapter six. Chapter seven describes the simulation of the Booster coupled-bunch mode instability using ESME using the measurements of Chapter four as the input data. In addition, the scaling of emittance growth is discussed. Conclusions and recommendations for follow-up studies are offered in the final chapter. Presentation of this work is necessarily sequential and obscures the iterative nature of the analysis. The diagram in Figure 1.5 depicts the multiple-step approach taken in this thesis.

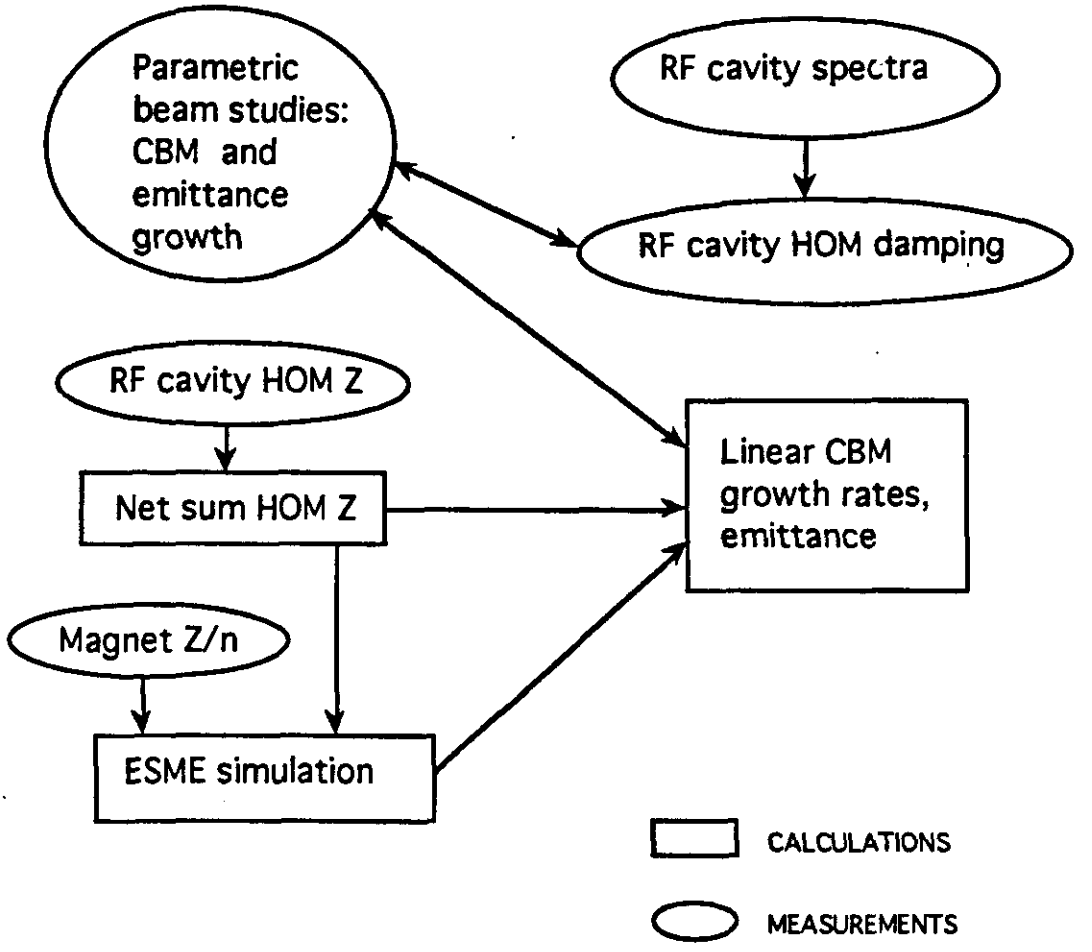

Figure 1.5 Approach Taken in Study of Booster Coupled-Bunch Instability to Compare Data with Analytical Results and Simulation.

2. BOOSTER SYNCHROTRON

2.1 Introduction

The machine of interest in our study is the Booster, a fast-cycling synchrotron, accelerating protons from 200 MeV to 8 GeV (kinetic energy). Design enhancements and fine-tuning over its 20-year lifetime (first beam obtained in 1971) have resulted in fairly reliable operation, despite the long-observed existence of instabilities. Its characteristics and operational constraints are rather unique among the Fermilab synchrotrons, but similar to low energy proton machines at other facilities.

The Booster came into existence as a necessary intermediary between the traditional injector, a linear proton accelerator (Linac), and what was then the main accelerator, the Main Ring. Practical constraints on size and cost placed a limit of a few hundred MeV on the Linac. However, such a low injection energy would have placed an unreasonable burden on the cost and design of the magnet and power supply systems in the Main Ring, a machine whose goal was to accelerate 5×10^{13} protons per pulse to 400 GeV. Incidentally, this intensity goal was never achieved, and with the addition of the superconducting Tevatron, the Main Ring now typically delivers 2.1×10^{13} protons at 150 GeV. In the final design, the Booster addressed the economic factor as well as other considerations. By employing multi-turn injection, it reduced the peak intensity required in the Linac. Fast cycling, whereby the Main Ring is filled in several successive pulses, was chosen for two reasons. First, since space charge is an important effect in low energy proton machines, this scheme reduced the intensity required in the Booster. Fast cycling also reduced its size and therefore cost while providing a reasonable Main Ring filling time of 0.8 sec. The majority of the material in this introduction to the Booster is documented in References 5 and 6. After a general description, particular attention will be given to the RF acceleration system and various aspects of operation relevant in this study of longitudinal instabilities.

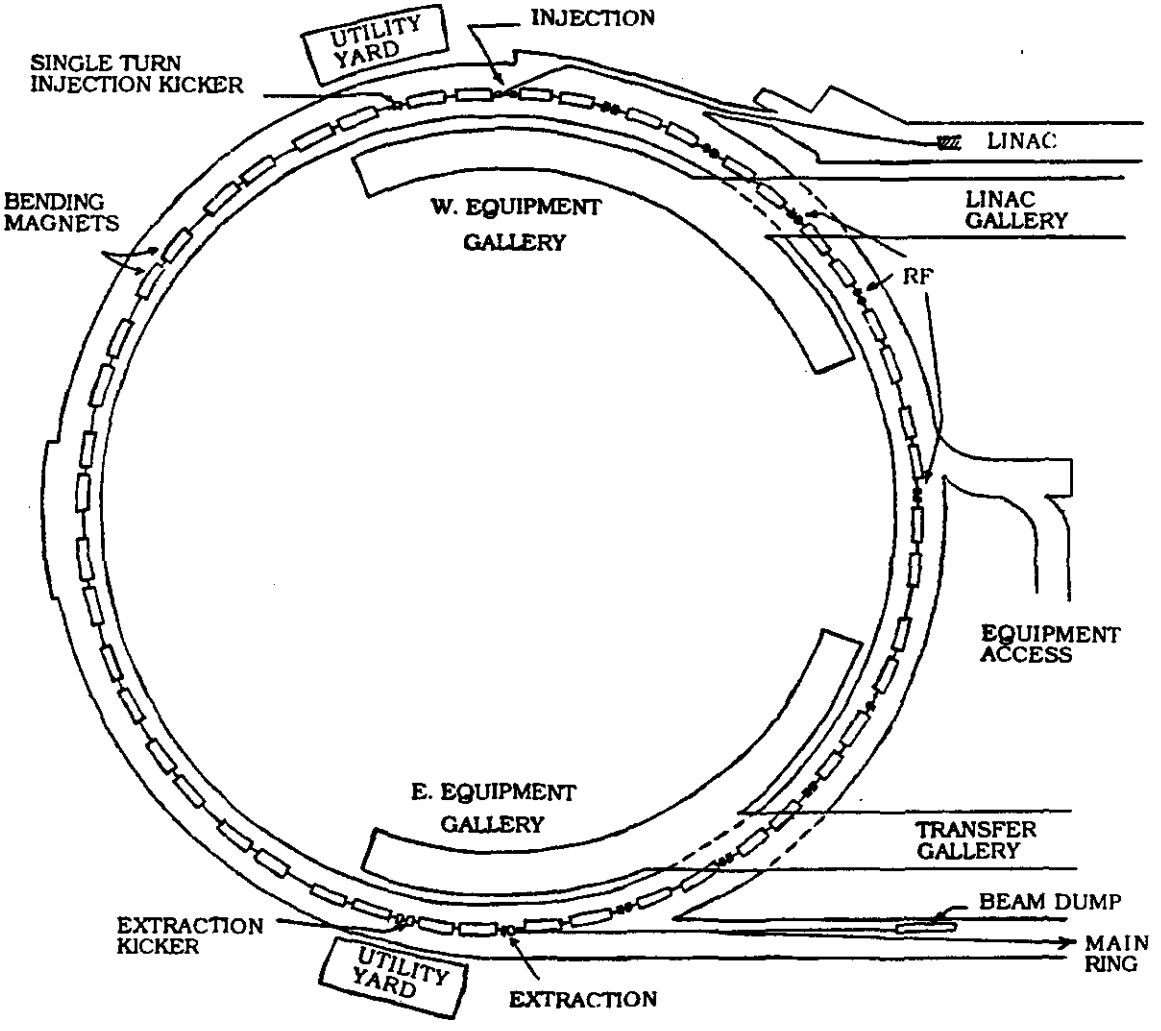

Figure 2.1 Layout of the Booster Synchrotron Ring. (Ref. 5)

A schematic of the Booster showing the major components is presented in Figure 2.1 Depicted are the injection and extraction lines, the magnets, and the radio-frequency (RF) accelerating cavities. The components of the ring are located in a tunnel 15 feet under the ground. The high-power supplies for the magnets, RF system, and injection/extraction kicker magnets are located at ground level either in the utility yards outdoors or in the equipment galleries above the tunnel. All operation has been controlled remotely through front-end PDP-11 computers originally, replaced in recent years by microVAXes.

Negative hydrogen ions (H^-) enter the transfer line from the Linac bunched with a 200 MHz structure. The timing of a "chopper" at the end of the Linac is adjusted to select a portion in the center of the long beam pulse to be deflected into the transfer line. A pulse 2.8 μsec in length is referred to as one "turn" because it is equal in length to a single period in the Booster at injection energy. A pulse equal in length to up to ten Booster turns may be injected; the nominal is six. A debuncher cavity in the transfer line rotates the beam 90° in phase space, converting the large momentum spread into a large phase spread, effectively debunching the beam. The electrons are stripped by a foil on injection into the Booster. This charge-exchange scheme was proposed to minimize the transverse emittance during multiple-turn injection. If protons are injected directly, successive turns can only be stacked side by side in the transverse aperture, parallel to the circulating beam. This results in a transverse beam spread much greater than that of the injected beam. Indeed, no scheme of magnets can be envisioned which can bend protons entering the synchrotron tangentially without also bending the circulating beam since they are of the same sign charge. Thus, a proton beam cannot be injected into the same phase space as the circulating beam. Anything otherwise would violate the well-known Liouville's theorem from statistical mechanics, which states that phase space area of an ensemble is conserved in closed system in the absence of dissipative forces.[7] With charge-exchange injection, however, we circumvent Liouville's theorem since the foil introduces collisional processes. The system now obeys instead the Boltzmann equation. Because they are of different species, the H^- and circulating proton beams can both pass through a single magnet at the injection point and be bent toward each other onto the same trajectory, and therefore, the same phase space, before impinging upon the foil. Therefore, new protons created at the foil are injected into the same phase space as the circulating beam, thus preserving approximately the transverse emittance of the Linac.

The protons debunch further over about one turn in the Booster and are subsequently recaptured adiabatically and rebunched with the RF system at 30 MHz. This gives a harmonic number of 84 (30 MHz x 2.8 μsec). Acceleration is provided by radio-frequency (RF) drive in 17 resonant cavities, while the bending guide field is provided by 96 combined-function magnets, each 3 meters in length. Over the 33 msec acceleration cycle, the RF frequency rises to 53 MHz as the protons circulate about 16,000 times and reach an energy of 8 GeV. The beam is extracted by fast kicker magnets. The ratio in circumference between the Main Ring and Booster is 13.25; therefore the Main Ring is filled in 13 pulses. The typical Booster operating parameters are summarized below in Table 2.1.

Table 2.1 Typical Booster Operating Parameters

Injection method		multiturn H^-
Injection energy (kinetic)		203 MeV
Extraction energy		8 GeV
Circumference		474 m
Cycling frequency		15 Hz
Harmonic number	h	84
RF frequency	f_{RF}	30.3 - 52.8 MHz
Revolution frequency (f_{RF}/h)	f_0	360 - 628 kHz
Total # RF cavities		17
Maximum RF voltage	V_{RF}	950 kV
Transition gamma	γ_T	5.446
Long. momentum spread (inj)	$\Delta p/p$	0.4 %
Long. emittance (inj)	ε_L	0.03 eV-sec
Horizontal, vertical tune	ν_X, ν_Y	6.7, 6.8
Trans. emittance (inj)	$\varepsilon_X, \varepsilon_Y$	10, 7π mm-mrad

Focusing of the off-momentum particle motion is a critical concern in a synchrotron. The absence of focusing in either the transverse or longitudinal planes would lead very quickly to beam loss of particles off the nominal trajectory. Modern

synchrotrons focus the beam in the transverse plane using the principle of strong focusing. This is achieved most commonly by using quadrupole electromagnets. The quadrupole fields focus off-centered particles in one plane and defocus them in the other. By alternating the orientation of the poles, one can provide alternating focusing and defocusing simultaneously in both the horizontal and vertical planes. This is called an alternating gradient lattice.[8] Just as in the optical analog with thin convex and concave lenses, a sequence of equal strength positive and negative magnetic lenses can provide a net positive focusing to the circulating charged particle beam. The current through the magnet coils fixes the focal length, which depends also on the beam energy. In the longitudinal plane, the RF system provides the phase stability in addition to acceleration. Phase focusing makes use of the fact that the revolution period varies with particle energy. Particles are trapped and oscillate at the synchrotron frequency in the RF potential, which for the Booster is about 2 kHz for much of the cycle. The magnet lattice fixes what is known as the transition energy, a relativistic effect which defines the point at which the revolution period of all particles is identical, independent of energy. Phase focusing is thereby temporarily lost at transition, an important effect in proton accelerators. Details on longitudinal particle focusing and transition energy will be discussed in Chapter 3.

In the Booster, the primary transverse focusing function is provided by the quadrupole-like fields of the combined-function magnets. Magnet coils in the shape of flat pancakes, located above and below the magnet midplane, provide the guide field that bends the beam around the vacuum chamber. The pole faces are shaped at an angle to one another like a wedge, resulting in a field which also focuses the beam. There are two types of magnets, called D and F, with different angles, focusing the beam either vertically or radially, respectively. The focusing characteristic of conventional quadrupoles is depicted in Figure 2.2, while the fields of the Booster magnets are represented in Figure 2.3. Off-momentum particles execute betatron oscillations of about 1 MHz as they move through the lattice in the Booster. This defines the transverse tune, which is the number of oscillations executed by the particles in one revolution. For historical reasons, these are known as betatron oscillations.

The magnets are made by stacking steel laminations, bonded by epoxy and heat treated, to minimize eddy currents, and the entire combined-function magnet is inside

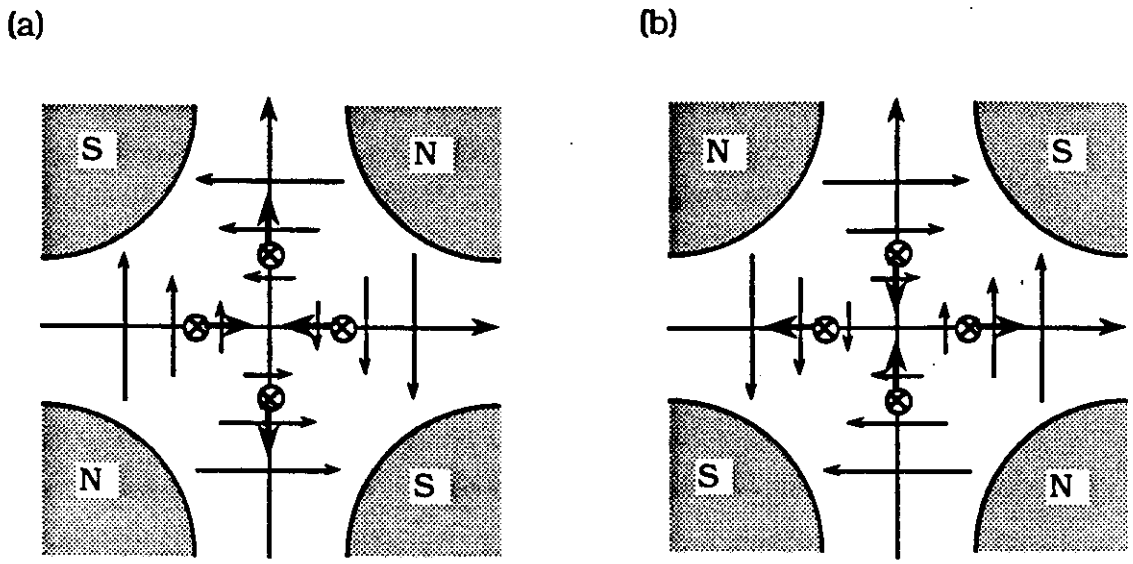

Figure 2.2 Standard Quadrupole Magnets. With the pole faces oriented as in view (a) the magnet is focusing in the horizontal plane, defocusing in the vertical; in view (b), the situation is reversed.

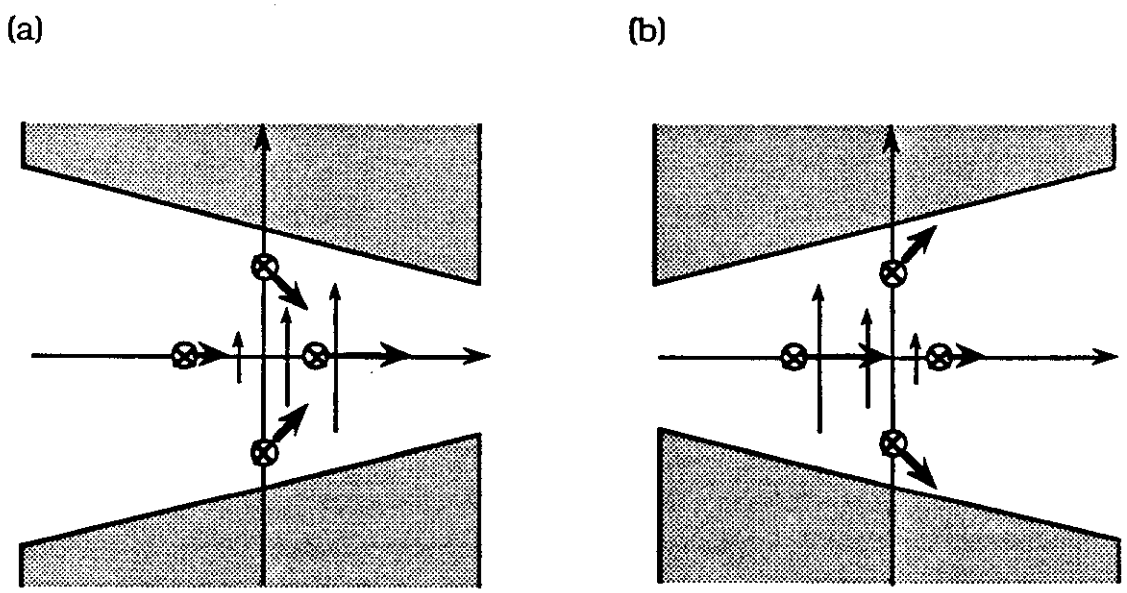

Figure 2.3 Booster Combined-Function Magnets. Positive x points towards the center of the ring. View (a) gives focusing in the vertical plane, defocusing in the horizontal ("D" magnet), while view (b) gives focusing in the horizontal plane, defocusing in the vertical ("F" magnet). The field lines are actually curved such that they are perpendicular to the pole faces.

the vacuum chamber. The beam is directly exposed to these laminations. While this design minimizes the aperture and thus the costs, this is the main source of the broadband impedance in the ring, as will be discussed at greater length in Chapter 6. The magnets are assembled into 48 modules, each consisting of a pair of D and F magnets, a choke, a capacitor bank, an ion pump, a set of correction magnets, and a beam position monitor. Two modules form one period in the Booster lattice. The magnet system is powered in a resonant circuit by a 15 Hz sinusoidal waveform. The magnetic flux density varies from 500 gauss at beam injection to 7000 gauss at extraction. Hence, only half of the cycle is used, where dB/dt is positive.

In order to compensate for remnant and stray field effects, two trim correction magnet assemblies are placed in each period. Fractional transverse tunes are used precisely to avoid resonances due to magnet errors. Each correction package contains horizontal and vertical dipoles to correct the closed particle orbit, quadrupoles to adjust the tune at injection, and skew quadrupoles to suppress coupling between the transverse planes. Skew quadrupoles are rotated 45° from the orientation of normal quadrupoles such that their pole faces are centered on the horizontal and vertical axes of the vacuum chamber. If the transverse tunes are coupled, unstable motion in one plane can be transferred to the other. This can lead to particle loss if, for example, large amplitude excursions in the horizontal plane become translated into the vertical, which generally has a smaller aperture.

Other major subsystems include the vacuum systems, cooling systems, beam injection and extraction, beam transfer, and safety. Details on these systems are not relevant to our study and will not be given here. A number of diagnostics are available to measure the properties of the beam. The detectors used to measure the beam current in the instability studies will be described in Chapter 4.

2.2 RF Cavities

Acceleration in modern synchrotrons is based on the use of RF drive, whereby the charges are bunched and phased to acquire energy from one or more stationary half- or quarter-wave cavity resonators. We will generally refer to these simply as cavities. RF frequencies in the range of several hundred MHz, rather than the particle

revolution frequency which is typically tens or hundreds of kHz, are used for the fundamental frequency in cavities for practical reasons. The cavity is driven externally with RF power coupled into the cavity in a number of ways with the goal of developing a voltage across the single or multiple accelerating gaps. The phase of the sinusoidal RF voltage when the bunches of the beam cross the gap is controlled in a proton machine to remain in the nearly linear portion of the waveform. The fundamental frequency, phase, and voltage in the RF system are programmed to achieve the required synchrotron radius and energy gain in the beam over the cycle. A description of the basic theory behind the design of the Booster RF cavities, based on References 9 and 10, is followed by the design specifics and operational aspects of the system.

Basic Theory

The Booster RF cavities by design fall into an important class known as coaxial cavities. The fundamental resonant frequency is comparable to the geometric length, and the cavity may be represented by a coaxial cable shorted at one end and capacitively loaded at the other. Transmission line theory may be used to find the voltage and current inside the cavity if we assume pure transverse electromagnetic fields, i.e. TEM modes. The fields oscillate in time, and the amplitudes along the line are determined by standing-wave solutions which satisfy the boundary conditions. At the shorted end, for example, the incident and reflected waves cancel, thus the voltage vanishes while the current is maximum. For a small capacitance, the other end of the line is essentially open, and therefore the voltage is maximum and the current minimum.

Figure 2.4 shows the basic geometry and equivalent transmission line for the coaxial cavity. For a lossless transmission line, we may write[9]

$$\begin{aligned} V(s) &= jZ_0 I(0)\sin\beta s \\ I(s) &= I(0)\cos\beta s \end{aligned} \tag{2.2.1}$$

where s is the distance along the line measured from the short (s=0), $Z_0 = \sqrt{L/C}$ the characteristic impedance per unit length, and $\beta=2\pi/\lambda$ the phase constant or wave number. The admittance Y at the gap is given by[9]

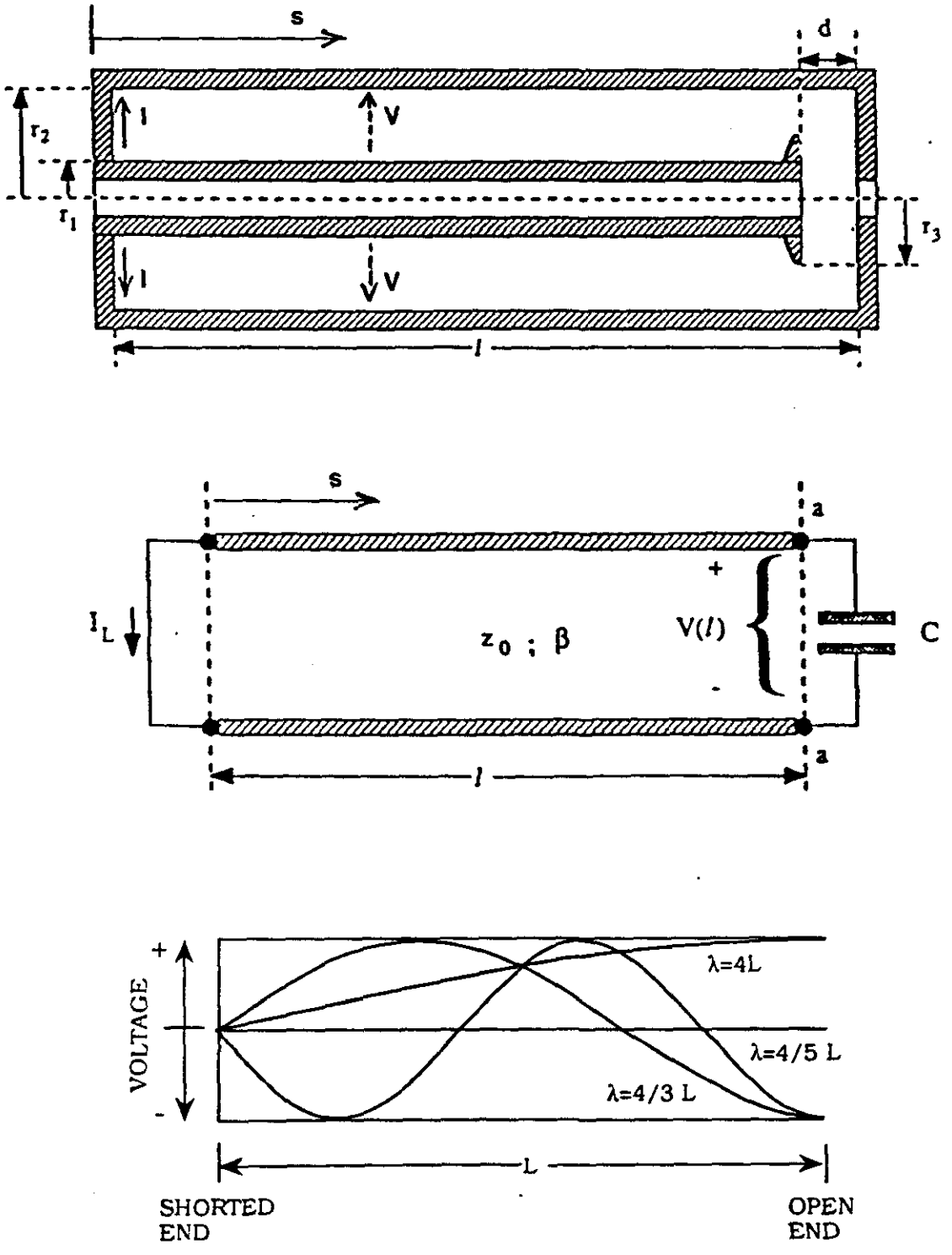

Figure 2.4 Geometry, Equivalent Transmission Line, and Field Pattern for the Quarter-Wave Coaxial Cavity Resonator. (Ref. 9, 10)

$$Y = \frac{1}{Z_C} + \frac{1}{Z(l)} = j\omega C + \frac{1}{jz_0 \tan\beta l} \tag{2.2.2}$$

where Z_C is the impedance due to the "tip capacitance" at the gap and $Z(l)$ is the impedance at the end of the line, at $s=l$, given by $V(l)/I(l)$. To satisfy the boundary condition that the line is open at the end means that $Y=0$ at the gap. By the resonance condition, if $C \rightarrow 0$ then $\tan\beta l \rightarrow \infty$ and thus $\beta l = m\pi/2$ and $l = m\lambda/4$, where m is any odd integer. This gives an infinite number of solutions for waves of wavelength equal to odd multiples of four times the length of the structure, hence the name quarter-wave resonator. The lowest frequency is the fundamental mode.

Booster Cavity Design

The Booster cavity is actually two quarter-wave cavities end to end with the common shorted ends replaced with a reactance. It thus becomes a double-gap structure and may be considered a half-wave structure. A schematic showing the field pattern for the fundamental accelerating mode is depicted in Figure 2.5. Note that at a given instant in time, the electric longitudinal field components at the two gaps are 180 ° out of phase. Net acceleration occurs for protons traversing the cavity if we take into account the time-of-flight in the drift tube between gaps, during which the sense of the field at the second gap changes sign. This is referred to as an even mode. For an odd mode, the fields at the gaps cancel.

A cut-away drawing of the nominal cavity is shown in Figure 2.6. Some of the important parameters of the system are summarized below in Table 2.1. RF power is capacitively coupled into the cavity at the midpoint with a 100 kW power amplifier (PA) mounted on top, while tuning is provided by the three ferrite tuners mounted at the center. The drift tube, a tapered copper structure with a 2-1/4 in beam pipe in the center and whose electrical length is 140 degrees, is situated between the gaps. Alumina insulators at either end provide a vacuum seal for the gaps, the rest of the cavity is open to atmospheric pressure. Not shown are small probes on either side of the PA near the gaps (in air) known as gap monitors, which are used for feedback

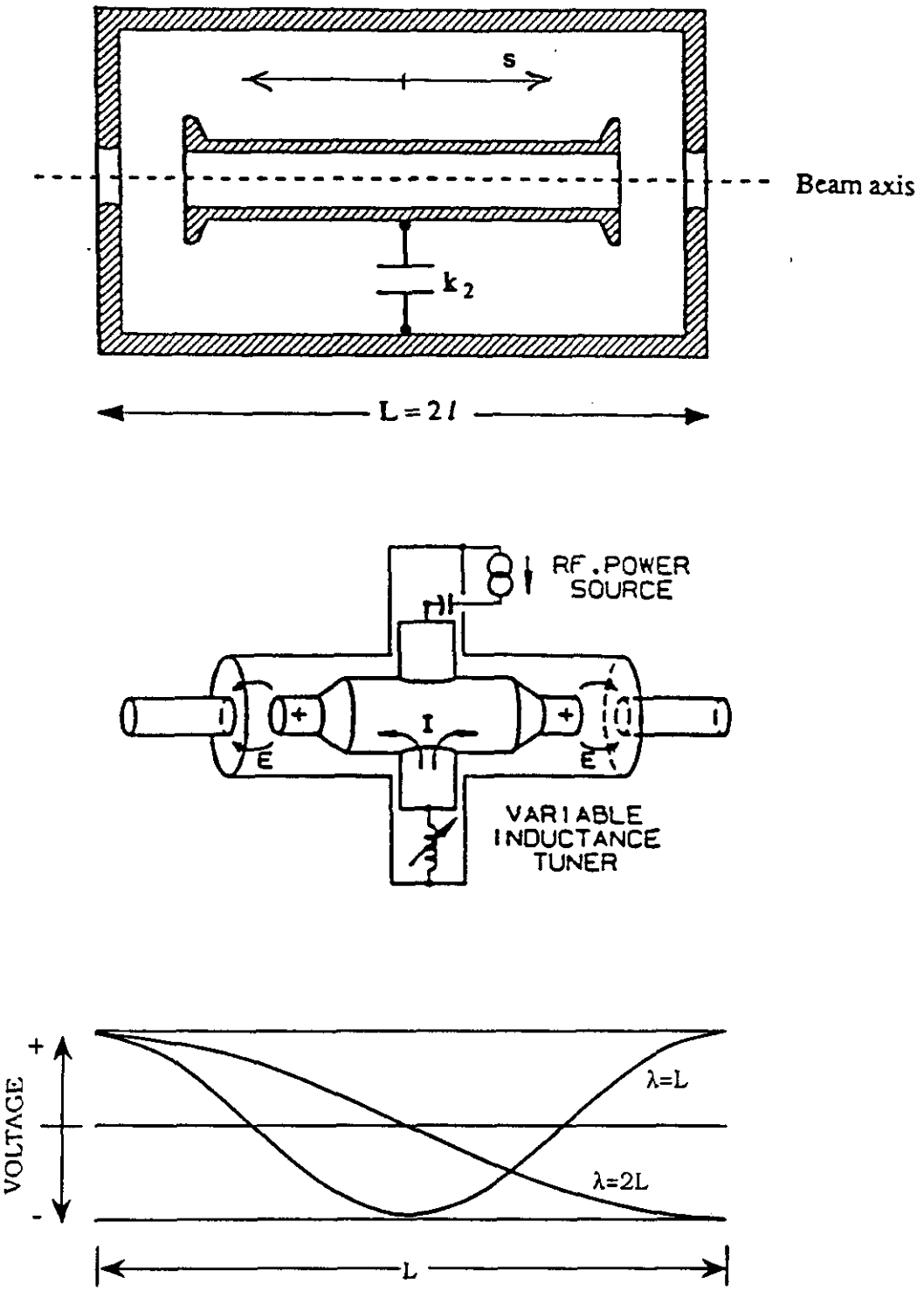

Figure 2.5 Geometry, Schematic, and Field Pattern for the Half-Wave Coaxial Cavity Resonator. (Ref. 9, 10)

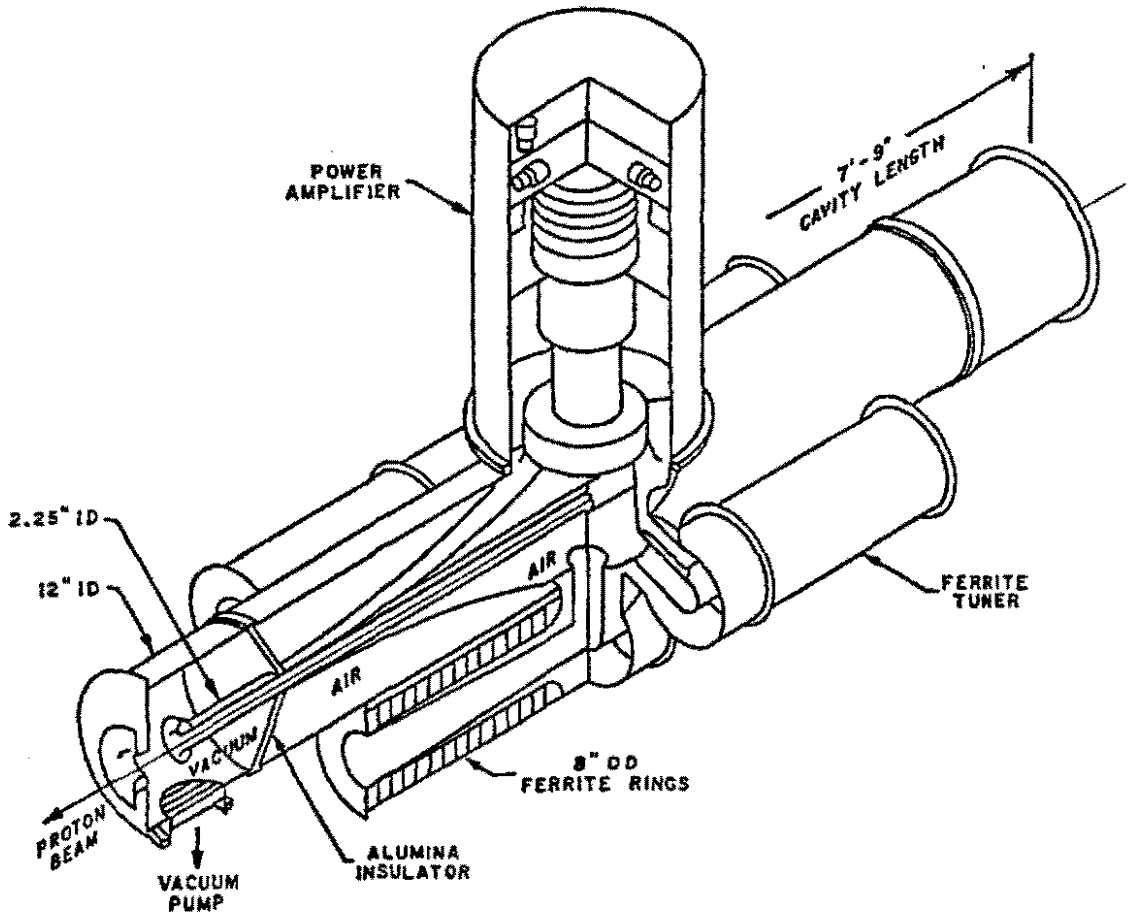

Figure 2.6 Cut-Away Drawing of RF Cavity. (Ref. 5)

control and are available for diagnostics. Also not shown is the cavity short, a ferrite-loaded copper rod on one side and near the PA which, when engaged, directly connects the outer and inner conductors. As such, the gaps are not technically shorted; however, the fields inside the cavity and at the gaps are altered in such a way that the impedance is severely reduced. Another fixture, shown in Chapter 5, Figure 5.12, are internal damping loops terminated in 50 Ω loads known as cantennas. More will be said about these loops in Chapter 5.

The anode of the final tube of the PA is connected through a capacitor to the drift tube, or inner conductor of the coaxial cavity. The blocking capacitor isolates the cavity any DC currents. The PA anode circuit is therefore an integral part of the resonant structure. Since the accelerating voltage and cavity impedance change through the cycle, the power output of the PA is programmed. The anode voltage, up to a maximum 25 kV DC, controls the gap voltage. RF current gain is varied by modulating the current through the cascode driver tubes. Waveforms for the anode voltage and cascode bias are computer generated.

Tune control and bandwidth in the Booster cavities is achieved by using parallel-biased ferrites which function as variable inductors in the equivalent resonant circuit. Ferrite tuners are coaxial transmission lines with shorted ends. The center conductor is connected to the center of the drift tube in the cavity, thus the tuners are a part of the resonating structure. 28 toroidal ferrite cores are mounted, with ten-turn

Table 2.2 RF Cavity Parameters. (Ref. 5)

Ferrite μ_Δ Injection	7.2
Ferrite μ_Δ Extraction	1.5
Cavity Peak Voltage (across two gaps)	54 kV
Axial field strength in gap	0.36 MV/m
Cavity RF current (at current max)	1300 A
Cavity Z_0 (tapers from 80 Ω at a gap to 20 Ω at center)	60 Ω
High Level RF (at location of ferrites)	850 A/m
RF stored energy/cavity at max voltage	0.03

bias windings linking them. The reactance of tuners and, consequently, the fundamental RF frequency of the cavity structure, is controlled by varying the current through the bias windings.

RF System Operation

In the Booster, the energy to accelerate the proton beam is supplied by up to 17 ferrite-tuned RF-driven cavities. They are located in pairs over approximately one third of the ring (see Figure 2.1). One of the original 18 cavities was permanently removed in 1989, together with its power supplies in the gallery directly upstairs, to make room for computers and diagnostic equipment. As noted earlier, the RF frequency sweeps from 30.3 MHz at injection (β=0.57) to 52.8 MHz at extraction (β=0.994) in 33.3 msec. This is nearly an octave (factor of two) in frequency. The frequency ramp rate peaks at 2.8 GHz/sec early in the cycle, falling exponentially to 10 MHz/sec at extraction. The high ramp rate and broad tuning range present design constraints on the RF system as well as on RF phase feedback and beam feedback systems.

In the Booster, beam "capture" into bunches begins at about 2.8 μsec after injection and continues over the next 100-200 μsec (about 50 turns). Ideally, one wishes to cause stable regions, known as RF buckets, to slowly form in the phase space. The coasting beam is thereby captured adiabatically with minimum loss. To this end, paraphasing of the RF cavities is employed. Prior to injection, the relative phase between cavities is adjusted such that the electric fields at the gaps for pairs of cavities are 180 degrees out of phase; hence, no net acceleration occurs. In paraphasing, the pairs of cavities are then slowly brought into phase. In this mode, the cavities are cycled from some fixed, non-zero voltage. This technique hence avoids multipactoring, an undesired cascading of electrons inside the cavity structure, which occurs in the Booster cavities at smaller voltages. After one millisecond into the cycle, the buckets are typically 80-95% filled. During acceleration, the system attempts to maintain the desired energy gain and, in principle, a constant bucket area. The total RF voltage rises up to a maximum of 810 kV just before the middle of the cycle.

An electronics system referred to as the low-level RF system (LLRF) maintains the correct phase relation between circulating beam bunches and the accelerating gap

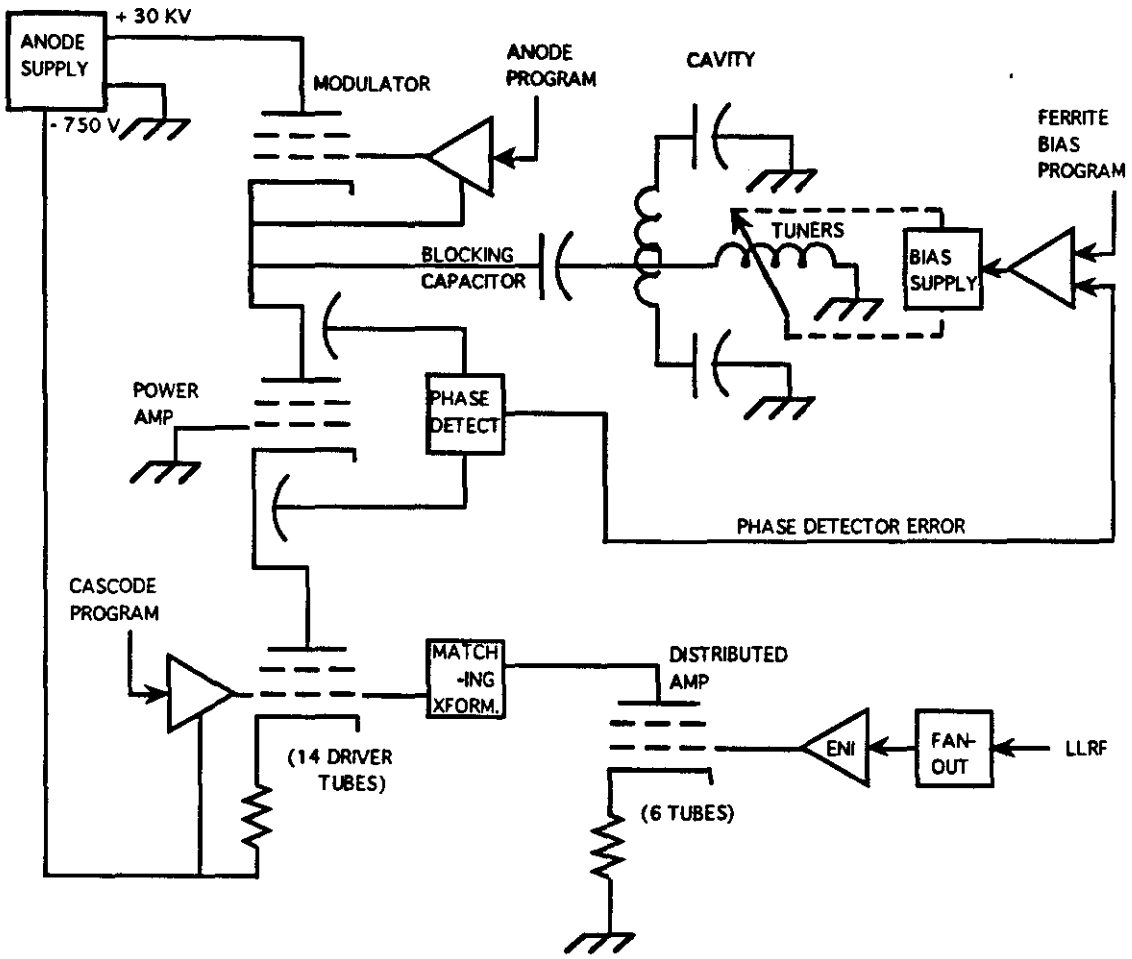

Figure 2.7 Major Components of Booster RF System. (Ref. 10)

voltage. The RF phase angle is continuously adjusted to maintain the required rate of energy gain. Slow feedback keeps the beam at the correct radial position, while fast feedback damps phase oscillations (n=0) through a feedback loop which minimizes the phase error between the RF drive and cavity field (bias running closed loop). By contrast, the high-power components make up the high-level system (HLRF). The major components of the Booster RF system, showing the input of the various programmed curves, is shown in Figure 2.7.

The LLRF uses three approximate programmed curves to control the acceleration process: FREQ, ROFF, RGAIN. The FREQ programs the voltage controlled oscillator (VCO) to generate the RF signal. A feedback loop corrects the approximate VCO frequency to match the beam frequency. A second feedback loop takes signal from the radial position (RPOS) compared with ROFF, which specifies the desired radial position through the cycle. The error signal, the difference between RPOS and ROFF, is multiplied by RGAIN and delivered to the "phase shifter" to correct the accelerating voltage.

At end of cycle, the RF system is phase-locked to that of the Main Ring to achieve a bucket-to-bucket transfer of the beam. In practice, the voltage is about 200 kV at extraction, which is larger than theoretically necessary. In fact, the RF voltage over the second half of the cycle is also larger than is necessary merely for acceleration. Empirically, one finds that the beam is susceptible to losses after transition with lowered RF voltage.

2.3 Operational Considerations

The Booster is a complex system of a multitude of devices by which several operational parameters can be manipulated remotely via computer control. This is typical of modern synchrotrons, and the allowable range over which these parameters can be changed varies in each machine. In a typical accelerator physics experiment, beam behavior is studied while one parameter, such as the beam intensity, is varied, keeping everything else fixed. Full control, or even knowledge, of all relevant parameters is not always possible. Also at issue is the long- and short-term repeatability of the studies. Discussion of some of the specifics of the operational

considerations and limitations is best appreciated after the synchrotron theory is presented, and it will thus be postponed until either the next chapter or Chapter 5, in which the experiments are described in detail. Below is a summary of the basic operation of the Booster, outlining the parameter space which can be explored. The discussion is limited to those aspects which impact the present study of the longitudinal coupled-bunch instability.

Operational parameters which may be varied are divided into two categories: those relating to the properties of the beam itself and those relating to its environment, the beam line. Foremost, as previously mentioned, the beam intensity can and is routinely varied from about 0.5 to 2.5×10^{12} protons per pulse. The timing of the "chopper", the device which selects the injected beam pulse length, is changed to choose one or more turns. In addition to intensity, the input longitudinal beam momentum spread can be changed in a limited way. By manipulating the acceleration system in the Linac, the momentum spread in the extracted beam can be increased by about 60%. Finally, the beam energy can be changed, again, in a very limited way. The 15 Hz cycle for the magnets is fixed; therefore the options are: standard acceleration from 200 MeV to 8 GeV, acceleration from 200 MeV to an energy less than 8 GeV, and fixed energy (injection). The magnet current and RF system program must be changed to extract at another energy. In order to achieve a coasting beam, neither the magnets nor the RF is ramped. The coasting beam lifetime is only a few seconds. In either non-standard case, a dedicated study period is required as these changes disrupt normal operations. After the proposed Linac upgrade during the summer of 1993, the injection energy will be raised to 400 MeV. It is expected that this will reduce early beam losses due to space charge effects. The extraction energy will remain fixed at a nominal 8 GeV.

Beam line components which are found to impact the longitudinal stability of the beam include, naturally, the RF cavities and the transition-jump system. Regarding the RF system, one may choose to accelerate with between a minimum of 12 to all 17 cavities turned on. The nominal number is 15 or 16, which allows for a few spares. The maximum RF voltage available obviously changes when alternating between cavity configurations, unless the RF voltage on individual cavities is changed simultaneously. There is a minimum RF voltage necessary for acceleration, and if running too few cavities, one risks frequent sparking inside the cavity. The RF drive

and bias current is normally disconnected and the shorts engaged in the cavities which are turned off. The cavity shorts are mechanically operated via computer control; therefore their effect can be studied separately. For studies, up to five cavities can be removed entirely from the ring and replaced by a simple beam pipe.

The transition-jump system affects the dynamics of the beam through transition energy. Its goal is to retain to the extent possible the linear properties of the beam during transition. The effect of the jump system on the coupled-bunch instability is highly variable, depending on the machine operating state, i.e. the way that the Booster is "tuned", and the timing of the jump. More will be said about this later. In general, this system is turned off for the coupled-bunch instability studies to isolate its effect and help simplify the analysis of the problem.

The afore-mentioned longitudinal beam damping system is also available. Some study was made recently with the system; however, it is old, has fallen into disrepair, has not influenced the longitudinal emittance at nominal intensities, and thus is not normally used. Therefore, the damper is turned off for the bulk of our studies. The ongoing upgrade of the system is beyond the scope of this work.

Before studies can be performed, a steady operating state must be achieved and maintained. While the Booster is available much of the time, normal operation periodically requires scheduled or emergency shutdown for maintenance. After magnet and RF systems are repowered, and especially after the beam line has been altered, the Booster must be tuned, whereby the proton beam is steered into and around the ring using the correction magnets. In the process, the transverse fractional betatron tune is also adjusted. Basic tuning after a major shutdown is an iterative process during which the injection efficiency and extracted intensity are maximized and early beam losses minimized. Because these losses are related to space charge effects which increase with intensity, the tuning procedure is repeated for ever higher intensity settings. This process may take weeks. Magnet settings are stored in individual tables for each intensity setting.

Ideally, all beam studies are performed with the machine in the same, controlled state. Once tuned, the machine can remain stable for weeks at a time. Each time the Booster is tuned, however, it is left in a new operating state. The

settings of major components are saved periodically, but because of the numerous variables in the system, very old tables cannot necessarily restore the previous operating conditions. The tune can be measured, but not automatically as of the study period. Slow drifts in the bending magnet current also occur on the scale of days. Fluctuations, drifts, or deliberate changes in the Linac or the H^- source change the initial conditions in the Booster. These all have a potential but unquantified effect on the longitudinal stability of the beam. Longitudinal emittance data from several years ago can be very different from recent data, even when no known changes were made to the Booster in the intervening period. Data obtained over a relatively short time, for example, on a scale of days or a week, are the most believably compared.

3. THEORETICAL BASIS

Beam instabilities is a rich and important area of study in accelerator physics. While the focus of this thesis is experimental, significant effort was devoted to interpreting and adapting the theory to explain the observations. In this work, we limit our discussions to the case of longitudinal bunched-beam instabilities in a proton machine. It is not my intent to reproduce in entirety the breadth of this subject as many good references abound; these will be cited where appropriate. The basic topics and equations extracted from the literature which are germain to this thesis are presented in this chapter. Detailed calculations and results, including discussions of the general and specific applicability of the linear formalism using the case of the Booster, are deferred to Chapter 6. In some cases, data reduction is included in the same chapter as that describing the raw measurements.

The motion of charged particles in an accelerator is, as for many other physical systems, approximately harmonic. The dynamics is classified into two categories: incoherent and coherent. The design of the magnets, focusing optics, and RF system concerns the incoherent, or single-particle, motion. The reference, or synchronous, particle is that which follows this design trajectory, and the motion of all other particles is described relative to it. In the presence of destabilizing forces, the beam responds in one or more of its coherent, or collective, oscillation modes. The methods of statistical physics are invoked to describe these collective effects. Although the physics is not unfamiliar, some of the terminology and concepts are specific to accelerator physics and therefore merit some discussion.

As a basis, then, we begin with an introductory discussion of single-particle longitudinal motion in phase space. The corresponding kinematics for the Booster are given. In the next section, we describe what we mean by collective, longitudinal coupled-bunch modes and spectral analysis. Finally, in the last section, we discuss the analysis of collective, unstable phenomena. Included is the derivation of expressions used to compute the linear instability growth. Also described are

wakefields and coupling impedance, including the model impedance for RF cavity resonant modes.

3.1 Introduction to Longitudinal Beam Physics

The basic figures-of-merit of a synchrotron are described in terms of the concepts which are described below. The material is drawn largely from References 8, 11, 12, 13 and 14, an assortment of basic texts and compendia of beam equations. The topics are arranged into four major areas. The single-particle kinematics such as accelerating voltage, energy gain, and related parameters are given first. Next, a derivation for transition energy is presented. Then, motion of the particles within the RF potential is described together with the conditions for longitudinal phase stability. To first order, the solutions to the equations of motion for the off-momentum particles are linear. The result for the nonlinear variation of the particle oscillation, important in our study of instabilities, is presented. Finally, the method adopted for computing longitudinal emittance from observable quantities is given. Included is a discussion of the intrinsic assumptions made in the calculation.

Single-Particle Kinematics

The relations among the dynamical quantities for a relativistic beam are given by the familiar expressions

$$\begin{aligned}
&\beta = \frac{v}{c} = \frac{cp}{E} \\
&\gamma = \frac{1}{\sqrt{1-\beta^2}} \\
&E = \gamma E_0 && \text{total energy} \\
&K = E - E_0 = E_0(\gamma - 1) && \text{kinetic energy} \\
&cp = \sqrt{E^2 - E_o{}^2} = E_0\sqrt{\gamma^2 - 1} && \text{momentum}
\end{aligned} \tag{3.1.1}$$

where the rest energy E_0 is 0.9383 GeV for protons. In an ideal accelerator, there is a reference particle, known as the synchronous particle, which travels along the axis of

the axis of the machine, known as the design trajectory. The velocity β of the design particle may be written as

$$\beta = \frac{\omega_0 R}{c} = \frac{cp}{E} \tag{3.1.2}$$

where R is the radius of the synchrotron ring, ω_0 is the angular revolution frequency, and c is the speed of light. Acceleration is provided by a time-varying electric field generated inside the radio-frequency (RF) resonant cavities. A consequence of this RF field is that the beam is bunched. The frequency ω_{RF} of the RF system is related to the revolution frequency by

$$\omega_{RF} = h\omega_0 \tag{3.1.3}$$

where h is known as the harmonic number, the maximum number of bunches. The energy gained by the design particle per passage (once per turn) through the RF cavities is

$$\Delta E_s = e\hat{V}\sin\phi_s \tag{3.1.4}$$

Here $\hat{V}$ is the total peak RF voltage and ϕ_S is the phase, with respect to the zero-crossing of the RF field, at the moment t that the synchronous particle arrives. The subscript s is used throughout this paper to denote the synchronous particle. In the Booster, the average energy gained by a proton during one turn may be roughly calculated using $\frac{8\,\text{GeV}}{33\,\text{msec}} \text{x} \frac{2\,\mu\text{sec}}{\text{turn}} = 0.5\,\text{MeV / turn}$ average.

The magnetic field B must also vary to keep the radius of the motion fixed. Recall that for circular acceleration of a charged particle under the influence of a magnetic field , the momentum is given by

$$p = e\rho B \tag{3.1.5}$$

where ρ is the radius of curvature of the motion inside the magnet. Because in general in a synchrotron, the magnets physically occupy only a portion of the circumference of the machine, the radii ρ and R are not exactly the same. The energy gain per turn of

the synchronous particle may be expressed in terms of B by computing the force per unit length integrated over the circumference C

$$\Delta E_s = \oint_C F \circ ds = 2\pi R \frac{dp}{dt} = 2\pi e \rho R \frac{dB}{dt} \tag{3.1.6}$$

All the kinematic parameters, including the RF frequency and voltage, may be derived from the desired momentum (or kinetic energy) at injection and extraction. In the Booster, the time variation of the magnet field, and hence also the momentum, is sinusoidal, following a 15 Hz repetition rate

$$cp(t) = A_1 + A_2 \cos(30\pi t) \tag{3.1.7}$$

where the constants $A_1 = \frac{1}{2}(cp_i + cp_f)$ and $A_2 = \frac{1}{2}(cp_i - cp_f)$ are determined by the boundary conditions. The time t refers to the time in the cycle after injection at t=0. The accelerating voltage is computed from the required energy gain using (3.1.6).

$$V_a(t) = \frac{\Delta E_s}{e} = \frac{2\pi R}{e} F(t) \qquad [\mathrm{V}] \tag{3.1.8}$$

$$F(t) = \frac{1}{c}\frac{d(cp)}{dt} = \frac{-30\pi A_2}{c} \sin(30\pi t) \qquad [\mathrm{eV/m}] \tag{3.1.9}$$

The phase of the accelerating RF voltage relative to the synchronous particle, assuming the peak RF voltage $\hat{V}$ is known as a function of time, is given by rewriting (3.1.8) using (3.1.4)

$$\phi_s = \arcsin\left(\frac{V_a(t)}{\hat{V}(t)}\right) \tag{3.1.10}$$

Transition

One may define several characteristic constants in an accelerator which are a function of the energy spread in the beam. For example, a particle with greater momentum than the design particle will bend less in the dipole guide field and thus

experience a larger radius. Off-momentum particles traversing the quadrupole fields off-axis are also bent with varying radii as if in dipole fields. All this leads to a difference in path length with respect to the design particle over the closed orbit. One defines a parameter known as the "momentum compaction" factor, the differential ratio of this path length difference to momentum difference. To first order, it is expressed as

$$\alpha = \frac{dR}{R}\frac{p}{dp} = \frac{1}{\gamma_T{}^2} \tag{3.1.11}$$

Note that α, and thus γ_T, are constants. As seen earlier, the quadrupole fields are responsible for defining the machine "tune". The momentum compaction factor may be formally derived in terms of the bending angles and strengths of the quadrupoles; here, we will only state that for most simple lattices, $\gamma_T \approx \nu_x$, the horizontal tune.[11]

Another parameter is η, the frequency dispersion or "slip factor", which relates the change in revolution period to the change in momentum for a fixed magnetic field. Again, to first order, it is given by

$$\eta = -\frac{d\omega_0}{\omega_0}\frac{p}{dp} = \frac{dT}{T}\frac{p}{dp} \tag{3.1.12}$$

From equation (3.1.2), we may express the period as $T = \frac{2\pi}{c}\frac{R}{\beta}$. Then, using equations (3.1.1), we may write

$$\frac{dT}{T} = \left(\frac{dR}{R} - \frac{d\beta}{\beta}\right) \qquad \frac{d\beta}{\beta} = \frac{1-\beta^2}{\beta\gamma}d\gamma = \frac{d\gamma}{\beta^2\gamma^3} \qquad \frac{dp}{p} = \frac{\gamma\, d\gamma}{\left(\gamma^2-1\right)} = \frac{d\gamma}{\beta^2\gamma} \tag{3.1.13}$$

Combining terms and substituting into eqn. (3.1.12), we have

$$\eta = \left(\frac{dR}{R} - \frac{d\gamma}{\beta^2\gamma^3}\right)\frac{p}{dp} = \frac{dR}{R}\cdot\frac{p}{dp} - \frac{1}{\gamma^2} = \frac{1}{\gamma_T{}^2} - \frac{1}{\gamma^2} \tag{3.1.14}$$

The first term is just the momentum compaction factor. We associate γ_T with a specific energy known as the transition energy. In most proton machines, η changes sign over the acceleration cycle, starting out negative as initially, $\gamma < \gamma_T$. The

implication of this result is that there exists a beam energy $\gamma E_0 = \gamma_T E_0$ when η=0 for which the period of all particles is equal, independent of energy. This has consequences for longitudinal phase stability, as discussed below. The expression (3.1.14) is not strictly valid exactly at transition, where nonlinear effects must be taken into account (higher-order terms in $\delta p = dp/p$). While changing the dynamics of the beam when crossing transition is seen experimentally to affect the coupled-bunch instability, a theoretical treatment of transition is beyond the scope of this work.

RF Phase Stability

Acceleration in a synchrotron would be impossible without longitudinal phase focusing. That particles are trapped and oscillate in the potential provided by the RF system is attributed to the existence of frequency dispersion, i.e. that the revolution period varies with particle energy. This will become clear as we derive the longitudinal equations of motion.

The trajectory of an arbitrary particle may be described in the particle frame of reference. We will use the phase space coordinates $(\Delta E, \Delta\phi)$, the deviation in energy and phase relative to the synchronous particle. As these deviations are typically very small, the derivative and difference operators $d \leftrightarrow \Delta$ are often used interchangeably in the literature. By eqns. (3.1.4), the energy gained and the rate of phase advance by an off-momentum particle are expressed as

$$dE = e\hat{V}(\sin\phi - \sin\phi_s) \tag{3.1.15}$$

$$d\dot{\phi} = -h\, d\omega_0 \tag{3.1.16}$$

Recalling the relativistic relations (3.1.1) and eqn. (3.1.12), we write

$$\frac{dp}{p} = \frac{1}{\beta^2}\frac{dE}{E} \tag{3.1.17}$$

$$\eta = -\frac{d\omega_0}{\omega_0}\frac{\beta^2 E}{dE} = -\beta^2 \frac{d\omega_0}{\omega_0}\frac{\gamma}{d\gamma} \tag{3.1.18}$$

Solving for $d\gamma$ in terms of η in eqn. (3.1.18) and using (3.1.16),

$$dE = E_0 d\gamma = \frac{E_0 \gamma \beta^2}{\eta h \omega_0} d\dot{\phi} = \frac{2\pi E_0 \gamma \beta^2}{\eta h \omega_0{}^2} \frac{d\dot{\phi}}{dt} \tag{3.1.19}$$

In writing eqn. (3.1.19), we have assumed that β, η, γ, and ω_0 vary slowly with respect to the synchrotron oscillation. Equating eqns. (3.1.15) and (3.1.19) leads to the classical differential equation for synchrotron motion:

$$\ddot{\phi} + \frac{\eta h \omega_0{}^2 e\hat{V}}{2\pi E_0 \gamma \beta^2}(\sin\phi - \sin\phi_s) = 0 \tag{3.1.20}$$

The trajectory in phase space is obtained using the standard procedure of multiplying (3.1.20) by $\dot{\phi}$ and integrating over time. The result gives total "energy" $T+V=U$:

$$\tfrac{1}{2}\dot{\phi}^2 + \frac{\eta h \omega_0{}^2 e\hat{V}}{2\pi E_s \gamma \beta^2}(\cos\phi - \phi\sin\phi_s) = \text{constant} \tag{3.1.21}$$

Using eqn. (3.1.19), we rewrite (3.1.21) to obtain the contours of the motion in $(\Delta E, \Delta\phi)$ phase space

$$\Delta E^2 + \frac{E_s \gamma \beta^2 e\hat{V}}{\pi \eta h}(\cos\phi - \phi\sin\phi_s) = \text{constant} \tag{3.1.22}$$

In small amplitude oscillations, the influence of the sinusoidal RF wave on particle motion is essentially linear. In this limit, eqn. (3.1.22) describes circular contours. For small amplitudes $\Delta\phi = (\phi - \phi_s) << 1$; therefore,

$$\sin\phi = \sin(\phi_s + \Delta\phi) \approx \sin\phi_s + \Delta\phi\cos\phi_s \tag{3.1.23}$$

Expression (3.1.20) simplifies to simple harmonic motion about the synchronous phase with the so-called synchrotron frequency ω_s:

$$\ddot{\phi} + \omega_s{}^2(\phi - \phi_s) = 0 \tag{3.1.24}$$

$$\omega_s = \sqrt{\frac{\eta h \omega_0{}^2 e\hat{V} \cos\phi_s}{2\pi E_s \gamma \beta^2}} \tag{3.1.25}$$

In the case of larger amplitude oscillations, the particles are affected by an increasingly nonlinear RF waveform, and the path in phase space given by eqn. (3.1.22) becomes distorted as seen in Figures 3.1 and 3.2. The maximum path for which the particle motion is still bounded defines the separatrix. In eqn. (3.1.24), stability of motion requires that ω_s be real; therefore, $\eta \cos\phi_s > 0$, leading to the conditions

$$\begin{aligned} &\text{before transition:} \quad \eta < 0, \quad \frac{\pi}{2} < \phi_s < \pi \\ &\text{after transition:} \quad \eta > 0, \quad 0 < \phi_s < \frac{\pi}{2} \end{aligned} \tag{3.1.26}$$

Phase stability may be understood as follows, using the illustrative diagram in Figure 3.1. Before transition, a particle with less energy than the synchronous particle will lag in phase because of its smaller velocity. It will arrive later at the RF gap and, because the longitudinal electric field is sinusoidal, see a larger RF voltage, and gain more energy than the synchronous particle. Half a synchrotron period later, it will have overtaken the synchronous particle and arrive earlier, whereupon it sees a smaller RF voltage and falls behind once more. The particle trajectory follows a closed ellipse in phase space and is therefore stable. After transition, because of the relativistic effect, particles with more or less energy have virtually equal velocity. Instead, the increased path length of a particle with greater energy causes it to lag behind, so now, a lagging particle needs a smaller energy gain to remain stable. This is achieved by satisfying the stability criterion in eqn. (3.1.26): at transition, where η changes sign, the RF phase ϕ_s must be suddenly shifted by π. A particle arriving late at the RF gap will consequently experience a smaller voltage.

The enclosed regions in phase space of stable particle motion are called the "RF buckets." All the particles trapped within these buckets may be accelerated or otherwise controlled, and are collectively known as the "bunches." The area, height, and length of a single bucket may be calculated using the following expressions:[13]

$$\text{bucket area} = \frac{16\beta}{\omega_{RF}} \sqrt{\frac{e\hat{V}E_s}{2\pi|\eta|h}}\, \alpha(\Gamma) \qquad [\text{eV} - \text{sec}] \tag{3.1.27}$$

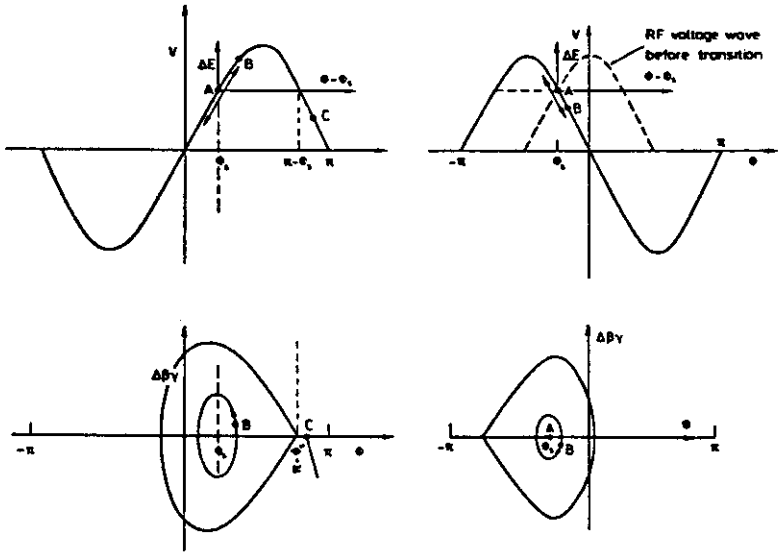

Figure 3.1 Longitudinal Phase Stability of Synchrotron Motion. The view at left shows the case before transition, while the one at right shows after transition. [Ref. 12]

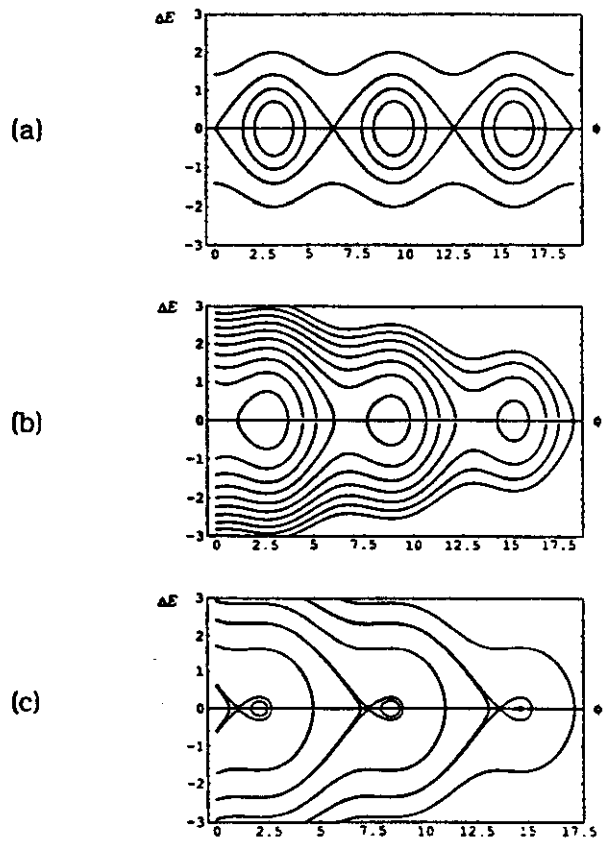

Figure 3.2 Contours of Particle Motion in Longitudinal Phase Space. All cases are after transition; the synchronous phases are (a) $\phi_s=\pi$, (b) $\phi_s=5\pi/6$, and (c) $\phi_s=2\pi/3$. [Ref. 8]

$$\text{bucket height} = \pm\frac{2\beta}{\omega_{RF}}\sqrt{\frac{e\hat{V}E_s}{2\pi|\eta|h}}\,\beta(\Gamma) \qquad \text{[eV - sec]} \qquad (3.1.28)$$

$$\text{bucket length} = \phi_2 - \phi_1 = \pi - \phi_s - \phi_1 \qquad \text{[rad]} \qquad (3.1.29)$$

The functions $\alpha(\Gamma)$ and $\beta(\Gamma)$, where $\Gamma = \sin\phi_s$, are the "moving bucket" parameters and may be found in table form in Ref. 14. Reference to "moving" means that the beam is being accelerated. When Γ=0, the beam is "coasting" at fixed energy, and the bucket is called "stationary." The effect on the RF bucket of varying the synchronous phase angle can be seen in Figure 3.2. The moving bucket parameters, in addition to the variation in the phase ϕ_1 of the bucket edge, are plotted in Appendix A, Figure A.1.

The synchrotron frequency can no longer be assumed constant for large amplitude particles. The spread in frequencies is an important effect in the case of coherent longitudinal instabilities as this provides the only stabilizing mechanism. Derivation of the amplitude dependence of the synchrotron frequency involves solving for the period of the motion in eqn. (3.1.21) by solving for $\dot{\phi}$ and integrating $T_s = \int dt = \int d\phi/\dot{\phi}$. The result involves elliptic integrals. An alternate approximate approach follows the method of Kryloff and Bogoliuboff, in which an approximate solution for ϕ is applied, assuming an amplitude-dependent frequency, the amplitude itself unchanged by the nonlinearity.[15] For the stationary bucket, the widely-quoted result is[8,11,13,15]

$$\omega_s(\phi_L) = \omega_s(0)\frac{\pi}{2}\frac{1}{K\left(\sin^2\frac{\phi_L}{2}\right)} \approx \omega_s(0)\left(1 - \frac{\phi_L^{\,2}}{16}\right) \qquad (3.1.31)$$

where ϕ_L is the half bunch length in [rad], $\omega_s(0)$ is the synchrotron frequency in eqn. (3.1.25), and $K(x) = \int_0^{\pi/2}\left(1 - x\sin^2\theta\right)^{-\frac{1}{2}}d\theta$ is the complete elliptic integral of the first kind. The approximate expression on the right hand side in (3.1.31) is valid for small bunch lengths ϕ_L <<1. For the moving bucket, the case in which we are more interested, two authors offer the solution[9,16]

$$\omega_s(\phi_L) \approx \omega_s(0)\left(1-\left(1+\frac{5}{3}\tan^2\phi_s\right)\frac{\phi_L{}^2}{16}\right) \tag{3.1.32}$$

A derivation for the approximate expression in (3.1.32) is given in Ref. 9 using an expansion around ϕ_s, keeping terms to fourth order. A graphical representation of the amplitude-dependent synchrotron frequency is shown in Appendix A, Figure A.2 in a family of curves for various values of ϕ_s taken from Ref. 11.

Longitudinal Emittance

The energy-time (2-dim) phase space area occupied by a "bunch", an ensemble of particles trapped within an RF bucket, is known as the longitudinal emittance. In a machine of several bunches, the quantity of interest is the average single-bunch emittance. As this is a pivotal quantity in this thesis, careful attention is given to the varying definitions and assumptions in the literature. The beam area is estimated by assuming that the outer boundary of the phase space distribution of the particles in the bunch is "matched" to the contours of constant energy in the RF bucket (recall eqn. (3.1.22)). As the bucket parameters are easily calculated by eqns. (3.1.27) - (3.1.29), the beam parameters may be obtained as a ratio of bunch to bucket length multiplied by the appropriate bucket quantities:[13]

$$\varepsilon_L = \text{beam area} = (\text{bucket area})\left(\frac{\text{total bunch length}}{\text{total bucket length}}\right)^2 C_A(\Gamma) \quad [\text{eV - sec}] \tag{3.1.33}$$

$$\Delta E = \text{beam height} = (\text{bucket height})\left(\frac{\text{total bunch length}}{\text{total bucket length}}\right) C_H(\Gamma) \quad [\text{eV}] \tag{3.1.34}$$

The beam parameters may be determined from the plot in Appendix A, Figure A.3 (Ref. 13). The bunch length may be directly observed using a resistive-wall monitor, which samples the longitudinal charge distribution. This signal was shown in Figure 1.1. The bunch length measured must be consistent with one of two definitions of emittance commonly used: the r.m.s. and the 95% emittance. In this thesis, we adopt the notion that the emittance gives the area occupied by 95% of the particles. Then, the bunch length represents nearly all of the particles (97%).

Several difficulties present themselves in calculating the emittance of the beam. Often, it is difficult to determine the baseline in the signal from which to determine the edge of the bunch. There can be noise or undesired reflections in the signal. Measurements using a digital oscilloscope facilitate recording the measurements, but limits on resolution may impede precision. More will be said about the specific limits in our case in Chapter 4. Many authors suggest assuming a specific phase space distribution for analyzing the beam. For proton beams, most adopt the elliptic distribution, which has a parabolic projection (charge density.) The gaussian is preferred as describing electron beams. The longitudinal bunch signal may then be fitted with such a function and the bunch length deduced. In the case of stable beams, this approach is probably adequate. However, as we shall see in the Booster, on development of instabilities, the bunch becomes irregular and often asymmetric. The simulation results, presented in Chapter 7, suggest that strong filamentation of the beam may be occurring. The result is that the above calculation of the emittance overestimates the true beam area.

A program was written to produce tables of the time variation of the Booster parameters for various initial conditions. It should be noted that at Fermilab, a distinction is made between the machine's acceleration cycle and the global cycle. The latter is a relative timeline which is used to trigger specific processes and programs for operations. Hereafter, most references to the "cycle" will indicate this global timeline. Output for the standard Booster kinematic conditions in increments of 1 msec is found in Appendix A, Table A.1 (all 17 cavities). The bucket length has been converted from [rad] to [sec] by dividing eqn. (3.1.29) by ($h\omega_0$); likewise, the bucket height is expressed in [eV] by multiplying eqn. (3.1.28) by ($h\omega_0$). Note that beam is injected at 2 msec in the cycle, so that extraction occurs at 35.3 msec. One variation, with the extraction energy changed to 4 GeV, is given in Table A.2. Table A.3 shows the parameter set for operation after the Linac upgrade is completed, when the injection energy is changed to 400 MeV. Typical values for the dynamic RF and beam parameters in the Booster are also plotted in Appendix A. The titles of these figures are self-explanatory.

3.2 Coupled-Bunch Modes

We were introduced briefly in Chapter 1 to the signature of coupled-bunch motion in the time domain in the case of the Booster. Before discussing how they arise and become unstable, we will illustrate the coupled-bunch mode structure with a simple example of M=6 bunches first graphically, then using spectral analysis. We adopt the notation of Sacherer,[4] while the graphical representation is inspired by Baartman[9]. The coupled-bunch modes are denoted by the index n. There are two associated intrabunch synchrotron oscillation modes; the rigid azimuthal mode and the non-rigid radial mode. It can be shown that the azimuthal modes, denoted by index m, are dominant[9]; therefore, we assume the radial modes can be neglected.

Consider first a single bunch in phase space. For the bunch to be rigid, we assume that the synchrotron frequency ω_s is constant for all particles. The normalized phase space coordinates are $(\tau, \dot{\tau}/\omega_s)$, where τ is the arrival time of a particle relative to the synchronous particle and $\dot{\tau} = \eta \Delta p/p$ is proportional to the momentum spread. In the drawing at the upper left of Figure 3.3, view (a) , the bunch is shown in phase space centered on the synchronous position. Below it is the charge density, which is the longitudinal projection or the signal $s_{||}$ that would be detected in a resistive wall current monitor. At the right, the bunch is displaced a distance τ_a. As it rotates in phase space, $s_{||}$ is seen to execute harmonic motion about the synchronous equilibrium position with amplitude τ_a. This is the dipole bunch mode m=1.

If the bunch becomes distorted, say elongated, and is no longer matched to the RF bucket, it will "tumble" as it rotates. In the drawing in the middle of Figure 3.3, we see two views timed one quarter synchrotron turn apart in phase space. The oscillations in $s_{||}$ remain centered on the synchronous position, but the charge density amplitude appears to be varying. This is the quadrupole mode m=2, also called the "breathing" mode. When the synchrotron phase goes through an angle π, the bunch distribution returns to its original orientation, so the effective frequency is $2\omega_s$.

Higher modes are possible. In the sextupole mode m=3, the frequency is $3\omega_s$. It shown in three views at the bottom of Figure 3.3 each separated in synchronous

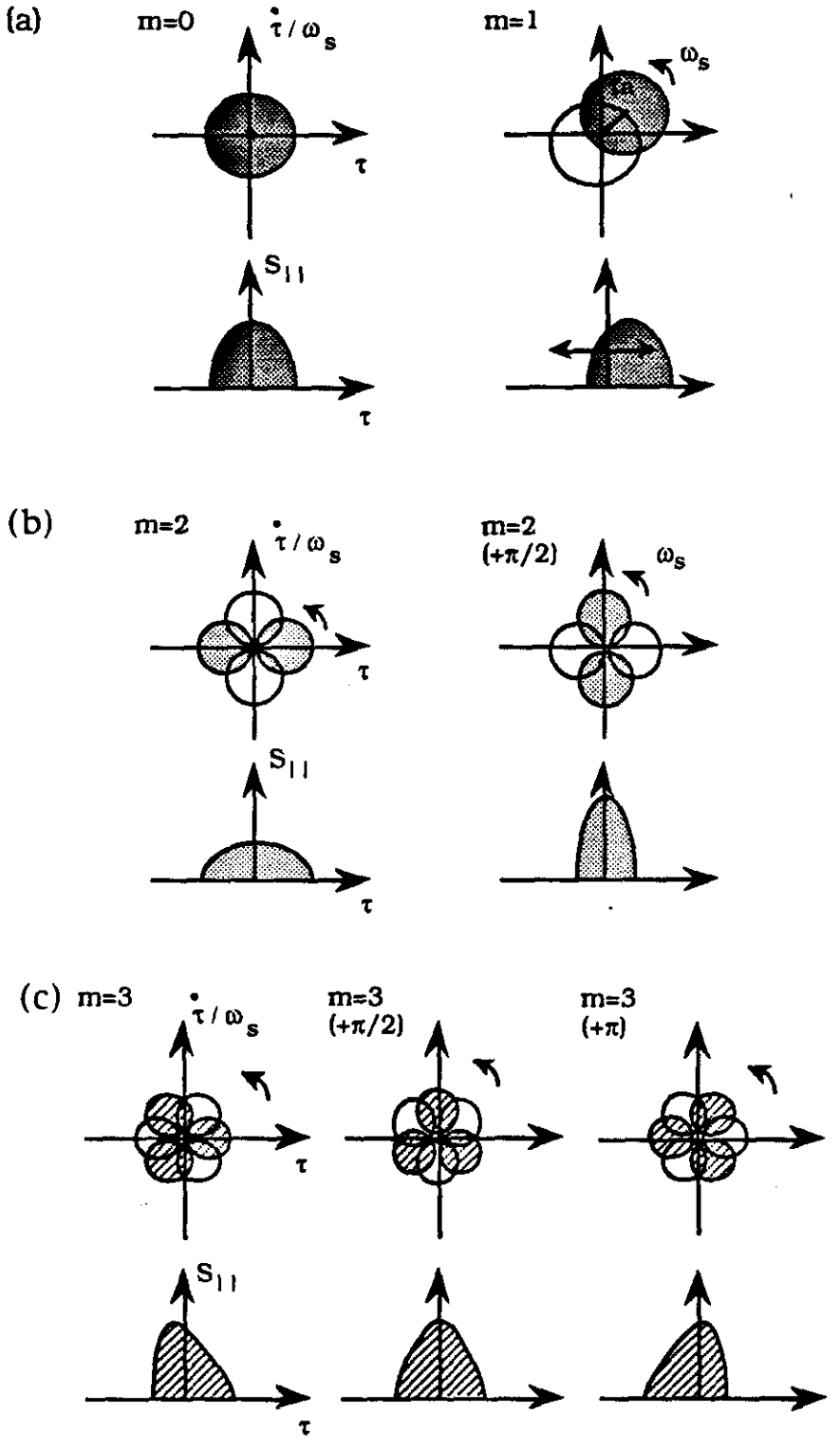

Figure 3.3 Phase Space Area and Charge Density Representations of Synchrotron Oscillation Modes: (a) dipole, (b) quadrupole, and (c) sextupole.

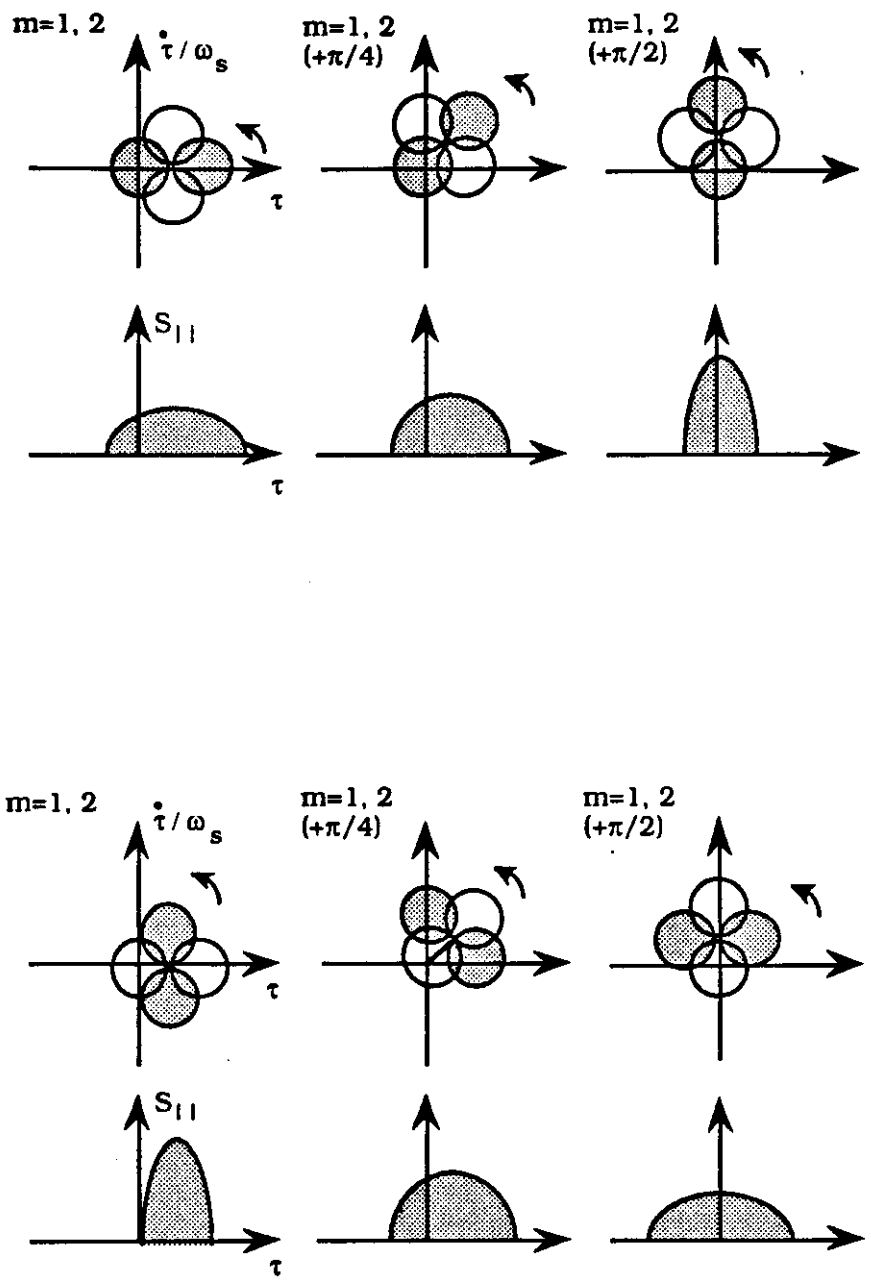

Figure 3.4 Phase Space Area and Charge Density Representations of a Combination of Dipole and Quadrupole Synchrotron Oscillation Modes.

phase by $\pi/2$. A combination of two or more azimuthal modes are also possible. In Figure 3.4, we see an illustration for the dipole and quadrupole rigid bunch modes occurring simultaneously. The distorted bunch is shown with two initial orientations differing by $\pi/2$. We would see two associated frequencies: ω_s and $2\omega_s$

Consider now the train of all M=6 bunches. The equilibrium case is shown in Figure 3.5 for coupled-bunch mode n=0 and synchrotron mode m=0. Each bunch is centered on the synchronous phase with a spacing of T_0/M, where T_0 is the revolution frequency around the ring. The first bunch is repeated at far right, so the drawing represents one turn.

In the first coupled-bunch dipole mode n=1 and m=1, each bunch is displaced $2\pi/M = \pi/3$ in phase space from the previous bunch (see Figure 3.6). If we trace the centroid positions of the bunches in phase space, we see a "wave" of one wavelength over the circumference of the ring. The relative phase between bunches is preserved as each bunch oscillates about its synchronous phase. Because the synchrotron frequency is several orders of magnitude smaller than the revolution frequency, one turn in phase space occurs after hundreds of turns around the ring.

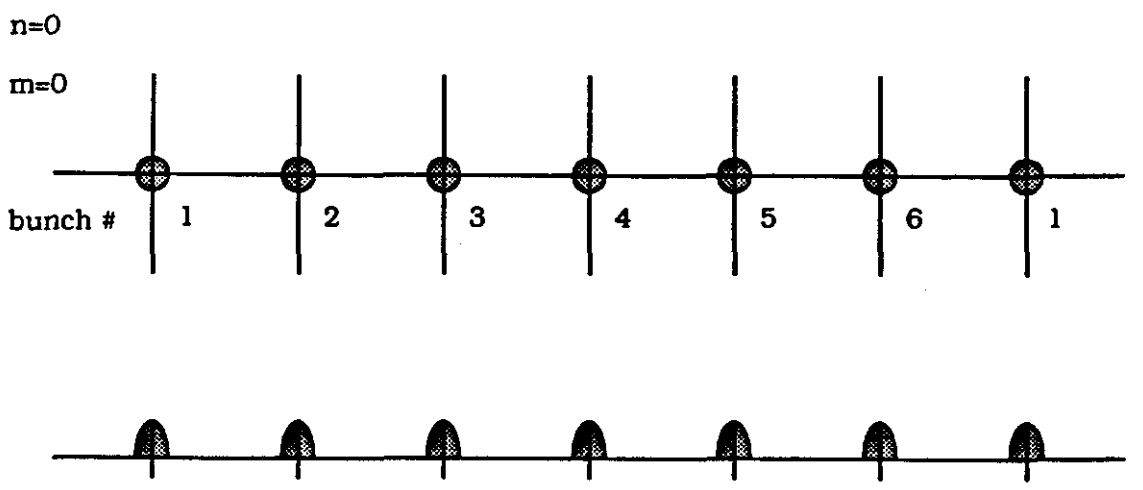

Figure 3.5 Equilibrium Phase (n=0) Representation of Coupled-Bunch Modes for an Example Train of Six Bunches.

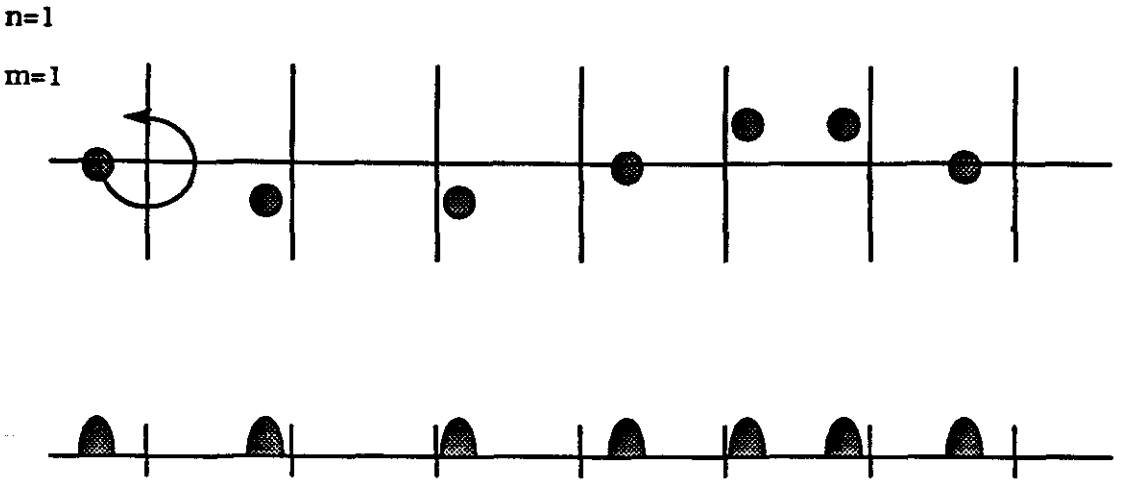

Figure 3.6 Phase Oscillation Representation for n=1 Coupled-Bunch Dipole Mode m=1 for Six-Bunch Example. The phase advance of both the bunch centroid as well as each bunch is 2π over one turn.

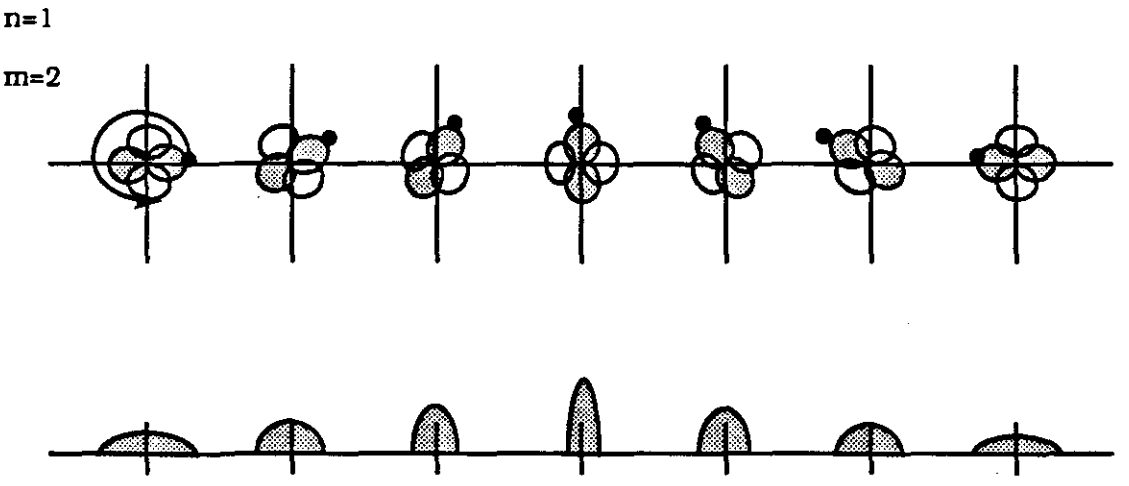

Figure 3.7 Phase Oscillation Representation for n=1 Coupled-Bunch Quadrupole Mode m=2 for Six-Bunch Example. The phase advance of the perturbed distribution is again 2π over one turn while that of each individual particle is only π.

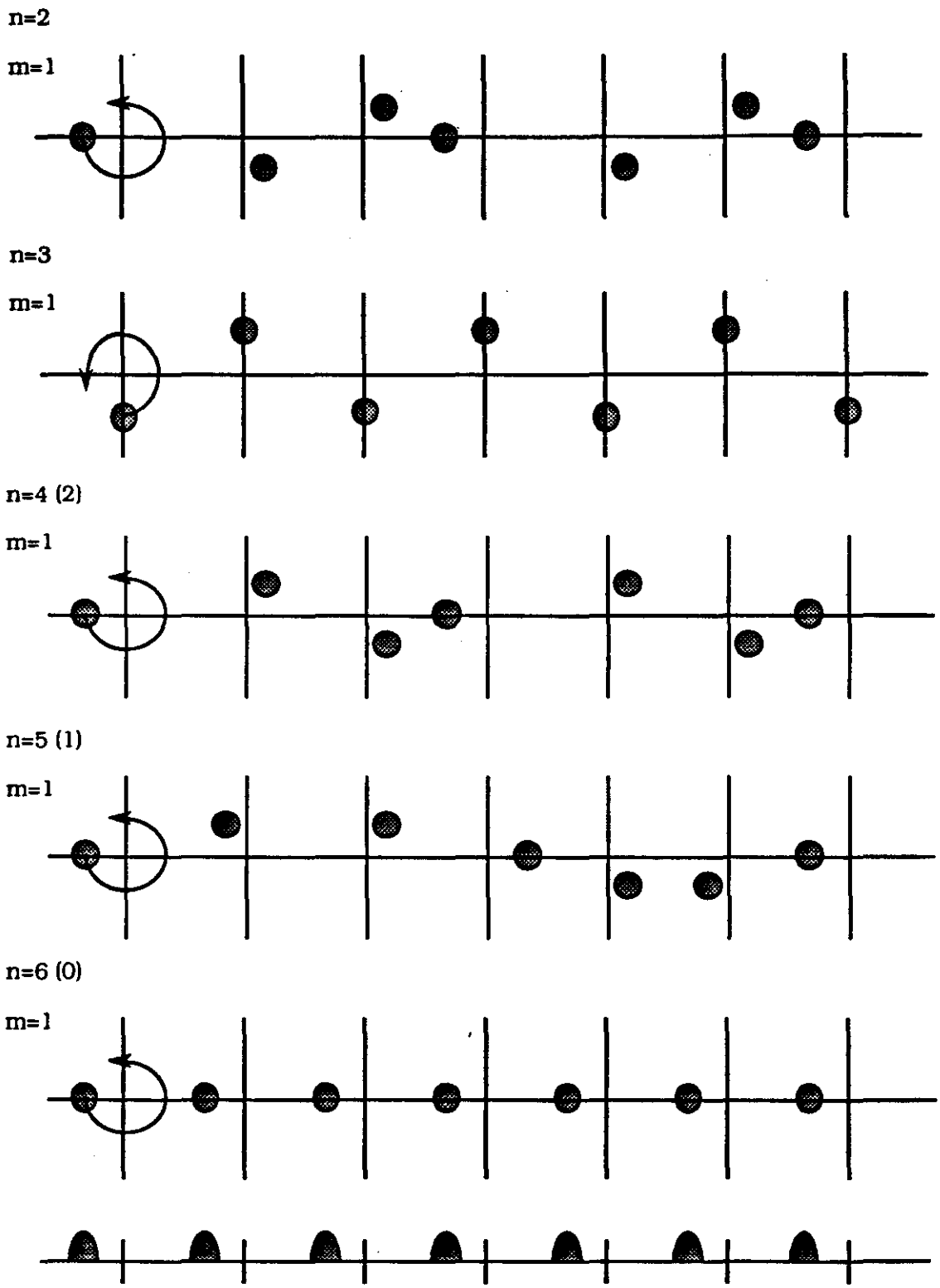

Figure 3.8 Phase Oscillation Representation for Higher-Order (n=2,3,4,5,6) Coupled-Bunch Modes in Example.

The first coupled-bunch quadrupole mode m=2 is depicted in Figure 3.7. One particle on one edge of the bunch is marked. The perturbed bunch is seen to return to its original orientation after one turn, giving mode n=1. However, now the phase offset between bunches is $2\pi/mM = \pi/6$, as noted by the marked particle. Higher-order synchrotron modes can be illustrated in a similar fashion.

We may examine the higher order coupled-bunch dipole modes n=2,3,4,5,6 in the sequence in Figure 3.8. In each case, the phase between bunches is $n\pi/3$. Mode n=2 has two wavelengths over one turn, n=3 has three. Note that mode n=4 looks exactly like n=2, n=5 looks like n=1, and n=6 looks like n=0 except for the phase. These modes therefore cannot be distinguished by the frequency alone. As with the single-bunch modes m, two or more coupled-bunch modes n can exist simultaneously in the beam.

Spectral Analysis

On development of instabilities in the Booster, the manifestation in the time domain of multiple coupled-bunch modes becomes complicated very quickly. The beam spectral data are rich in structure and detail, and are more amenable to analysis. The spectral analysis is straightforward, using the standard technique of Fourier analyzing the temporal signal. To describe the coupled-bunch modes, great care must be exercised to correctly express the interbunch phase advance. Obvious but common errors can arise when attempting to extrapolate the result from phase modulation of a single bunch. The derivation which follows is based in part on Ref. 9 and 17.

Consider a train of M bunches of N particles with an arbitrary charge density distribution circulating in a ring and undergoing longitudinal coupled-bunch phase oscillations. We will assume that a single coupled-bunch mode n (of possible range $0 \le n \le M$-1) is present. The motion of each bunch may be described in normalized phase space coordinates $(\tau, \dot{\tau}/\omega_s)$. Again, τ is the arrival time of a particle in the bunch relative to the synchronous particle, while $\dot{\tau}/\omega_s$ is related to the momentum spread. It is entirely equivalent to use the radial and azimuthal coordinates $(\hat{\tau}, \theta)$, where the angle θ is measured relative to the synchronous particle:

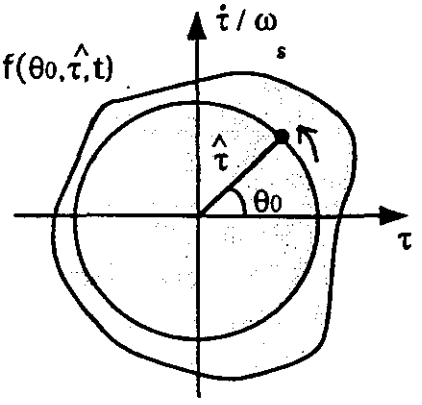

$$\hat{\tau}^2 = \tau^2 + \frac{\dot{\tau}^2}{\omega_s^2}$$
$$\tau = \hat{\tau}\cos\theta, \qquad \frac{\dot{\tau}}{\omega_s} = \hat{\tau}\sin\theta \tag{3.2.1}$$

We observe the signal developed in a detector located in the machine at a phase chosen (with no loss of generality) to be $\psi = 0$. The signal (in volts) is proportional to the perturbed current, and may be expressed as an infinite train of nearly periodic δ-functions. To analyze M bunches each with identical distributions $f(\theta_0,\hat{\tau},t)$ and N particles per bunch, we write

$$S_{\parallel}(t) = Ne\alpha \sum_{\nu=-\infty}^{\infty} \int_0^{2\pi}\int_0^{\infty} f(\theta_0,\hat{\tau},t)\,\delta(t-\tau_\nu-\nu t_b)\,\hat{\tau}\,d\hat{\tau}\,d\theta_0 \tag{3.2.2}$$

where α is the "impedance" of the detector, ν refers to the ν-th bunch, $t_b = 2\pi/M\omega_0$ is the time between bunches, and ω_0 is the revolution frequency.

We will use θ_{mn} to describe the phase relation among the bunches for a coupled-bunch mode n. The index m is interpreted as before as the synchrotron mode. The phase modulation is at the synchrotron frequency ω_s. The arrival time of each individual particle is therefore expressed as

$$\tau_\nu = \hat{\tau}\cos(\omega_s t + \nu\theta_{mn} + \theta_0) \tag{3.2.3}$$

In writing eqn. (3.2.3), we have assumed that there is no coupling of synchrotron modes; this is the zero current limit. The distribution has the usual normalization $2\pi\int f(\hat{\tau},\theta_0,t)\,\hat{\tau}\,d\hat{\tau} = 1$. We can expand this function in the azimuthal synchrotron modes using

$$f(\theta_0,\hat{\tau},t) = \sum_{m=-\infty}^{\infty} f_m(\hat{\tau})\,e^{-im\theta_0}\,e^{i\Omega_m t}, \quad \text{where } f_0 = f_0(\hat{\tau}) \tag{3.2.4}$$

Here f_0 and f_m are the stationary and perturbed distributions, respectively, and Ω_m is the complex, coherent frequency of the unstable mode. The detected signal (3.2.2) may thus be written

$$S_1(t) = Ne\alpha \int_0^{2\pi}\int_0^{\infty} \sum_{m=-\infty}^{\infty} f_m(\hat{\tau})\, e^{-im\theta_0}\, e^{i\Omega_m t} \sum_{\nu=-\infty}^{\infty} \delta(t - \tau_\nu - \nu t_b)\, \hat{\tau}\, d\hat{\tau}\, d\theta_0 \qquad (3.2.5)$$

In the absence of coupled-bunch motion, the bunches are indistinguishable and the periodicity in the signal is $t_b = T_0/M$, where $T_0 = 2\pi/\omega_0$ is the revolution period. In the presence of a coupled-bunch instability, however, the bunches are displaced from the synchronous position at various phases. Since the synchrotron frequency $\omega_s << \omega_0$, the oscillatory motion of the mode appears to be approximately rigid in time over one turn. Therefore, the true periodicity in the signal over one turn is T_0. Also, the problem may be separated into fast (T_0) (in which $\omega_s t$=constant) and slow (T_s) time scales. We drop the subscript T_0=T in the discussion below.

Any function periodic in T, such that $F(t) = F(t+T)$, may be expressed as a Fourier series. The coefficients c_k are strictly constant in time and are given as an integral over one period

$$F(t) = \sum_{k=-\infty}^{\infty} c_k\, e^{ik\omega_0 t}, \qquad \text{where } \omega_0 = \frac{2\pi}{T}$$
$$c_k = \frac{1}{T}\int_{-\frac{T}{2}}^{\frac{T}{2}} F(t)\, e^{-i\omega t}\, dt \qquad (3.2.6)$$

We proceed by first expressing a single coefficient s_k of the periodic delta-function in (3.2.5) using (3.2.6)

$$s_k = \frac{1}{T}\sum_{\nu=1}^{M}\int_{-\frac{T}{2}}^{\frac{T}{2}} \delta(t - \tau_\nu - \nu t_b)\, e^{-ik\omega_0 t}\, dt \qquad (3.2.7)$$

$$s_k = \frac{1}{T}\sum_{\nu=1}^{M} e^{-ik\omega_0(\tau_\nu + \nu t_b)} \tag{3.2.8}$$

In our case, the coefficients are independent of time in the fast time scale. In limiting the integration to cover only one period, the sum over bunches is truncated to total M. Substituting τ_ν from (3.2.3) and τ_b gives

$$s_k = \frac{1}{T}\sum_{\nu=1}^{M} e^{-ik\omega_0\hat{\tau}\cos(\omega_s t + \nu\theta_{mn} + \theta_0)} e^{-i\frac{2\pi k \nu}{M}} \tag{3.2.9}$$

The first exponential may be expanded in cylindrical functions using the following well-known relation[18]

$$e^{-ir\cos\phi} = \sum_{q=-\infty}^{\infty} i^{-q} J_q(r) e^{iq\phi} \tag{3.2.10}$$

where J_q are the Bessel functions. Making this substitution, and collecting terms in $\exp(i\nu)$

$$s_k = \frac{1}{T}\sum_{q=-\infty}^{\infty} i^{-q} J_q\left(k\omega_0\hat{\tau}\right) e^{iq(\omega_s t + \theta_0)} \sum_{\nu=1}^{M} e^{i\nu\left(q\theta_{mn} - \frac{2\pi}{M}k\right)} \tag{3.2.11}$$

The Fourier series as given in eqns. (3.2.6) may now be summed:

$$s(t) = \frac{1}{T}\sum_{k=-\infty}^{\infty}\sum_{q=-\infty}^{\infty} i^{-q} J_q\left(k\omega_0\hat{\tau}\right) e^{iq\theta_0}\, e^{i(k\omega_0 + q\omega_s)t} \sum_{\nu=1}^{M} e^{i\nu\left(q\theta_{mn} - \frac{2\pi}{M}k\right)} \tag{3.2.12}$$

Substituting eqn. (3.2.12) into the signal (3.2.5) yields

$$S_\parallel(t) = \frac{Nea}{T}\sum_{mpq} e^{i(k\omega_0 + q\omega_s + \Omega_m)t}\; i^{-q}\int_0^{\infty} f_m(\hat{\tau}) J_q\left(k\omega_0\hat{\tau}\right)\hat{\tau}\, d\hat{\tau}\int_0^{2\pi} e^{i(q-m)\theta_0}\, d\theta_0 \sum_{\nu=1}^{M} e^{i\nu\left(q\theta_{mn} - \frac{2\pi}{M}k\right)} \tag{3.1.13}$$

Note that the last integral, being of a periodic function, vanishes unless

$$\int_0^{2\pi} e^{j(q-m)\theta_0} d\theta_0 = 2\pi\delta_{qm} \tag{3.1.14}$$

Thus only terms with $q=m$ survive. The sum over ν vanishes unless $k = \left(pM + m\frac{\theta_{mn}}{(2\pi/M)}\right)$, where p is an integer. Although we have not written θ_{mn} explicitly, it is periodic in $2\pi/M$ and thus k is also an integer. Making this substitution, we can use

$$\sum_{\nu=1}^{M} e^{-j2\pi p\nu} = M \qquad \text{and} \qquad \sum_{k=-\infty}^{\infty} \rightarrow \sum_{p=-\infty}^{\infty} \tag{3.2.15}$$

Let $\omega_{pmn} = \left(pM + m\frac{\theta_{mn}}{(2\pi/M)}\right)\omega_0$, such that $\omega_{pn,m=0} = pM\omega_0$. Using eqn. (3.2.14) and (3.1.15), the time signal in eqn. (3.1.13) becomes

$$S_{\parallel}(t) = \frac{2\pi NMe\alpha}{T} \sum_{pm} e^{j(\omega_{pmn} + m\omega_s + \Omega_m)t}\, j^{-m} \int f_m(\hat{\tau}) J_m(\omega_{pmn}\hat{\tau})\, \hat{\tau}\, d\hat{\tau} \tag{3.2.16}$$

We now Fourier transform using the definitions

$$F(\omega) = \frac{1}{2\pi} \int_{-\infty}^{\infty} F(t)\, e^{-j\omega t}\, dt \tag{3.2.19}$$

$$\int_{-\infty}^{\infty} e^{-i(x-x')t}\, dt = 2\pi\, \delta(x - x') \tag{3.2.20}$$

We may consider the spectrum in (3.2.16) due to the stationary and perturbed beam separately; i.e., $S_{\parallel}(t) = S_{\parallel}^{(0)}(t) + S_{\parallel}^{(m)}(t)$. For $m=0$, recall that $\omega_{pn,m=0} = pM\omega_0$ and substitute $\omega_0 = 2\pi/T$. We obtain

$$S_{\parallel}^{(0)}(\omega) = NMe\omega_0\alpha \sum_{p,m} \delta(\omega - pM\omega_0) \int_0^{\infty} J_0(pM\omega_0\hat{\tau}) f_0(\hat{\tau})\, \hat{\tau}\, d\hat{\tau} \tag{3.2.21}$$

We similarly obtain for $m \neq 0$,

$$S_1^{(m)}(\omega) = NMe\omega_0\alpha \sum_{p,m=-\infty}^{\infty} \delta\left(\omega - \omega_{pmn} - m\omega_s - \Omega_m\right) \Gamma^m \int_0^{\infty} J_m\left(\omega_{pmn}\hat{\tau}\right) f_m(\hat{\tau})\,\hat{\tau}\,d\hat{\tau} \quad (3.2.22)$$

The expressions (3.2.21) and (3.2.22) together give the full signal for a given coupled-bunch mode n in (volts/Hz) valid for all m. We have chosen the index m in eqns. (3.2.3) and (3.2.4) to have the same interpretation; i.e. it refers to the synchrotron oscillation mode. These signals are discrete spectra at the frequencies ω given by the δ-functions. Recall that $\omega_{pmn} = \left(pM + m\frac{\theta_{mn}}{(2\pi/M)}\right)\omega_0$, where θ_{mn} is the phase relation among the bunch oscillations for a given coupled-bunch mode n and synchrotron mode m. The phase angle θ_{mn} was defined previously in the discussion of the mode structure as

$$\theta_{mn} = \frac{2\pi n}{mM} \quad (3.2.23)$$

Writing ω_{pmn} explicitly in eqn.(3.2.22), we obtain the perturbed beam spectrum

$$\omega = k\omega_0 \pm |m|\omega_s + \Omega_m, \quad \text{where} \quad k = (pM + n) \quad (3.2.24)$$

For a stable beam, spectral lines appear only at harmonics of the RF frequency. In the case of a perturbed beam, the spectrum is that of a signal phase-modulated at those rotation harmonics $k\omega_0$ corresponding to the specific coupled-bunch mode n which is being driven. Spectral lines appear at the frequencies given by ω: synchrotron sidebands appear around the rotation lines $k\omega_0$ in each RF order p offset by the coherent frequency Ω_m. In the presence of multiple coupled-bunch modes, the perturbed spectra are superimposed. The integrals over time are interpreted as form factors, forcing an envelope over the spectral lines and determining their relative amplitudes. The form factor is a convolution of the particle distribution with the Bessel functions.

It is possible to extract from the spectra in eqns. (3.2.21) and (3.2.22) both the stationary (f_0) and perturbed (f_m) phase space distributions for the particles. There is a

different set of radial functions f_m for each coupled-bunch mode. The first moment of the distribution f_1 gives the dipole coupled-bunch mode amplitude τ_a. The bunch length τ_L may be derived from the stationary distribution f_0. This will be shown explicitly in Chapter 5. This analysis provides a technique to experimentally study the radial time evolution of the motion in phase space. Instability theory always describes the beam in this radial parameter. In reality, we are limited to direct measurements of only the projections of these distributions.

We will illustrate in Figure 3.9 a pure dipole $|m|=1$ coupled-bunch mode spectrum with the same example of $M=6$ bunches. The schematic is based on Sacherer.[4] The arrows represent all possible frequencies ω and are directed down for sidebands which are damping, up for anti-damping (i.e., unstable). The case shown corresponds to above transition, where the upper sidebands are unstable. The reason for this will be discussed in the next section in greater detail. The real spectrum is depicted at the top of the figure. In a measurement, the negative frequencies will be aliased as positive frequencies. This is equivalent to folding the chart over onto the positive ω/ω_0 axis, as seen at the bottom of the same figure. To describe the case of higher-order synchrotron modes m, additional sidebands in ω must be included in the figure.

If an instability at coupled-bunch mode n begins as a linear dipole oscillation, a sideband at $(\omega_s+\Omega_m)$ appears at a particular rotation harmonic $k(n)\omega_0$. The relative amplitudes of the lines in each RF order p will be determined by the form factor with Bessel function J_1. In the case of a quadrupole $m=2$ oscillation, a $(2\omega_s+\Omega_m)$ line appears at $k(n)\omega_0$. The envelope of these lines is determined by J_2, and so on for higher-order synchrotron modes. In the case of small amplitude oscillations, azimuthal symmetry may be assumed and we may limit discussion to the dipole mode $|m|=1$. If we consider dipole modes of larger amplitude, or if the distribution becomes distorted in the nonlinear part of the RF potential, the second term ($|m|=2$) cannot be neglected. In the Booster spectra, we cannot resolve the synchrotron sidebands; therefore all the signal power appears at the rotation harmonic k. We may estimate the relative importance of the various synchrotron modes from either the time domain ("mountain range") or by the aid of simulation.

In order for any coupled-bunch mode to appear, it must be driven by an external impedance. If the impedance is narrow enough, such that the width is smaller than ω_0, it may couple to a single beam mode. Higher-order resonant modes in RF cavity structures typically have this characteristic. The arrangement of the stable and unstable lines in Figure 3.9 shows that if a narrow resonance drives the M=6 beam at a frequency corresponding to a coupled-bunch mode at a multiple of 3 (or generally, $M/2$), sideband cancellation occurs and it will not grow. This is also true if two resonances drive the beam simultaneously at n and at (M-n), even if in different RF orders p. However, a resonance width need not be smaller than ω_0 to drive an instability. Especially with large M, a single impedance may drive several neighboring beam modes.

It should be noted that the analysis presented here is valid only for a full ring of M=h bunches, where h is the harmonic number. For a non-uniformly filled ring, the perturbed bunch distributions are no longer identical because bunches with only one or no neighbors will experience a different wake field and hence potentially a different amplitude of coherent motion. The analysis is complicated as the sum over bunches in eqn. (3.2.15) can no longer be performed. The form factor also changes.

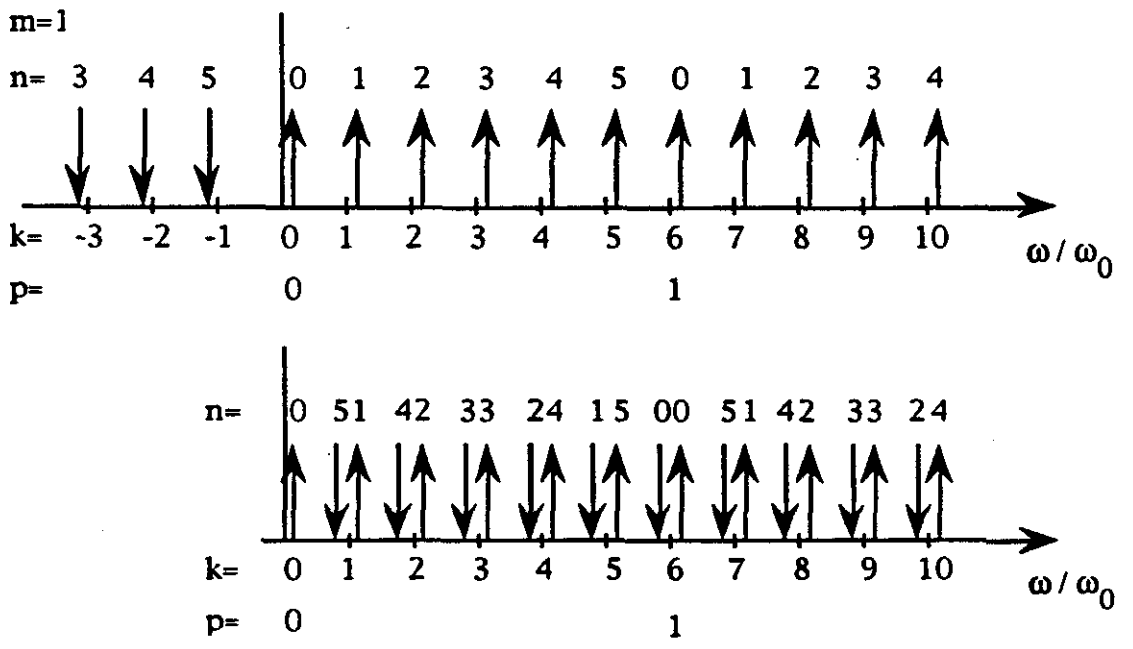

Figure 3.9 Frequency Spectrum Chart for Dipole Synchrotron Oscillation Mode. The real spectrum is shown at top, while the measured is depicted below. Only those lines which are excited or driven will actually appear.

3.3 Linear Coupled-Bunch Mode Instability Theory

In the previous section, we examined the mathematical and physical manifestation of longitudinal coupled-bunch modes. We had used prior knowledge of the nature of the instability to derive the expression for the perturbed current. Here, we will describe by what means the unstable modes are driven and under what conditions they grow.

There are two views which characterize the electromagnetic coupling between the beam and its environment, specifically, the RF cavities. In the frequency domain, we may decompose the beam current into its Fourier components $I(\omega)$, each of which gives rise to a voltage $-V(\omega)$ as it traverses the cavity gaps. The impedance is defined as the ratio of the output and the input; i.e. $Z(\omega) = -V(\omega)/I(\omega)$. With sufficient beam intensity and impedance, the resulting force may drive the beam fluctuations and cause unstable motion. An equivalent view is in the time-domain: as the beam passes through the RF cavity, it excites time-varying electromagnetic fields known as wake fields. The fields which are supported as standing waves in the cavity are sustained, and under the right conditions, these in turn act back on the beam and cause a collective response. The transient response at the gap may be found by Laplace transforming the impedance using an appropriate model. Hence, we focus on the impedance as this is far more readily measured so that solutions are attainable.

The time evolution of this collective behavior of the beam is determined by solving the Vlasov equation. Included is a forcing term due to the response of the beam to an external impedance. Before proceeding with the derivation of the linear instability theory, we will first characterize this coupling impedance.

Longitudinal Coupling Impedance

For a coupled-bunch instability to occur, the impedance must have very specific characteristics. It must have a frequency equal to the beam mode frequencies

ω of eqn. (3.2.24) and be of sufficient magnitude. In order to couple effectively with the beam, the frequency must lie within the response envelope of the beam determined by the form factor. The wake field which is excited by the beam must be of sufficient duration to affect neighboring bunches, providing a means by which the bunches are coupled, or "communicate" with each other. These conditions favor the high-Q higher-order parasitic resonant modes in the RF cavities. They are called parasitic because they are only driven by the beam.

The series-parallel LRC lumped-element circuit model, represented in Figure 3.10 (a), can be applied in a limited way to the coaxial cavity to represent the frequency response of a high-Q mode near resonance.[9,19] In this physical analog, a gap capacitance is resonating with an inductance with relatively small losses (R_L). Obviously, a real cavity has many modes; the circuit has but one. The energy stored in the circuit may be expressed, including the exponential decay due to the losses, by $U = \frac{1}{2}L\hat{I}^2e^{-2\alpha t}$. We introduce the quality factor Q, a convenient, dimensionless figure-of-merit given by

$$Q = \omega_r \frac{\text{(energy stored)}}{\text{(average power loss)}} = \omega_r \frac{U}{W} \tag{3.3.1}$$

The negative rate of change of the stored energy over several cycles is equal to the average power loss:

$$-\frac{dU}{dt} = 2\alpha U = W, \qquad \text{therefore} \qquad \alpha = \frac{\omega_r}{2Q} \tag{3.3.2}$$

Instantaneously, neglecting the decay, for the case of resistance R_L in series with L, the energy is stored in the inductance and the power dissipated in the resistance,

$$U = \tfrac{1}{2}L\hat{I}^2 \quad \text{and} \quad W = \tfrac{1}{2}R_L\hat{I}^2, \quad \text{therefore} \quad Q = \frac{\omega_r L}{R_L} \tag{3.3.3}$$

It is equivalent and perhaps more appropriate to use the conventional parallel LRC circuit in Figure 3.10 (b), with a high shunt resistance R_s, to characterize the beam coupling impedance. The impedance may be expressed as

$$\frac{1}{Z(\omega)} = \frac{1}{R_s} + \frac{1}{i\omega L} + i\omega C \tag{3.3.4}$$

In this case the resonant frequency is $\omega_r = 1/\sqrt{LC}$. It can be shown[19] that the resistances in circuits (a) and (b) are related by $R_s = Q^2 R_L$. Therefore, using also eqn. (3.3.3), we write $Q = \omega_r C R_s = R_s/(\omega_r L)$. With these substitutions, eqn. (3.3.4) becomes

$$Z(\omega) = \frac{R_s}{1 - iQ\left(\frac{\omega_r}{\omega} - \frac{\omega}{\omega_r}\right)} \tag{3.3.5}$$

The quality factor is related to the resonator bandwidth $\Delta\omega$. For a narrow resonance, Q is large and ω is always close to resonance. Then Q may be approximated using

$$Q \approx \frac{\omega_r}{\Delta\omega} \tag{3.3.6}$$

where $\Delta\omega$ is the distance between points on the curve for which the real amplitude response is 1/2 of maximum (or the magnitude is $1/\sqrt{2}$ of maximum). The real and imaginary response curve of the parallel resonance in eqn. (3.3.5) is depicted in Figure 3.11.

This impedance model assumes a steady-state harmonic solution for a driven oscillator and is implied in the usual analytic treatment given below of the linear instability. In reality, the situation can be very dynamic as the Fourier components of the beam current sweep rapidly across resonances over the duration of the acceleration. The response in this case is reduced. The analysis is derived in a paper by Hok,[20] who treats the problem of the excitation of an LRC resonator by a linearly swept frequency. The criterion he derives for the relative rate of change in the swept frequency as compared with the resonant width without invalidating the impedance model is given by

$$\dot{\omega}_0 < \frac{k}{8}\left(\frac{\omega_0}{Q}\right)^2 \tag{3.3.7}$$

If we write approximately $\dot{\omega}_0 = \dot{\beta}c/R$, then in the Booster for t=17 to 35 msec in the cycle, with R=75 m, we have for the left hand side of (3.3.7)

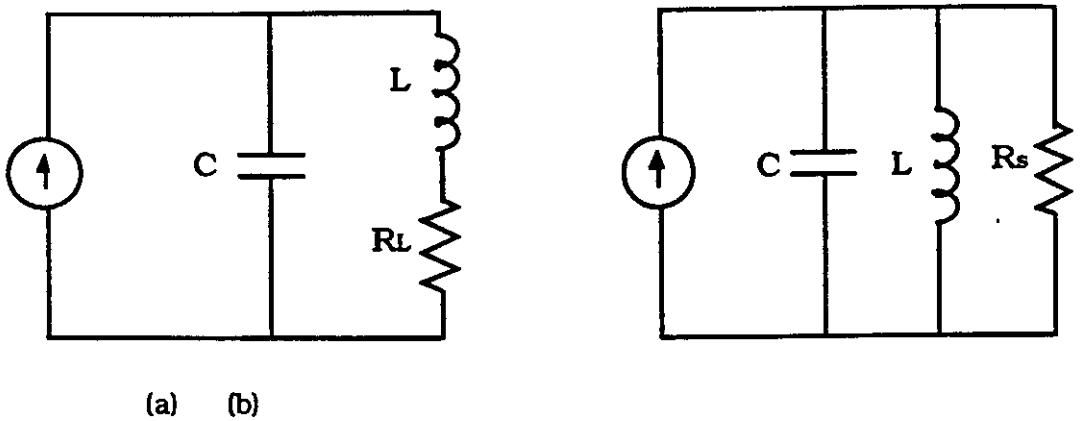

Figure 3.10 Model Resonant LRC Circuits. Shown in (a) is the series-parallel circuit of two branches, the physical analog of a single RF cavity mode, and in (b) is the parallel circuit, the model longitudinal coupling impedance.

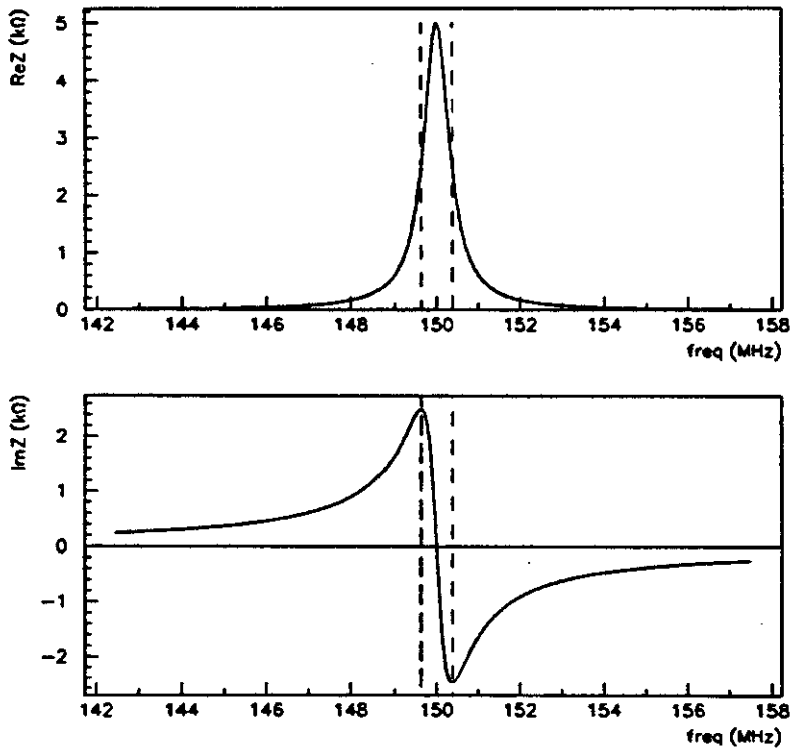

Figure 3.11 Resonant Response of Parallel LRC Circuit in Figure 3.10 (b). In this illustration, f_r=150 MHz, R=5kΩ and Q=200.

$$\frac{\Delta\omega_0}{\Delta t} = \frac{c}{R}\frac{\Delta\beta}{\Delta t} = \frac{3\text{x}10^8}{75}\frac{(0.9945-0.9751)}{0.018} = 4.3\text{x}10^6 \tag{3.3.8}$$

The average angular revolution frequency over this range in the cycle is $\overline{\omega}_0 = 2\pi(616+629)/2 = 2\pi(622)$ krad/sec. We see in Table 3.1 that for the RF cavity higher-order modes around 83, 169, 220 MHz, designated as f2, f4, f6, respectively, the criterion in eqn. (3.3.7) is satisfied over the portion of the Booster cycle of interest.

Table 3.1 Criterion for Swept LRC Resonator in Booster

	$k = (ph+n)$	Q	$\frac{k}{8}\left(\frac{\overline{\omega}_0}{Q}\right)^2$
f2	132	170	$8.7\text{x}10^9$
f4	268	170	$1.8\text{x}10^{10}$
f6	352	240	$1.2\text{x}10^{10}$

In a longitudinal particle tracking code such as ESME, which treats the instability in the time domain, the transient response may be modeled directly. To derive an expression for the voltage produced in an LRC circuit by a single passage of a discrete circulating charge q, we perform a Laplace transform on the current using the impedance in eqn. (3.3.4). Solving for the voltage, the current is replaced by $i(t) = q\delta(t)$. This is just a Green's function, and is equivalent to q multiplying the wake field, the Fourier transform of the impedance:[9,19]

$$\tilde{v}(t) = q\tilde{Z}(t) = q(\alpha R_s)e^{-\alpha t}\left[\cos\overline{\omega}t - \frac{\alpha}{\overline{\omega}}\sin\overline{\omega}t\right]\Theta(t)$$

$$\text{where} \quad \alpha = \frac{\omega_r}{2Q}, \quad \overline{\omega}^2 = \omega_r^2 - \alpha^2, \quad \text{and} \quad \Theta(t) = \begin{cases} 1 & \text{if} \quad t \geq 0 \\ 0 & \text{if} \quad t < 0 \end{cases} \tag{3.3.9}$$

The simulation results are deferred to Chapter 7. We now proceed with the linear instability theory.

Dispersion Relation

The accelerator beam is an ensemble of a large number of particles. To study collective instability phenomena, one may apply the techniques of statistical mechanics as used in the study of gases and fluids or plasmas. The evolution of a distribution of particles is given by the Boltzmann equation which, in the absence of collisions, may be written[21]

$$\frac{d\bar{f}(\mathrm{r},\mathrm{p},t)}{dt} = \frac{\partial \bar{f}}{\partial t} + \dot{\mathrm{r}}\frac{\partial \bar{f}}{\partial \mathrm{r}} + \dot{\mathrm{p}}\frac{\partial \bar{f}}{\partial \mathrm{p}} = 0 \tag{3.3.10}$$

In this form, this equation is commonly known as the Vlasov equation. The function $\bar{f}(\mathrm{r},\mathrm{p},t)$ represents the particle distribution function in six-dimensional phase space. The motion of a relativistic beam in the longitudinal plane is approximately decoupled from the transverse plane, so it is appropriate to study the 2-dimensional longitudinal problem independently. An assumption is made that the external force $\mathrm{F}(\mathrm{r}) = \dot{\mathrm{p}}$ is independent of the velocity; i.e., that electric fields predominate. This condition is satisfied in our case as the force is due to perturbing fields at the RF accelerating gaps.

The goal is to solve the Vlasov equation using an appropriate expression for the force in order to determine the time evolution of the ensemble. In effect, this becomes an eigenvalue problem in which we are solving for the normal modes of the system. A number of authors have adapted Sacherer's original general formalism for beam instabilities[4] to characterize the coupled-bunch instability. Here, we present a derivation which combines the approaches of Pellegrini[21] and Wang.[22]

Consider the rotating reference frame (ϕ, ε), which is related to the normalized phase space coordinates $(\tau, \dot{\tau}/\omega_s)$ of sections 3.1 and 3.2 through

$$\phi = -\omega_0 \tau \qquad \text{and} \qquad \varepsilon = \frac{\Delta E}{E} = \beta^2 \frac{\Delta p}{p} = \frac{\omega_s \beta^2}{\eta}\frac{\dot{\tau}}{\omega_s} \tag{3.3.11}$$

Note that the phase ϕ here is a global coordinate, unlike before in (3.1.30). The equations of motion for M bunches, where the subscript refers to the ν-th bunch, are derived from the following Hamiltonian

$$\overline{H} = -\sum_{\nu=1}^{M}\left(\frac{1}{2}\frac{\omega_0\eta}{\beta^2}\varepsilon_\nu^{\,2} + \frac{1}{2}\frac{\omega_s^{\,2}\beta^2}{\eta\omega_0}\phi_\nu^{\,2}\right) + \overline{U} + \overline{U}_{NL} \tag{3.3.12}$$

$$\begin{aligned} \dot{\phi}_\nu &= \frac{\partial\overline{H}}{\partial\varepsilon_\nu} = -\frac{\omega_0\eta}{\beta^2}\varepsilon_\nu \\ \dot{\varepsilon}_\nu &= -\frac{\partial\overline{H}}{\partial\phi_\nu} = \frac{\omega_s^{\,2}\beta^2}{\eta\omega_0}\phi_\nu - \frac{\partial\overline{U}}{\partial\phi_\nu} - \frac{\partial\overline{U}_{NL}}{\partial\phi_\nu} \end{aligned} \tag{3.3.13}$$

where $\overline{U}$ is due to the wake field "potential" and gives the average energy loss per bunch per turn. $\overline{U}_{NL}$ is due to the nonlinear RF potential, averaged over azimuth. We may transform to the action-angle coordinates (J,ψ)

$$\phi_\nu = \left(\frac{2|\eta|\omega_0 J_\nu}{\omega_s}\right)^{\frac{1}{2}}\cos\psi_\nu \qquad \text{and} \qquad \varepsilon_\nu = -\beta^2\left(\frac{2\omega_s J_\nu}{|\eta|\omega_0}\right)^{\frac{1}{2}}\sin\psi_\nu \tag{3.3.14}$$

The Hamiltonian may be separated into unperturbed and perturbed components, becoming, in these new variables

$$\begin{aligned} \overline{H} &= \overline{H}_0 + \overline{H}_1, \qquad \text{with } |\overline{H}_1| << |\overline{H}_0| \\ \overline{H}_0 &= -\omega_s\frac{\eta}{|\eta|}\sum_{\nu=1}^{M} J_\nu + \overline{U}_{NL} \\ \overline{H}_1 &= \overline{U} \end{aligned} \tag{3.3.15}$$

The bunches are assumed identical but for the interbunch coupled-bunch mode phase, which is accounted for in the term $\overline{U}$. Acknowledging that the Hamiltonian describes the average bunch, the subscript ν may be dropped. For a particle distribution function $f(J,\psi,t)$, the Vlasov equation for may be written

$$\frac{\partial f}{\partial t} - \frac{\partial f}{\partial J}\left(\frac{\partial H}{\partial\psi}\right) + \frac{\partial f}{\partial\psi}\left(\frac{\partial H}{\partial J}\right) = 0 \tag{3.3.16}$$

We may introduce a perturbation by expanding the distribution f in multipole modes, as before,

$$f(J,\psi,t) = f_0(J) + f_1(J)e^{j\psi}e^{-j\Omega t}, \qquad \text{with} \quad |f_0| >> |f_1| \tag{3.3.17}$$

Here, Ω are the normal modes of the instability. This quantity is complex, therefore a positive $\Omega_I = \mathrm{Im}(\Omega)$ will lead to growth of the perturbation and $\Omega_r = \mathrm{Re}(\Omega)$ gives a frequency shift. A negative Ω_I will be stable. In this analysis, we consider a pure dipole oscillation only, ie. $m=1$, and hence, no coupling of higher multipoles. We also assume no time variation of the stationary distribution f_0. Using eqns. (3.3.15) and (3.3.17), we linearize the Vlasov eqn. (3.3.16) by dropping second order terms in $f_1 H_1$. We obtain

$$-j\Omega\left(f_1 e^{j\psi}e^{-j\Omega t}\right) - \frac{\partial f_0}{\partial J}\left(\frac{\partial U}{\partial \psi}\right) + j\left(f_1 e^{j\psi}e^{-j\Omega t}\right)\left(-\omega_s\frac{\eta}{|\eta|} + \frac{\partial U_{NL}}{\partial J}\right) = 0 \tag{3.3.18}$$

We call

$$\omega_s(J) = \left(\omega_s(0)\frac{\eta}{|\eta|} - \frac{\partial U_{NL}}{\partial J}\right) \tag{3.3.19}$$

the same amplitude dependence of the synchrotron frequency as described in the previous section.

The term $\mu = \left(\frac{\partial U}{\partial \psi}\right)$ is the self-induced force on the beam due to its wake fields in the beamline environment. This force may be written as the sum of products of the Fourier components of the charge density and the impedance. Because the charge density is a longitudinal parameter, the Fourier components Λ_{km} are expanded in the coordinate ϕ. For one bunch,

$$\mu = -j\frac{\omega_0}{\beta^2 E_0}\sum_k \frac{Z_k(\omega)}{k}\Lambda_{km}\, e^{j(k\phi - \Omega_m t)} = -j\frac{e}{E_0}\sum_k \frac{Z_k(\omega)}{k}\Lambda_{km}\, e^{jkr\cos\psi}e^{-j\Omega_m t} \tag{3.3.20}$$

$Z_k(\omega)$ is the impedance evaluated at $\omega = k\omega_0 + \omega_s + \Omega$ as in eqn. (3.2.24). Recall that the index $k = hp + n$, where h is the harmonic number, p the RF harmonic, and n the coupled-bunch mode (wave) number. To simplify the notation, we have written

$$r = \omega_0 \hat{\tau} = \left(\frac{2|\eta|\omega_0}{\omega_s} J \right)^{\frac{1}{2}} \tag{3.3.21}$$

Here the coordinate $\hat{\tau}$ is the same as in eqn. (3.2.1) in the previous section. Then we may write

$$\mu = -j \frac{\omega_0}{\beta^2 E_0} e^{-j\Omega_m t} \sum_k Z_k(\omega) \Lambda_{km} \sum_{k'} j^{-k'} J_{k'}(kr) e^{-jk'\psi} \tag{3.3.22}$$

where we have used the expansion in Bessel functions as in eqn. (3.2.10).

We obtained an expression earlier for the longitudinal perturbed current $S_{\parallel}(\omega)/\alpha$ generalized to M bunches (eqn. (3.2.22)). Substituting $\hat{\tau} = r/\omega_0$, we write

$$\Lambda_k = \frac{S_{\parallel}^{k}(\omega)}{\alpha} = \frac{eNh}{\omega_0^{\,2}} \sum_m j^{-m} \int r dr \; f_m(r) J_m(kr) \tag{3.3.23}$$

Note that $J_1(x) = -J_{-1}(x)$. Substituting eqn. (3.2.23) into eqn. (3.3.22),

$$\mu = \frac{eNh}{\beta^2 E_0 \omega_0} e^{-j\Omega t} \sum_k \frac{Z_k(\omega)}{k} \sum_{k'} j^{-k'} J_{k'}(kr) e^{-jk'\psi} \int r' dr' \; f_1(r') J_1(kr') \tag{3.3.24}$$

We may now evaluate the Vlasov equation in eqn. (3.3.18), noting that the explicit time dependence $e^{-j\Omega t}$ now cancels. Also, transforming to $(\hat{\tau}, \psi)$ coordinates, we use the definition in eqn. (3.2.21) to obtain

$$\frac{d}{dJ} = \frac{dr}{dJ}\frac{d}{dr} = \frac{1}{r}\frac{|\eta|\omega_0}{\omega_s}\frac{1}{dr} \tag{3.2.25}$$

$$j(\Omega - \omega_s(r)) f_1 e^{j\psi} = \frac{1}{r}\frac{\partial f_0}{\partial r}\left(\frac{eNh|\eta|}{\beta^2 E_0 \omega_s} \sum_k Z_k(\omega) \sum_{k'} j^{-k'} J_{k'}(kr) e^{-jk'\psi} \int r' dr' f_1(r') J_1(kr') \right) \tag{3.3.26}$$

Noting the ψ-dependence, this expression will be valid only for $(k' = -1)$, therefore,

$$(\Omega - \omega_s(r))f_1(r) = -j\frac{eh|\eta|N}{\beta^2 E_0 \omega_s}\frac{1}{r}\frac{\partial f_0(r)}{\partial r}\sum_k \frac{Z_k(\omega)}{k}J_1(kr)\int r'dr'\, f_1(r')J_1(kr') \quad (3.3.27)$$

Dividing by $(\Omega - \omega_s(r))$, multiplying by $r\,J_1(k'r)$, and integrating both sides over r leads to the dispersion relation

$$1 = -j\frac{|\eta|Neh}{\beta^2 E_0 \omega_s}\sum_{k,k'}\frac{Z_k(\omega)}{k}\int_0^\infty dr\frac{\frac{\partial f_0(r)}{\partial r}J_1(kr)J_1(k'r)}{(\Omega - \omega_s(r))} \quad (3.3.28)$$

where

$$\omega_s(r) = \left(\omega_s(0)\frac{\eta}{|\eta|} - \frac{|\eta|\omega_0}{\omega_s}\frac{1}{r}\frac{\partial U_{NL}}{\partial r}\right) \quad (3.3.29)$$

The dispersion relation relates the unstable frequencies Ω with the corresponding impedance. We are interested in solving (3.3.28) for each coupled-bunch mode n=0,1,...,h, to find those eigenfrequencies Ω which are unstable. The calculation results are deferred to chapter 6. We proceed now to discuss the measurements and the experiments.

4. MEASUREMENTS

Several quantities are measured under varying beam intensity and RF configurations in the Booster for use in the comparison with the theory. First, the impedance due to the RF cavity higher-order modes (HOM) is measured using bench techniques. Because the RF fundamental frequency is programmed to sweep from 30 to 53 MHz, many of the HOMs also tune, so data are recorded corresponding to several times through the cycle. Cavity spectral measurements are also made with beam *in situ* to isolate those parasitic modes excited most strongly by the beam. This helped to determine the source of coupled-bunch oscillations which have long plagued the Booster. Prior measurements of the impedance due to the magnets, which is the major source of the broadband ring impedance, are described but not repeated in this work. The properties of the beam are also examined in detail. The beam perturbations due to the instability are observed by sampling and recording the image currents driven by the beam through a wideband resistive-wall pickup. The beam fluctuation spectra are obtained by performing a fast Fourier transform on this signal using a Tektronix Digital Signal Analyzer (DSA) 602. The spectra are recorded at several times through the cycle and the unstable mode amplitudes extracted. Finally, the full (95%) bunch lengths are measured through the cycle in order to calculate the longitudinal emittance and synchrotron frequency spread. The techniques and hardware are described below.

4.1 RF Cavity Impedance

Central in the effort to characterize and quantify the coupling between the HOMs and the beam is the need to accurately represent in the theory the total cavity impedance. We undertook to construct this impedance experimentally. Bench measurements using a variety of techniques were carried out on a fully-functional Booster RF cavity in a test area. The results are extrapolated to form a net impedance based on analysis of how the cavities are excited by the beam. This sum impedance lumps the effect of all the cavities around the ring into one as if it were a single

localized impedance. This technique is justified because since the RF cavity parasitic modes are excited by the beam, they are phase-locked with the beam in each cavity and will add in phase, regardless of position in the machine.

Three methods commonly used to measure the impedance due to resonant accelerator structures are (a) signal response on a thin coaxial wire stretched along the beam path, (b) perturbation techniques inserting small metallic beads into the cavity, and (c) beam measurements using a coasting beam *in situ*. Of these, only the first two bench methods are readily applicable to the Booster. The third method,[25,26] often called the beam transfer function measurement, is best applied in fixed-energy machines, and was not attempted. A single-gap, stretched wire method combined with a de-embedding process to extract the impedance proved to be the most general and practical approach. In order to reconstruct the actual impedance presented to the beam from up to 17 such dual gap cavities, an equivalent coupling matrix is developed to account for the multiple gaps, and the spread in mode frequencies among the cavities is incorporated in the analysis. For resonances with Q values above about 200, typical for the Booster HOMs, it was possible to verify the stretched-wire results using the cavity perturbation technique. A third, independent bench measurement of the gap impedance was made at the fundamental, using power dissipation arguments, for further verification. An absolute impedance measurement accuracy of about 20% was achieved.

We undertook a series of measurements on the test cavity while manually varying in steps the bias current in the ferrite-loaded tuners. Normally, the bias is programmed such that the RF fundamental frequency sweeps from 30 to 53 MHz over each 33 msec acceleration pulse. Since many HOMs also tune, in this way we could produce a set of impedance data corresponding to several different times in the Booster acceleration cycle. Data are recorded with and without the recently installed higher-order mode dampers, with the cavity shorted, and with zero bias. The cavity dampers themselves will be described in the next chapter. The measurements are performed on a warm cavity, i.e. when the cavity reached a steady state temperature after the bias current had been turned on. A frequency shift in the resonant modes of about 1 MHz is observed between the warm cavity and when it was cold. Although the cavities in the tunnel are actually cycled, we estimate that the differences are small compared with running the cavity continuous-wave on the test stand. The power amplifier (PA) is

mounted but with no RF drive. There is no observable change in the resonant modes when the PA was conducting.

Stretched-Wire Method

The basic stretched-wire method has been described in the literature.[25,27] A complication arises from the fact that the Booster RF cavity has two gaps. Spurious modes exist on a wire spanning both gaps which couple the gaps, unlike the beam; these would need to be deconvolved. The single-gap wire was chosen to avoid this issue. The experimental setup for the measurement is shown in Figure 4.1. A swept signal from a Hewlett Packard 8753C Network Analyzer (NA) through the wire is used to excite the cavity over a spectrum of frequencies. Commercial optoelectronic RF devices made by Ortel are used to avoid coupling to the second gap. The swept, frequency-modulated signal from the network analyzer is converted to amplitude modulation by an RF transmitter and 1.3 μm laser diode (LW-620S). It is propagated along an optical fiber and converted back by a PIN photo diode and receiver (PL050-PMS). The laser system modulation bandwidth is 6 GHz; this was measured and verified. The signal suffers an attenuation of about -28 dB due primarily to the conversion efficiency in the optoelectronic device. The network analyzer sensitivity is sufficient despite this attenuation and no further amplification is required.

Depicted at the bottom in Figure 4.1 is a close-up of the single-gap stretched wire assembly. A 10-mil copper wire, soldered to SMA connectors, is strung coaxially across a single accelerating gap. The two copper endplates are edged with flexible copper braid to allow a good electrical ground contact with the inner beam pipe wall. Carbon resistors at one endplate match the output impedance of the laser receiver with the characteristic impedance of the wire assembly. Not shown are two RG238 rods used to keep the wire rigid between the two endplates. The characteristic impedance of the assembly is measured to be $Z_0 = 326\ \Omega$. For proper gain in the laser system, a resistance matching network is required on the input end of the wire assembly to match to the 50 Ω impedance looking into the receiver.

The function of a network analyzer is to characterize a two-port microwave device in terms of S, or scattering, parameters.[28,29] The impedance of the device

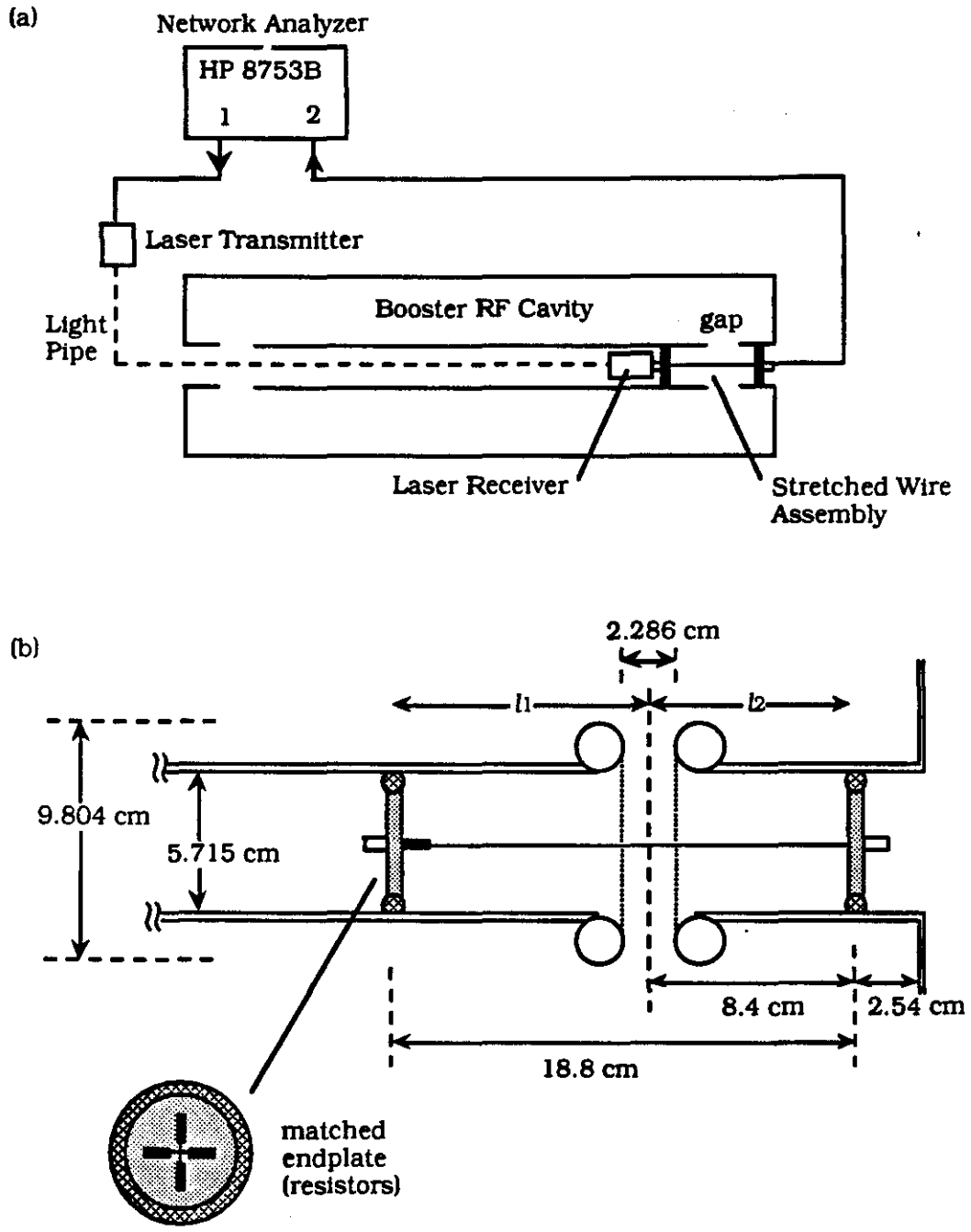

Figure 4.1 Single-Gap Stretched Wire Measurement of RF Cavity Gap Impedance. Experimental setup is shown in (a), the wire assembly close-up in (b).

under test may be extracted from the measured S-parameters through a de-embedding procedure. Consider the generic 2-port network in Figure 4.2, representing in our case the coaxial stretched-wire assembly inserted in the cavity gap. It is embedded in a terminated transmission line, representing the network analyzer. A traveling wave incident on the device causes a response wave reflected from or transmitted through the device. In the figure, E_{1r} and E_{2r} are the voltages reflected from ports 1 and 2, respectively, while E_{1i} and E_{2i} are those of the incident waves. These voltages are often normalized by the characteristic impedance of the line Z_0 using $a_n = \frac{E_{ni}}{\sqrt{Z_0}}$ and $b_n = \frac{E_{nr}}{\sqrt{Z_0}}$. Then a_n^2 and b_n^2 have the units of power. The S-parameters are obtained from the equations

$$
\begin{aligned}
b_1 &= S_{11}a_1 + S_{12}a_2 \\
b_2 &= S_{21}a_1 + S_{22}a_2
\end{aligned}
\tag{4.1.1}
$$

$$
S_{11} = \left.\frac{b_1}{a_1}\right|_{a_2=0} \qquad S_{12} = \left.\frac{b_1}{a_2}\right|_{a_1=0}
$$

$$
S_{21} = \left.\frac{b_2}{a_1}\right|_{a_2=0} \qquad S_{22} = \left.\frac{b_2}{a_2}\right|_{a_1=0}
$$

In our measurements, we record S_{21}, which is the forward transmission coefficient with the output matched. Referring to Figure 4.2, we see it may also be expressed as the voltage ratio between the output and input to the device.

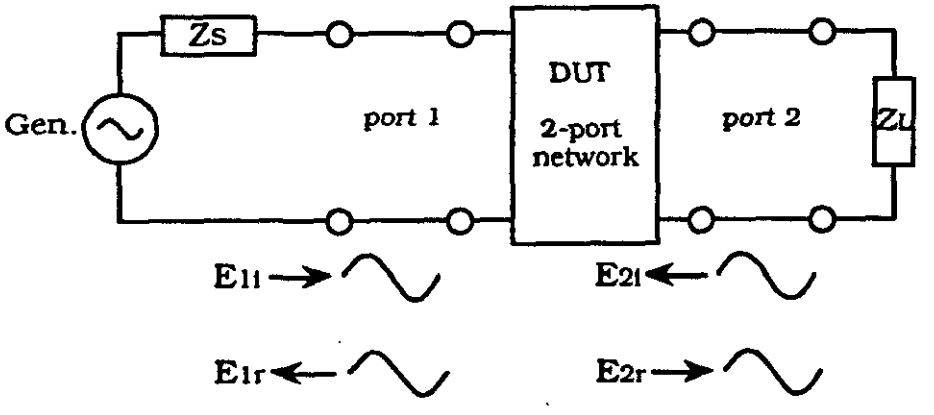

Figure 4.2 Network Analyzer Measurement Illustrating S-Parameter Set. (Ref. 29)

All data are recorded through a GPIB interface on the Fermilab ACNET computer system. Memory limitations in the system and a desire for fine resolution lead to a scheme by which the desired frequency span is scanned in several segments. The scans are automated. Each dataset consists of 31 files x 401 points = 12431 points to cover a range of 45 to 355 MHz, giving a resolution of 0.025 MHz/point. The 31-file sets are concatenated for analysis on a VAX. The various conditions for each dataset are listed in Appendix B, Table B.1. The archive numbers refer to the recording scheme on the ACNET GPIB program. A sample S_{21} measurement in which the wire assembly is inserted into the gap, without HOM dampers corresponding to t=15 msec in the cycle, is shown in Figure 4.3. Notches appear in the signal at the frequencies corresponding to the resonant modes in the cavity. The phase appears as it does as we have not compensated for the phase delays introduced by the cables leading from the cavity to the NA. To analyze the data, two additional measurements are made. For reference, the transmission S_{21REF} is measured with the assembly pushed completely into the central beam pipe. A calibration measurement S_{21CAL} through the laser system is also performed. These are shown in Figures 4.4 and 4.5, respectively.

The stretched wire is relatively low impedance, and when inserted into the gap it effectively loads the cavity, lowering the Qs of the resonant parasitic modes. In order to extract the true magnitude and recover the unloaded Q for impedance due to these modes, a de-embedding procedure is devised using a circuit endcap model. Any impedance may be represented by a generalized Π-network, and it can be shown that the parallel impedance can be neglected for a high-Q mode on resonance.[28,30] The equivalent circuits for the measurements are given in Figure 4.6, where the gap is represented as a series impedance. The gap impedance Z is de-embedded by transforming along the circuit using voltage division and transmission line equations:

$$V_{out} = V_A \tag{4.1.2}$$

$$Z_A = R_3 \tag{4.1.3}$$

$$V_{A'} = V_A\left(\cos\beta l_2 + i\frac{Z_0}{Z_A}\sin\beta l_2\right) = V_{B'}\frac{Z_{A'}}{Z + Z_{A'}} \tag{4.1.4}$$

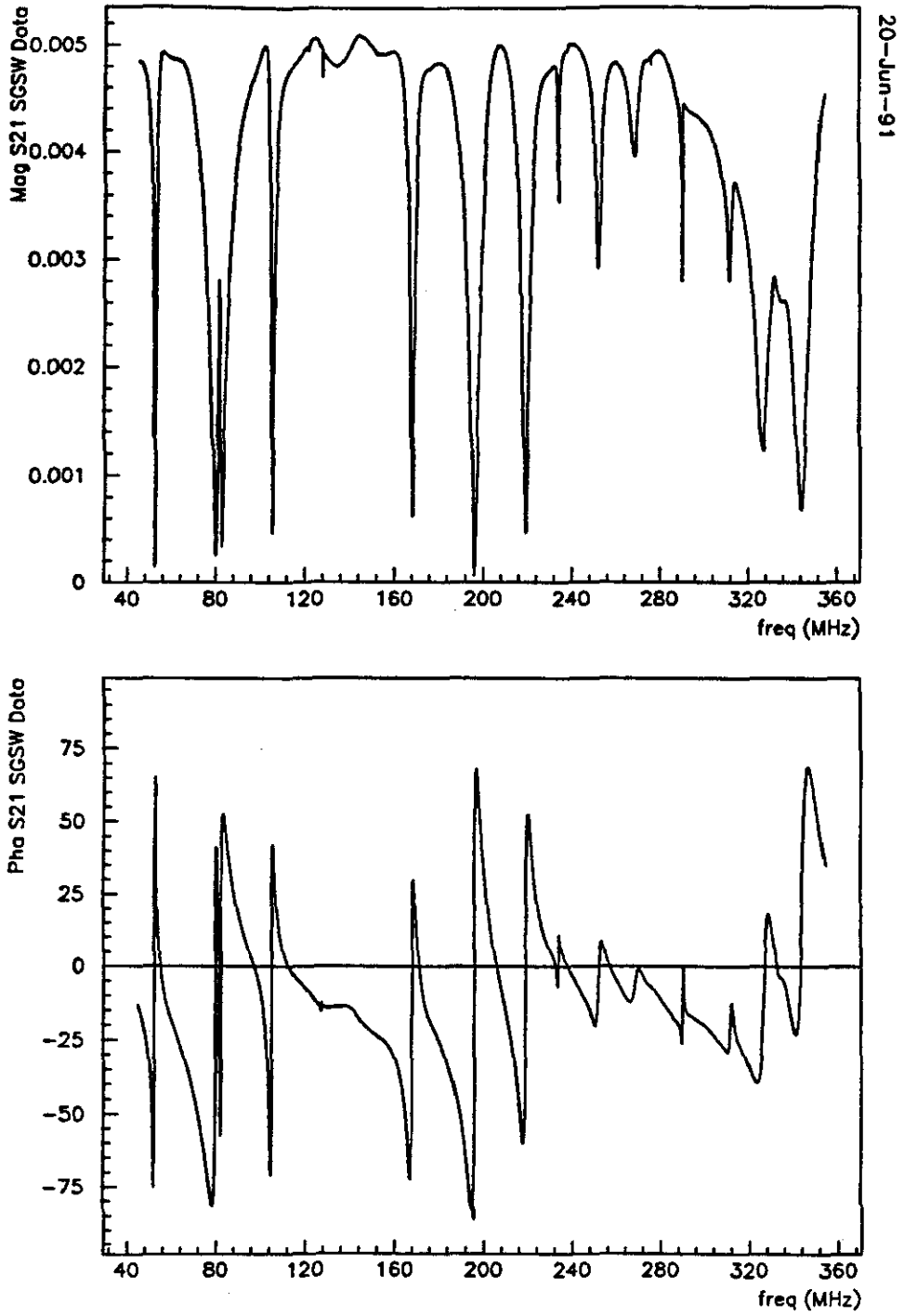

Figure 4.3 Transmission S_{21} Data Through Gap Using Single-Gap Stretched-Wire Assembly. This example corresponds to t=21msec in the cycle, and no higher-order mode dampers are installed in the cavity. An electrical delay of 18.9 μsec has been added to the phase data.

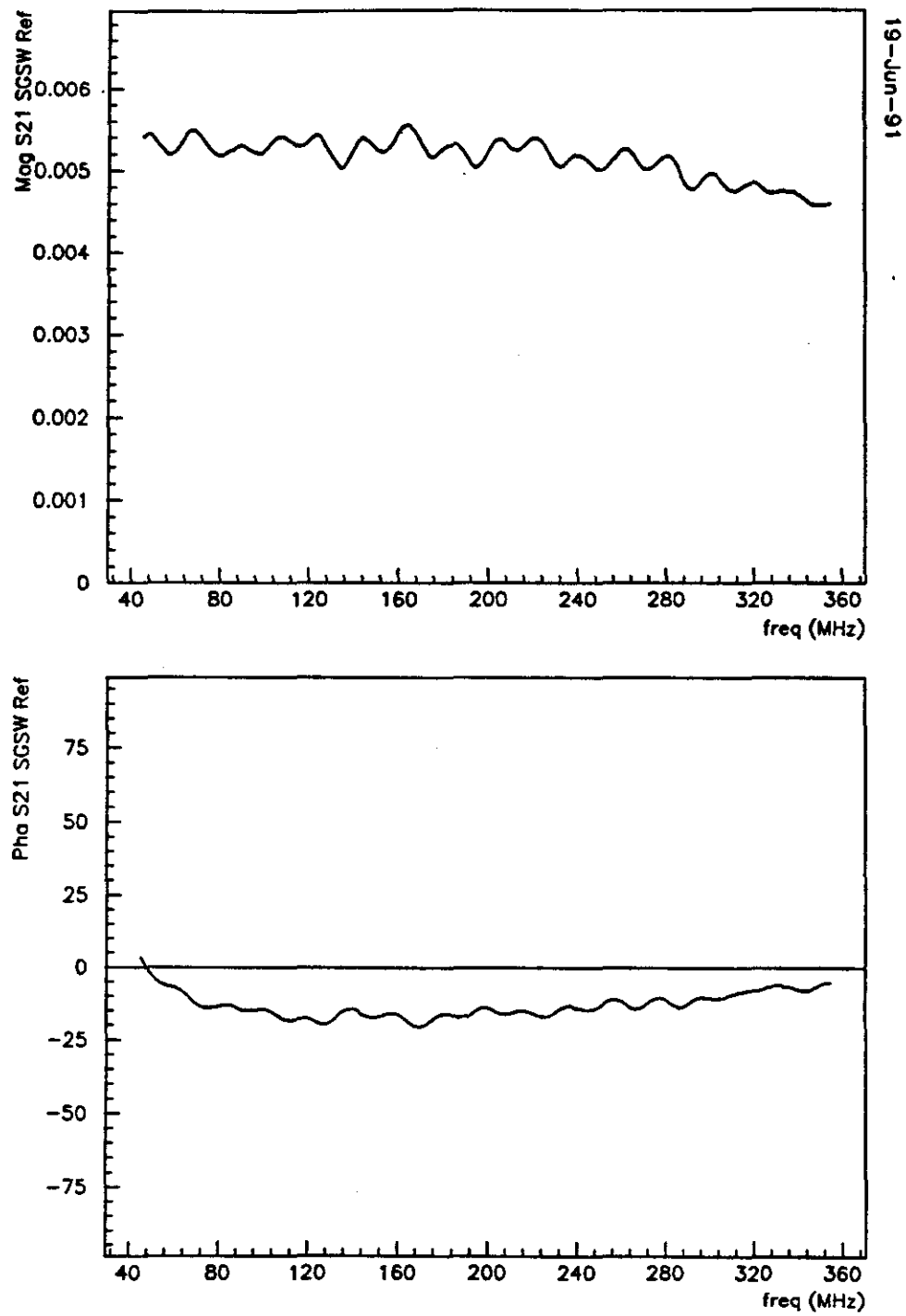

Figure 4.4 Reference Transmission S_{21REF} with Assembly Inside Beam Pipe. An electrical delay of 18.9 μsec has been added to the phase data. The signal level is about -46 dB (0.005 V).

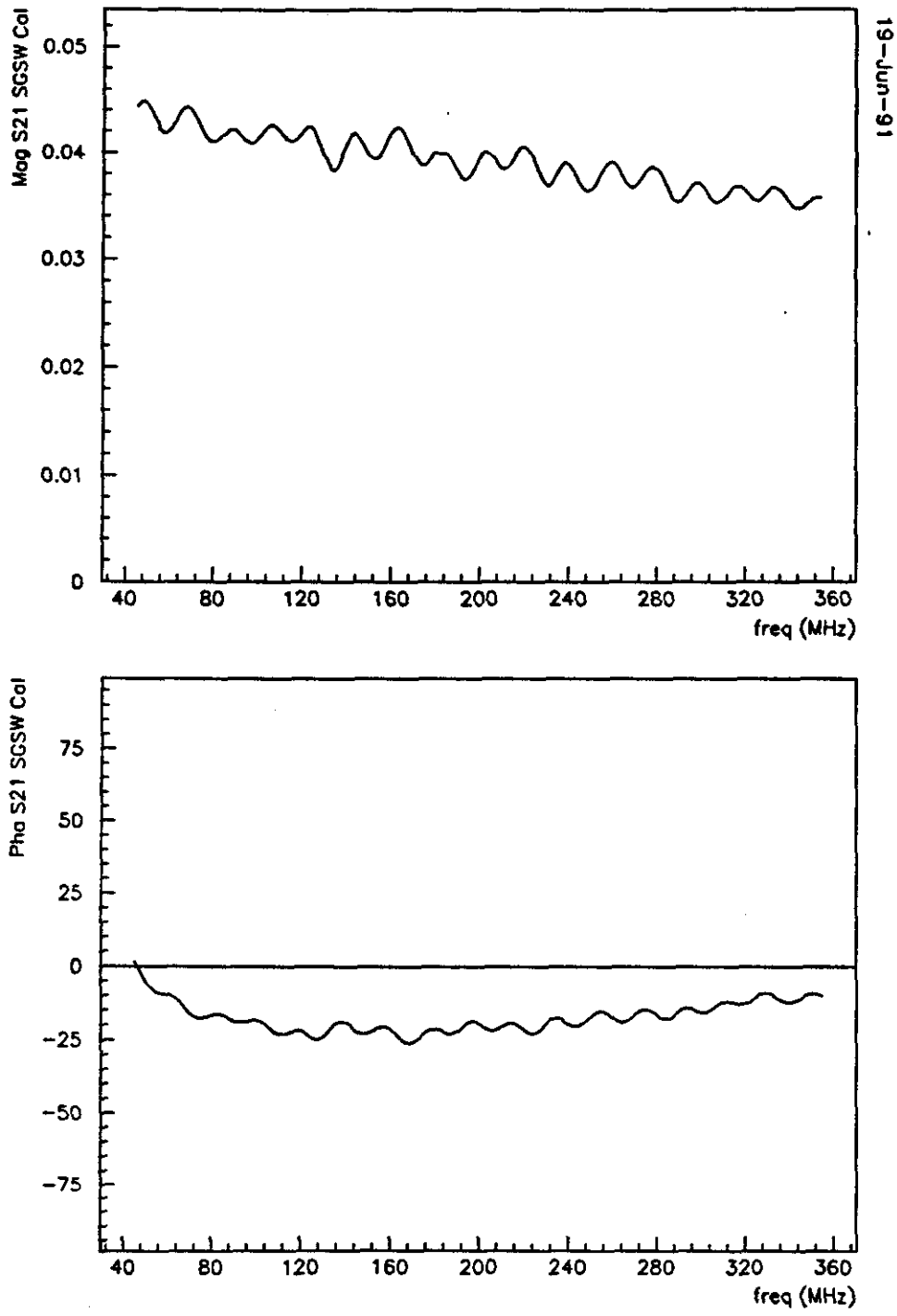

Figure 4.5 Calibration Transmission $S_{21\,CAL}$ Through Optoelectronic System. An electrical delay of 18.6 μsec has been added to the phase data. The signal level is about -28 dB (0.04 V).

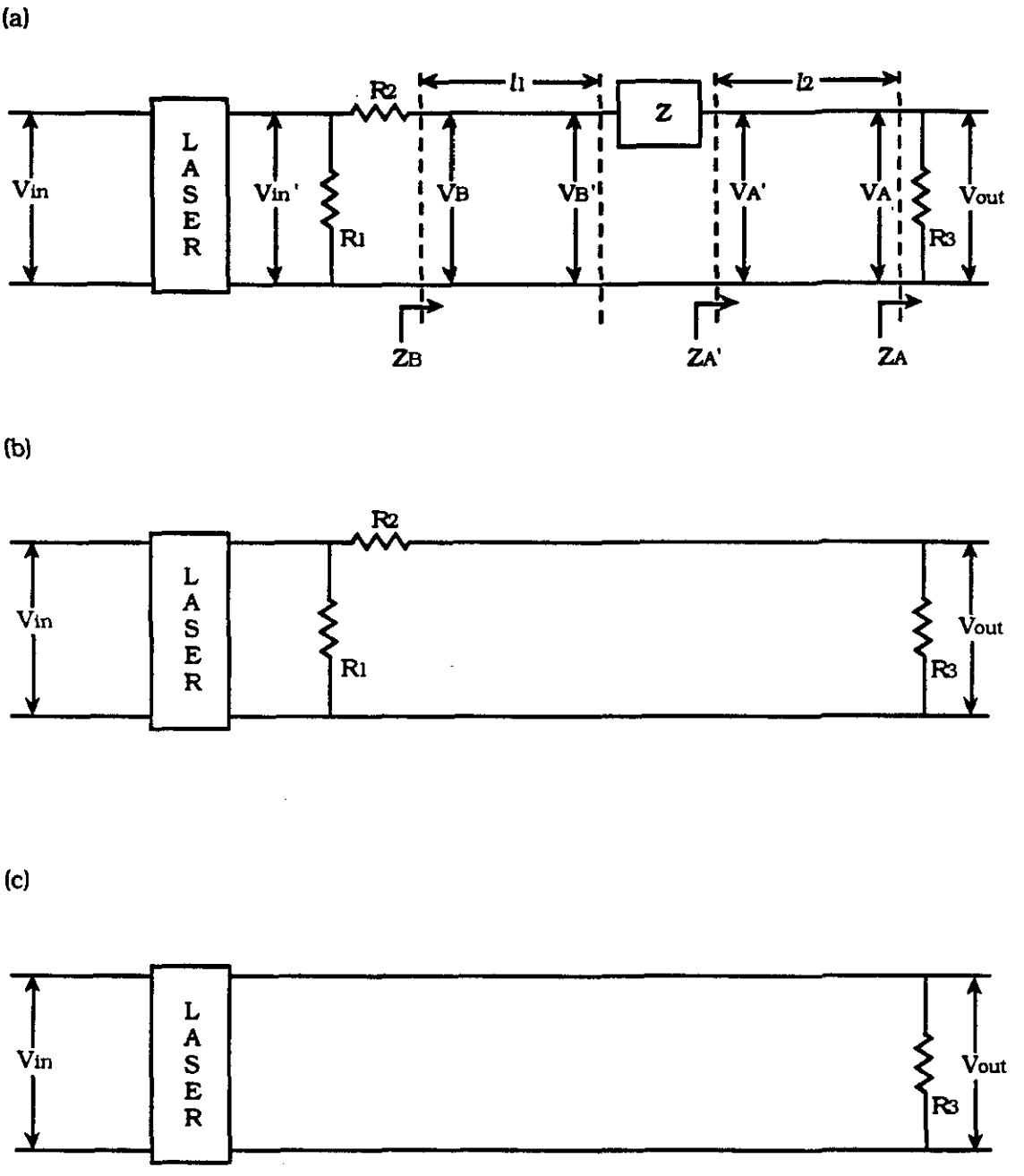

Figure 4.6 Equivalent Circuits for Single-Gap Stretched Wire RF Cavity Impedance Measurement. The measurement inserted in the gap is shown in (a), the reference measurement in an empty beam pipe in (b), and the calibration through the laser in (c).

$$Z_{A'} = Z_0 \frac{R_3 + iZ_0 \tan \beta l_2}{Z_0 + iR_3 \tan \beta l_2} = R_0 \frac{\left(1 + i\dfrac{Z_0}{R_3} \tan \beta l_2\right)}{\left(1 + i\dfrac{R_3}{Z_0} \tan \beta l_2\right)} \tag{4.1.5}$$

$$Z_B = Z_0 \frac{Z + Z_{A'} + iZ_0 \tan \beta l_1}{Z_0 + i(Z + Z_{A'}) \tan \beta l_1} \tag{4.1.6}$$

$$V_B = V_{B'}\left(\cos \beta l_1 + i\frac{Z_0}{Z + Z_A} \sin \beta l_1\right) = V_{in'} \frac{Z_B}{R_2 + Z_B} \tag{4.1.7}$$

Combining equations (4.1.2), (4.1.4), and (4.1.7)

$$V_{in'} \frac{Z_B}{R_2 + Z_B} = \left(\cos \beta l_1 + i\frac{Z_0}{Z + Z_{A'}} \sin \beta l_1\right)\left(\frac{Z + Z_{A'}}{Z_{A'}}\right)\left(\cos \beta l_2 + i\frac{Z_0}{R_3} \sin \beta l_2\right) V_{out} \tag{4.1.8}$$

$$\frac{V_{in'}}{V_{out}} \frac{Z_{A'}}{\left(1 + i\dfrac{Z_0}{R_3} \tan \beta l_2\right) \cos \beta l_2} = \cos \beta l_1 \left[(Z + Z_{A'}) + iZ_0 \tan \beta l_1\right]\left(\frac{R_2}{Z_B} + 1\right) \tag{4.1.9}$$

Dividing both sides by $\cos \beta l_1$ and substituting Z_B gives, after a few steps,

$$\text{R.H.S.} = (Z + Z_{A'})\left(1 + i\frac{R_2}{Z_0} \tan \beta l_1\right) + R_2 + iZ_0 \tan \beta l_1 \tag{4.1.10}$$

$$\text{L.H.S.} = \frac{V_{in'}}{V_{out}} \frac{Z_{A'}}{\left(1 + i\dfrac{Z_0}{R_3} \tan \beta l_2\right) \cos \beta l_1 \cos \beta l_2} \tag{4.1.11}$$

Solving for the gap impedance Z

$$Z = \frac{\text{L.H.S.} - \left[Z_{A'} + R_2 + i\left(Z_0 + Z_{A'} \frac{R_2}{Z_0} \right) \tan \beta l_1 \right]}{1 + i \frac{R_2}{Z_0} \tan \beta l_1} \tag{4.1.12}$$

Note that for the reference S_{21REF}, measured with the stretched-wire assembly pushed inside the beam pipe, $Z = 0$. The second term in the numerator in equation (4.1.12) can therefore be associated by choice with $1/S_{21REF} = (V_{in'}/V_{out})_{REF}$. The calibration measurement through the laser system is defined by $S_{21CAL} = (V_{in'}/V_{in})$. The ratio $S_{21} = V_{out}/V_{in}$ by definition (equations 4.1.1). Then, using

$$\frac{V_{in'}}{V_{out}} = S_{21CAL} \frac{V_{in}}{V_{out}} = \left. \frac{S_{21CAL}}{S_{21}} \right|_{Z \neq 0} = \left. \frac{S_{21CAL}}{S_{21REF}} \right|_{Z=0} \tag{4.1.13}$$

and writing out $Z_{A'}$ explicitly, after algebraic manipulation we have finally

$$Z = \frac{R_3 \left[\left(\frac{1 - S_{21}}{S_{21}} \right) - \left(\frac{1 - S_{21REF}}{S_{21REF}} \right) \right] S_{21CAL}}{\left(\cos \beta l_1 + i \frac{R_2}{Z_0} \sin \beta l_1 \right) \left(\cos \beta l_2 + i \frac{R_3}{Z_0} \sin \beta l_2 \right)} \tag{4.1.14}$$

The values for the resistances are $R_3 = 50\ \Omega$, $R_2 = 300\ \Omega$, $Z_0 = 326\ \Omega$. To solve for Z in practice, we use the relation $\beta l = \omega t$, where t is the delay. By trial-and-error, looking at the phase of Z, we estimate the total delay through the fixture to be about 1 nsec. We estimate from design drawings[31] the position of the gap along the stretched-wire assembly (pushed in to a depth of one inch) to obtain $t_1 = 0.6$ nsec and $t_2 = 0.4$ nsec.

A routine was written to read the data files and calculate the gap impedance Z according to eqn. (4.1.14). A typical result for the nominal cavity (no HOM dampers), corresponding to t=21 msec in the cycle, is given in Figure 4.7, based on measurements comparable to those shown previously. The data show a series of narrow resonances that exist in the cavity above the fundamental. A tabulation of frequencies for these data, including the mode designation used throughout this thesis, is given in Table 4.1. The case for the damped cavity is also included. It is

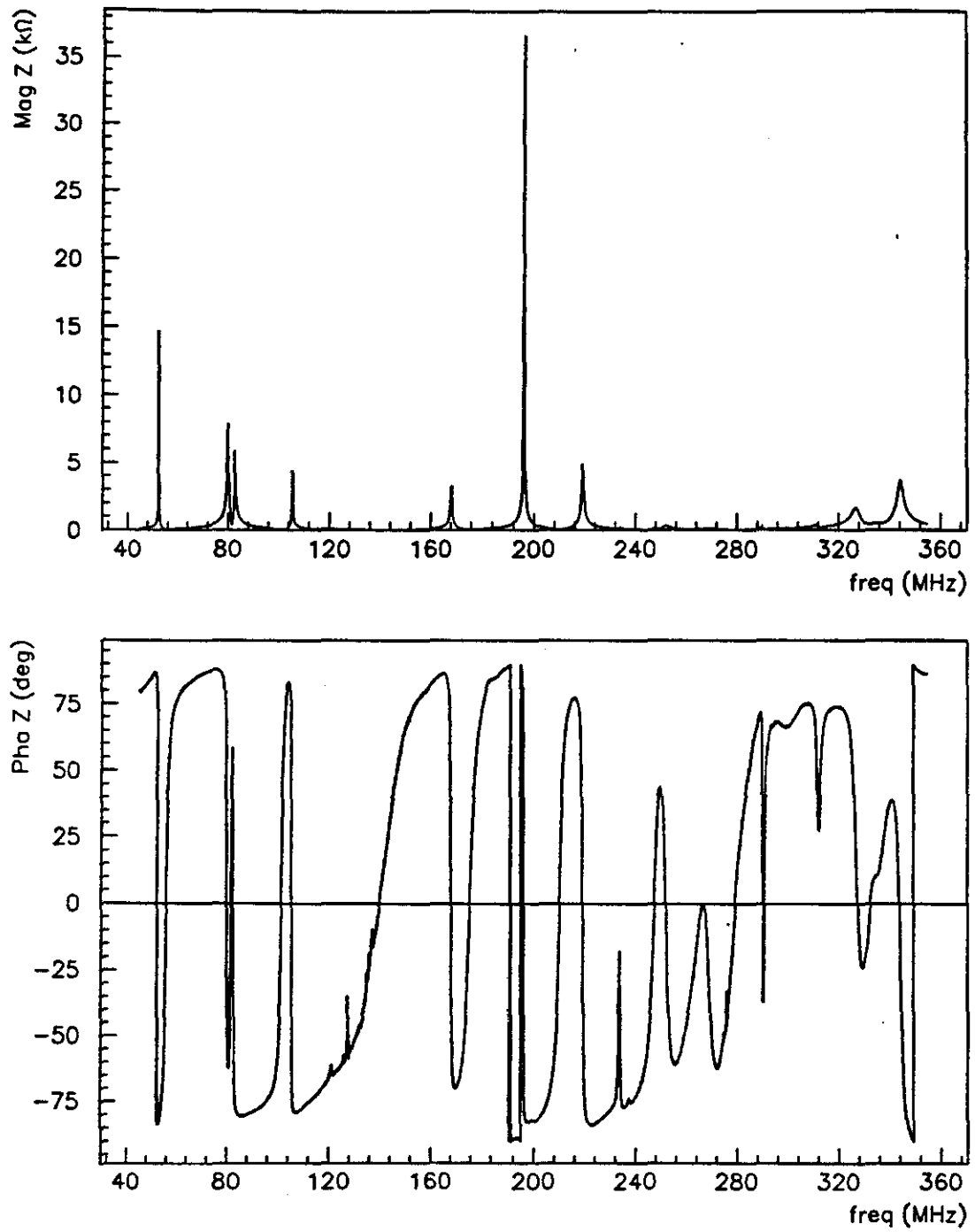

Figure 4.7 Calculated Single-Gap Impedance of Booster RF Cavity De-embedded from Single-Gap Stretched Wire Measurement. The graphs show the result using the datasets in Figures 4.1.2,3,4 (t=21 msec, no higher-order mode dampers).

to be noted that the frequencies are significantly shifted when the dampers are installed. More will be said about the dampers in the next chapter.

Table 4.1 Designations of Booster RF Cavity Resonant Modes (example at t=21 msec)

	NOMINAL		DAMPED	
	freq (MHz)	even /odd	freq (MHz)	even /odd
f_{RF}	52.39	E	52.34	E
f1	79.9	O	82.1	O
f2	82.7	E	84.7	E
f3	105.4	E	105.2	E
f4	168.1	E	164.9	E
f5	196.0	O	196.8	O
f6	219.0	E	--	
f9	--		263.7	E
f10	--		302.1	O
f11	--		305.4	E
f7	326.8	O	--	
f8	344.3	E	340.9	E

A full tabulation of the single-gap data, both before and after installation of the HOM dampers, is presented in Tables B.2 and B.3, respectively.

Bead-Pull Method

A number of references describe the theory of the perturbation technique for measuring cavity impedances so the derivation will not be repeated here.[32,33,34] Essentially, a small metallic or dielectric object is introduced into a resonant structure, perturbing the electric and magnetic field. This causes the phase of a given mode to shift in proportion to field displacement. In the case of a metallic sphere in a region assumed to have negligible magnetic field H, we obtain

$$\frac{E^2}{U} = -\frac{\delta\omega}{\omega_r}\frac{4}{3\varepsilon_0\delta v} \tag{4.1.15}$$

where E is the electric field in the sphere, U the total energy stored in the resonator, ω_r the resonant center frequency, $\delta\omega/\omega_r$ the relative frequency shift, ε_0 the permittivity of space, and $\delta v = 4/3\pi r_B^3$ the volume of the sphere. The potential drop V over the length L across the gap may be written

$$V = \int_L \bar{E} \circ dz \quad \longrightarrow \quad V = \sqrt{U}\int_L \left(-\frac{\delta\omega}{\omega_r}\frac{4}{3\varepsilon_0\delta v}\right)^{1/2} dz \tag{4.1.16}$$

We may apply the definitions

$$R_s = \frac{V^2}{P} \quad \text{and} \quad Q = \frac{\omega_r U}{P} \tag{4.1.17}$$

where R_s is the effective shunt (parallel) resistance, Q the quality factor, and P the power dissipated in the resonator. Making the substitutions, we obtain the relationship for the shunt resistance:

$$R_s = \frac{Q}{\omega_r}\frac{4}{3\varepsilon_0\delta v}\left\{\int_{-\infty}^{\infty}\left[-\frac{\delta\omega}{\omega_r}\right]^{1/2} dz\right\}^2 \tag{4.1.18}$$

For resonances which do not tune and with the cantenna loads disconnected as a test, we easily obtain results using this method. Although the old cavity damping loops (Figure 5.12) couple preferentially to the modes around 80 MHz, the cantennas attenuate several other modes as well. In this configuration, one obtains the maximum mode impedance and Q. For the tuning modes, drifting in the phase due to thermal fluctuation in the bias current or mechanical vibration effects make accurate measurements difficult, with or without the cantenna. We wish to compare the bead-pull technique with the stretched-wire result; therefore, the cantenna is connected for the data recorded below. In general, we are limited to resonant modes with Q greater than about 200.

The experimental setup is depicted in Figure 4.8. A spherical brass bead with a small hole (diameter=1 mm) bored through the center is strung upon and glued to a cotton string and pulled on axis across the gap by a small motor. The bead is slightly oblong (2%) with average diameter 6.199 mm measured with a micrometer. An HP 8753C network analyzer (NA) is used to excite the cavity through the gap monitors. A 40 dB HP461A amplifier is used on the input to the NA. With this arrangement, we are measuring the same single-gap impedance as with the single-gap stretched wire. We observe the phase between the NA input and output by displaying the transmission coefficient S_{21} on resonance using very high resolution (10 Hz). This allows a phase scan at a virtually fixed frequency with the phase appearing virtually flat at zero. The network analyzer is triggered to slowly scan the phase synchronized with the bead passing over the gap (10 sec). The bead is centered without mechanical guides on axis in the beam pipe, and the phase shift seems not to depend strongly on small radial shifts. The measurements are symmetric for scans in either direction. In order to determine the Q, the linear phase slope $\Delta\theta$ is measured over a somewhat expanded frequency range $\Delta\omega$ (100 kHz). The bead-pull results are recorded for the nominal cavity (cantenna connected) with the bias current off and equal to 1500, 1800, and 2125, corresponding to 15, 21, and beyond 35 msec (not used) in the cycle, respectively. The frequency, phase shift, and phase slope data are presented in Table B.4.

The phase shift caused by the perturbing bead is clearly seen in two typical phase scans in Figure 4.9. In this test, the center frequency is (a) 79.7 MHz and (b) 164 MHz, the tuner bias current is 1500 A, and the cantennas are disconnected. The phase shift for virtually all modes is negative. Curiously, for two modes, at 532 MHz

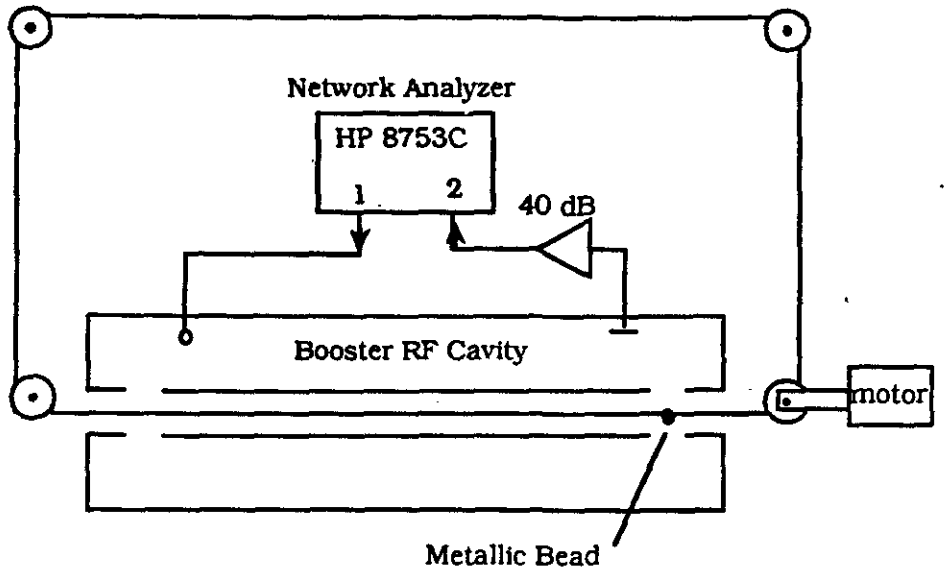

Figure 4.8 Experimental Setup for Bead Pull Measurement of RF Cavity Single Gap Impedance.

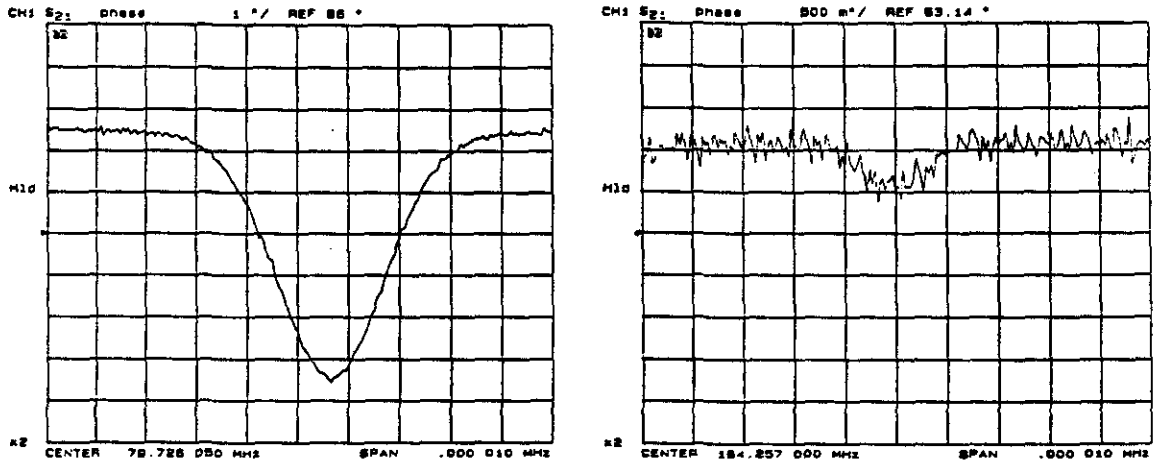

(a) (b)

Figure 4.9 Typical Scans in Bead Pull Measurement Showing Resulting Phase Shift. The cavity mode frequency and vertical scales are (a) 79.7 MHz, 1.0 °/div and (b) 164 MHz, 0.5 °/div , respectively. Note the increased noise in (b), a tuning mode.

and 1.5 GHz, it is positive. The phase shifts seen for the cases of interest are generally less than 1°, therefore well within the linear region of the phase slope for the modes of interest.

For a resonant response function, the equation governing the relationship between a frequency shift $\Delta\omega$ and a phase shift $\Delta\theta$ is given by

$$\frac{\Delta\omega}{\omega_r} = \frac{1}{2Q}\tan\Delta\theta \approx \frac{\Delta\theta}{2Q}\bigg|_{\Delta\theta<<0} \tag{4.1.19}$$

We may use the small angle approximation, as the phase shifts are small in our measurements. Using eqn. (4.1.19), the quality factor Q is determined using the linear phase slope, and the maximum frequency shift is determined from the phase shift in the mode due to the presence of the bead. If we assume a gaussian for the spatial variation in z of the relative mode frequency shift across the gap, we may write

$$\frac{\delta\omega}{\omega_r} = \Theta e^{-\left(\frac{z}{\sigma}\right)^2}, \quad \text{where} \quad \Theta = \frac{\delta\omega}{\omega_r}\bigg|_{\max} = \frac{\delta\theta_{\max}}{2Q} \tag{4.1.20}$$

That the gap field is well approximated by a gaussian is verified by a simple calculation of the normalized field profile using 2-dimensional solutions of Laplace's equation (PE2D).[35] The gap is modeled as a flat-plate capacitor using the dimensions given in Figure 4.1 with infinite extent in the plane of the paper. The result is shown in Figure 4.10 (a). The fit parameters shown correspond to $G = P1\exp\left(-\frac{1}{2}\left(\frac{x-P2}{P3}\right)^2\right)$. Note that $\sigma = \sqrt{2}\,P3$. Substitution of eqn. (4.1.20) into eqn. (4.1.18) gives

$$R_s = \frac{Q}{\omega_r}\frac{4\Theta}{3\varepsilon_0\left(\frac{4}{3}\pi\bar{r}_B^{\,3}\right)}\left\{\int_{-\infty}^{\infty} e^{-\left(\frac{z}{\sigma}\right)}dz\right\}^2 = \frac{\delta\theta_{\max}}{f_r}\frac{1}{4\pi^2\varepsilon_0 r_B^{\,3}}\left\{2\sigma\int_0^{\infty} e^{-x}dx\right\}^2 \tag{4.1.21}$$

We ignore the small hole bored through the bead as the field lines will not penetrate it well. The value of the integral is unity. The full width at half maximum Δ for a gaussian is related to the half width σ through $\sqrt{\ln 2} = \frac{\Delta}{2\sigma}$. The result becomes

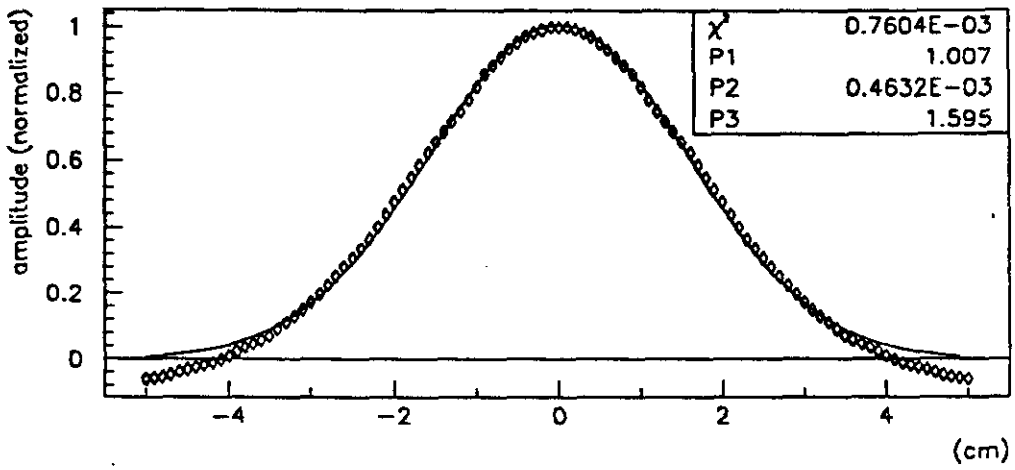

(a)

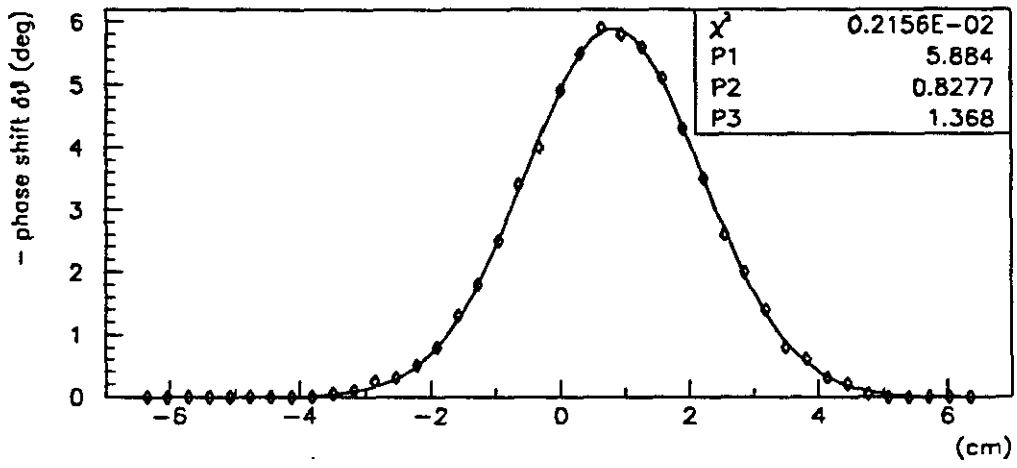

(b)

Figure 4.10 Gaussian Fits of (a) Calculated Gap Profile and (b) Measured Phase Shift Scan. Plot (b) shows the data from 164 MHz in Figure 4.9.

$$R_s = \frac{\delta\theta_{\max}}{f_r}\frac{\left(4\sigma^2\right)}{4\pi^2\varepsilon_0\bar{r}_B{}^3} = \frac{\Delta^2}{4\pi^2\varepsilon_0 r_B{}^3\ln 2}\frac{\delta\theta_{\max}}{f_r} \tag{4.1.22}$$

A sample gaussian fit of the phase shift scan for 164 MHz is shown in plot (b) in Figure 4.10. The average full width Δ measured for several scans is (3.3±0.15) cm. We use ε_0=8.854x10^{-12} F/sec, $\bar{r}_B$ = 0.003099 m, and convert $\delta\theta$ to radians to obtain

$$R_s = \frac{(0.033)^2}{4\pi^2\left(8.854x10^{-12}\right)(0.003099)^3\ln 2}\frac{\pi}{180}\frac{1}{10^9}\frac{\delta\theta_{\max}\,(\text{deg})}{f_r\,(\text{MHz})}\ (\text{k}\Omega)$$

$$R_s = \left(2.6x10^3\right)\frac{\delta\theta_{\max}\,(\text{deg})}{f_r\,(\text{MHz})}\ (\text{k}\Omega) \tag{4.1.23}$$

The results for gap impedance are tabulated for t=15 msec in Table B.5 and compared with the stretched-wire technique. The single-gap R and Q are plotted in Figure 4.11 to demonstrate the comparison between the wire and bead-pull result. The slope is 0.92 in the comparison of impedance R and it is 0.9 for Q. Note that the de-embedding technique for the wire recovers the unloaded Q.

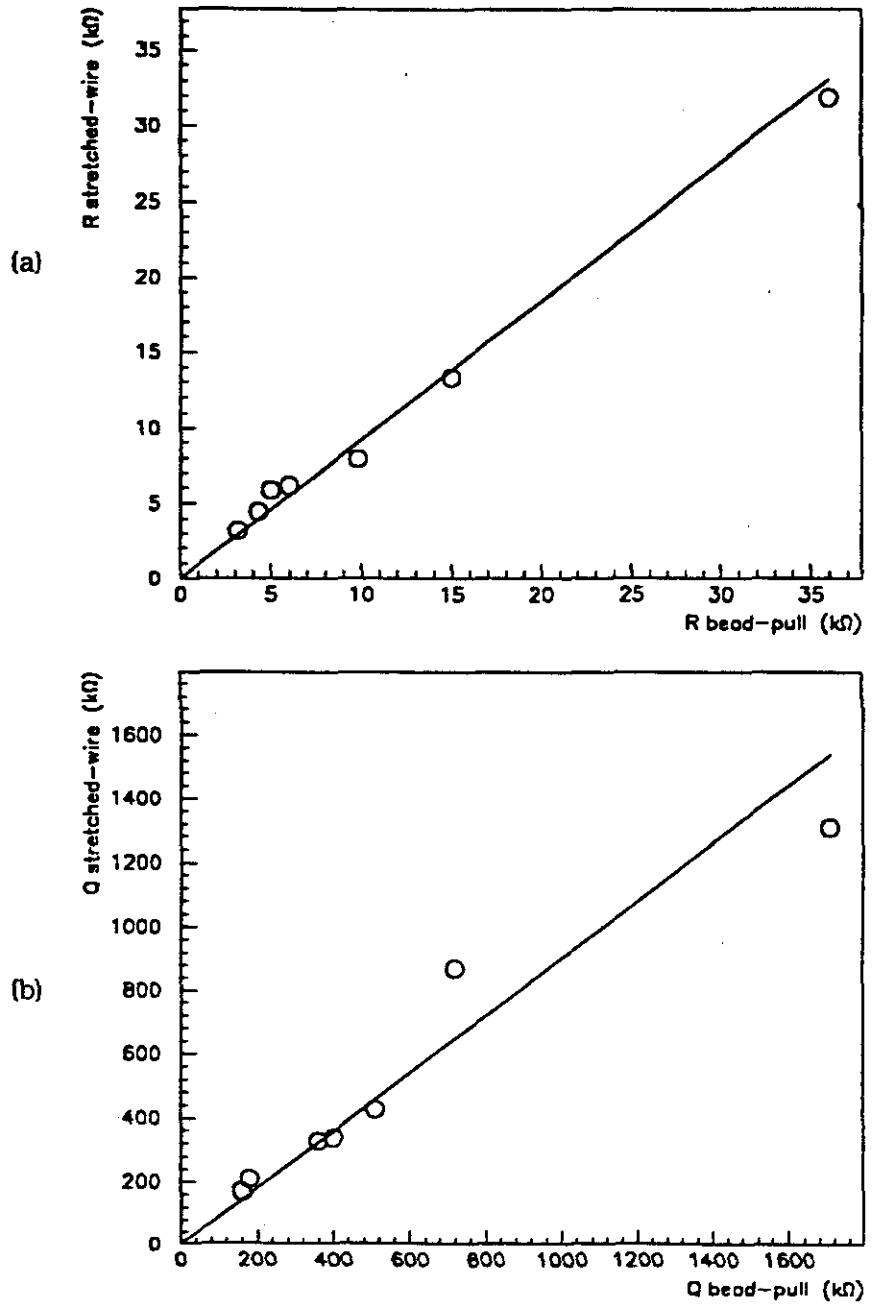

Figure 4.11 Correlation Between Stretched-Wire and Bead Pull Measuremements of Single-Gap Impedance and Q. View (a) shows R, (b) Q.

Power Dissipation Method

A third, independent bench method was employed as an order-of-magnitude verification of the above results for the single-gap impedance at the fundamental frequency. The gap impedance is deduced making use of a simple circuit model: one measures the power delivered to the cavity, which is dissipated in the shunt resistance of the resonator. In the measurement, the cavity is tuned to 45.25 MHz and excited through one of the large loops by a power amplifier. The HOM damper is installed. The experimental setup is depicted in Figure 4.12. The forward power into the cavity is recorded by a network analyzer after directing a small portion (about 10%) of the signal using a directional coupler into port B. The coupling factor, or ratio of input/B, is measured to be $(-44.677-(-4.483)) = -40.194$ dBm. The reflected power is recorded by reversing the coupler. The gap monitor response is observed through port A.

The results are tabulated in Table 4.2. The measured signal power exciting the cavity is increased by the coupling factor and, recalling the definition $\text{dBm} = 10\log(P/(1\,\text{mW}))$, converted to watts and subtracted. This appears as steps 1a-1c in the table. In step 2, the gap monitor signal is scaled to give the resulting peak gap voltage. The step-up voltage ratio between the gap monitor and the gap was designed to be $10^4 = 80$ dBm in the original cavity at the fundamental frequency;[36] the addition of the internal HOM hardware shifts this somewhat. Measurement of the step-up ratio by inserting the stretched-wire assembly (recalling Figure 4.1) into the gap yields a result of $((-2.56+18.06)-(-63.00)) = 78.5$ dBm. The first number is the signal on the stretched-wire, scaled by a factor of 8 due to the resistors in the assembly $V_{msrd} = V_{gap}\dfrac{50}{50+350}$; the second number is the signal on the gap monitor. The peak voltage at the gap after scaling is determined using the relationship $P = \frac{1}{2}V^2/R$, where R=50Ω is the input impedance of the network analyzer.

The effective shunt impedance of a single gap is calculated using half the power in 1c: $R_{SH} = \frac{1}{2}\dfrac{(23.1)^2}{(0.07213/2)} = 7.4$ kΩ. Comparison with the stretched-wire value of 9.0 kΩ at 45.3 MHz with the HOM dampers installed (see Table B.3) gives a difference of 20%. This is within the accuracy of this power dissipation measurement result, estimated also to be about 20%.

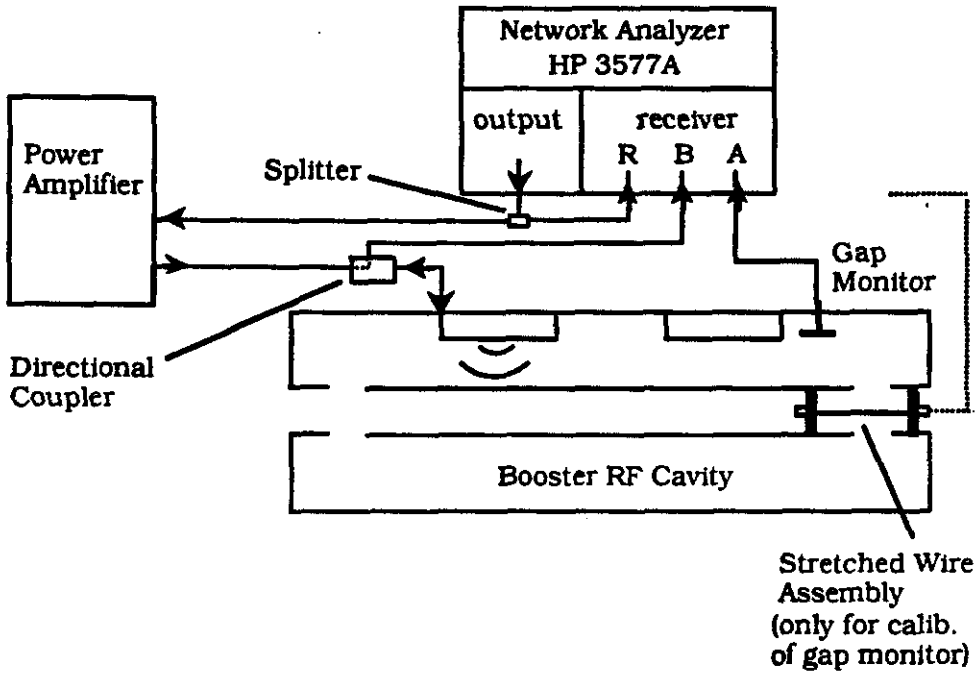

Figure 4.12 Power Dissipation Measurement Setup to Determine RF Gap Impedance. A sweeping signal from the NA is amplified and directed into the large loop through coupler. Dashed line indicates direction for forward-power measurement B/R. Coupler is reversed for reflected-power measurement. A/R gives gap monitor response. The stretched wire is inserted only for the calibration measurement of the gap monitor.

Table 4.2 Measurement Results for Power Dissipation Method

	(port) signal	msrd power (dBm)	coupling or scaling factor (dBm)	scaled power (W)	peak voltage (gap)
1a	(B) forward power	-16.062	40.194	0.25894	
1b	(B) reflected power	-17.48	40.194	0.18681	
1c	power dissipated in load (2 gaps)			0.07213	
2	(A) gap monitor	-41.21	78.5	5.358	23.1

Net RF Cavity Impedance

In order to use the single-gap data to construct a net total impedance and calculate the overall instability growth rates, two important corrections have to be made. First, since there are two gaps per cavity, the phase of each mode must be taken into account in addition to the intergap transit time factor. The latter is a function of both beam energy and mode frequency. The principle of superposition is applied in the frequency domain to calculate the single cavity impedance, based on Ref. 37. The result is a net partial addition or cancellation. Second, the higher-order modes vary about a nominal value due to slight differences in the cavity geometries, although the fundamental frequency is by definition locked in all cavities to the same value. Among the 17 Booster cavities, the higher-order mode frequency spread is on the order of 1%, which is considerably larger than the natural widths due to the Q values. Thus, the net sum is not a simple factor of 17 times the individual cavity impedance.

To record the intergap phase angle ϕ for the higher-order modes, monopole probes are inserted into the gaps and the transmission measured using the network analyzer. The data giving the log magnitude and phase (Figure 4.12) show which modes are even and which are odd. Because the probes face one another, ϕ is shifted from the data by π. For even modes, $\phi=\pi$, and for odd, $\phi=0$. The fundamental f_{RF} and f2, f3, f4, f6, f8, f9, f11 are even, while f1, f5, f7, f10 are odd. Note that in addition to parallel resonances (magnitude maxima), a few series resonances exist between even modes. The monopole measurement is made at one bias current value (1500 A). For analysis, then, the intergap phase is constructed at all times based on the probe measurement, using the mode frequencies from the wire measurements (Tables B.2, B.3). An example of the reconstructed, idealized intergap phase angle is shown in Figure 4.13. The intergap phase delay α due to the transit time of the beam was calculated using $\alpha = \omega\Delta t$, where $\omega = 2\pi f_{HOM}$, $\Delta t = L/\beta c$, and $L = 2.14$ m, the distance between gap centers.[31]

Let the indices 1 and 2 refer to the first and second gaps, respectively. Consider a single Fourier component of the beam current I traversing the cavity. Define Z_{11} as the impedance due to the first gap when the current in the first gap I_1 is finite while the current in the second $I_2 = 0$. Z_{12} is the mutual impedance, or the impedance due to

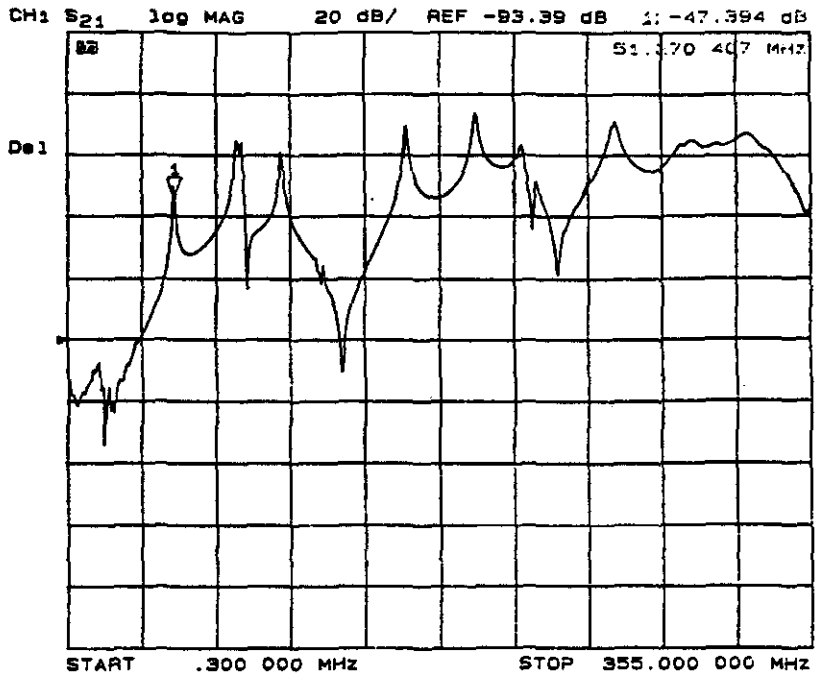

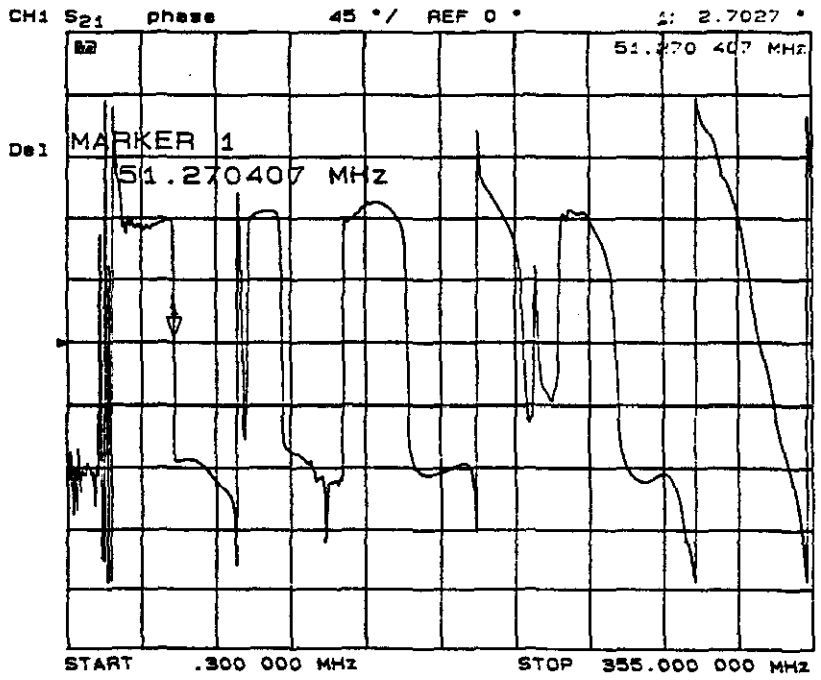

Figure 4.13 Log Magnitude and Phase Measured with Monopole Probes Inserted into RF Cavity Gaps. Intergap phase for modes is 180 degrees out of phase with these data.

(a)

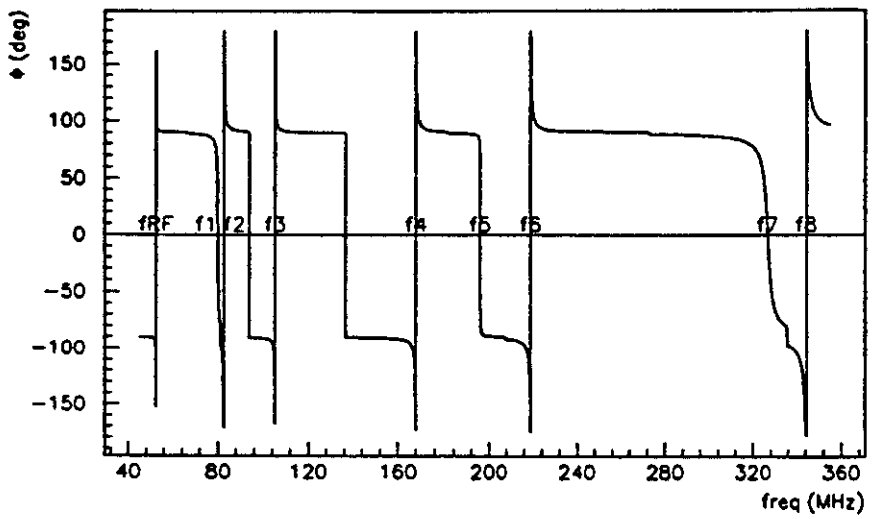

(b)

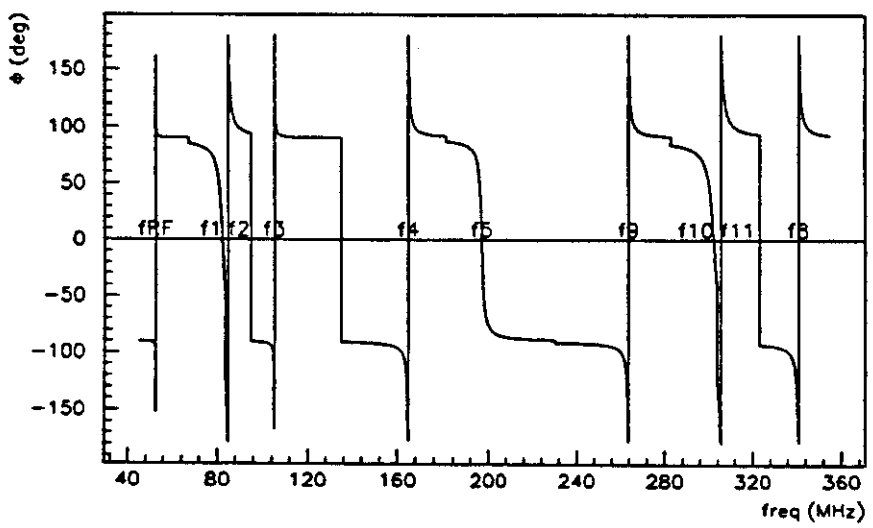

Figure 4.14 Intergap Mode Phase Angle Constructed for Analysis. Shown is the example corresponding to t=21 msec for (a) HOM dampers out and (b) HOM dampers in.

the first gap when $i_1 = 0$ and i_2 is finite. Z_{22} and Z_{21} are defined similarly for the second gap. The single-gap measurement is by definition $Z_0 = Z_{11} = Z_{22}$. For strongly coupled gaps, we assume $|Z_{12}| = |Z_{21}| = |Z_0|$. To account for the mode phase angle, we write $Z_{12} = Z_0 e^{j\phi}$ and $Z_{21} = Z_0 e^{-j\phi}$. The sign difference in the phase factor accounts for the fact that we assign as positive the forward propagation in time from left to right. The beam current at the second gap has a phase shift relative to the current at the first given by $i_2 = i_1 e^{j\alpha}$. The voltage at each gap may be expressed in matrix form as

$$\begin{pmatrix} V_1 \\ V_2 \end{pmatrix} = \begin{pmatrix} Z_{11} & Z_{12} \\ Z_{21} & Z_{22} \end{pmatrix} \begin{pmatrix} i_1 \\ i_2 \end{pmatrix} = Z_0 \begin{pmatrix} 1 & e^{j(\phi+\alpha)} \\ e^{-j(\phi+\alpha)} & 1 \end{pmatrix} \begin{pmatrix} i_1 \\ i_2 \end{pmatrix} \tag{4.1.18}$$

The total impedance may be calculated from

$$Z_T = \frac{V_1}{i_1} + \frac{V_2}{i_2} = Z_0\left(1 + e^{j(\phi+\alpha)}\right) + Z_0\left(1 + e^{-j(\phi+\alpha)}\right) \tag{4.1.19}$$

$$Z_T = 2Z_0\left(1 + \cos(\phi + \alpha)\right) \tag{4.1.20}$$

One additional correction is made. The attenuation in each resonance ω_r between the successive passage of each bunch is accounted for using

$$Z_T = \alpha Z_T = \left(e^{-\frac{\omega_r}{2Q} t_b}\right) Z_T \tag{4.1.21}$$

where Q is for the single-gap and the time between bunches is $t_b = 1/f_{RF}$. Equation (4.1.21) gives a maximum $Z_T = 4\alpha Z_0$ at those frequencies for which $(\phi+\alpha) = m\pi$ when m is even. Complete cancellation occurs when m is odd. The result is shown graphically in Figure 4.14 for the odd-even pair of the Booster RF cavity modes around 80 MHz (f1 and f2). Note the cancellation in the real part for the odd mode f1 on the left, and that the imaginary part no longer resembles a classical LRC resonator. Twice the single-gap impedance is shown superimposed using a dashed line for comparison.

Data on the relative variation in the HOMs among cavities are obtained from transmission measurements through the gap monitors. A power amplifier is used in

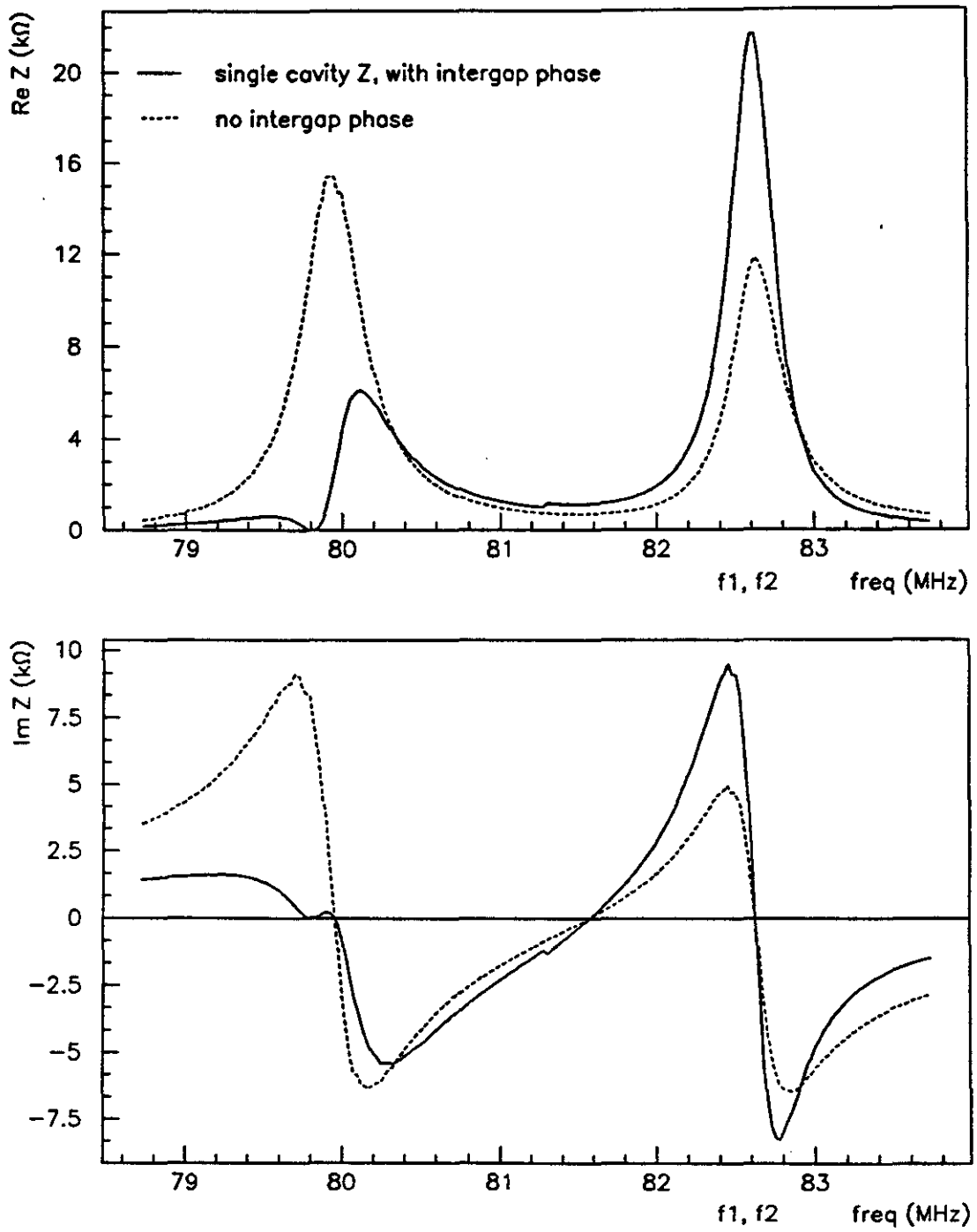

Figure 4.15 Single Cavity vs. Twice Single-Gap Impedance.

the input to the cavity in order to excite it to a sufficient level as the gap monitors are not strongly coupled at all frequencies. The results are tabulated in Table B.6. The cavity labeled no. 8 is the one that was removed from the tunnel and measured on the test stand. The data for cavity modes f4, f6, and in column (a) under f2 are supplied courtesy of D. Wildman, while the others are obtained more recently with his assistance. In fact, these latter data (f1, f2 column (b), and f5) were made after HOM damper hardware was installed in cavities 9, 10, 11, and 12. Note the frequency shift in f1 and f2 for these cavities . For the f2 mode, the average of the two sets of measurements is taken, with the exception of cavities 9-12. The cavity position data, for reference, are supplied by J. Steimel. For the fixed modes f1 and f2, the bias current is zero for the measurement. The data for f4 and f6 correspond to around extraction, while f5 (also fixed) is measured around transition. In all cases the cavity short is out.

The data in Table B.6 indicate an intercavity frequency spread of about 1%, roughly proportional to frequency. The distributions may be visualized by creating histograms, depicted in Figure 4.15. This example shows 15 cavities, centered on the average value among all cavities, with a bin width chosen to equal the rms value $\sigma = \sqrt{\frac{\sum x^2 - n\bar{x}^2}{n}}$. As we have only partial information for some of the modes, the data points are scaled appropriately. The spread in modes f7-f11 is not measured and is assumed to be that of f6.

The net sum impedance is constructed by shifting and superimposing the single-cavity impedance data mode-by-mode according to the measured values in Table B.6. For each mode, the intermediate result is scaled to the desired number of cavities using (total no. cavities/total no. data points). The result is about 40% less than a straight multiplication. The net sum for 15 cavities is shown with the solid line in Figure 4.16 again for the odd-even mode pair around 80 MHz. The two shorted cavities are removed from the distribution. The dashed lines represent the result when neglecting the intercavity spread. For the even mode on the right, note that a simple multiplication of 2 gaps x 15 cavities x single-gap impedance is similar to the calculation of the net impedance, but is shifted and more narrow. The odd mode is completely different.

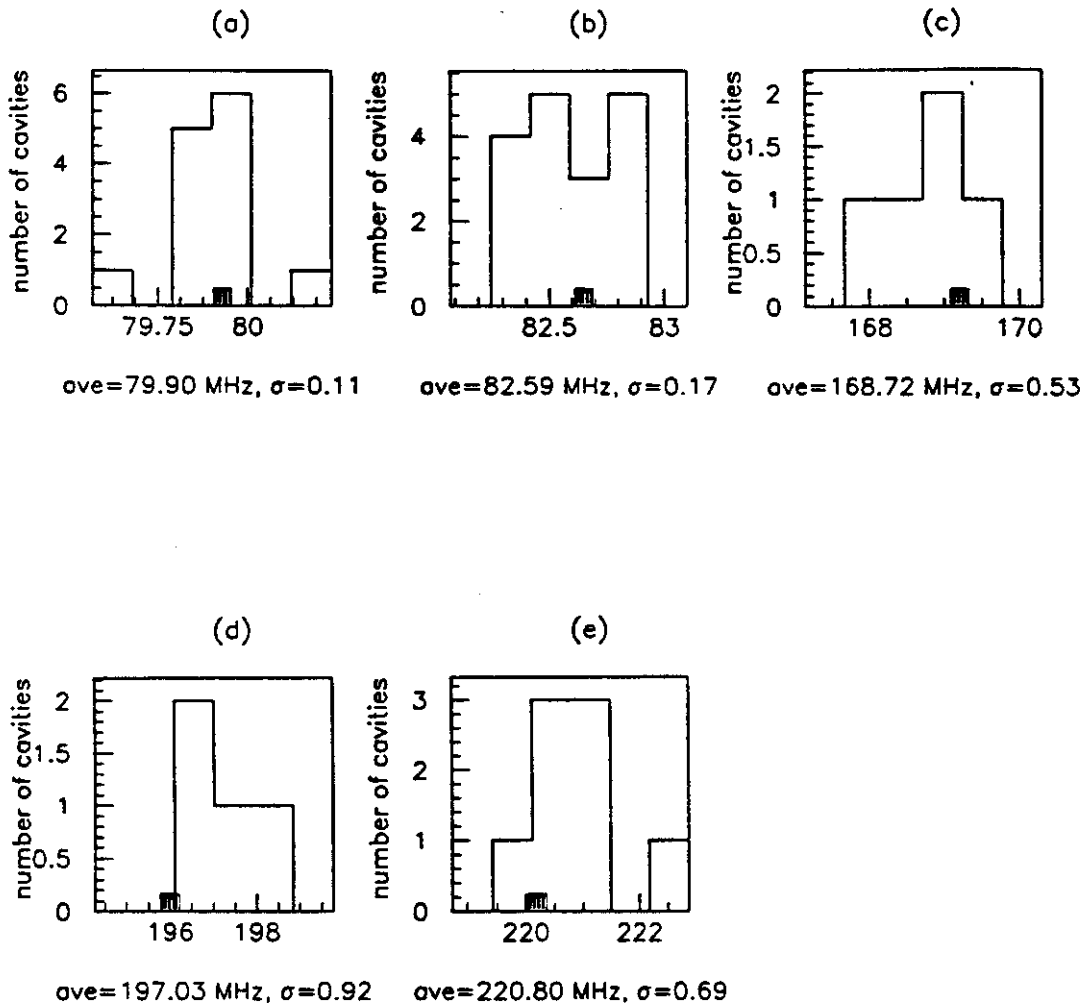

Figure 4.16 Representative Distributions in RF Cavity Higher-Order Modes. Shown are histograms of bin width σ for (a) f1, (b) f2 (c) f4, (d) f5, and (e) f6 Cavity Modes.

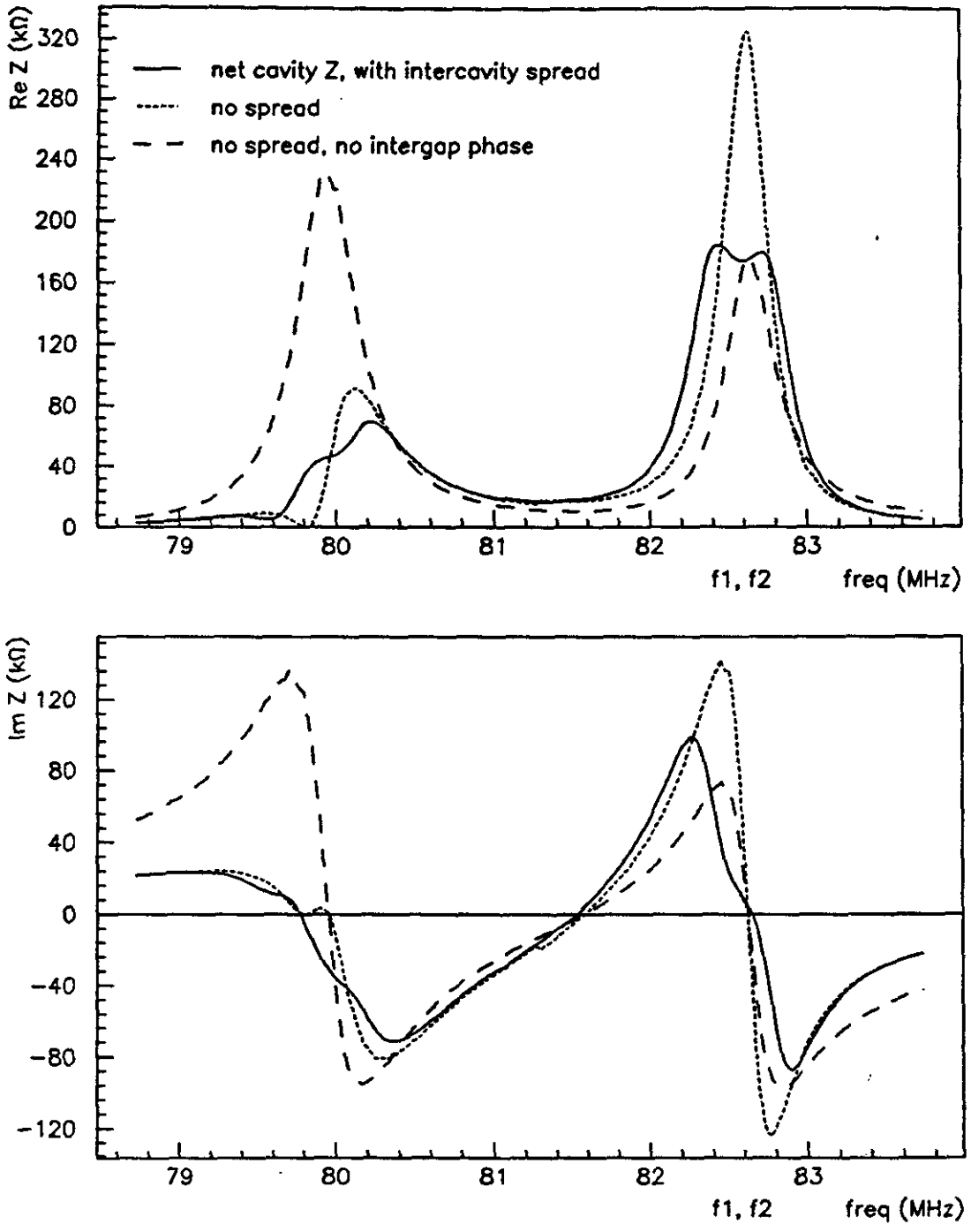

Figure 4.17 Net Impedance With and Without the Intercavity Spread. The example given is for 15 cavities, t=21 msec, showing the f1 and f2 modes. The solid line shows the result including the spread in frequencies, the small dashes show 15 times the single cavity impedance of Figure 4.15 (no spread), while the broad dashes show 30 times the single gap impedance (no spread, no intergap gap phase effect).

A set of plots showing an example in detail for the major modes, corresponding to t=21 msec in the cycle, is presented in Appendix B. The single-gap impedance for the nominal and damped cavities is shown in Figures B.1 and B.2, respectively. The single cavity and net impedance are shown in Figures B.3, B.4 for the nominal cavity, and B.5, B.6 for the damped case. The real part of the impedance is plotted with a solid line, the imaginary part is superimposed with a dashed line.

A few observations may be made about this net impedance result. The modes found to couple strongly to the beam are f2, f4, and f6, and possibly f8. The single cavity impedance for these modes may be represented fairly well by equivalent LRC resonators. This equivalence is not as straightforward for the net sum impedances, especially for the nominal cavity (HOM dampers out). In general, mode f8 is smooth. Mode f2 is more square than a classical resonator. Modes f4 and f6, on the other hand, are asymmetric and appear to have structure which may be artificial because of the limited sample of data points. The single cavity representation of mode f5, which has the largest single-gap impedance, shows cancellation, as expected for an odd mode, but the shoulders are still large. However, the width is very narrow and the sample of data points small, so most probably, this mode doesn't add from one cavity to the next as assumed in Figure B.4. We know there is no coupled-bunch mode excited in the beam at this frequency. The net for f5 is probably a series of closely spaced narrow impedances at about the single-cavity magnitude, and thus not important to the beam.

In summary, the result of the above analysis is that the impedance due to all the cavities may be replaced by a single source. This analysis offers what we expect to be a realistic representation of the impedance presented to the beam due to the parasitic modes in multiple cavities. Verification is made when implemented in both the analytical calculations and in the longitudinal simulation of the Booster instability properties. No impedance model is used in the analytic linear coupled-bunch instability growth calculation (Chapter 6). For the simulation (Chapter 7), the net impedance is represented by a set of model resonances with equivalent magnitude and Q. The equivalent cavity and net sum impedances are tabulated for the fundamental and higher-order modes of interest in Tables B.7 and B.8 for the nominal and damped cavities, respectively. Further discussion regarding this analysis is deferred to the later chapters.

4.2 RF Cavity Spectra

Parasitic excitation by the beam of the RF cavity higher-order modes may be observed directly through the calibrated, capacitively-coupled, gap voltage monitors referred to in Chapter 2. Of the two gap monitors on each cavity, one (downstream to the beam direction) is dedicated to the phase feedback loop, while the other (upstream) is used for the read-back of the RF voltage sum signal. This second monitor may also be used as a passive probe of the fields in the RF cavity. A complete set of measurements were made of the beam excitation of the HOMs in each of the 17 Booster RF cavities. The cavity spectra were recorded for different beam intensities and for 14- and 16-cavity configurations. Indeed, these measurements became the most unequivocal indication of which cavity modes couple strongly to the beam. Although these data alone cannot strictly establish that these cavity modes in fact cause the observed coupled-bunch instability, supporting evidence from the beam studies led to this conclusion. The analysis will be presented later in Chapter 5; here, we describe the measurement.

A signal from one gap monitor from each cavity is fed to the input of an HP 8568B spectrum analyzer. The goal is to record the spectral peaks of the beam-induced RF cavity modes. In the instrument, narrow bandpass filters are used to record the frequency components of the input signal. The resolution bandwidth (RBW) determines the frequency resolution width, while the video bandwidth (VBW) limits the signal fluctuation due to noise. The spectrum analyzer is first used in the linear sweeping mode, in which the signal is scanned across the chosen frequency range using several filters end-to-end. The signal in the cavity has the characteristics of the beam spectrum, which is discrete and is sweeping in frequency due to acceleration (Chapter 3, section 2,3). Because the input signal is discrete and sweeping while the instrument is also sweeping, the full cavity frequency response will not necessarily coincide with the filters on a single sweep. For this reason, the spectrum analyzer is swept continuously from 100 Hz to 400 MHz and, using the maximum-hold feature of the instrument, the beam-induced spectrum is obtained over a period of several hours.

After the spectral peaks are identified in a given cavity, the center frequency of the spectrum analyzer is set in the zero-span mode to the peak of each resonance and triggered at the start of each Booster cycle. This produces a time record of the HOM excitation during the cycle. A typical example of the zero-span output is shown in the plots in Figure 4.18 for the odd 79.9 MHz mode using different RBWs. The frequency of this cavity mode remains fixed over the acceleration cycle. The beam intensity is 1.9×10^{12} protons per pulse and 16 cavities are energized. The full scale sweep time of the measurement is 50 msec.

In the low resolution measurement in Figure 4.18 (a), the RBW is chosen to be 1 MHz so as to assure that at least one rotation harmonic of the beam is included. Recall that the rotation frequency increases from 360 to 628 kHz over the 33 msec acceleration cycle. The amplitude of the cavity mode begins to rise at about 25 msec in the cycle and continues to grow until extraction. The beam signal is very noisy near the beginning of the cycle and the rate at which the beam modes are sweeping is maximum, which is why we see the cavity mode excited also during the first 10 msec or so.

In the high resolution measurement in (b), the RBW is 100 kHz. Now we see a Hok-like (Chapter 3.3) excitation as the rotation harmonics of the beam pass through or come into resonance with the cavity mode. The VBW in these two measurements is approximately the same. The amplitude of the cavity response depends on the crossing time of the beam coupled-bunch mode through the cavity resonance of width ω_{res}/Q. In this case, the crossing time may be expressed as $\Delta t_{cross} = \frac{\omega_{res}}{Q} \Big/ \frac{d\omega}{dt}$, where ω is the beam mode frequency in eqn. (3.2.24). For longer dwell times as happens later in the cycle, the amplitude of the cavity response increases. The concept of coupled-bunch modes sweeping over cavity resonances will be illustrated later in Chapter 5 in more detail.

(a)

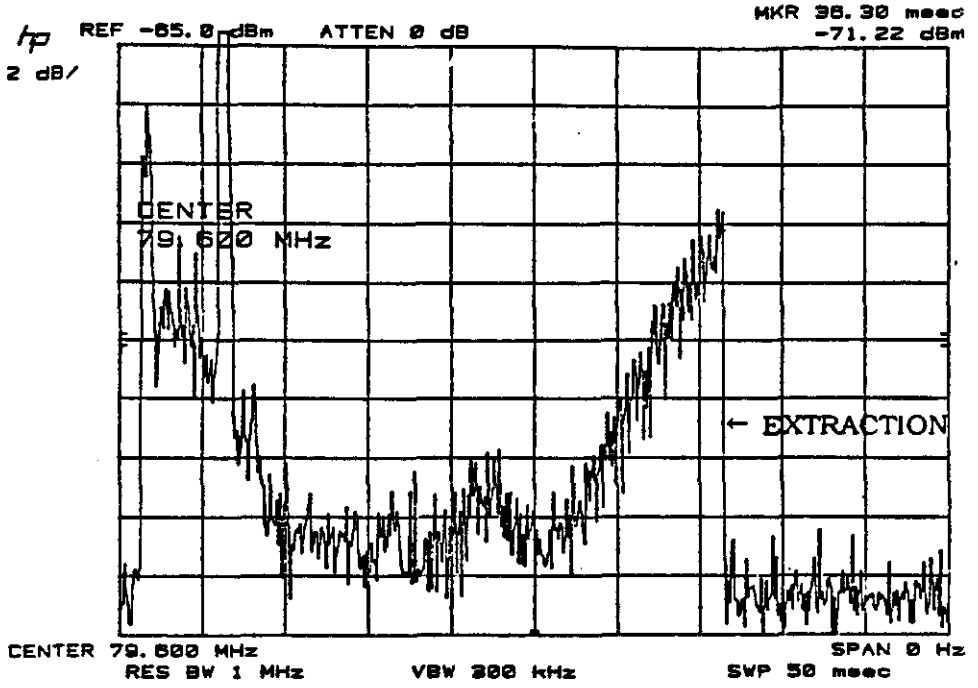

(b)

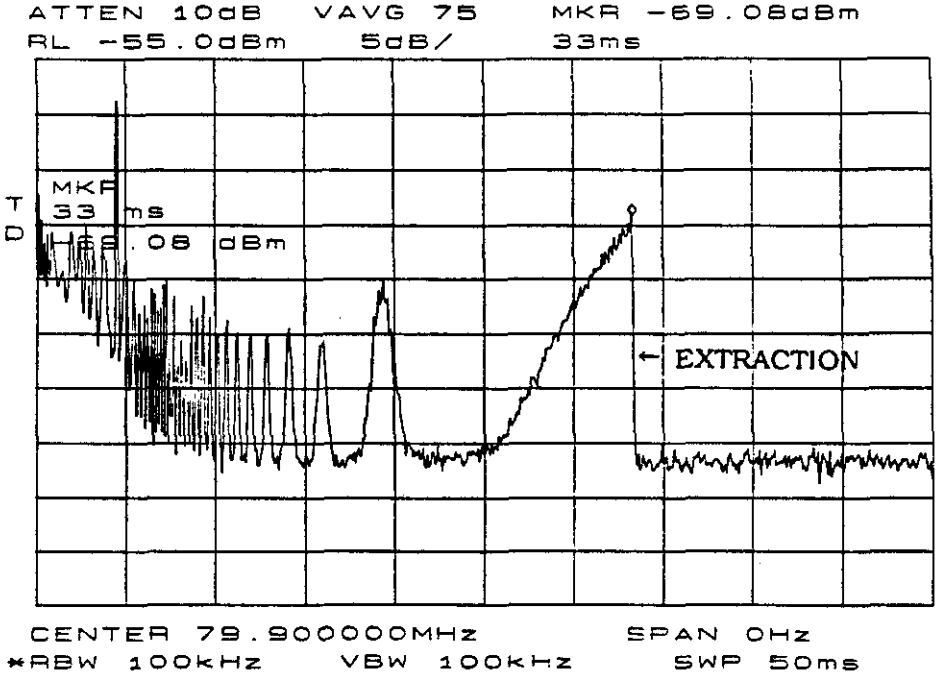

Figure 4.18 RF Cavity Spectrum due to Beam. Measurements are in zero-span, with sweep time of 50 msec. View (a) shows a low resolution (1 MHz RBW) measurement at 79.6MHz (Ref. 36), while (b) shows high resolution (100 kHz RBW) at 79.9 MHz.

4.3 Beam Spectra and Emittance

A number of parametric beam studies were performed to study the coupled-bunch instability. Beam intensity, number of cavities energized, and transition jump timing were systematically varied and the beam response observed. The data run designations (R01, R02, etc.) are given in the next chapter in Table 5.1. In order to later analyze the time evolution of the beam during acceleration, a digital record was made for each data run at two- or three- msec intervals in the cycle.

Beam measurements are all made using a non-intercepting beam monitor known variably as a resistive wall, wall current, or gap monitor. It is a wideband device (~ 6 GHz) which measures the return image current in the beam pipe wall as the beam passes a small ceramic gap loaded with resistors. The design is described in detail in Refs. 45, 46, 47. The image current is equal and opposite the beam current. The signal developed in the detector is proportional to the instantaneous intensity $\hat{I} = Nef_0$ and is independent of the transverse beam position. In the case of a stable beam, this signal is given by the expression derived in eqn. (3.2.21), while for a coupled-bunch instability, it is given by eqn. (3.2.22).

With such a monitor, we may observe the longitudinal charge density distribution of the bunched beam in detail during the acceleration cycle. There are two resistive wall monitors in the Booster, located one each in the long straight sections L17 and L18. They are identical except that the detector in L17 has microwave absorbers added. One of these is normally connected to the "mountain range" display. The other is available for studies. The signals are carried up from the tunnel to the low-level RF room (LLRF) above. The minimum distance and 3/4" heliax cable assure that the high frequency components of the beam are preserved. The time- and frequency-domain data may be displayed and optionally recorded through a computer interface using one of several available instruments, analog and digital.

The time development of the coupled-bunch instability is most striking with the analog mountain range display. The signal from the resistive wall monitor is acquired with a 1 GHz Tektronix (Tek) R7103 analog scope (with microchannel plate CRT)

connected to a modified Tek C1001 video camera to display the traces on a TV screen. The video image can be printed using a Tek HC02 video copy processor. The scope is triggered at the desired time in the cycle, and a chosen number of traces are displayed simultaneously, offset in the vertical plane for clarity, so that a particular bunch may be observed for a chosen number of turns around the ring. The mountain range has a separate clock which counts RF cycles, and therefore remains synchronous with the bunch centroid. The mountain range parameters are controlled either locally or through the Accelerator Network (ACNET). The time scale may be changed manually to display up to 84 bunches. As presently configured, the system can display a maximum of about 60 traces per 33-msec beam pulse. This could be increased with multiple triggers and other modifications.

To measure the bunch motion over the entire cycle with the mountain range display, it is necessary to view successive beam pulses. This is the manner in which the plots for Figure 1.1 were generated. On viewing the beam over many pulses, however, it is obvious that the pulse-to-pulse variation in the coupled-bunch instability amplitude is large. An example of this is given in two mountain range views in Figure 4.19. On some pulses, a large-amplitude dipole oscillation of the order of the bunch length is clearly observed to develop near the end of the cycle, as in (a). In other pulses, as in (b), the beam is far more stable. Each plot shows a time span of one msec at 33 msec in the cycle, and the oscillation frequency is equal to the synchrotron frequency, about 2 kHz.

While the spatial resolution of this analog display is high, the average time development over the entire cycle is of greater interest. Furthermore, we wish to record and analyze the spectral content of the beam current. A Tek Digitizing Signal Analyzer (DSA) 602 is preferred, therefore, to digitally record the beam signals. The DSA has a maximum real-time digitizing rate of 2 Gsps, giving a 0.5-nsec time resolution. The DSA has an 8-bit ADC, with an effective 7-bit resolution. The record length can be up to 32k points. Data may be averaged, and when this feature is used, we trigger the scope using the synchronous trigger of the mountain range. Several math functions are available on the DSA for real-time analysis, for example the fast Fourier transform (FFT) with a choice of windowing functions. The data acquired by the scope was recorded on disk by a PC using commercial software: ASYSTANT and DaDisp. The data record can be plotted directly using a HP-GL color plotter.

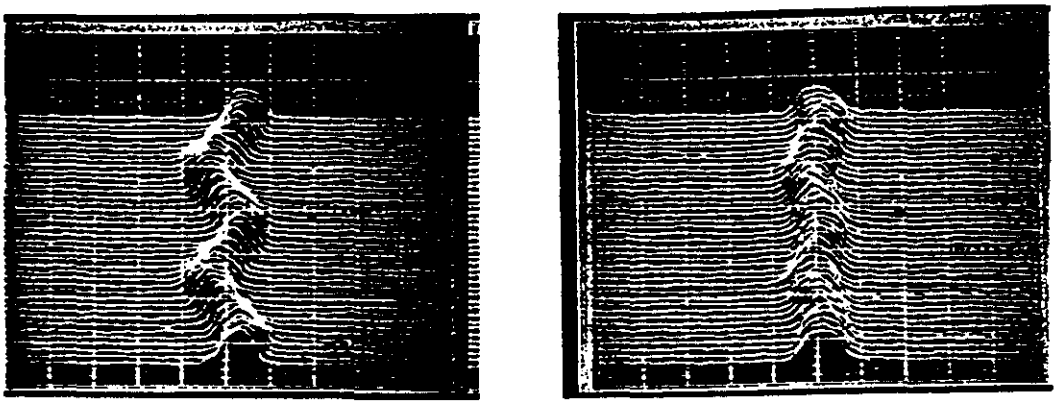

(a) (b)

Figure 4.19 Pulse-to-Pulse Variation of Coupled-Bunch Instability Amplitude. In this example, the bunch length is 2.6 nsec at 33 msec, and the dipole oscillation amplitude varies from (a) 1.7 nsec to (b) 0.8 nsec (the scale is 2 nsec/div). The beam intensity is 1.3e12 ppp with 17 cavities, 4 of which have HOMs damped. (R16)

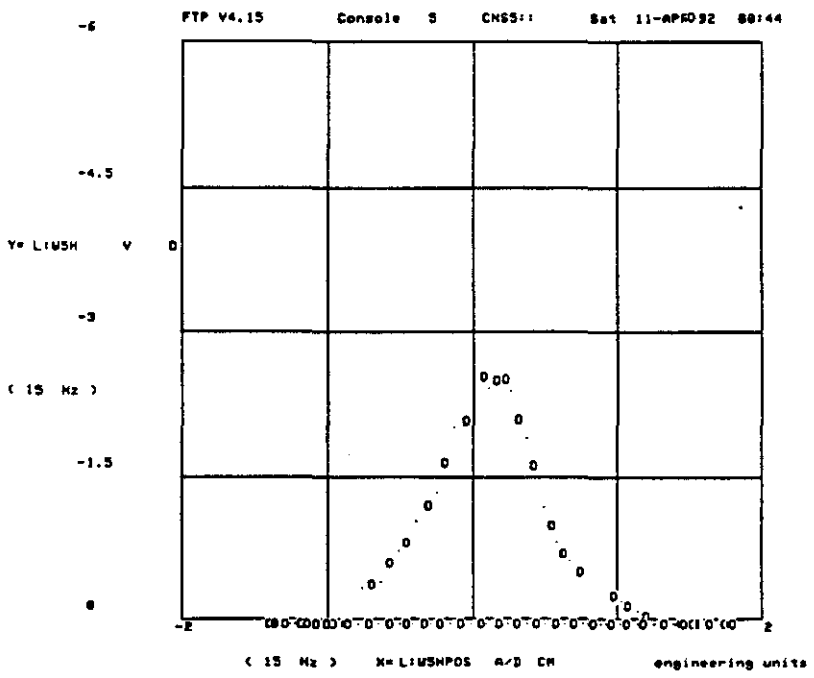

Figure 4.20 Nominal Beam Momentum Spread. Assuming a gaussian profile, the width σ gives an rms $\Delta p/p$ of 0.15% (the scale is given as σ(1cm) = $\Delta p/p$ (0.22%).

For each data run, supporting data are recorded to later reconstruct the characteristics of the beam instability. These include the injected beam momentum spread, the beam current, and the sum RF voltage. The momentum spread of the incoming Linac beam may be measured directly. Rather than being deflected into the transfer line to the Booster, the beam may be directed through a spectrometer magnet. The beam momentum profile is measured by a vertical wire which sweeps through the beam. For "nominal" conditions, the momentum spread is shown in Figure 4.20. Each division horizontally is 1 cm in wire position, and the system is calibrated such that 1 cm corresponds to a $\Delta p/p$ of 0.22%. The rms momentum spread is given in the plot. By the Fermilab convention, emittances are expressed in terms of the 95% area; therefore, the corresponding full $\Delta p/p$ is measured on the same plot to be 0.35%.

The average beam intensity is measured by detecting the secondary current induced in a wound toroidal ferrite core transformer surrounding the beam pipe. The Operations group periodically calibrates the output of the intensity monitors; however, while the absolute accuracy is unknown, the relative measure is precise for a study sequence of a short period of, e.g. one week duration. The intensity signal B:CHG0 for 5 turns injected beam is shown in Figure 4.21, recorded by the DSA. The scale, comparing with the calibrated B:PBOOST output of 1.7e12 protons per pulse (ppp), is found to be 0.53 V/10^{12} ppp.

Finally, we record the RF cavity sum voltage, which is used to determine the dimensions of the RF bucket. The signal from the upstream cavity gap monitor from each cavity is summed using phase-matched cables and then peak-detected to produce a curve such as that shown in Figure 4.21. The signal was calibrated[43] and, assuming a linear fit of the data with frequency, gives a scaling of

$$V_{RF}(\mathrm{kV}) = V_{\mathrm{msrd}}(\mathrm{V})\left(64971 + 2\pi(341.26) f_{RF}(\mathrm{MHz})\right) \tag{4.3.1}$$

The RF sum signal circuitry has recently been upgraded, and the scaled new RF sum voltage is greater than the old by about 30%. All the data presented in this work uses the old values. This difference introduces an uncertainty in the calculation of the RF bucket.

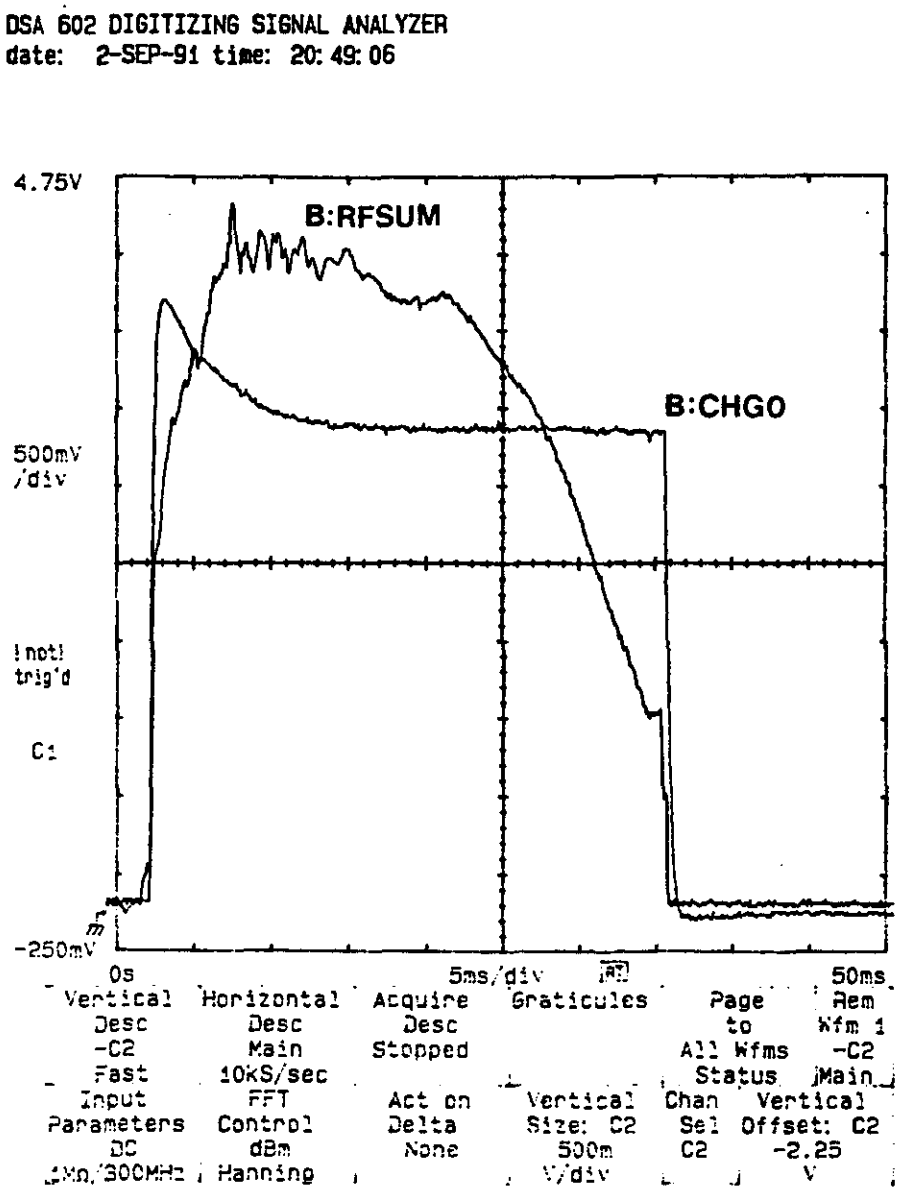

Figure 4.21 Booster RF Sum and Charge Signals. This example is for 17 cavities with a beam intensity of 1.7e12 protons per pulse (ppp). The intensities cited always refer to the injected beam intensity. Typically, for this nominal case, about 20% of the beam is lost to space charge forces and aperture restrictions in the first few msec of the cycle. The vertical scale is identical for both signals; the scaling to real values is given in the text.

Beam Spectra

Two different FFT setups were used on the DSA to record the beam spectra. In each case, a Hanning window is chosen somewhat arbitrarily to multiply the time signal; this determines to spectral line shape. A 8192-pt FFT is performed on a time base of 10 μsec (or 5 μsec), giving a maximum frequency of 500 MHz (or 1 GHz) and a frequency resolution of 61 kHz/pt (or 122 kHz/pt). Individual coupled-bunch spectral lines, spaced at the rotation frequency of about 625 kHz, are resolved in either case. In general, 8 or 16 beam pulses are averaged to obtain the data. A typical, averaged Fourier transform of the beam signal measured near the end of the cycle (29 msec) is shown with the 1 GHz setup in Figure 4.22. Dominant lines due to the periodic passage of the bunches at harmonics of the RF drive can be seen, as well as a ubiquitous pattern of four coupled-bunch mode lines repeated in each RF period. The power spectrum envelope of the RF lines corresponds, as we will see later, to a parabolic-like bunch charge distribution. The two unstable lines are centered at rotation harmonics 16 and 48 (out of a possible 84); the other lines are aliased. Due to a problem in the DSA, aliased lines at subharmonics of 1 GHz (250, 500, 750 MHz) were evident. Also, oversampled aliased RF harmonics from > 1 GHz produced spectral lines appearing as if they were single-sided coupled-bunch sidebands. These lines are disregarded in the analysis, although unfortunately, sometimes they obscure the real coupled-bunch mode lines.

Longitudinal Emittance

The maximum digitizing rate of 2 Gsps (0.5 nsec/pt) was used with a 4096 record length on the DSA to measure the bunch length. This corresponds to a pulse train of 2.5 μsec, just over one turn of 84 bunches. As in the FFT, 4, 8, or 16 pulses are first averaged. A sample output is shown in Figure 4.23. The bunch length is directly measured averaging three bunches using cursors on DSA screen. Given the RF voltage and bunch length, the beam area (emittance) is calculated assuming it is matched to the RF bucket using the formulae presented in Chapter 3. The error in the emittance $\Delta\varepsilon_L$ is assumed to be due only to the uncertainty in the bunch length $\Delta\tau_L$: Δ=0.7 nsec. Therefore, $\Delta\varepsilon_L = \frac{d\varepsilon_L}{d\tau_L}\Delta(\tau_L) = \frac{2\varepsilon_L}{\tau_L}\Delta\tau_L$.

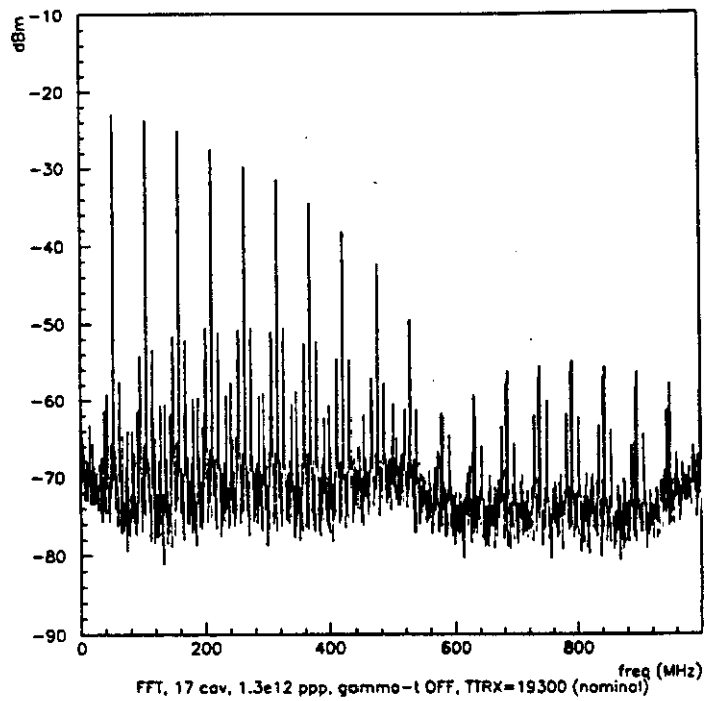

Figure 4.22 Typical Frequency Spectrum Showing the Coupled-Bunch Mode Signal. The conditions correspond to the case in Figure 4.19, but at 29 msec. The data are averaged over 16 beam pulses. The RF harmonics, spaced at 52.76 MHz, are most prominant. In each RF period up to about 500 MHz, four spectral lines appear, indicative of two coupled-bunch modes. The L17 beam monitor is used. (R16)

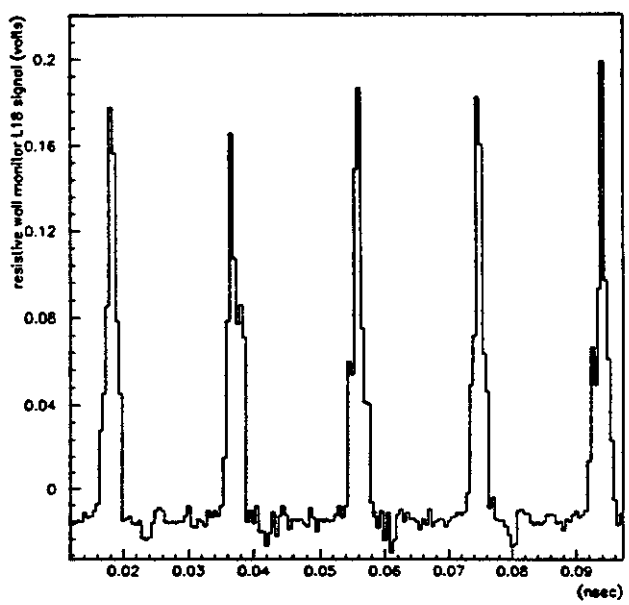

Figure 4.23 Typical Charge Distribution Signal in the Booster. These data are digitized at 2 Gsps using the Tek DSA 602. In this example, the beam conditions are: intensity 1.8e12 ppp, 16 cavities on, 4 cavities have HOMs dampers, 29 msec in the cycle, and averaged over 8 pulses. The L18 beam monitor is used. (R06)

5. EXPERIMENTAL STUDIES

As mentioned in Chapter 1, several approaches had been taken with little success over the years 1975-1987 to eliminate or curtail the coupled-bunch instability in the Booster. However, the problem was not understood in entirety. While the RF cavities were suspected of contributing to, if not of being the prime source of the instability, there was disagreement as to which of the higher-order modes (HOM) were most damaging.[48] As a matter of fact, the precise connection between the instability and emittance growth was not unequivocally established, although some linear approximations were made.[49,50] A preliminary, linear estimate of the emittance growth for higher beam intensities suggested that if nothing were done, the instability would limit the goals of the Linac upgrade (see Figure 1.4). It was decided to re-address the coupled-bunch instability in the Booster systematically.

Coupled bunch oscillations can be stabilized by either increasing the spread in synchrotron frequencies, actively damping the longitudinal motion of each bunch, or reducing the impedances of the resonators responsible for the bunch to bunch coupling. In the case of the Fermilab Booster, the third method of reducing the coupling impedances was chosen because of its simplicity, low cost, and reliability. With this choice the problem could be simplified into three steps: 1) identifying the unstable modes in the frequency domain in the beam current spectrum, 2) finding the specific higher order RF cavity modes responsible for the coupling, and 3) building a set of HOM dampers to remove energy from the RF cavity higher order modes.[51]

Experimental beam studies were carried out in parallel with extensive measurements of the RF cavities. The parametric beam studies are described first, in which the beam intensity, RF cavity configurations, and beam momentum spread are varied. This is followed by the discussion of the RF cavity spectral measurements, in which the amplitude and time dependence of the beam-induced parasitic modes is observed. This collection of data, the equivalent characteristic time dependence coupled with the agreement in the mode numbers between the perturbed beam spectra

and bench measurements of the impedance, led us to identify three particular RF cavity modes as being responsible for the coupled-bunch instabilities. Passive HOM dampers were designed, and after installation, the longitudinal beam emittance was reduced by a factor of three, never before achieved. The HOM damper design is described, and the results shown after they are installed. Finally, some remarks are made of the case when the beam momentum spread is varied.

5.1 Observations of the Coupled-Bunch Instability

The parametric, experimental beam studies were performed in four stages. First, the dependence of the emittance growth, as measured by the bunch length, on intensity and cavity configurations was studied. Spectral measurements established the unstable coupled-bunched beam modes. Data of the standard 8 GeV extracted beam were compared with acceleration to 4 GeV are reported in Ref. 56 but will not be discussed here. After the bench measurements of the RF cavity impedance and the HOM damper design and fabrication, but prior to installation, the beam measurements were largely repeated. Next, four RF cavities were modified with the HOM dampers, and beam measurements were made first with only the internal hardware, then with the external circuits. Although no changes were observed in the beam, it was determined that as the dampers caused no unexpected ill effects, all the cavities were subsequently modified. Finally, the beam measurements were made with all the dampers. The data run designations are given in Table 5.1.

The results for the emittance growth in the first set of studies show a strong dependence on both intensity and number of RF cavities energized. The intensity dependence with a fixed 16 cavities is shown in a family of curves in Figure 5.1 (a) (dat16). At the maximum intensity of 2.5e12 ppp (3.0e10 ppb), the emittance at extraction is 0.25 eV-sec. The emittance growth begins around transition energy (19 msec) and appears to be generally linear with time. The result with fixed intensity (2.5e12 ppp), but with one, three, and five cavities off and shorted is shown in Figure 5.1 (b). The topmost curve is identical to that in (a). The signal was improperly terminated for 12 cavities; the emittance does not actually decrease to zero at transition. Again, the dependence of the emittance growth is significant. To eliminate the possibility that the cavity shorts affect the HOMs and hence the beam in an

Table 5.1 Data Run Designations of Parametric Beam Studies

	intensity (10^{12} ppp)	# cav	FFT **	HOM dampers	date	comments
dat16	(1-6 turn)*	16	0	out	Aug 89	cavities shorted
dat14	(1-6) *	14	0	out	Aug 89	and/or removed
dat12	(1-6) *	12	0	out	Aug 89	"
R01	1.7	15	1	out	Sep 91	L18 pickup
R02	1.7	16		out	Sep 91	
R03	1.4	16		out	Sep 91	
R04	1.0	16		out	Sep 91	
R05	0.6	16		out	Sep 91	
R06	1.8	17	1	4 cav	Sep 91	HOM: int. H/W
R07	1.8	15	1	4 cav	Sep 91	HOM: int. H/W
R08	1.8	15	1	4 cav	Sep 91	HOM: full H/W
R09	1.8	17	1	4 cav	Sep 91	HOM: full H/W
R10	1.9	17	2	4 cav	Sep 91	large $\Delta p/p$
R12	1.3	16	3	4 cav	Nov 91	L17 pickup, no τ_L
R13	1.3	16	3	4 cav	Nov 91	large $\Delta p/p$, no τ_L
R15	1.3	16	3	4 cav	Nov 91	γ_T jump on, no τ_L
R16	1.3	17	3	4 cav	Nov 91	
R30	1.8	16	3	in	Apr 92	
R35	1.9	15	3	in	Apr 92	no τ_L
R36	1.9	16	3	in	Apr 92	
R37	1.9	16	3	in	Apr 92	large $\Delta p/p$
R38	1.9	19	3	in	Apr 92	small $\Delta p/p$
R39	1.9	16	3	in	Apr 92	γ_T jump on
R47	0.45	16	3	in	Apr 92	
R48	1.3	16	3	in	Apr 92	
R49	1.6	16	3	in	Apr 92	
R50	0.9	16	3	in	Apr 92	

* Beam intensities: (1) 0.6e12, (2) 1.1e12, (3) 1.5e12, (4) 1.8e12, (5) 2.1e12, (6) 2.5e12 ppp

** FFTs: (0) various setups; (1) 8192 pts, 1 Gsps, 500 MHz (10 μs), 1 ave;
(2) 8192 pts, 1 Gsps, 500 MHz (10 μs), 16 ave; (3) 8192 pts, 2 Gsps, 1 GHz (5 μs), 16 ave

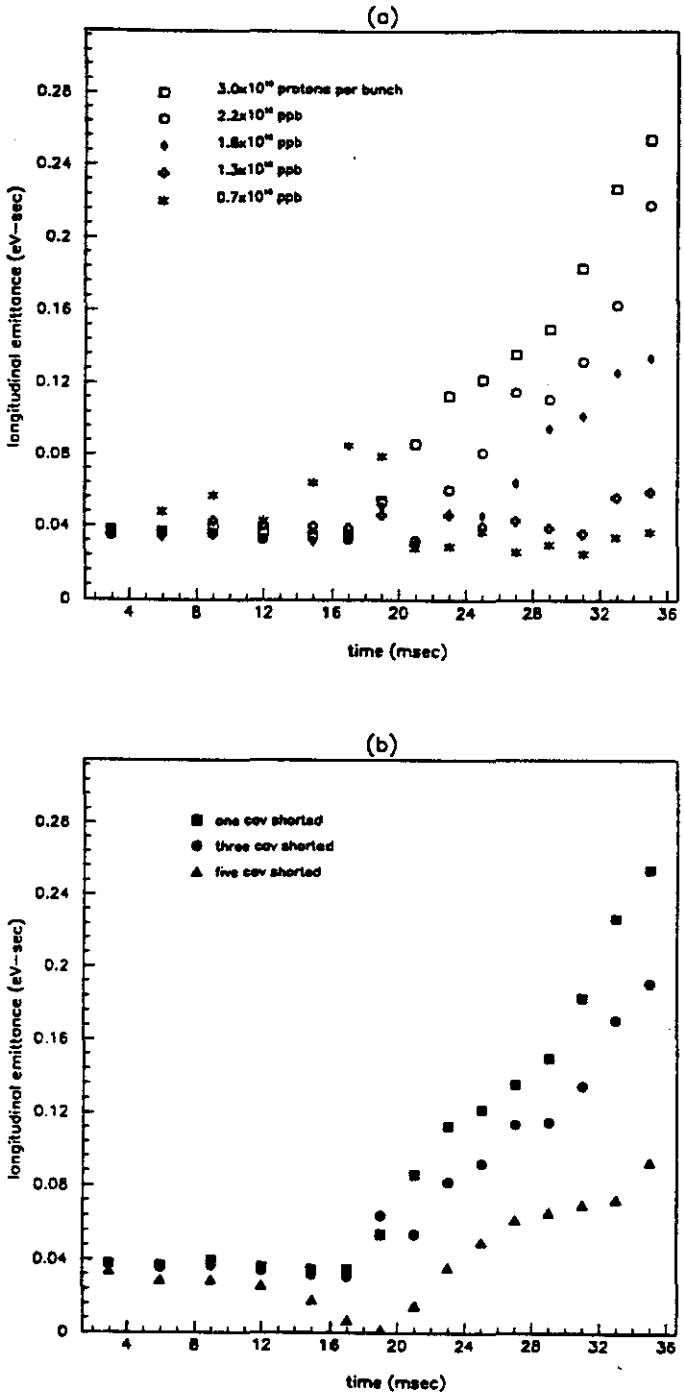

Figure 5.1 Longitudinal Emittance Growth as a Function of Time in the Booster Cycle. Shown in (a) is the emittance, as determined from the measured bunch length, for several beam intensities and fixed number of accelerating cavities (16). Emittance growth occurs mainly after transition and is most pronounced at the highest intensities. Shown in (b) is the emittance at fixed intensity, 3.0e12 ppb, but with one, three and five cavities off and shorted.

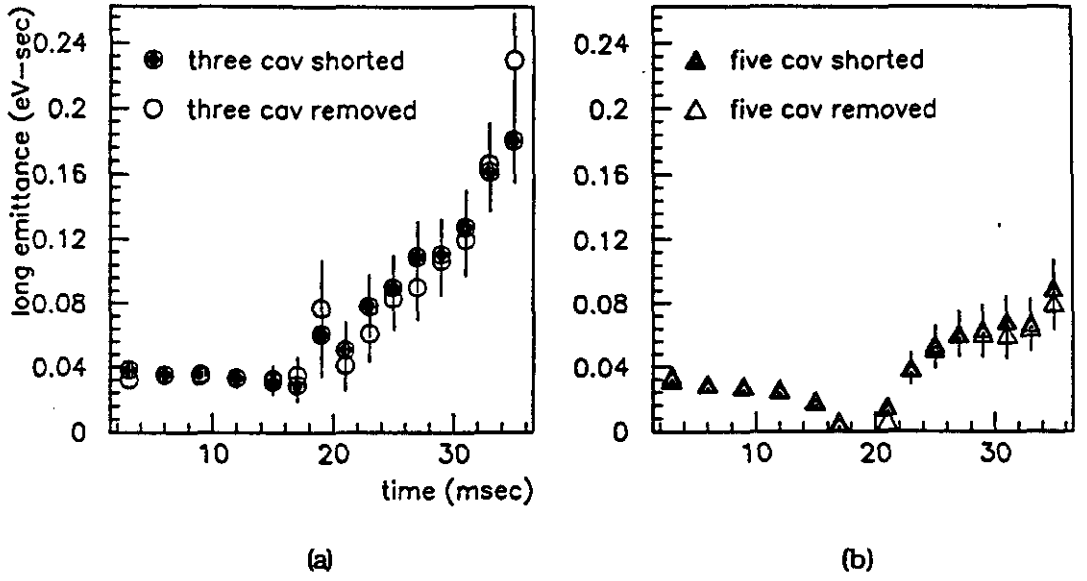

Figure 5.2 Effect on Emittance of Shorting vs. Removing RF Cavities. The results for (a) 14 and (b) 12 cavities show that there is virtually no difference in the longitudinal emittance growth between removing and simply turning off and shorting RF cavities.

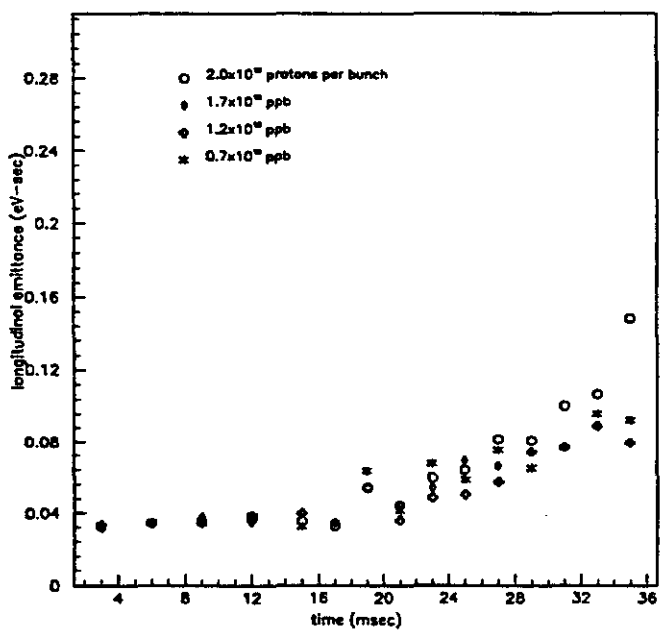

Figure 5.3 Repeat of Longitudinal Emittance Growth Studies vs Intensity. The apparent emittance growth for low intensities was not seen previously (see Figure 5.1), although the scaling at the highest intensity is comparable.

unexpected way, the studies were repeated with the same cavities removed from the ring. The results are virtually identical to the plots in Figure 5.1 (b), this is demonstrated in Figure 5.2. The spectral data proved to be rich in detail. Coupled-bunch mode lines appear at transition centered around n=16 and 48, shifting down from around n=18 and 50 when they first appear. It was decided to repeat the studies and more systematically measure and study the spectral data in conjunction with the study of damping the RF cavity parasitic higher-order modes.

Prior to studies with installing the RF cavity HOM dampers, the beam intensity studies were repeated. The results are shown in Figure 5.3 (16 cavities, R02-R05). The maximum intensity available at the time for study for which the Booster was well tuned was only 1.7e12 ppp (2.0e10 ppb), with a 0.15 eV-sec emittance at extraction. The small emittance growth at low intensities was not seen previously. Obviously, during the intervening two years, regular maintenance and repairs were performed in the beam line. No changes known or expected to affect the longitudinal instability were made, although the injected Linac momentum spread had not been recorded for comparison. Another consideration in comparing data from different time periods is the fact that the beam intensity signal B:CHG0 is periodically re-calibrated or upgraded. Therefore, a variation in absolute intensity is possible. Before we discuss the RF cavity HOM damper studies, we digress to describe the beam spectral analysis and extraction of coupled-bunch mode amplitude from the data.

Extraction of Particle Distributions and Coupled-Bunch Amplitude

Study of only the longitudinal emittance growth to fully characterize the coupled-bunch instability in the Booster is not possible. First, there is evidence that the charge density develops higher-moment structure, indicating nonlinear processes. Also, two coupled bunch modes are seen to grow in the beam, and it is unknown whether they are independent or affect each other. The coupled-bunch mode amplitudes may be calculated from the first moment of the corresponding perturbed bunch distributions introduced in Chapter 3. The distributions themselves may be extracted from the spectra. The envelope of the peaks in the signals given in eqns. (3.2.21) and (3.2.22) is written as

$$\sigma_m(\omega) = i^{-m}\rho\int_0^\infty J_m(\omega\hat{\tau})f_m(\hat{\tau})\hat{\tau}\,d\hat{\tau} \tag{5.1.1}$$

where $\rho = NMe\omega_0\alpha$ and m=0,1. We can perform an inverse Hankel transform to invert this equation in order to extract the distributions f_m. We multiply eqn (5.1.1) from the left by $J_m(\omega\hat{\tau}')\omega\,d\omega$ and integrate, then use the following orthogonality condition on Bessel functions[57]

$$t\int_0^\infty J_\nu(\alpha t)J_\nu(\alpha t')\,\alpha\,d\alpha = \delta(t-t') \tag{5.1.2}$$

$$f_m(\hat{\tau}) = \frac{i^m}{\rho}\int_0^\infty J_m(\omega\hat{\tau})\,\sigma_m(\omega)\,\omega\,d\omega \tag{5.1.3}$$

A program was written to read the spectra and evaluate the integral in (5.1.3) numerically and determine the functions f_m. There is a different f_m for each coupled-bunch mode envelope. We use the normalization condition on f_0 to determine the scaling factor ρ, since we are actually measuring ρf_0

$$2\pi\int_0^\infty \rho f_0(\hat{\tau})\hat{\tau}\,d\hat{\tau} = \lambda \tag{5.1.4}$$

The charge density is just the projection of f_0 on the τ axis:

$$\Lambda(\tau) = 2\pi\int_0^\infty \rho f_0\left(\hat{\tau} = \sqrt{\tau^2 + (\dot{\tau}/\omega_s)^2}\right)\frac{d\tau}{\omega_s} \tag{5.1.5}$$

The coupled-bunch mode amplitude is given by the first moment of the perturbed function

$$\tau_a = 2\pi\int_0^\infty \hat{\tau}\rho f_1(\hat{\tau})\hat{\tau}\,d\hat{\tau} \tag{5.1.6}$$

An example of the bunch distributions are plotted in Figure 5.4 for 29 and 35 msec in the cycle. Because we truncate the frequency data at 500 MHz, there is an artificial

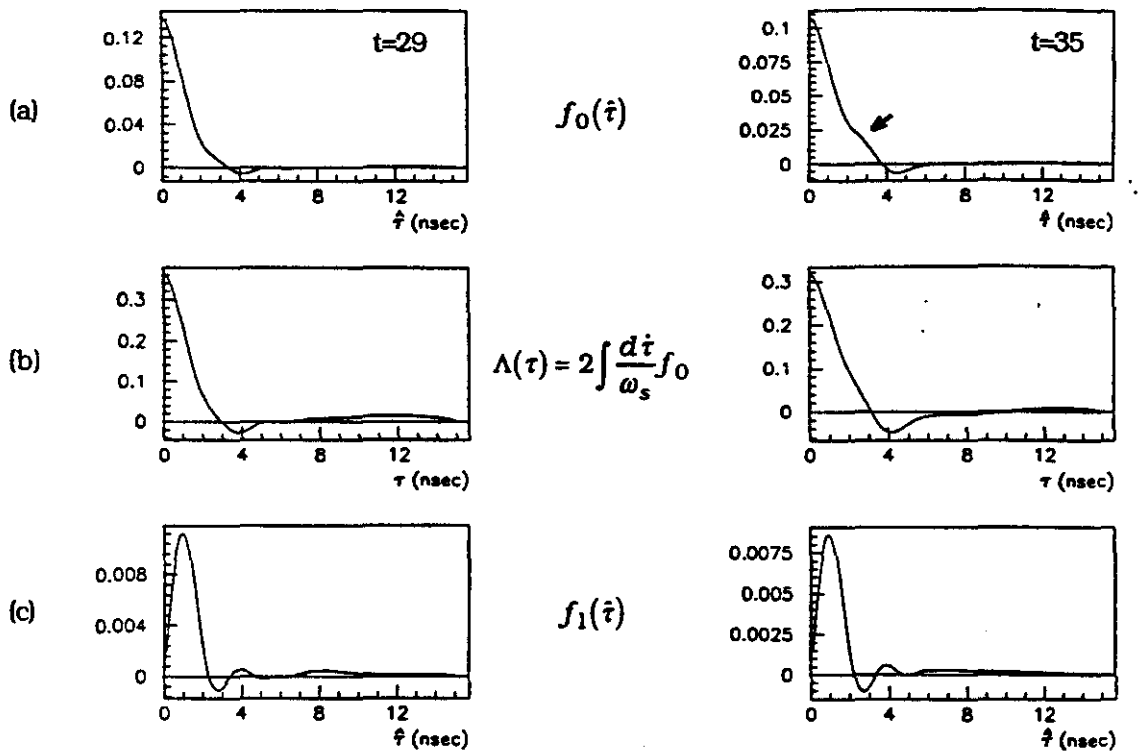

Figure 5.4 Extraction of Bunch Charge Distributions from Spectrum. The example gives the result for data run R01 at two different times in the cycle. Shown are (a) the stationary radial distribtion, (b) the charge density, and (c) the perturbed dipole distribution for coupled-bunch mode 16. The first column corresponds to 29 msec and the second column to 35 msec.

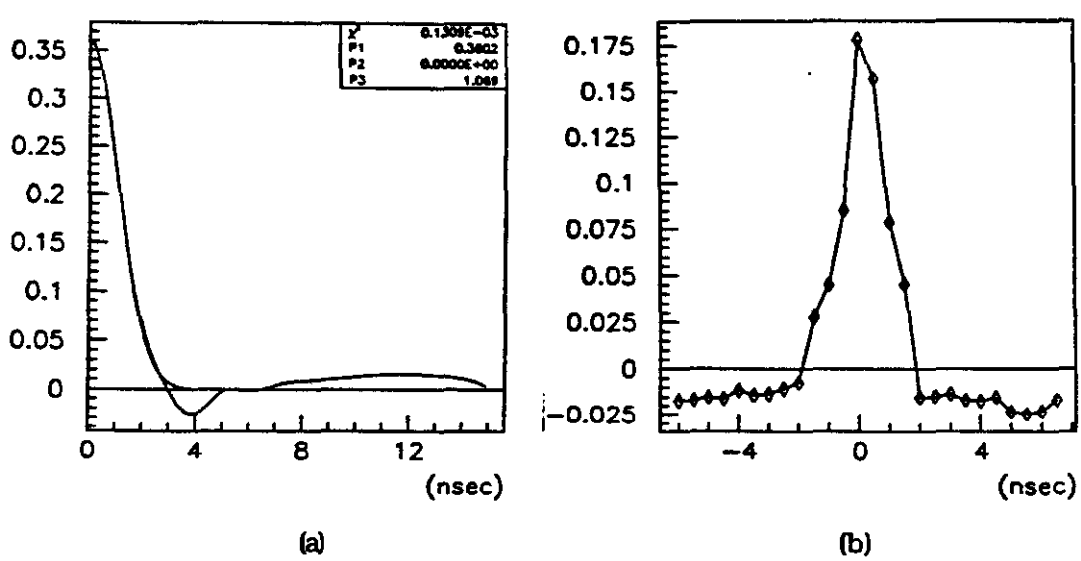

Figure 5.5 Verification of Spectral Analysis of Charge Density. The (a) analyzed result for R01 at 29 msec is compared with the (b) digitized data. The 4σ width is 4.3 nsec for the calculation fitted with a gaussian, while the averaged measured bunch length is 4.7 nsec.

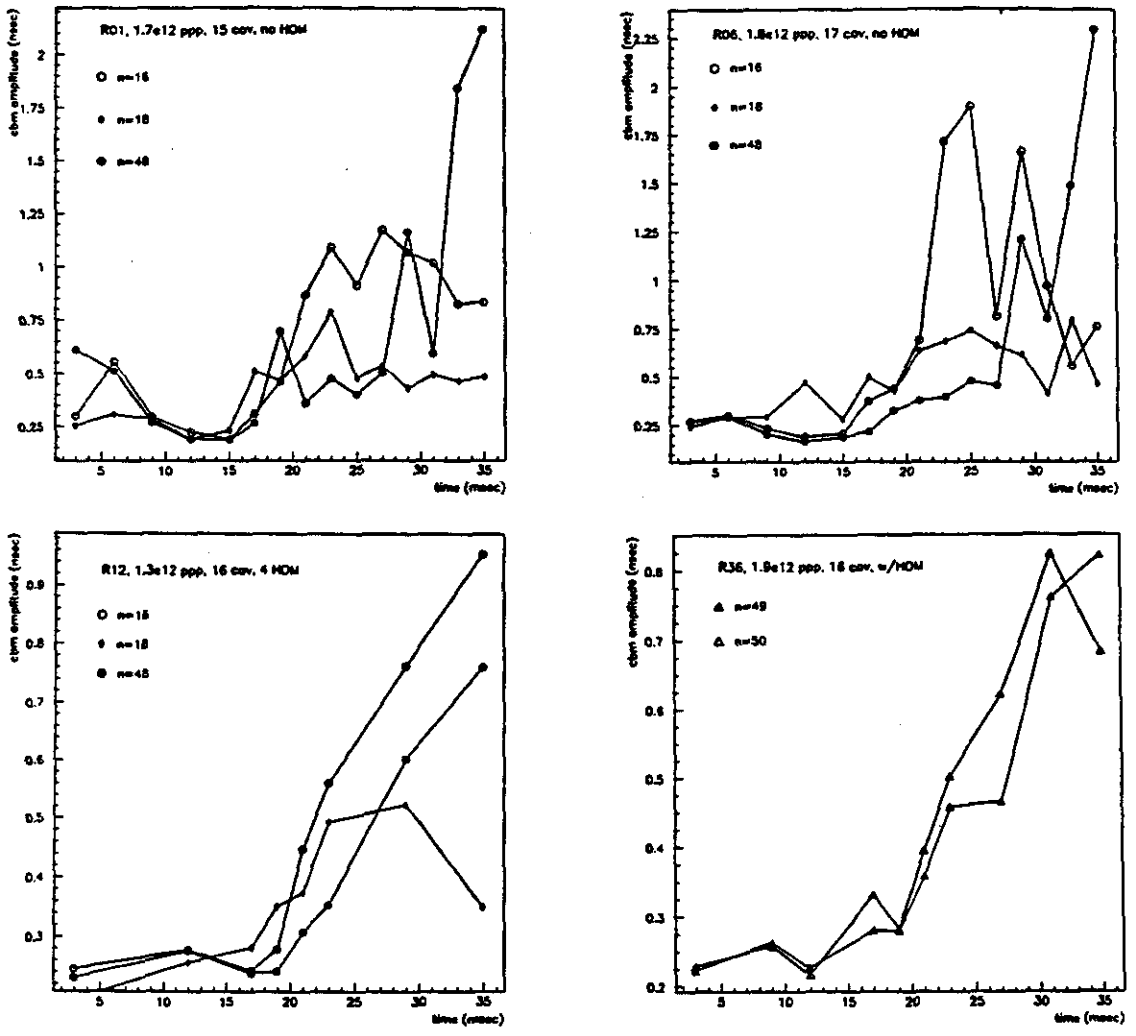

Figure 5.6 Coupled-Bunch Mode Amplitude as a Function of Time in the Booster Cycle. Shown plotted are various data runs (see captions).

fluctuation of about 2 nsec superimposed on the plots due to Gibb's phenomenon. Since we do not know the dc offset in the signal, the dc component of the spectrum is chosen to force the distribution functions to zero at large values of the argument. There is a distortion appearing in the radial stationary distribution f_0 at 35 msec indicated by the arrow in Figure 5.4 (a). This may simply be a numerical artifact; otherwise, it may be indicative of a diffusion process leading to emittance growth (turbulent bunch lengthening). Higher-frequency resolution is necessary for more definitive analysis of this kind. A verification of this analysis may be seen in Figure 5.5 (a) in which the bunch length for the extracted charge distribution is found by fitting with a gaussian. A corresponding digitized bunch charge signal is shown in (b). Remember that several bunches are averaged to obtain the experimental bunch length.

The coupled-bunch amplitudes are calculated according to eqn. (5.1.6) and plotted in Figure 5.6 for four different data runs for the most prominent coupled-bunch modes. Mode n=16 is seen to saturate for high intensity and maximum RF cavities, but grows linearly at low frequency. Only modes around n=50 remain after the HOM are damped. This is discussed now below.

5.2 RF Cavity Higher-Order Mode Damping

Figure 5.7 shows an FFT of the beam current signal taken from a wideband resistive wall monitor using the Tektronix DSA 602 digital signal analyzer. The beam current is sampled at 35 msec into the Booster cycle when the coupled bunch oscillations are fully developed. The FFT shows the harmonics of th RF frequency separated by the 84 coupled bunch lines. The dominant coupled bunch mode lines are seen to occur at n=16 and n=36. The individual bunch motion is predominantly a dipole oscillation. FFT beam spectra taken at 2 msec intervals throughout the acceleration cycle show both the n=16 and n=36 mode structure appearing shortly after transition. The n=16 mode reaches a maximum amplitude at approximately 10 msec before extraction and remains constant or decreases slightly. The amplitude of the n=36 monotonically increases after transition reaching its maximum value at the extraction time.

(a)

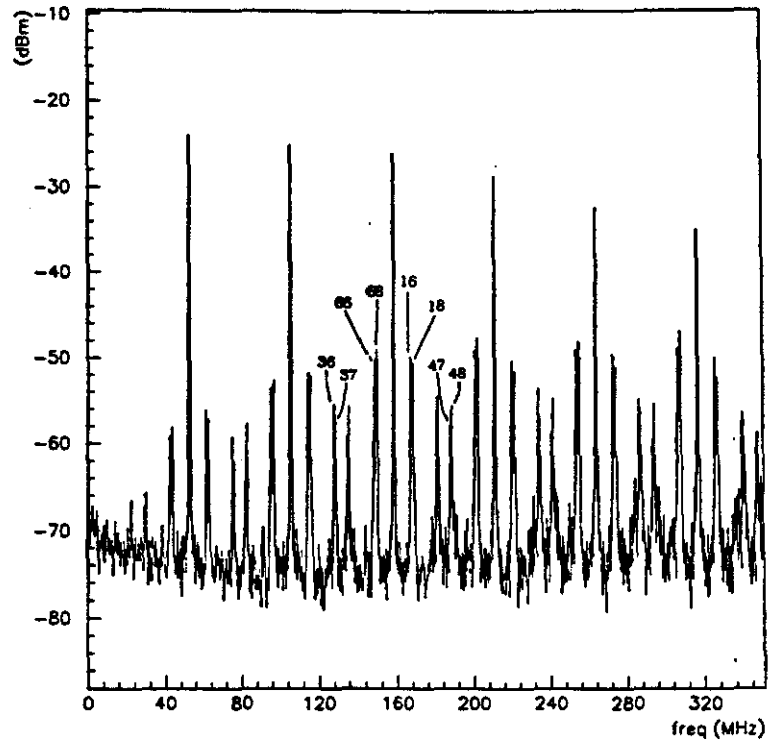

(b)

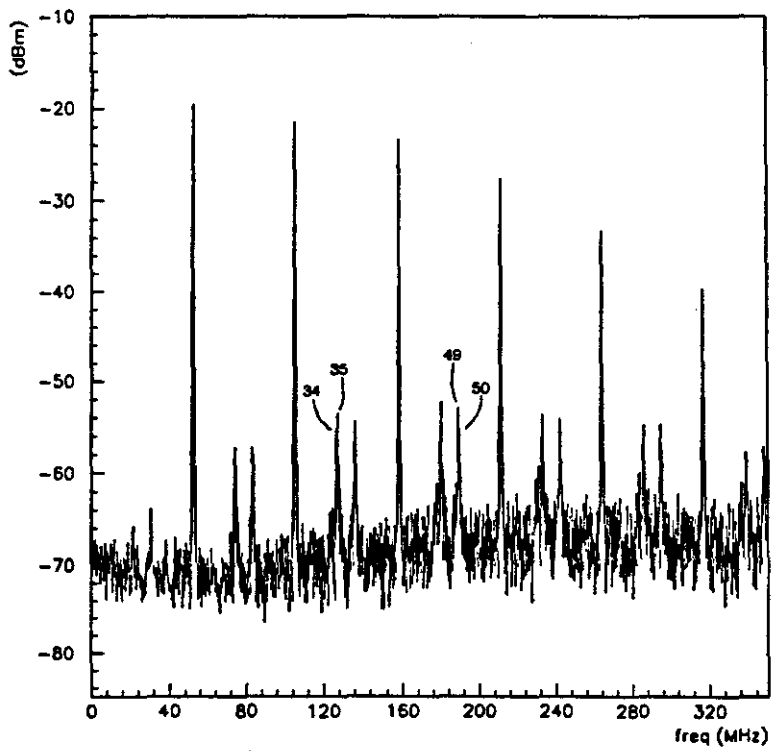

Figure 5.7 Frequency Spectra Showing the Coupled-Bunch Mode Signal Before and After RF Cavity HOM Damping. In (a), the beam intensity is 1.3e12 protons per pulse (HOM dampers out) and in (b), it is 1.9e12 ppp (HOM dampers in). In each case, 16 RF stations are on and the data correspond to 35 msec in the cycle. Mode 16 has been completely suppressed and mode 48 attenuated (recall, the intensity is greater in (b)).

Identification of the Offensive RF Cavity HOMs

A number of measurements were performed which, when taken together, lead to the decision to design and install passive dampers on three of the RF cavity HOMs: 83, 168, and 220 MHz (f2, f4, f6). The agreement in the mode numbers between the FFT beam current data and the cavity gap monitor data, along with the same characteristic time dependence, led us to identify these three modes as being responsible for the coupled bunch instabilities.

A set of bench measurements were made of the RF cavity impedance corresponding to different times in the cycle, as reported in detail in Chapter 4. The results were compared with beam spectral measurements to determine which parasitic modes, if any, correspond to modes excited in the beam. Such a comparison is depicted in Figure 5.8 (R12, 35 msec). We see that f2 (83 MHz, n=48), f4 (169 MHz, n=18), f6 (220 MHz, n=16), and f8 (345 MHz, n=46) correlate closely with the indicated beam coupled-bunch modes. The mode at 345 MHz is rather high and should be attenuated by the form factor according to the theory.

A complete set of measurements were also made of the beam excitation of the HOMs in each of the 17 Booster RF cavities (Wildman). The measurement setup was described in Chapter 4. The cavity spectra were recorded for different beam intensities and for 14- and 16-cavity configurations. The result for 16 cavities is shown for cavity modes f2, f4, and f6 in Figures 5.9, 5.10, and 5.11, respectively. The amplitude for f4 (169 MHz) and f6 (220 MHz) is seen to reach a maximum shortly after transition and then decrease slightly. Alternately, the f2 mode (83 MHz) continually increases after transition. The cavity fields increase with beam intensity. This time structure and intensity dependence is mirrored in the coupled-bunch amplitude growth as shown in R01 or R012 in Figure 5.6, for example. Indeed, these measurements became the most unequivocal indication of which cavity modes couple strongly to the beam, although cause-and-effect had yet to be established.

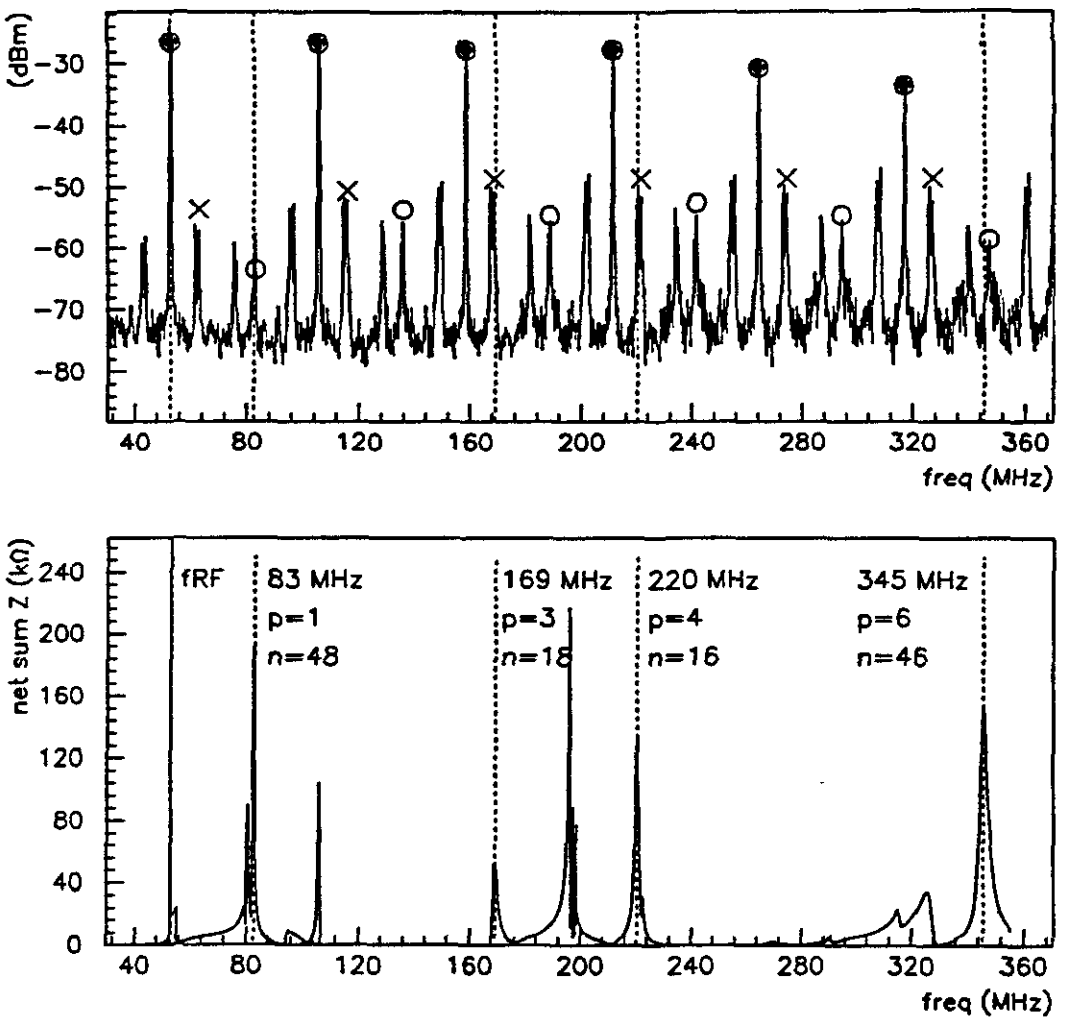

Figure 5.8 Correspondence of RF Cavity HOM Impedance and Coupled-Bunch Mode Spectrum Before HOM Dampers. The RF harmonics are marked with a filled "O", mode 16 with an "X", and mode 48 with an open "O". (R12)

(a)

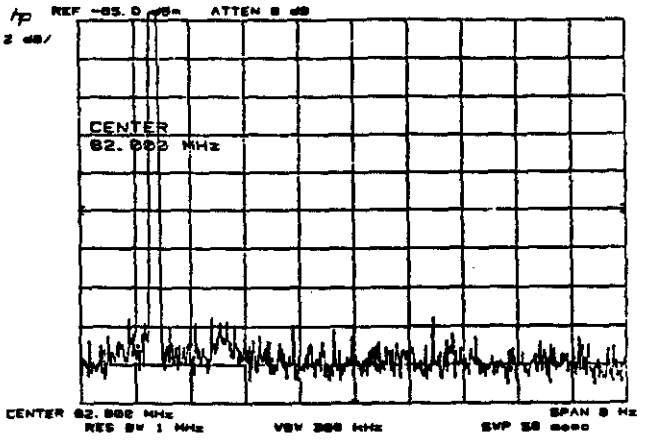

(b)

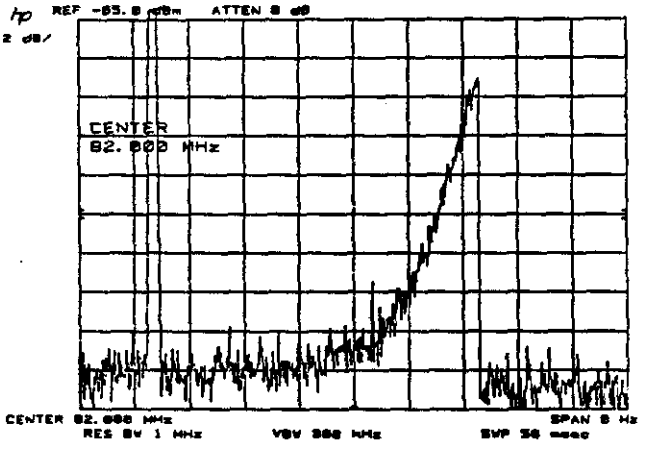

(c)

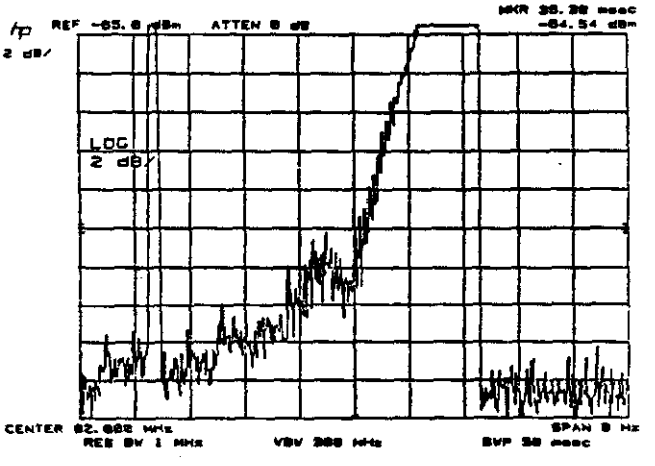

Figure 5.9 Excitation of RF Cavity Mode f2 (82.0 MHz). Shown are three beam intensities: (a) 0.52e10, (b) 1.5e10, and (c) 2.2e10 protons per bunch.

(a)

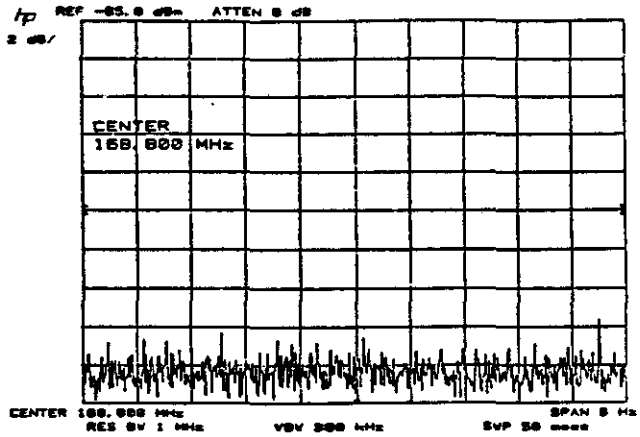

(b)

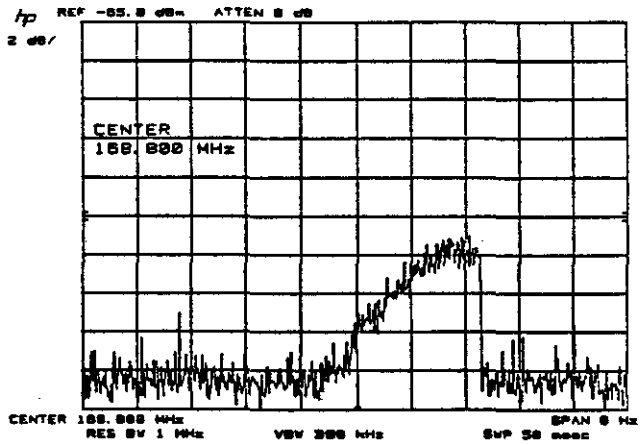

(c)

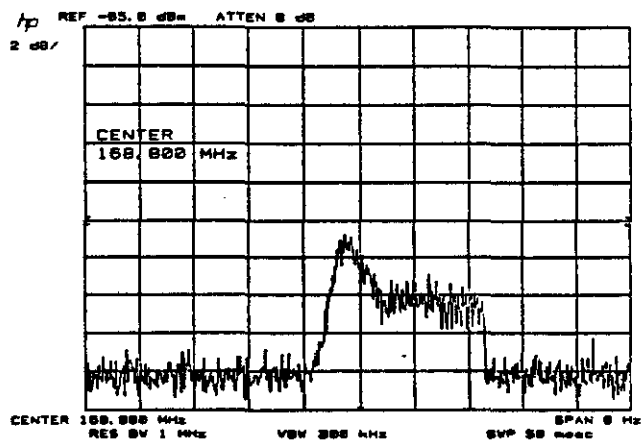

Figure 5.10 Excitation of RF Cavity Mode f4 (168.8 MHz). Shown are three beam intensities: (a) 0.52e10, (b) 1.5e10, and (c) 2.2e10 protons per bunch.

(a)

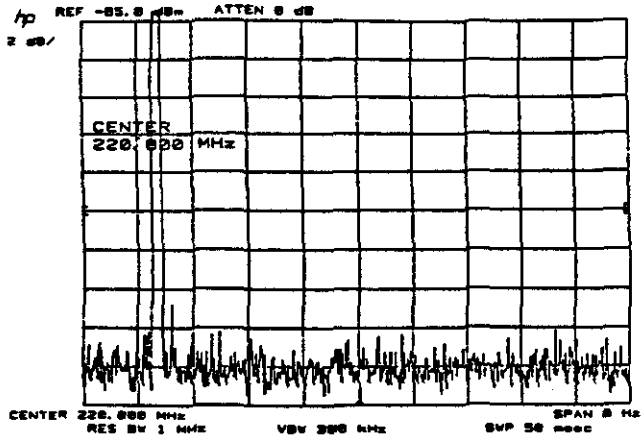

(b)

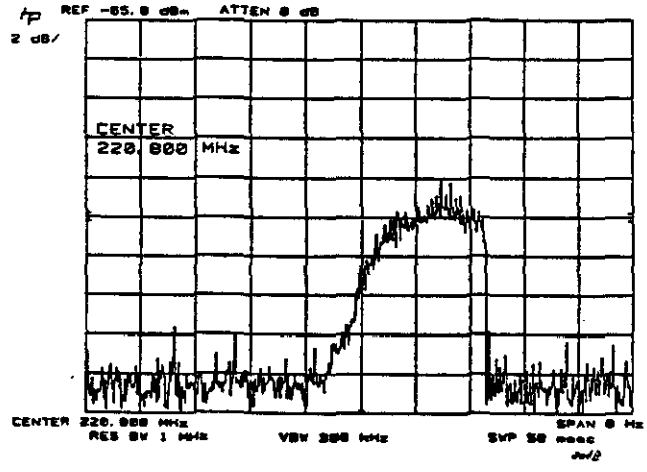

(c)

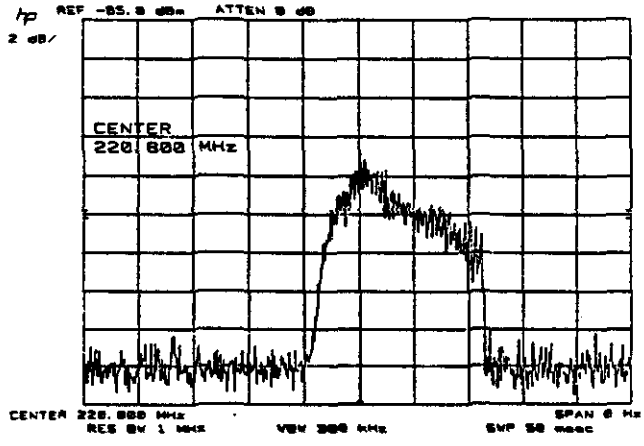

Figure 5.11 Excitation of RF Cavity Mode f6 (220.8 MHz). Shown are three beam intensities: (a) 0.52e10, (b) 1.5e10, and (c) 2.2e10 protons per bunch.

RF Cavity HOM Damper Design[51]

The frequency of the non-tunable mode at 83 MHz is determined by the physical length of the cavity's drift tube. This mode along with another fixed frequency mode at 79 MHz were already being damped by two coupling loops terminated into 50Ω loads. The nominal RF cavity prior to any modifications is shown in Figure 5.12 (a). To increase the damping at 83 MHz, the loop area was increased with a 0.5" copper spacer, and a notch filter was inserted between the loop and the 50 Ω load to reduce the additional power dissipated in the load at the fundamental frequency (see (b)). This modification produced an additional 10 dB of damping at 83 MHz. A photograph of the old loop and new spacer is shown in Figure 5.13, while an equivalent circuit is shown in Figure 5.14 (a). Also shown in Figure 5.13 is the 217 MHz damper.

The mode dampers for the 165 and 217 MHz modes are similar in design and are installed on only one half of the cavity. The location is indicated in Figure 5.12 (b). They both consist of capacitively-coupled 0.125" thick x 6" long x 2" (3.5") wide OFHC copper flaps located at a voltage maximum for each mode. These locations were found by probing the excited fields inside the cavity with a hand-held loop. The flaps are curved to be concentric with the outer cavity wall and are supported by a 0.5" dia copper rod which is soldered to the center conductor of an HN type connector. The center pin of the HN connector unscrews from the connector body for easy installation of the damping flaps through the side wall of the cavity. The center pin also acts as the inductor L_1 shown in Figure 5.14 (b). Outside of the cavity, the damping flaps are connected to three 10 Ω, 40 W low inductance resistors in parallel, R, and through a short length of 0.080" dia. copper wire, L_2, to two 100 pF transmitting capacitors, C_2. L_2 and C_2 are adjusted to be series resonant at 48 MHz with a Q of approximately 25. The center value of 48 MHz was chosen to minimize the total integrated power, over the entire acceleration cycle, dissipated in the resistor R at the fundamental frequency. The 165 and 217 MHz dampers have a bandwidth of 15 MHz and reduce the HOMs by approximately 20 dB and 25 dB respectively. The entire external damping network is enclosed in a 2" x 3" x 5" shielded aluminum box with a 28 CFM all metal fan attached to the box top to provide extra cooling. Under normal Booster operating conditions the added cooling provided by the fan is not necessary; however, with the additional cooling, the dampers have been tested at the maximum Booster cycle rate of 15 Hz.

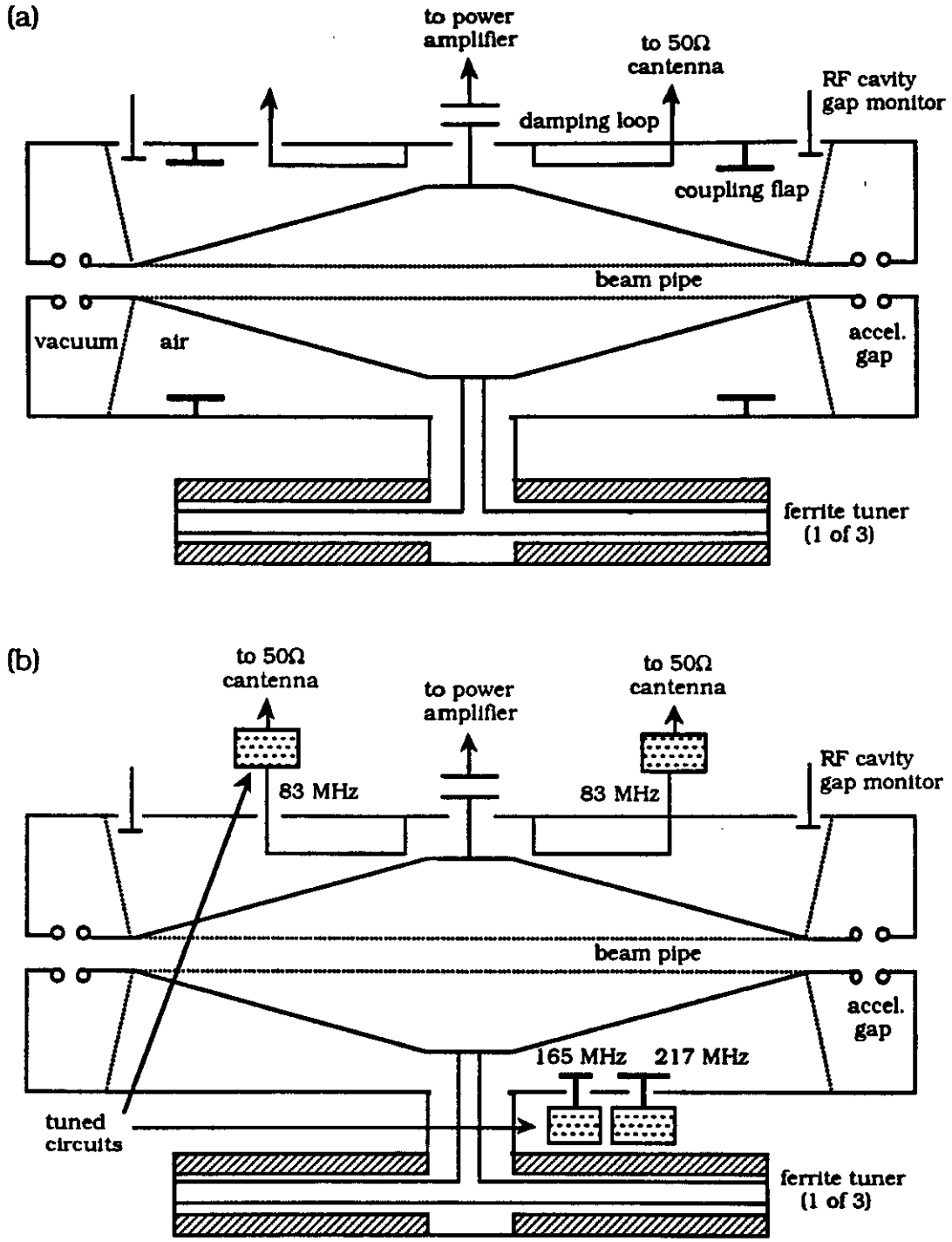

Figure 5.12 RF Cavity Showing Installation of HOM Dampers. Depicted are the (a) nominal and (b) modified cavities.

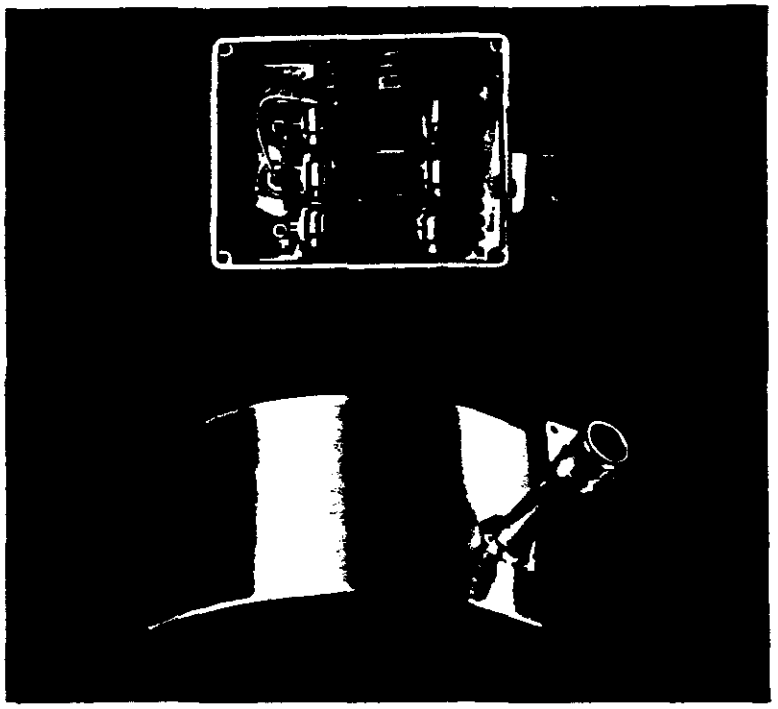

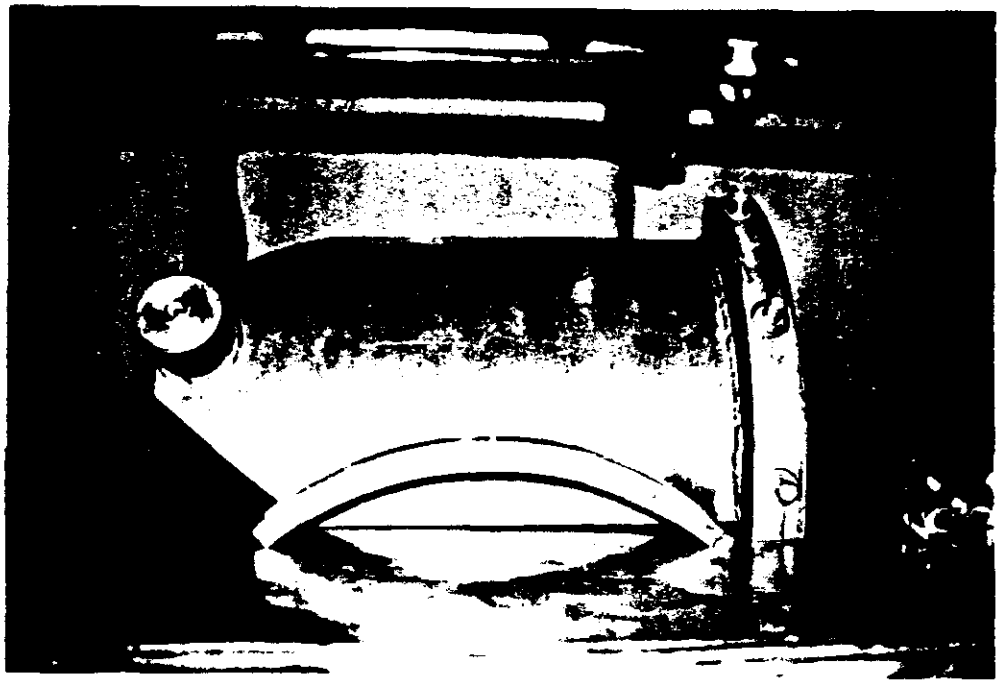

Figure 5.13 Photographs of RF Cavity HOM Dampers. Shown are the coupling flap and resonant circuit for the 217 MHz damper (above) and the old coupling loop with new spacer for the 83 MHz damper (below). The hardware for the 167 MHz damper is very similar to that for the 217 MHz one, only the flap is about half as wide.

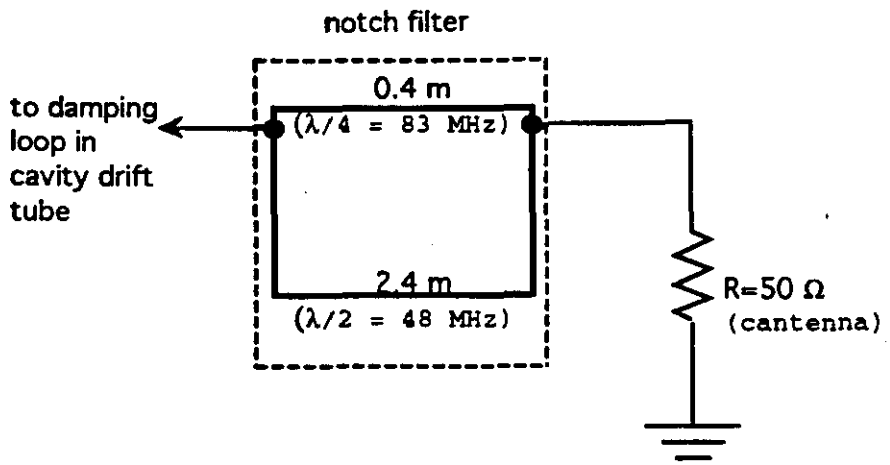

(a)

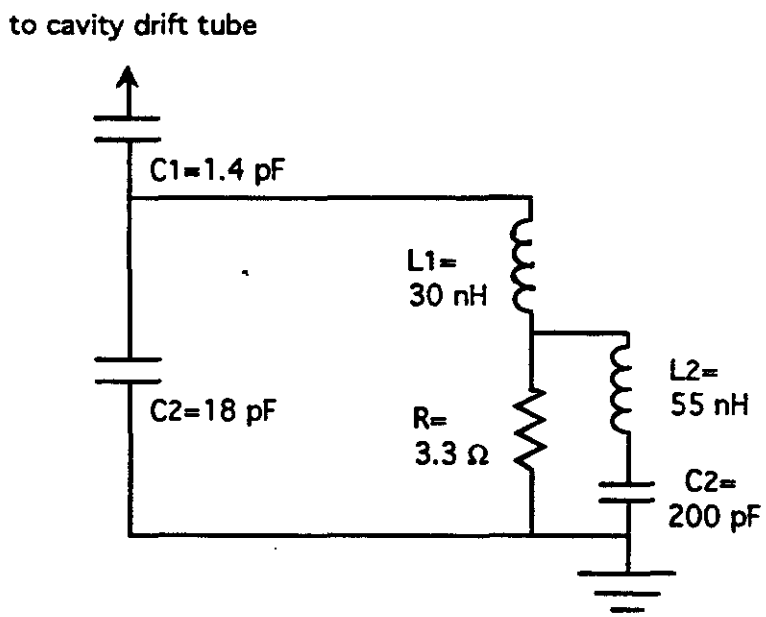

(b)

Figure 5.14 HOM Dampers Represented as Circuits. Depicted in (a) is the equivalent circuit for the 83 MHz mode, and in (b) is the circuit for the 165, 220 MHz modes. In circuit (b), at the lower RF frequency, C_2 is nearly a short and the R load is bypassed; at the higher HOM frequencies, the LRC branch is at resonance and now, power is dissipated in R.

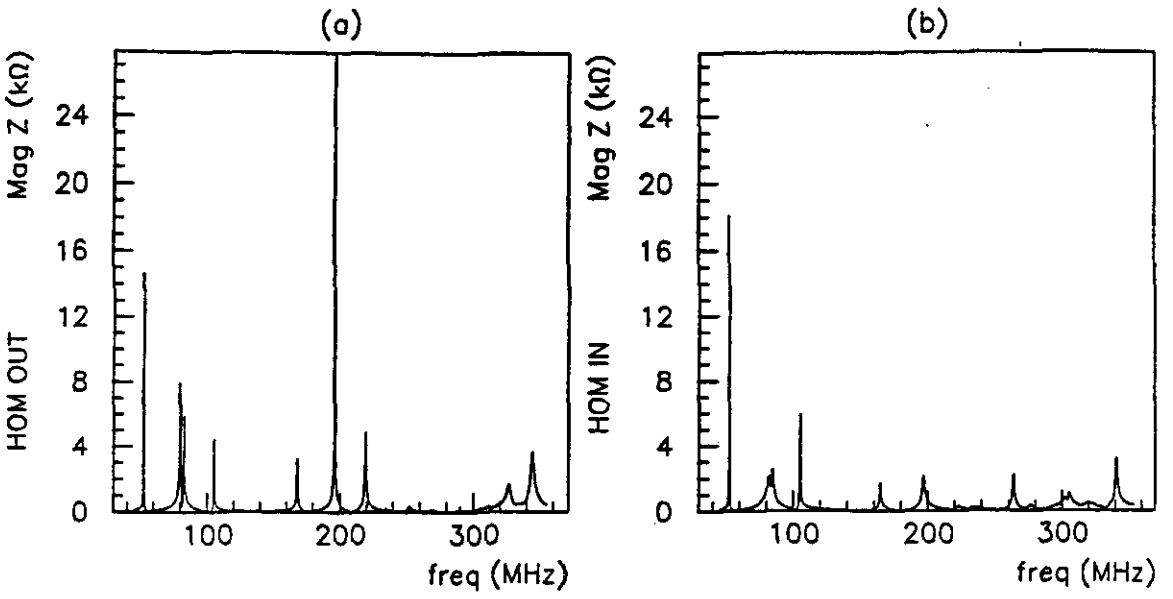

Figure 5.15 Comparison of RF Cavity Single-Gap Impedance Before and After HOM Dampers. The nominal case is shown in (a), and the damped in (b). The modes are attenuated as well as shifted in frequency (see Appendix B).

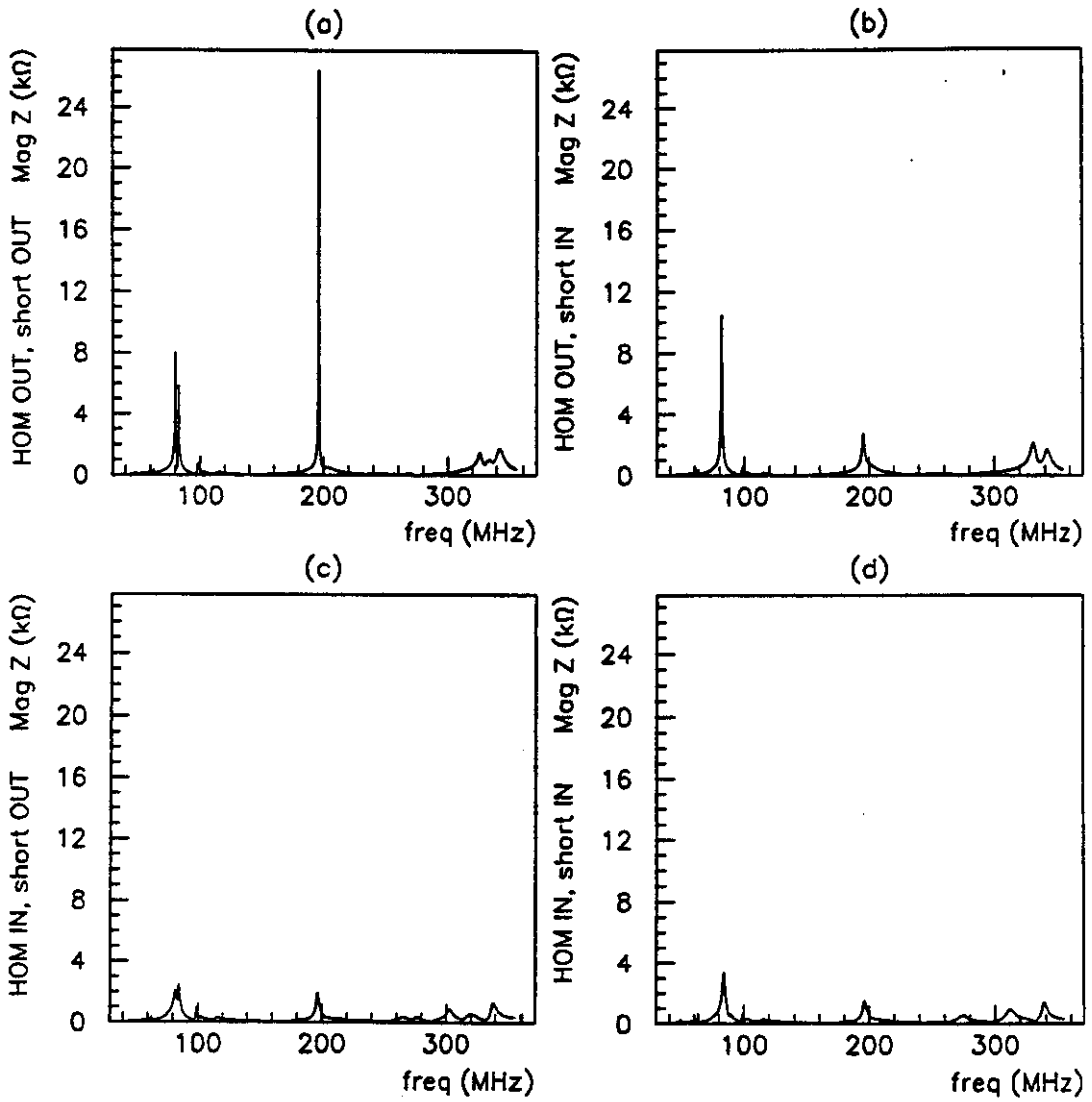

Figure 5.16 Effect of the Cavity Short on the Impedance. The vertical scale is identical in all cases, and the tuner bias current is zero. Shown are the (a) nominal cavity, HOM dampers out, short out, (b) nominal cavity, HOM dampers out, short in, (a) modified cavity, HOM dampers in, short out, (a) modified cavity, HOM dampers out, short in.

A typical result for the single-gap impedance of the nominal cavity (no HOM dampers), corresponding to t=19 msec in the cycle, is given in Figure 5.15 (a) using the technique described in Chapter 4. The data show a series of narrow resonances that exist in the cavity above the fundamental. By comparison, the gap impedance for the cavity in which selected higher-order modes are damped is shown beside it in (b). A comparative tabulation of frequency, magnitude R, and ratio R/Q for these data is given in Table B9. It is to be noted that the frequencies are significantly shifted and R/Q, a quantity theoretically fixed in a resonant structure, varies by up to 50% after damping. Addition of the dampers alters the cavity geometry and equivalent reactance.

The changes in the impedance at the gap due to the use of the cavity short is depicted in Figure 5.16. At the upper left is the nominal cavity with zero bias current, while to its right the same is shown after the short has been inserted. There is only one short on each cavity; in this measurement, the wire is inserted in the gap on the far end, the "unshorted" gap. The impedance at the "shorted" gap (not shown) is reduced again by about 20% but otherwise similar. There are similarities in the higher-order mode structure between the damped cavity (Figure 5.15 (b)) and the shorted cavity with zero bias (Figure 5.16 (b)). For completeness, the same measurements were performed on the cavity after the dampers were installed. These data are shown plotted in Figure 5.16 (c) and (d) and tabulated in Table B.10. The vertical scale on all the impedance plots is the same.

Results

For better control of the beam conditions and as a test of the HOM dampers, four cavities were modified in two steps. First, the cavities were fitted with only the internal hardware (R06, R07). Beam measurements were repeated after a short beam enclosure access to add the external tuned circuits (R08, R09). No changes were seen in either the emittance or the beam spectrum with these changes. As the HOM dampers presented no ill effects, it was decided to install them on all the RF cavities. The result now is dramatic. Figure 5.17 (b) is the beam current FFT spectrum taken with dampers installed in all 17 Booster RF cavities. The coupled bunch mode 16 line is no longer present and the amplitude of the n=36 line has been reduced by 5 dB. The

reduction in the longitudinal emittance growth with the dampers in place is shown in the lower trace of Figure 1.1 in Chapter 1. The correlation of the beam spectral lines and the HOM-damped cavity impedance is also shown in Figure 5.17. The modes at 166 and 342 MHz do not correspond to observed, excited beam modes, but could become important at higher beam intensities.

5.3 Anomalous Emittance Growth

As a final discussion, the ubiquitous coupled-bunch modes are absent under special conditions. Actually, this was found unintentionally when the Linac acceleration tanks were accidentally mistuned and the CBM mode lines in the Booster were surprisingly found to be absent. Curiously, the longitudinal emittance growth was still present in this case. Systematic studies later on showed that this result could be reproduced for 17 cavities by deliberately increasing the longitudinal momentum spread of the injected beam. The nominal and increased momenta are shown in Figure 5.18. The corresponding beam spectrum, showing only the RF harmonics and no coupled-bunch mode structure, is given in Figure 5.19 (data run R10). The emittance growth and coupled-bunch mode amplitudes for the case with large momentum spread (R10) are shown in Figure 5.20 compared with a nominal case (R09). While a larger momentum spread may explain the absence of the coherent coupled-bunch mode oscillations due to increased Landau damping, the continued presence of the emittance growth is not so readily explained. Presumably, with the greater injected momentum spread, we are filling the RF bucket and thus maximizing the emittance. This observation needs further study to understand the rapid emittance growth at transition with 17 cavities.

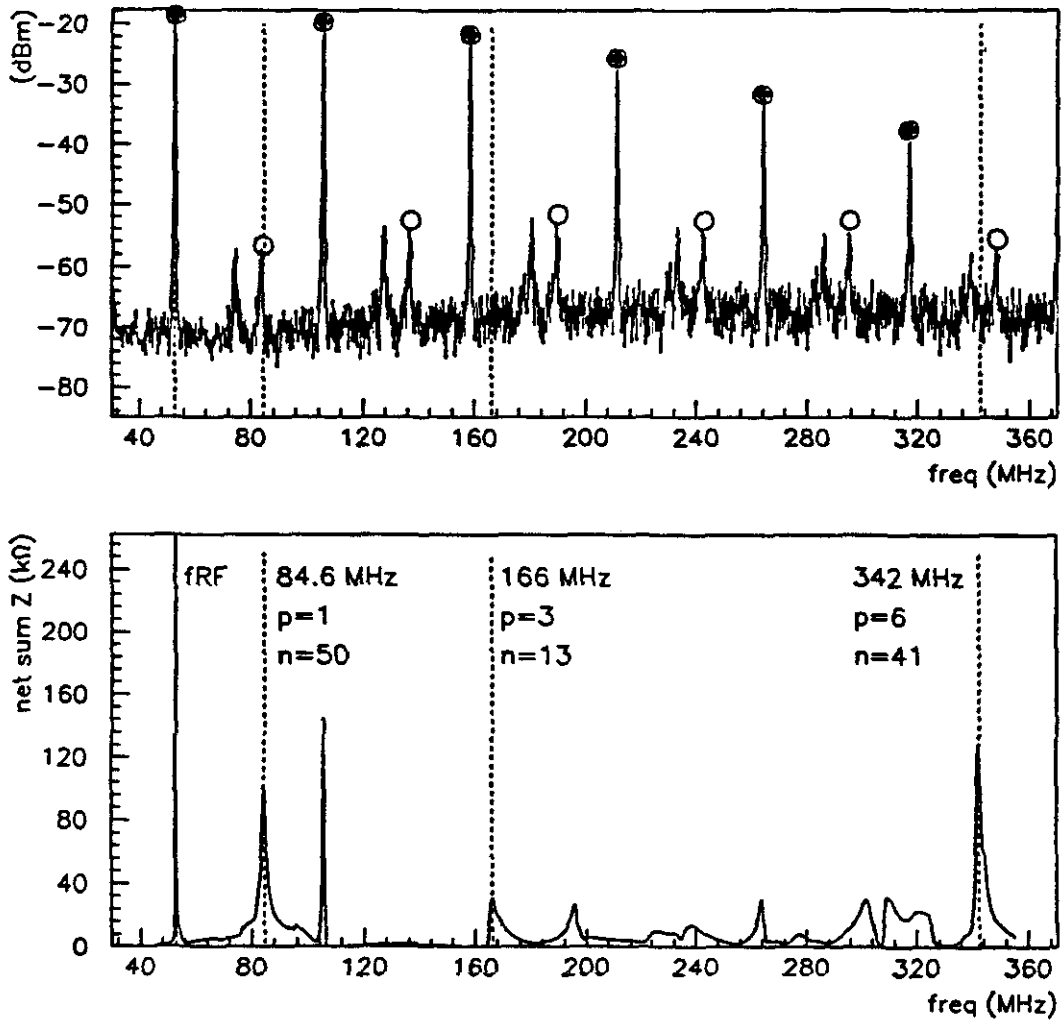

Figure 5.17 Correspondence of RF Cavity HOM Impedance and Coupled-Bunch Mode Spectrum After HOM Dampers. The RF harmonics are marked with a filled "O" and mode 50 with an open "O". (R36)

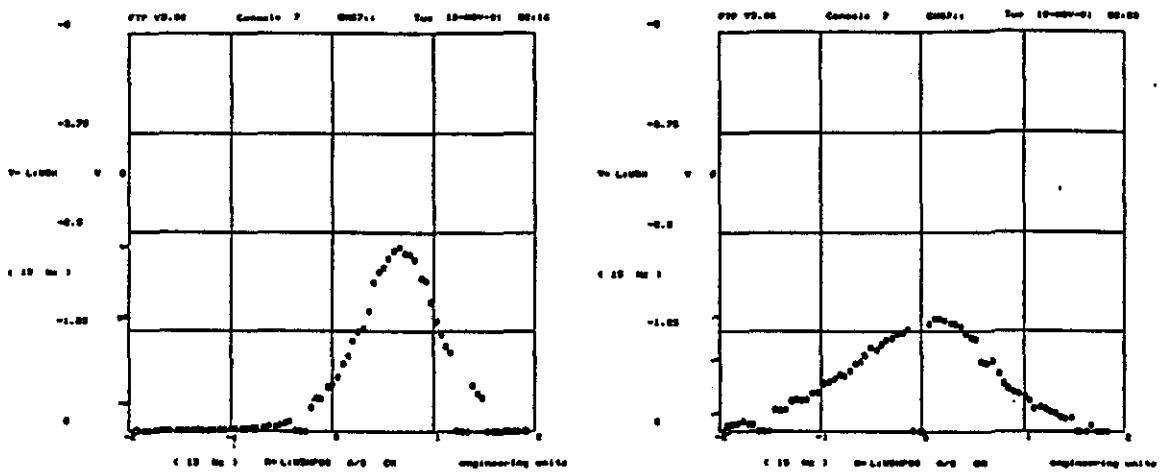

(a) (b)

Figure 5.18 Nominal and Increased Beam Momentum Spread. The momentum spread in (a) is the nominal $\Delta p/p$=0.38% (96% area), while in (b), it has been changed to 0.62%.

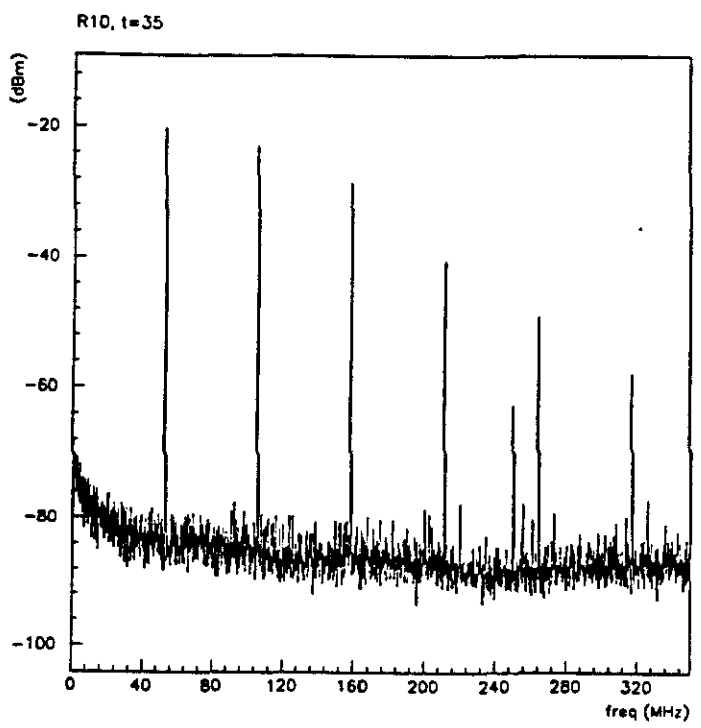

Figure 5.19 Spectrum for Large Momentum Spread. Although no coupled-bunch modes are evident, we observe emittance growth for this case. The beam intensity is 1.9e12 ppp with 17 cavities, four of which have HOM dampers. (R10)

(a)

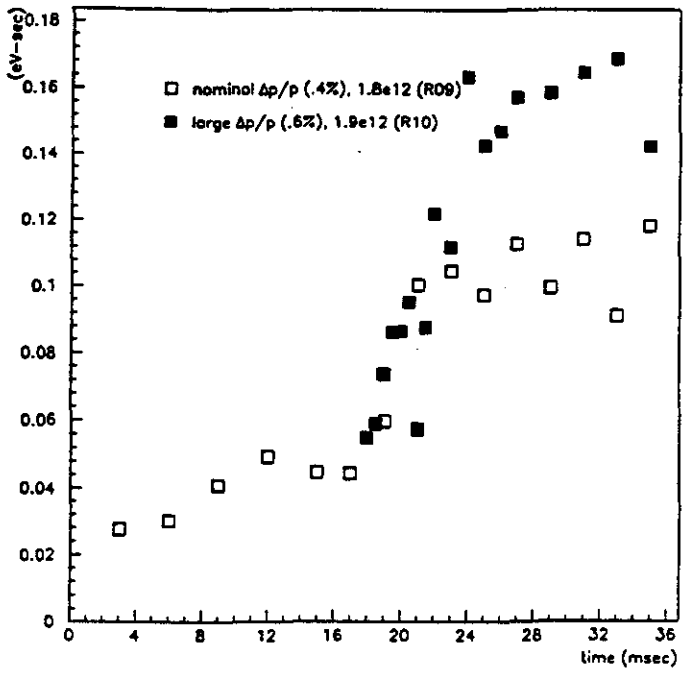

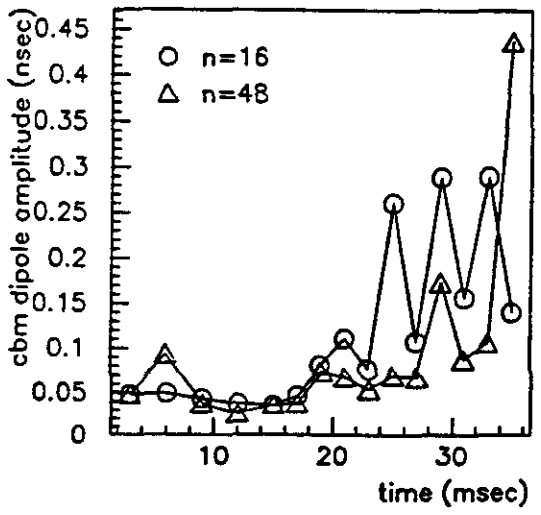

(b)

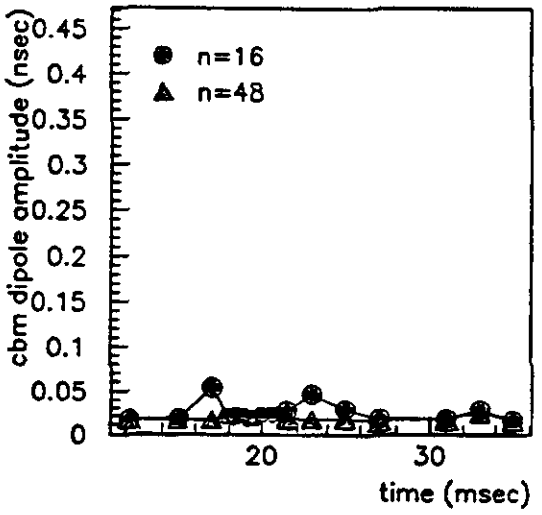

(c)

Figure 5.20 Coupled-Bunch Mode Amplitudes and Emittance Growth for Large Momentum Spread. Data runs R09 and R10 are compared, with nominal and large momentum spreads, respectively. The intensity is 1.8 (1.9) e12 ppp with 17 RF cavities. The coupled-bunch amplitudes are plotted for (b) the nominal and (c) large $\Delta p/p$.

6. CALCULATIONS

The linear coupled-bunch instability theory has been widely studied and is generally accepted as being well understood. Of interest here is how well it applies in the case of the Booster, which presents the added complexity of multiple unstable modes and slewing frequencies. We seek also to verify the impedance model, as these modes are driven off-resonance at times during the cycle. The formulae are derived from the available literature, but the analysis involves rigorous testing and modification of some of the assumptions for proper application to the Booster. The effects of the beam momentum spread and non-linear accelerating RF potential leading to Landau damping are included self-consistently. In all cases, measurements of the beam momentum spread and the longitudinal coupling impedance due to the RF cavities are used. In a comparison between the observed final coupled-bunch amplitude growth and predictions of the theory, we may draw conclusions as to the applicability of this theory to extensions of the Booster beam operating parameters. Finally, we are interested in whether we may specify a maximum emittance given knowledge of the driving mechanism, such as the high-Q impedance.

The quantitative analysis of the data was an iterative process. Observations of the mountain range display verified the bunch length and dipole coupled-bunch mode amplitudes extracted from the spectral data. Calculation of the linear instability growth rates based on the RF cavity impedance measurements in part verified the identification of the offensive parasitic modes. Estimates of the growth rate from the mountain range display guided the correct interpretation of the RF cavity bench impedance data. The results from simulation (next chapter) using these impedance data guided our understanding of the phase space time evolution and sensitivity of the instability to the particle distribution.

6.1. Calculation of Linear Instability Growth Rates

The details of the calculations are discussed below. Recalling the analysis of the beam spectral data in Chapter 5, we extract the unstable coupled-bunch mode amplitudes as a function of time in the Booster cycle. These data are compared directly with a calculation of the time-integrated linear growth of each unstable coupled-bunch mode. This calculation is done in two steps. First, the linear instability growth rate is computed at several different times in the cycle. The results are integrated over the cycle assuming slow time variation (WKB) in the impedance.

Recall the dispersion relation, eqn. (3.3.28) from Chapter 3, which governs the relationship between the coherent unstable modes and the driving impedance:

$$1 = -i\frac{\eta\omega_0{}^3 h}{\beta^2 E}\sum_{k,k'}\frac{Z_k(\omega)}{k}\int_0^\infty dr\,\frac{\frac{\partial f_0(r)}{\partial r}J_1(kr)J_1(k'r)}{(\Omega-\omega_s(r))} \tag{6.1.1}$$

Normally, we are interested in solving eqn. (6.1.1) for each coupled-bunch mode n=0,1,...,h, to find those eigenfrequencies Ω which are unstable. As this is an infinite dimension matrix equation, a number of simplifications are generally made. In the literature, the small-argument expansion is substituted for both $J_1(kr)$ terms. This is the short bunch approximation: kr is the ratio of coupled-bunch mode amplitude to perturbing wake field wavelength. Also, to allow analytical solutions, ω_s is often assumed constant, so that Landau damping can be neglected. However, in the case of the Booster, kr is not small. We studied both regimes, ω_s constant and $\omega_s(r)$, to examine the effect of Landau damping.

Before proceeding, we digress on the concept of form factors introduced in the discussion of the coupled-bunch mode beam spectra in Chapter 3, eqns. (3.2.21) and (3.2.22). The form factors are envelope functions corresponding to individual perturbed modes (stationary, dipole, quadrupole, etc.) and determine the frequency response of the beam to external driving impedances. The form factor essentially modifies the effect of the impedance, and therefore the product (or convolution) is referred to as the effective impedance. Sample parabolic and gaussian amplitude particle distributions are written[17]

$$f_o(\hat{z})_{\text{parabolic}} = \frac{2}{\pi\left(\frac{\tau_L}{2}\right)^2}\left(1-\hat{z}^2\right) \qquad \Lambda(z)_{\text{parabolic}} = \frac{8}{3\pi\left(\frac{\tau_L}{2}\right)}\left(1-z^2\right)^{\frac{3}{2}}$$

$$f_o(\hat{z})_{\text{gaussian}} = \frac{2}{\pi\left(\frac{\tau_L}{2}\right)^2}\exp\left(-2\hat{z}^2\right) \qquad \Lambda(z)_{\text{gaussian}} = \sqrt{\frac{2}{\pi}}\frac{1}{\left(\frac{\tau_L}{2}\right)}\exp\left(-2z^2\right) \tag{6.1.2}$$

where $z = \frac{\tau}{\tau_L/2}$ and $\hat{z} = \frac{\hat{\tau}}{\tau_L/2}$. We illustrate the form factors in Figure 6.1, where the linear functions are shown in (a) and (c), and the envelopes for the power spectra in (b) and (d). From the sample beam spectrum in Figure 4.22, we may conclude that a parabolic distribution with sharp cut-off best fits the data, corresponding the case shown in Figure 6.1 (b). However, towards the end of the cycle, the beam spectral lines tends toward the view in Figure 6.1 (d). To be most general, we decided to study the theory using a gaussian distribution.

For a constant synchrotron frequency $\omega_s = \omega_{s_0}$, valid in the case of a small bunch in a large RF bucket, the denominator in eqn. (6.1.1) may be pulled out of the integral. Let $\Delta\Omega = \left(\Omega - \omega_{s_0}\right)$. In the Booster, there are two unstable "modes" (actually doublets), each driven by two RF cavity parasitic modes. The modes around n=16 are driven by 169 and 220 MHz (RF harmonics p=3,4). Modes around n=48 are driven by 83 and possibly 345 MHz (p=1,6). For each n, eqn. (6.1.1) becomes a 2x2 matrix equation with solutions for $\Delta\Omega$ given by $\left|1-M_{ij}\right| = 0$. For a gaussian particle distribution, using relations in Ref. 58, the matrix elements may be written

$$M_{ij} = i\frac{1}{\Delta\Omega}\frac{\eta I_0 e}{2\pi\beta^2 E}\frac{\omega_0^2}{\omega_{s_0}^2}\frac{1}{L}\frac{Z_{k_i}}{k_i}e^{-\frac{1}{2}\left(k_i^2+k_j^2\right)L^2} I_1\left(k_i k_j L^2\right) \tag{6.1.3}$$

where $L = \frac{1}{2}\omega_o\tau_L$ is the bunch half length in radians and I_1 are modified Bessel functions. The envelope of this effective impedance is shown in Figure 6.2 for k_i=k_j=k compared with the result for the parabolic bunch. The matrix elements are evaluated for n=16,48 at different times t through the cycle using the measured impedance Z_k. In each case, the larger $\Omega(t)$ of the two solutions is taken to dominate. The result for the instability growth rate is given as a function of coupled-bunch mode number by the

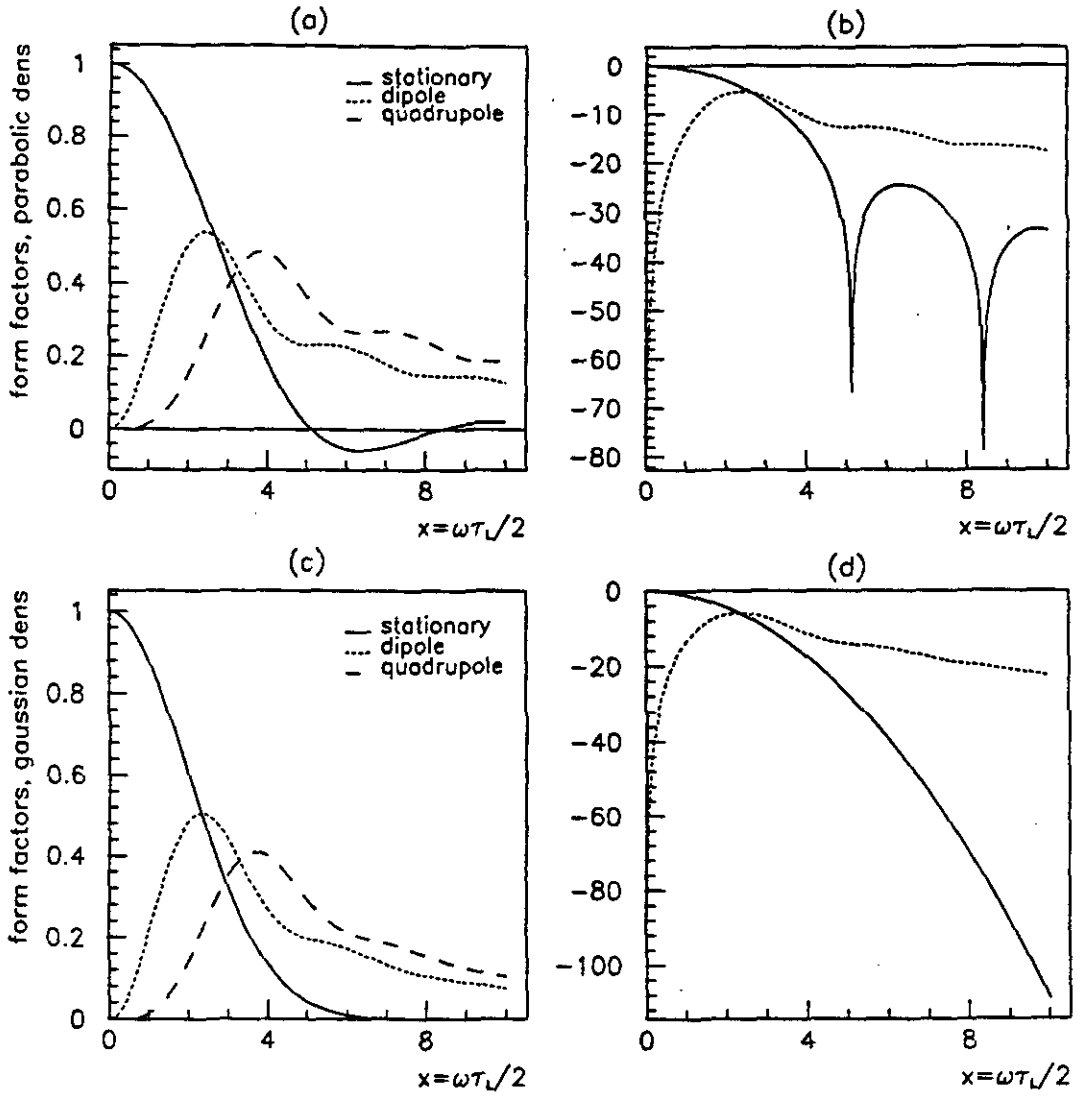

Figure 6.1 Form Factors for Coupled-Bunch Instability. Depicted are the envelope functions which multiply the impedance in the simple case without Landau damping for the (a) parabolic amplitude and (b) gaussian amplitude particle distributions. The envelopes of the power spectra for these same distributions are given in (c) and (d), respectively.

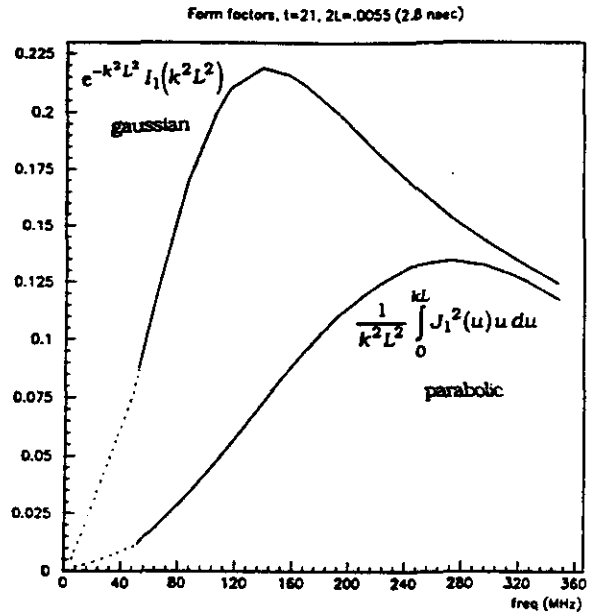

Figure 6.2 Form Factors Comparing the Dipole Coupled-Bunch Mode for Different Particle Distributions.

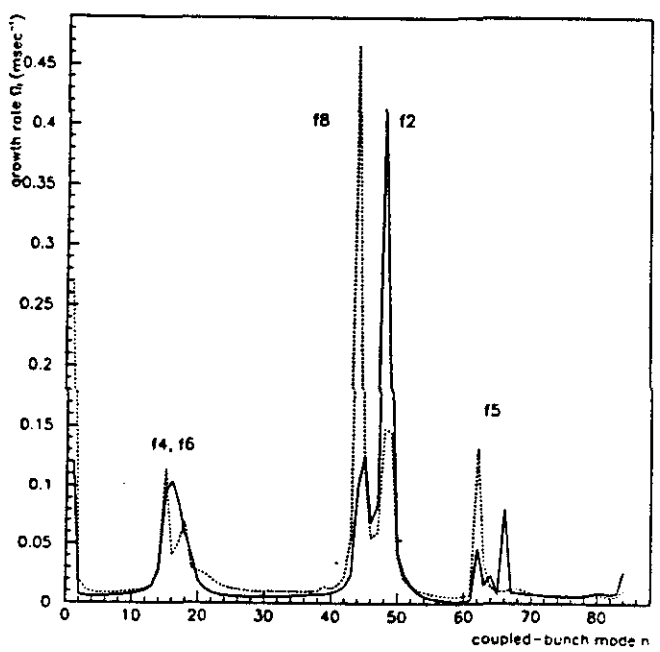

Figure 6.3 Linear Instability Growth Rates in Booster. Compared are the results using the net sum RF cavity impedance (solid line) and scaled single-gap impedance (broken line).

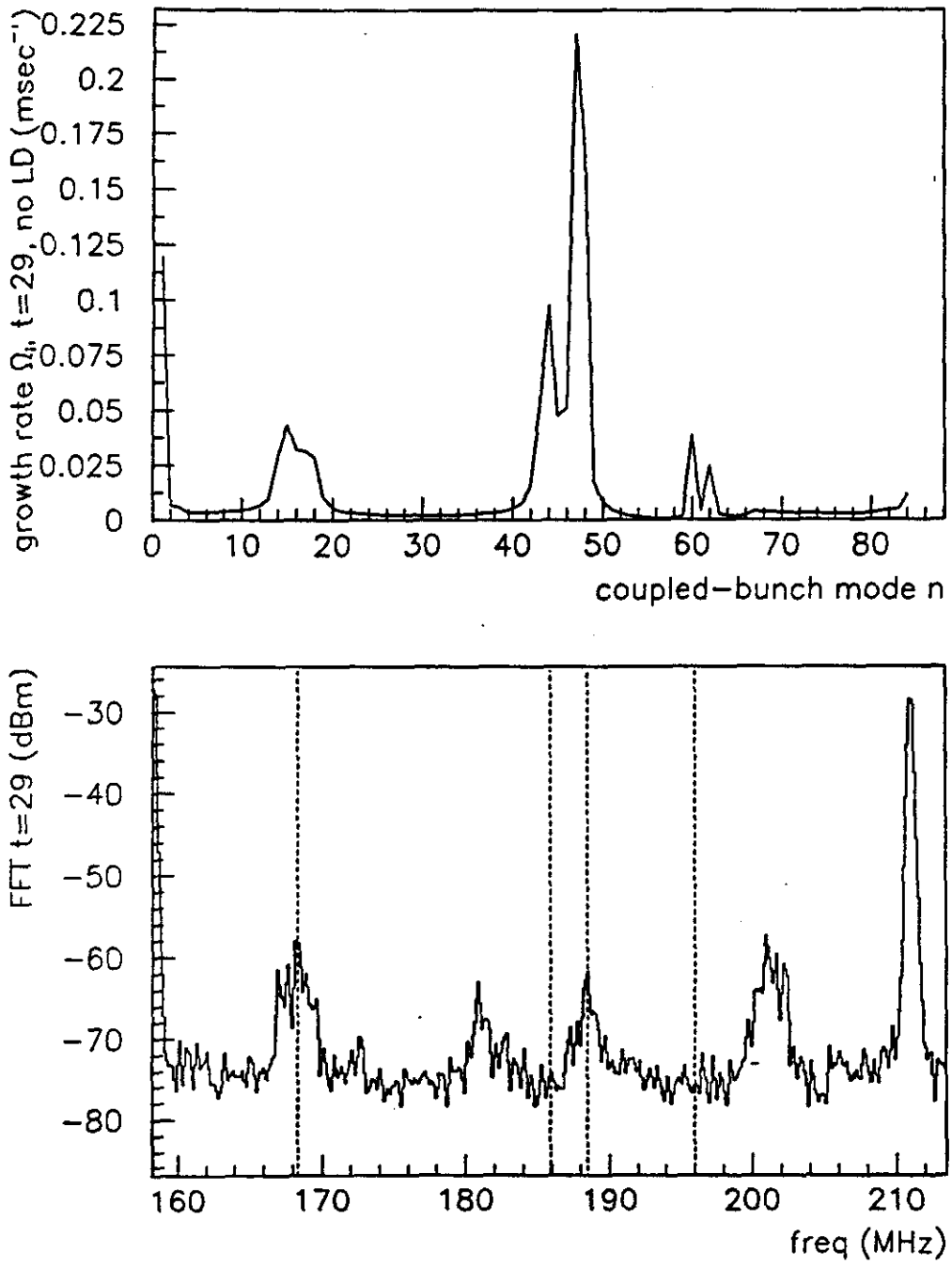

Figure 6.4 Correspondence of Linear Instability Growth Rate and Perturbed Beam Spectrum. Depicted are the results using data run R01 as an example (see Table 5.1).

solid curve in Figure 6.3 for the example of data run R01 at 21 msec. Shown next to each nontrivial mode is the dominant responsible impedance identified by its RF cavity mode number (Table 4.1). Superimposed on the plot with the broken line is the result if we naively take the single-gap cavity gap impedance and multiply simply by 2x15 cavities. Figure 6.4 shows the correspondence with the data (R01, 29 msec); we see that modes n=16 and 48 appear in the spectrum, while n=46 and 60 do not.

In the case of Landau damping, the frequency spread must be included. We use the approximation

$$\omega_s(r) = \omega_{s_0} + \Delta\omega_s \approx \omega_{s_0}\left(1 - \frac{r^2}{16}\right), \quad r = hL \tag{6.1.4}$$

We eliminate the sum by choosing the dominant Z_k only and write

$$\begin{aligned} 1 &= i\frac{\eta I_0 e}{2\pi\beta^2 E}\frac{\omega_0{}^2}{\omega_s{}^2}\frac{16}{\omega_s h^2 L^4}\frac{Z_k}{k}\int_0^\infty dx\,\frac{e^{-x}J_1{}^2\left(kL\sqrt{2x}\right)}{x-y} \\ y &= -\frac{8}{\omega_s h^2 L^4}\Delta\Omega \\ \Delta\Omega &= \left(\Omega_r - \omega_{s_0}\right) + i\Omega_i \end{aligned} \tag{6.1.5}$$

The integral in equation eqn. (6.1.5) is solved numerically, fixing Ω_i and varying Ω_r. The curves may be plotted in the complex Z-plane as shown in Figure 6.5 (a). This example corresponds to Booster parameters in R01 at 29 msec in the cycle: $(\omega_s, \Delta\omega_s)$ = 2π (2200, 78) Hz. The solution for $\Omega(t)$ is found graphically by finding the intersection of one of the curves with the measured $\frac{Z_k}{k}$. The innermost curve, whose true asymptote should be zero, delineates zero growth rate; the offset is a numerical artifice. If the impedance falls inside this curve, the system is stable. For an effective impedance (3.2+i0.5) kΩ as plotted with a large dot in Figure 6.5 (b), the growth rate predicted is 0.913 msec^{-1} without Landau damping and 0.845 msec^{-1} with Landau damping.

We may use a WKB approximation to get the integrated growth of the instability, since the $\Omega(t)$ are slow functions of time. The coupled-bunch mode amplitude $\psi(t)$ normalized is calculated using

(a)

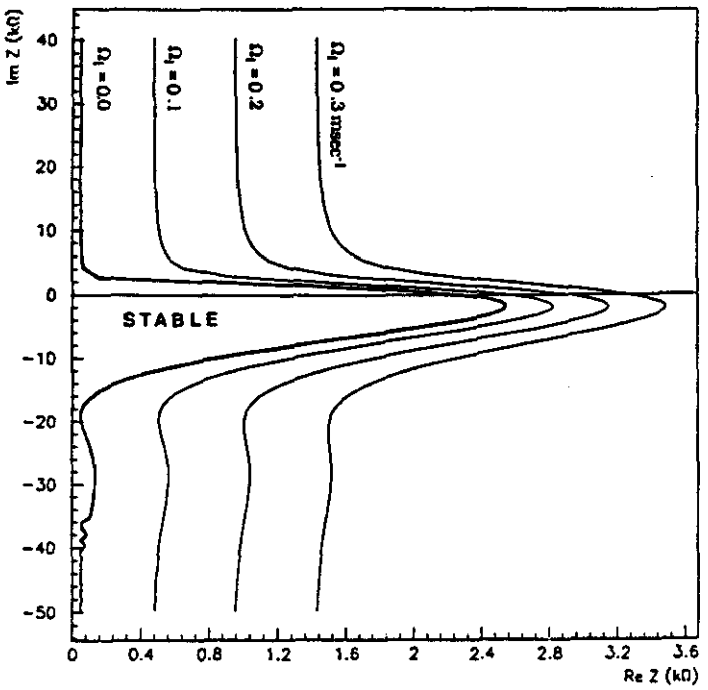

(b)

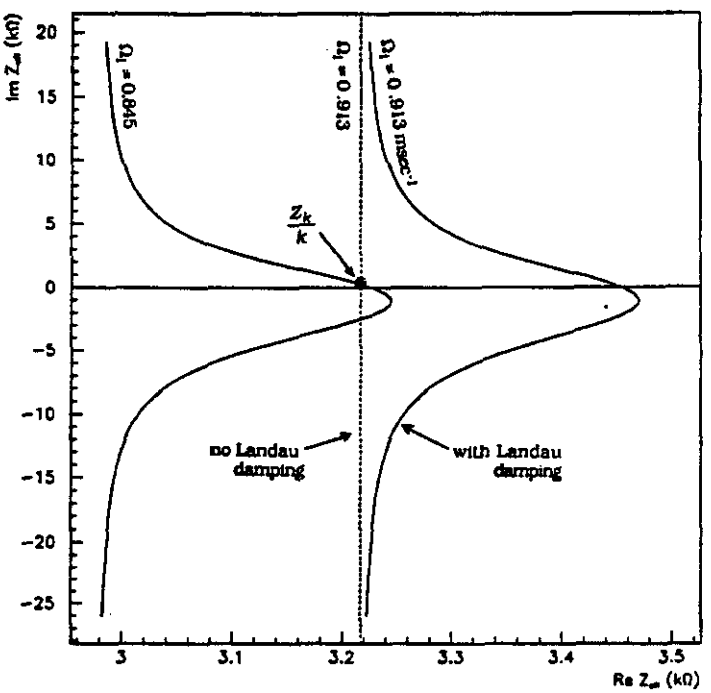

Figure 6.5 Instability Curves Showing Graphical Solution of Growth Rate. Illustrated are the solutions for a gaussian particle distribution plotted in the complex impedance plane. In (a), curves of constant growth rate are shown. The system is stable if the effective impedance falls inside the leftmost curve. In (b), we see the effect that Landau damping has in reducing the growth rate. For the effective Z_k/k plotted, the growth rate is reduced from 0.913 to 0.845 $msec^{-1}$. (R01, t=29, $\Delta\omega_s$=0.48 msec-1 (75 Hz))

$$\frac{\psi(t)}{\psi_0(t_0)} = \exp\left(-\int_{t_0}^{t} \left|\Omega_I(t)\right| dt \right) \tag{6.1.6}$$

6.2 Comparison with Observations

The results, comparing the cases without and with Landau damping are shown plotted in Figure 6.6 along with the data (R01) for coupled-bunch modes n=16 and 48. Results from the linear coupled-bunch instability theory show good quantitative agreement with the measured growth, with the caveat that Landau damping must be invoked to predict the observed saturation in mode n=16. This is despite the fact that the oscillation amplitude (~1 nsec) is a significant fraction of the bunch length (Figure 5.6). Mode n=48 appears not to be Landau damped according to the linear theory; however, note that even larger amplitudes of 2 nsec are reached. The growth times of the instability may be compared with the decoherence time of an impulse perturbation in a simplified yet instructive analysis. We may estimate the decoherence, or mixing, time of the bunch in the RF bucket by $\approx 1/\Delta\omega_s$, the inverse of the spread in synchrotron frequencies among the particles in the beam. The results, plotted in Figure 6.7, suggest that the beam may decohere up to about 22 msec, consistent with the saturation of n=16, whereupon the instability growth times exceed the decoherence time.

A number of corrections should be noted to the analysis described above. First, the expression for the radial dependence of the synchrotron frequency in eqn. (6.1.4) (also eqn. 3.1.31) is strictly true only for a stationary bucket, i.e. when $\phi_s = 0$. A more general expression gives a moving bucket dependence of $\left(1 + \frac{5}{3}\tan^2\phi_s\right)$ (eqn. (3.1.32)). This result, by the same analysis as eqn. (6.1.5), would predict growth rates reduced by up to a factor of ten when, as near transition energy, $\phi_s = 65°$. This seems, however, inconsistent with observations. Second, the analytical results depend strongly on the evolving particle distribution, as noted in the simulations in the next chapter. This dynamic picture is not taken into consideration in this analysis.

Finally, other sources of impedance, such as due to space charge and the broadband components, have been neglected. In the Booster, the major contribution to the broadband impedance is due to the magnets. There is no smooth beam pipe: the

(a)

(b)

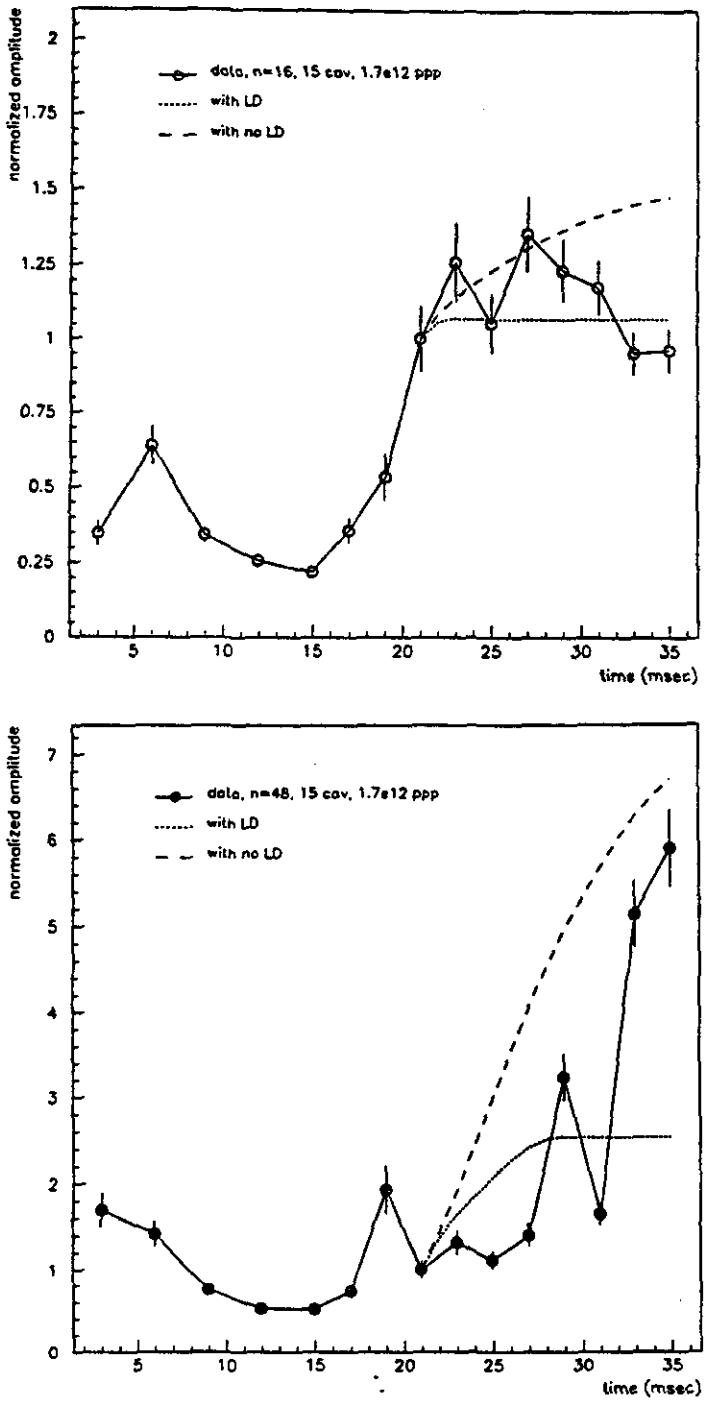

Figure 6.6 Comparison of the Linear Instability Theory With the Data. The plots show the comparison of measured dipole coupled-bunch mode amplitude (from Chapter 5) for modes (a) 16 and (b) 48 in the Booster with the growth predicted by linear instability theory both without and with Landau damping. (R01)

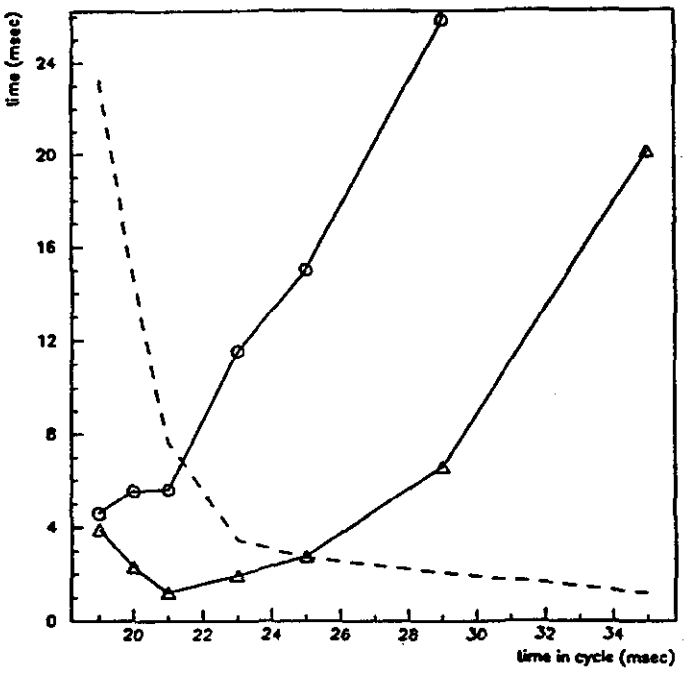

Figure 6.7 Coherent Instability Growth Time vs Decoherence Time. Plotted are the growth times for coupled-bunch modes n=16 (circles) and n=48 (triangles). Superimposed with a broken line is an estimate of the decoherence time given by the inverse of the synchrotron frequency spread $\Delta\omega_s$.

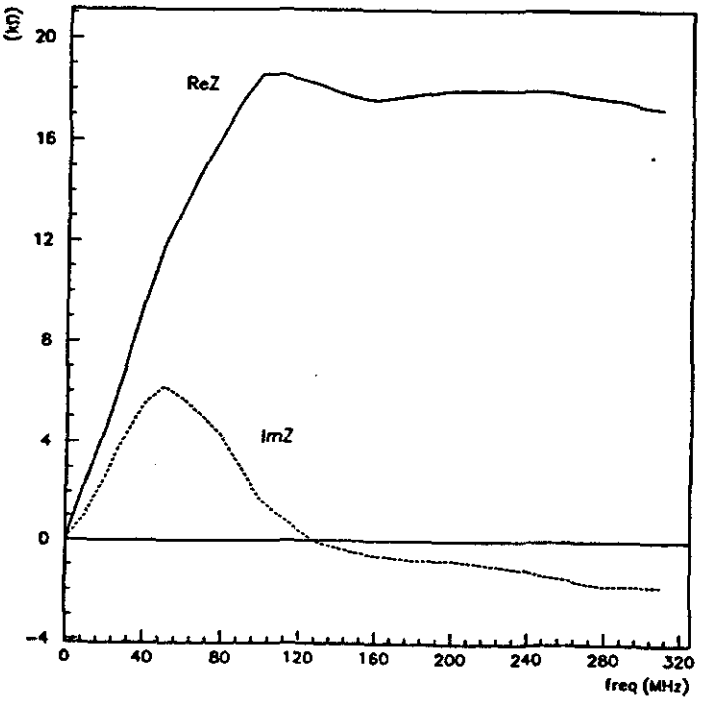

Figure 6.8 Measured Impedance due to Booster D Magnets. This impedance compares fairly well with a model LRC resonance with f=100 MHz, R= 12 kΩ, and Q=1. (Ref. 3,43)

bending magnets are inside the vacuum chamber and thus the beam is exposed directly to the laminations. The small spaces between the laminations create the effect of tiny cavities, which allows for short-range wake fields to be generated by the beam at high frequency. The impedance was studied extensively in the early days of the Booster, with a resulting energy loss estimated to be between 50-100 keV per particle per turn around transition.[39,40] The impedance also has been measured in the past using the stretched-wire technique, and the result is shown in Figure 6.8.[3,43]

Analysis of the instability properties of the beam due to the broadband impedance proceeds similarly to that for narrowband resonances. One writes the proper expression for the dispersion relation and solves for growth rate and frequency shift for a particular mode. In the literature, the stability threshold is determined by calculating the threshold Z/n using the Boussard criterion for bunched beams[38]

$$\frac{|Z|}{n} \leq 2\pi \frac{E}{e} \frac{|\eta|}{\hat{I}} \left(\frac{\Delta E}{E} \right)^2 \tag{6.2.1}$$

where $\hat{I}$ is the peak beam current and n=int(ω/ω_0). Eqn. (6.2.1) is a special solution of the dispersion relation eqn. (6.1.1) applied to a single bunch[38] and compares the frequency shift due to the reactive impedance with the frequency spread in the beam (Landau damping). Although the energy spread cannot readily be measured directly through the cycle, it can be estimated from the bucket parameters and the bunch length using eqn. (3.1.34). For the typical case of 15 cavities and 1.7×10^{12} protons per pulse (R01, no HOM dampers), the Z/n threshold is calculated using the values in Table 6.1 and plotted in Figure 6.9. Recall that $K=E-E_0$ is the kinetic energy.

One can, in principle, compare these results with the measured magnet $|Z|/n$. There are different interpretations in the literature of the lowest unstable mode n to use. Some use the lowest propagating mode, i.e. the cutoff frequency, which corresponds to the frequency at which the measured reactance becomes capacitive.[44] This would give Z/n=(6.2kΩ)/(100MHz/628kHz)=40Ω. The result suggests that the microwave instability threshold limit is exceeded through transition (see Figure 6.9). However, this analysis is oversimplified, since other conditions such as $\Omega_l >> \omega_s$ and $\omega << 1$/bunch length must be met. However, there in no evidence of a microwave instability in the Booster, so we consider this analysis beyond the scope of this thesis.

Table 6.1 Criterion for Microwave Instability Threshold in the Booster

time (ms)	K (GeV)	η	bkt H (MeV)	bnch L (ns)	bkt L (ns)	$\Delta p/p$ (%)	I_pk (amp)	Z/n (kΩ)
3.0	0.2151	-0.6281	1.0897	19.8	24.3149	0.2578	1.7778	1.9460
6.0	0.3910	-0.4645	1.6486	13.5	15.5857	0.2366	2.6074	2.0964
9.0	0.8451	-0.2431	2.6027	9.2	10.4138	0.1952	3.8261	1.4184
12.0	1.5921	-0.1038	4.0046	6.0	7.6740	0.1649	5.8667	0.5687
15.0	2.5653	-0.0380	5.4278	4.2	5.5516	0.1466	8.3810	0.1848
17.0	3.2935	-0.0154	5.6938	3.3	3.9074	0.1335	10.6667	0.0620
19.0	4.0508	-0.0017	13.6224	2.	3.1666	0.2414	15.3043	0.0184
21.0	4.8079	0.0071	8.9888	3.2	3.6448	0.1549	11.0000	0.0526
23.0	5.5363	0.0127	8.6935	3.5	4.1926	0.1285	10.0571	0.0814
25.0	6.2090	0.0165	9.3316	4.5	4.7590	0.1325	7.8222	0.1606
27.0	6.8015	0.0190	12.0299	4.5	5.9809	0.1380	7.8222	0.2186
29.0	7.2921	0.0207	12.7078	4.7	6.6663	0.1304	7.4894	0.2371
31.0	7.6632	0.0218	13.8906	5.0	7.7587	0.1269	7.0400	0.2632
33.0	7.9014	0.0224	17.5090	5.3	10.2297	0.1287	6.6415	0.3038
35.0	7.9980	0.0227	23.0118	5.8	15.5864	0.1226	6.0690	0.3084

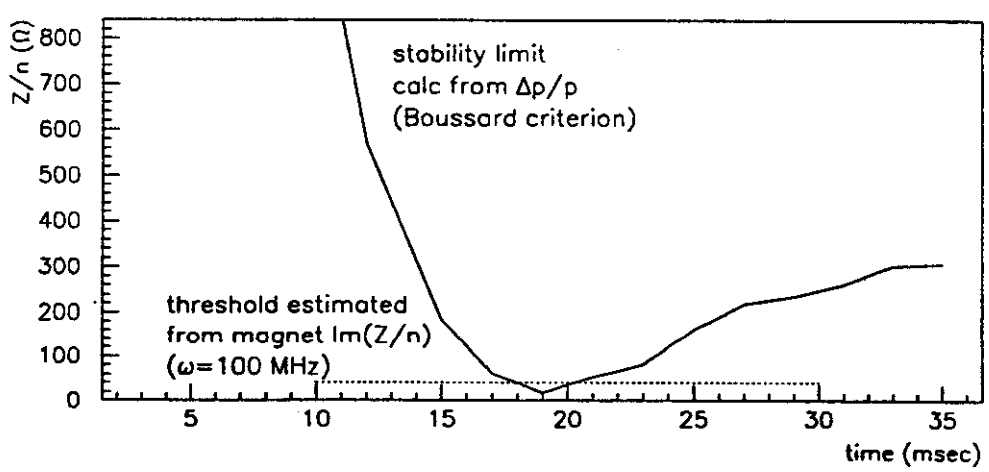

Figure 6.9 Microwave Instability Threshold for Booster. Shown is the calculated value of Z/n (Boussard criterion) vs. that estimated from the magnets in Figure 6.8.

7. SIMULATION

To study the detailed time evolution in phase space of a beam undergoing instabilities and the connection with emittance growth, we turn to the longitudinal particle tracking code ESME. This code was developed at Fermilab and has been validated independently by a number of users over the years. In our case, with the code we simulate the Booster beam under the influence of several RF cavity HOM impedances modeled as LRC resonators. In addition, the broadband component contributed by the magnets is included. All input parameters, e.g. initial emittance, beam intensity, RF voltage, and HOM and magnet impedance, are taken from the recent data described in earlier chapters. The goal is to reproduce, if possible, the observed coupled-bunch mode amplitude growth as well as the emittance growth, both before and after the RF cavity HOM dampers were installed. Once this is achieved, we can, with some confidence, predict the behavior in the Booster with increased intensity as envisioned for the Linac post-upgrade era. The present work is rather different from a prior coupled-bunch instability simulation study of the Booster, which was more a comparative study of conceptual stabilizing techniques using entirely different input impedance data.[55] We proceed now a description of the code followed by the results of our comprehensive, quantitative simulation study.

7.1. ESME: Longitudinal Particle Tracking Code

ESME is a computer program which calculates in a proton synchrotron the evolution of a distribution of particles in longitudinal phase space. It allows the user to study the behavior of the beam as it is acted upon by the RF system and, optionally, by longitudinal forces due to collective effects such as image currents in the resistive walls, excitation by the beam of RF parasitic modes, and space charge. The results may be viewed graphically in various forms, including phase space plots and output resembling the mountain-range display. ESME has been used at Fermilab as a tool in a number of applications: the design of the Antiproton Source and study of the

transition-jump system in the Booster, to name two. It has also been used at CERN to study RF manipulations. The code is documented, and the description below is summarized directly from References 52, 53, 54, 55.

At the heart of the program are a pair of single-particle difference equations which are derived from the Hamiltonian equations of motion of Chapter 3, section 1. These are used to calculate turn-by-turn the change in azimuth $\vartheta_{i,n}$ and energy $E_{i,n}$ for each i-th particle during the n-th turn of the synchronous particle. The time evolution of the particle distribution is produced by iterating a discrete map of the longitudinal motion from the n-th to the $(n+1)$-th turn, applied to each particle individually.

In the ESME mathematical framework, the RF force is applied impulsively at localized gaps at which the particle receives a finite energy increment followed by a force-free drift. The ring may be azimuthally divided into equal periods, one RF gap per period. Invoking periodicity can save computation time in that only a fraction of the total particles need be tracked. However, to study a coupled-bunch instability where the mode number n divided by the machine harmonic number h is not an integer, such periodicity cannot be imposed. The effect of all the RF cavities is instead lumped together as if acting at a single gap. This assumption is not unrealistic, recalling the argument presented in Chapter 4 where we describe the calculation of the net sum impedance. The parasitic modes are in phase with the beam because they are driven by the beam. Thus the impedance due to these modes also add in phase from one cavity to the next and can be lumped into a single net impedance.

The relation between the circulation periods of the synchronous and i-th particle is treated exactly. Therefore, the kinematic nonlinearities, such as within the RF potential, are also treated exactly. This is important in our study of the coupled-bunch instability because it is precisely this nonlinearity which gives rise to self-stabilization of the beam, or Landau damping. The stabilization of large-amplitude coherent oscillations in turn leads to a spreading or "filamentation" of the particles in phase space and can thus help explain the observed emittance growth. This is demonstrated dramatically in the simulation results to be shown later.

The beam-induced voltage from space charge and the longitudinal coupling impedance may be evaluated in ESME from data and specifications in the input file.

The various contributions to the impedance in the ring are first summed. The energy gain in the n-th turn for the i-th particle is then calculated by using the expression derived in Chapter 3, eqn. (3.3.20). In the Booster simulation, two sources of impedance are included: high-Q resonators and the broadband impedance.

The narrow resonant impedances due to the excitation by the beam of the RF cavity parasitic modes are represented in the simulation by a table list of resonant frequency, magnitude on resonance, and Q. To calculate the beam induced voltage due to the narrow resonance, ESME convolves the longitudinal charge distribution histogrammed as a function of time with the Green's function given earlier in eqn. (3.3.9). The convolution integral is evaluated for all times corresponding to the bins defining the current density $\Lambda_n(\Theta)$ so that the voltage acting on the particle can be found by determining which bin the particle populates. The solution for $\tilde{v}(t)$ for prior turns is updated to the present turn by relabling bins to account for the phase change and by reducing all values by $\exp(-(\omega_r/2Q)t)$. The voltage acting on a particular particle is evaluated by summing the voltage corresponding to the azimuth bin over how many voltage-azimuth tables are retained.

The broadband wall impedance is characterized in the code by a table of cubic polynomial values representing the real and imaginary part as a function of frequency. In the code, the impedance is evaluated at the frequencies $m\omega_s$ and added to the total to find the contribution to the beam induced voltage. This effect, in addition to the self-force due to space charge, is potentially important around transition, when the bunch length is minimum and the charge density maximum.

The self-impedance due to space charge forces is pure imaginary and behaves as a capacitive reactance. Assuming a uniform cylindrical beam of radius a in a beam pipe of average radius b, this impedance is evaluated using a formula well known from the literature: $\frac{Z_k^{sc}}{k} = -i\frac{Z_0}{2\beta\gamma^2}(1+2\log(b/a))$, where $Z_0 = \sqrt{\mu_0/\varepsilon_0} = 377\,\Omega$. Because of known problems with the implementation of this space charge calculation in version 7.2 of the code, we eliminate its effect by specifying b such that $2\log(b/a) = -1$. In order to justify this, we verified that the tracking results with and without the space charge calculation are identical with no other impedance present.

7.2 Booster Simulation Results

Study of the Booster coupled-bunch instability via simulation spanned approximately one year, during which about 140 runs were performed requiring over 1600 hours cpu time. For most of these , the UNIX version of the code was executed on a SUN SPARC 10 or a Silicon Graphics IRIX computer. Various cases were studied before the full simulation was attempted. Much effort was devoted to realistically represent in the code the RF cavity parasitic modes due to all 17 cavities. In the final analyses, conditions both before and after installation of the RF cavity HOM dampers were studied. The full simulations required about 30 hours cpu time to track 67,200 particles. A notable disadvantage of this UNIX version are the huge PostScript graphics files generated. This is alleviated somewhat by only plotting a fourth of the particles, sacrificing the finer graphical details of the collective particle motion in the phase space.

To simulate the baseline, undamped case with nominal RF cavities, the beam is driven by four resonances with intensity to compare directly with experimental data set R01, Table 5.1. For the case with the HOMs damped, and three resonances are input to compare with data set R36. Tracking is begun just before transition, starting with an initial elliptic charge distribution, and continued to extraction, totalling about 11,000 turns. Before presenting the final tracking results, the specifications and data in the input files are described in some detail. Next, some of the interim conclusions and difficulties which arose during the course of the parameteric studies are explained and illustrated.

Input Data Sets

The required input data to ESME can be seen in a set of files reproduced in Appendix C. This particular set describes the Booster running with 15 cavities and an intensity of 1.7e12 protons per pulse (ppp) before installation of the RF cavity dampers. Listed in the appendix are the main input file HOMBB.DAT, the broadband impedance file DMAGNET.DAT, and the high-Q resonance files RB*tt*H0.DAT and RB*tt*H1.DAT, where *tt* is the time in the cycle.

In the main file, the initial conditions are entered and the particle distribution is specified. The initial conditions, which include injection and extraction energy, transition gamma, ring dimensions, beam intensity, initial emittance, number of RF cavities, and RF voltage, are chosen to match a particular Booster experimental data set. All 84 RF buckets are populated to study the coupled-bunch instability, with between 500 and 1500 macroparticles per bunch, representing the specified total number of protons (intensity). The statistics in the azimuthal binning improve with the larger number of macroparticles, but it slows the calculation considerably. The RF voltage is specified at half- or one-msec intervals, with a linear interpolation assumed between values. For the nominal case of HOM dampers out, the RF voltage data are obtained from the earlier experimental data sets R08 and R06 for 15 and 17 cavities, respectively. In the case of HOM dampers in, the data are obtained for 16 cavities from a separate measurement recorded during the studies of set R36.

The magnet impedance, shown in Figure 6. , is fitted to a cubic polynomial over five frequency intervals using a standard minimization routine to obtain the required table. The results are given in the data file DMAGNET.DAT. In each of the five intervals, the data, line-by-line, are: starting frequency, and real and imaginary coefficients.

In the analytical calculations, we had used the net sum impedance derived from the single-gap stretched wire measurement directly, with no need for a functional model. Because the input for ESME requires that the HOMs be represented by a model resonance, the sum impedance for each mode of interest is fitted to a classical parallel LRC response (see Figure 3.11). Care was taken to match to the extent possible the area under the curves. The results for equivalent R and Q for the impedance measurements are tabulated in Appendix B, Tables B.7 and B.8. Sample fit results at one time in the cycle (t=21 msec) are shown in Figures 7.1 and 7.2. In the undamped case, for some higher-order modes, like f6, the representation is good, for others, like f2 or f4, only fair. The resonant impedance input files RBttH0.DAT and RBttH1.DAT are constructed on this basis.

There is some ambiguity in the determination of the equivalent Q. Physically, for the coupled-bunch instability, the Q determines the decay time between bunches

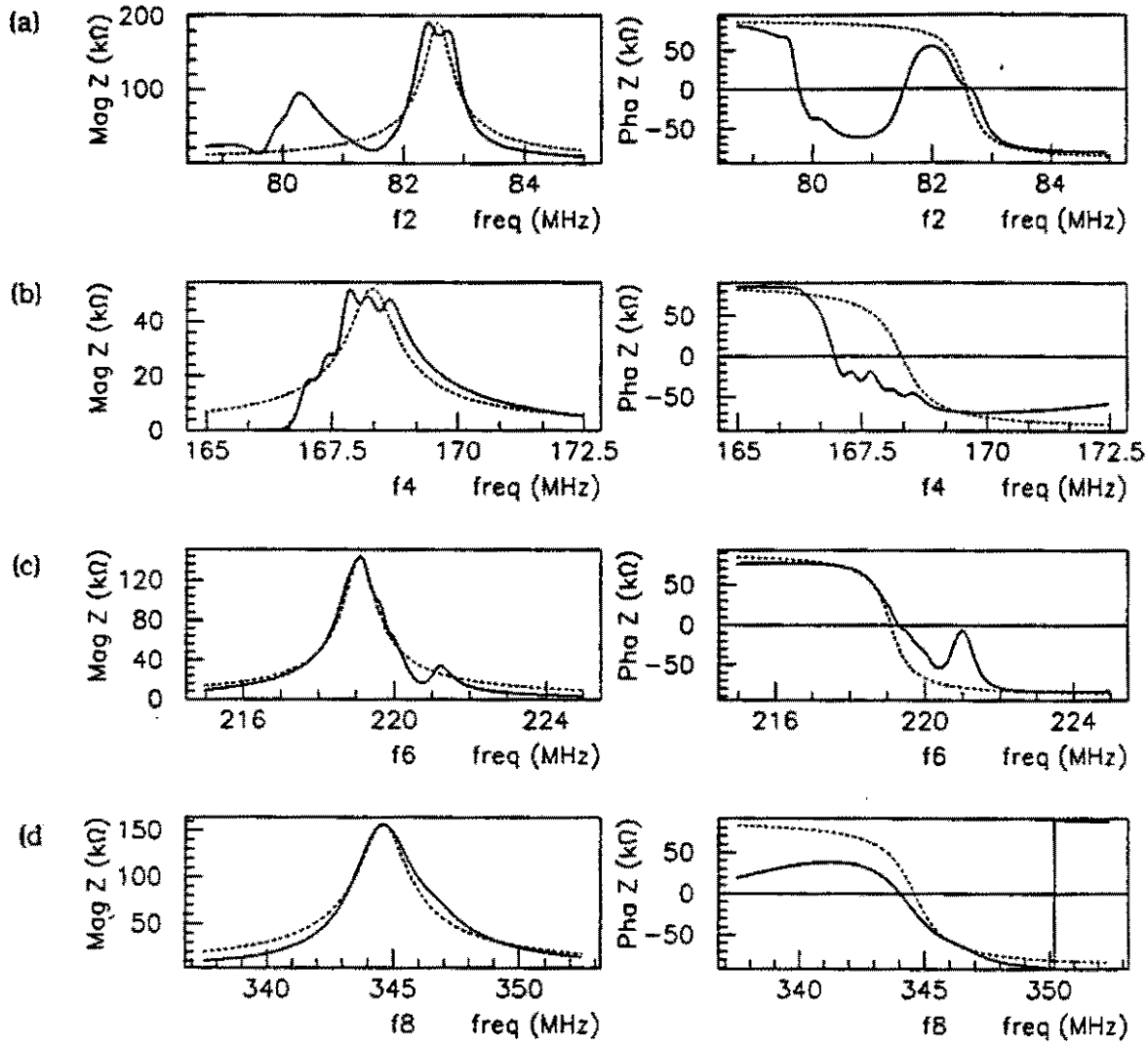

Figure 7.1 Model Parallel LRC Fit of Net RF Cavity HOM Impedance (Dampers Out).

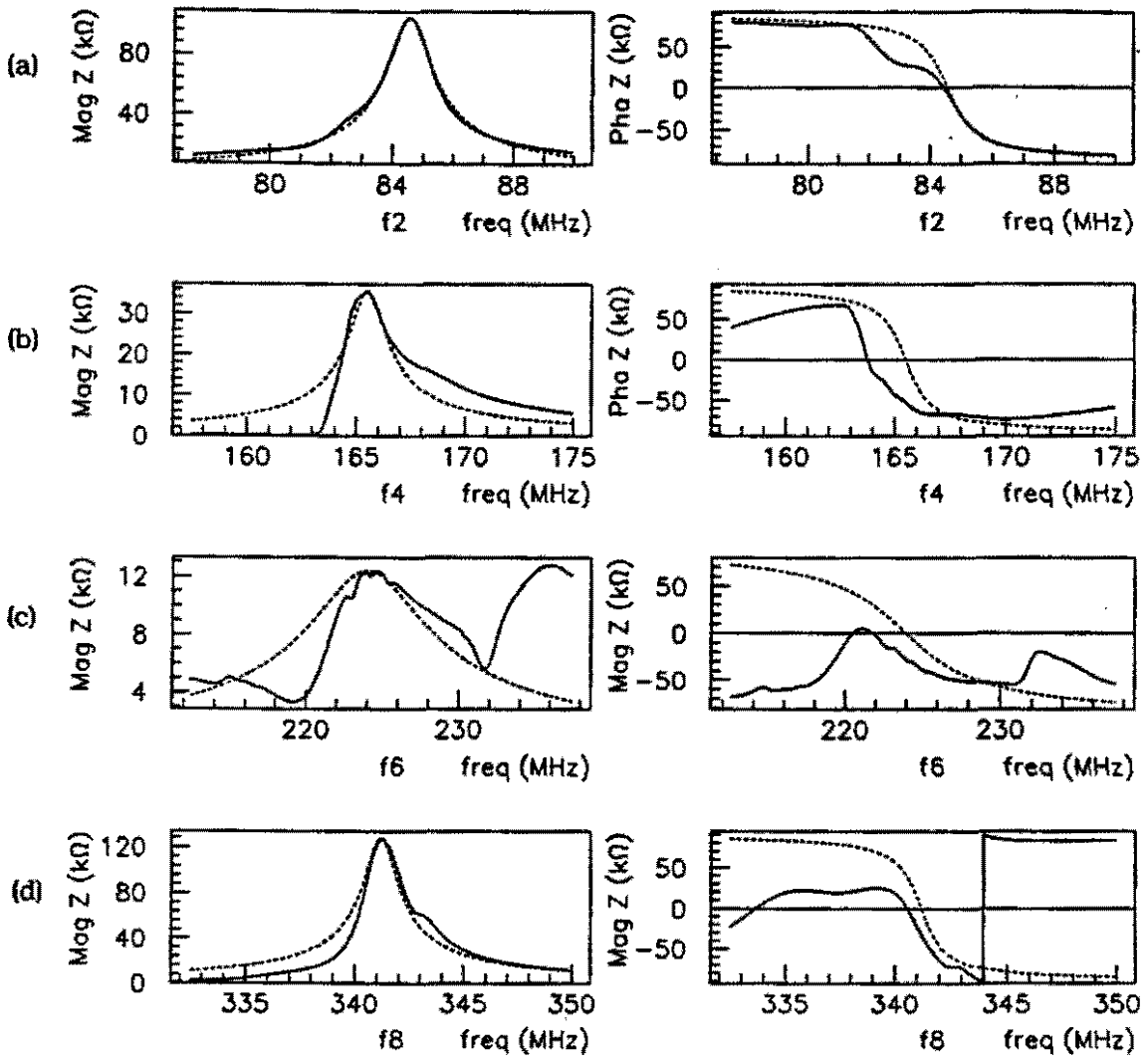

Figure 7.2 Model Parallel LRC Fit of Net RF Cavity HOM Impedance (Dampers In).

(a)

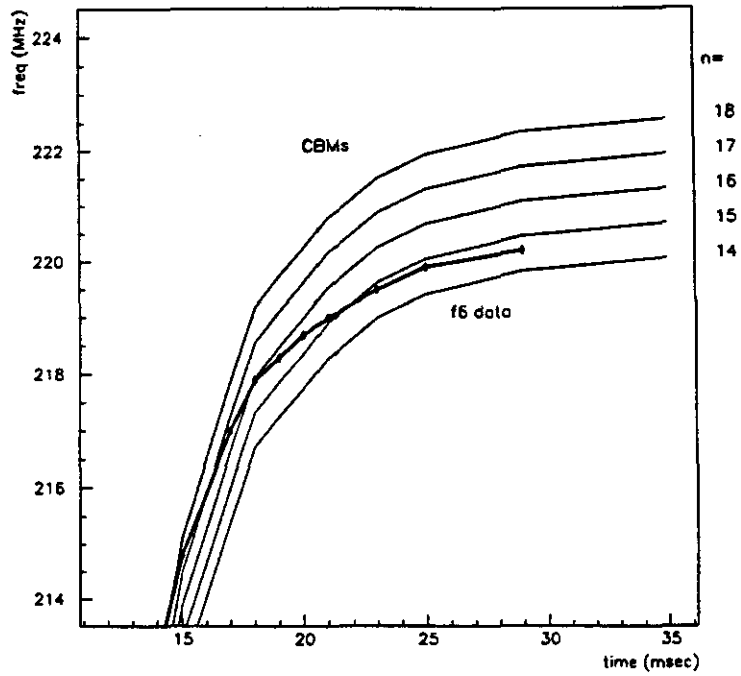

(b)

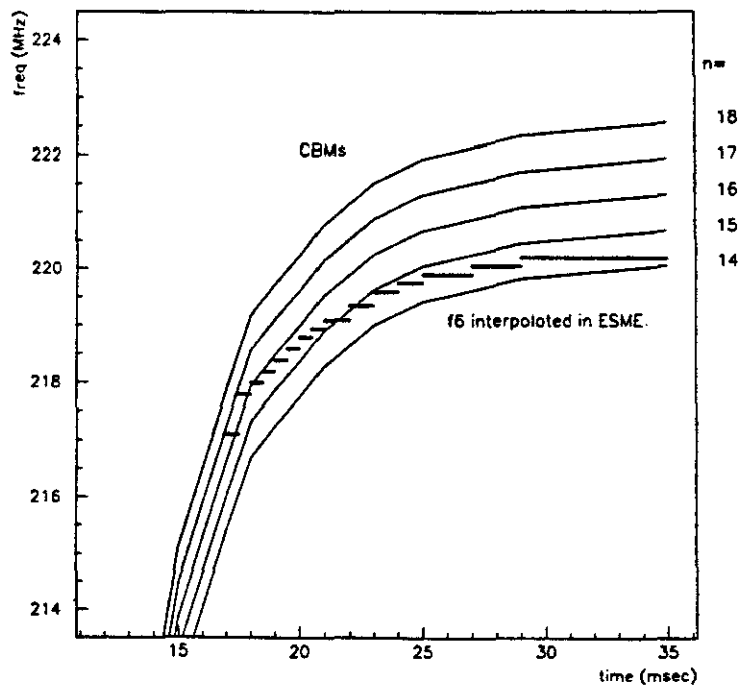

Figure 7.3 Effect of Tracking Step Size on Slewing Resonance in ESME. The RF cavity modes f2 and f4 tune with the fundamental frequency. As an example, (a) f6 is shown relative to the beam coupled-bunch modes n=14-18. To better represent the tuning RF cavity parasitic modes, (b) the frequency and impedance data are interpolated at 0.5- or 1-msec intervals and tracking interval adjusted accordingly.

for that particular parasitic mode in each cavity. For this reason, the Q of a single cavity might best describe the mode response. However, the Q also determines how many beam spectral lines are coupled to, and hence driven by, the parasitic mode. This is precisely what is represented by the effective broadening, or lowered Q, in the sum impedance when including the spread in HOM frequencies. The effect which dominates in the Booster determines which Q to specify in ESME. Using the example of cavity mode f6 (220 MHz) at 29 msec, HOM out (Table B.7), and using the time between bunches $\Delta t_b = 19$ nsec, we see that for a single cavity Z, Q=550, so the delay=0.98 and the width Δf=400 kHz. For the net sum Z, Q=260, so the delay=0.95 and Δf=850 kHz. Since the spacing of the beam spectral lines is the revolution frequency f_0=628 kHz, the lowered equivalent Q of the net sum Z means that two spectral lines may be excited simultaneously. As a test, we varied the Q in ESME keeping the magnitude constant. It was found that the beam becomes far more unstable for a lower Q as expected comparing with observation. The difference in decay time is insignificant; therefore, we choose the net sum equivalent Qs based on physical arguments.

Another important consideration in representing the HOMs in ESME is the fact that the frequencies of some of the modes sweep rapidly over a portion of the simulation time period. The data are read into the code at specified time intervals. The impedance data are recorded at t=17, 18, 19, 20, 21, 23, 25, 29 msec. Over the period between 17 and 25 msec, the step sizes are not fine enough. These data are therefore interpolated to obtain values at t=17.5, 18.5, 19.5, 20.5, 22, 24, 26, 27. The effect of the smaller step size is depicted in Figure 7.3, which shows the difference in smoothing out the sweeping impedance at f6.

Parametric Studies

Several parameters were varied to study the effect on beam stability: single-bunch vs. M-bunch simulation, the initial matched particle distribution, track starting time (in the cycle), RF voltage, one or multiple HOMs, space charge on/off, and broadband magnet impedance on/off. An alternate goal of these studies was to test-check the code.

To simplify the problem, it may seem reasonable to reduce the simulation to a single bunch, scaling the driving impedance by M and changing the harmonic number to h=1. However, the interbunch phase specified by the coupled-bunch mode cannot be accounted for by a single bunch, and hence the charge distribution which excites the parasitic mode is not realistic. Tests were made using one bunch, and the results indicate that the beam is wildly more unstable with this scaling analysis than as is observed. The particle distribution experiences a complicated fine-structure time development inconsistent with what the data indicate.

Two initial particle distributions were compared: the elliptic, with parabolic projections on the phase space axes, and the bi-gaussian. Analytically, proton beams are often described as elliptic, but a gaussian distribution adds the possibility of damping due to the presence of tails in the distribution. No significant difference is seen between these two distributions with respect to beam stability, whether tracked from just after or just before transition. One case tracked from injection resulted in a mostly elliptic beam near transition, so the elliptic was chosen.

A dramatic difference in the stability properties is seen if the beam is allowed to evolve through transition around t=19 msec. Initially, all simulations were begun at 20 msec in the cycle because we wanted to avoid the complications concerned with transition crossing. However, the time development of the unstable mode n=16 in the simulation did not correspond to the data. When tracking from 20 msec, it begins to grow only in the final few msec before extraction, while in reality, it is seen to begin around transition. For the case tracked from 17 msec in the cycle, the time development more closely follows the data. Note the tails which develop in the distribution in this case after transition, seen in Figure 7.5 in the fourth plot down (t=20 msec). This distribution has enhanced harmonic content as compared with a symmetric elliptic, and "seeds" the instability. Also, it is found that for approximately the same final coupled-bunch oscillation amplitude, the driving resonant impedance can be about a factor of two larger than the measurements when tracking only from t=20 msec. Because of these inconsistencies, the final simulations track the particles from 17 msec in the cycle.

The effect of the RF bucket area on beam stability was studied inadvertently. When the beam was driven by the resonant impedance of 15-cavity HOMs but

accelerated accidentally in a 17-cavity potential, the beam was more unstable than when the bucket was reduced to the correct 15-cavity area. In the two cases, the bucket fill ratio is similar in the last 10 msec in the cycle, but very different coming into and through transition. With 15 cavities, the bucket is about 90% full between t=17 and 24 msec. For 17 cavities, the ratio is closer to 50%. The synchrotron phase angle is also reduced, so the synchrotron frequency is more constant with small amplitude and thus, the beam is in a far more linear regime through this period. A comparison of the initial conditions is illustrated by comparing Figure 7.5 and Figure 7.8. In the former case, a bunch of initial area 0.028 eV-sec populates a bucket corresponding to a 15-cavity RF voltage. For the latter, the same beam populates a 16-cavity RF bucket. It is probable that some of the variation in emittance seen in the beam studies with varying the number of RF cavities has not only to do with the scaling in HOM impedance but the stability produced by the nonlinearity of the RF bucket as well.

A true advantage of simulation is that the effect of single resonant modes can be studied individually. In the present version of the code, there is no provision for the Fourier analysis of the bunch train, which would produce spectra such as shown in the beam studies. Instead, the influence of individual HOMs, known to drive one or two neighboring beam modes, is deduced by observing the time evolution of a bunch in phase space. Most likely, it would not have been possible to resolve the difficulties in reproducing the multiple-HOM Booster results had it not been for this simplifying step. Before installation of the RF cavity HOM dampers, two dominant beam modes are driven with different time structure. The simulation result indicates, as we will see later, that the final emittance growth in the beam cannot be easily predicted for excitations by multiple modes occuring at different times in the cycle.

Runs are compared with the nominal 1.7e12 proton intensity but with no resonant driving impedance to study separately the effect of the space charge force and the magnet broadband impedance. However, the space charge force calculation is suspect in the version 7.2 of the code, as stated earlier. With space charge and HOM impedance, bizarre particle losses of up to 40% are observed in the simulation on development of striation and filaments in the particle distribution soon after transition. This is a numerical artifact and not observed. No measurable differences are seen in the simulation results for any combination without HOM impedance (see Figure 7.10

(b)); therefore, we deduce that as far as ESME is concerned, the space charge effects are not important in the Booster study. For these reasons, we are justified in neglecting it. Although the Boussard criterion of eqn. (6.) would predict microwave instability around transition, the null result could be explained perhaps by the same dwell-time argument for the resonant mode response: the beam passes rapidly through the unstable condition. Because the magnet impedance causes no surprising effects, it is included in the final simulations for completeness.

Final Tracking Results

A summary of the final simulations are found in Table 7.1. The experimental data set R01 (15 cavities, 1.7e12 ppp) is chosen as the baseline for comparison before the HOM dampers were installed, and data set R36 (16 cavities, 1.9e12 ppp) for comparison after installation. The time development of each of the n=16 and n=48 coupled-bunch modes, the final mode amplitude, and the emittance growth are all compared with the data. The coupled-bunch mode amplitude and time development is estimated from the "mountain-range" graphical output. The program performs a calculation of the rms emittance, but in order to best compare the results with the observations, we measure the "bunch length" from the azimuth histogram in a way comparable to the digital oscilloscope (without averaging, however). Note that in the simulations with a 15-cavity RF bucket, about 10% of the particles are lost from the bucket during the first 10 msec (from t=17 to 27 msec in cycle), which is not generally seen in the Booster. This may be attributed to numerical noise$\approx\sqrt{800}$/bunch. Although fast losses are sometimes observed at transition and slow losses late in the cycle, the causes are most likely not related to the coupled-bunch instability.

In the first six runs listed in the table, the beam is driven by a single resonant impedance. The starting time of the tracking is varied, as is the scaling of the measured HOM impedance. The results for the cases tracked from 20 msec proved to be very stable, even when the impedance is increased by 40%. For the remaining cases, tracked from 17 msec, scaling the impedance by 40% compared somewhat better with the expected coupled-bunch mode growth than no scaling. The results are shown in mountain range plots in Figure 7.4. The vertical scale shows turn number; the corresponding time in the cycle is shown in Figure 7.7 (b). In Figure 7.4 (b), excitation

Table 7.1 Final ESME Simulations.

name	comparative data run *	VRF (# cav)	intensity (ppp)	HOM in/out	high-Q modes **	Z scaling ***	time start (msec)
homaa	-	15	1.7e12	out	f2	1	17
hom96	-	15	1.7e12	out	f2	1.40	17
hom94	-	15	1.7e12	out	f2	1.40	20
hom99	-	15	1.7e12	out	f6	1	17
hom97	-	15	1.7e12	out	f6	1.40	17
hom95	-	15	1.7e12	out	f6	1.40	20
hombb	R01	15	1.7e12	out	f2,f4,f6,f8	1	17
homcc	R01	15	1.7e12	out	f2,f4,f6,f8	1.25	17
homgg	R36	16	1.9e12	in	f2,f4,f8	1	17
homhh	R36	16	1.9e12	in	f2,f4,f8	1.25	17
homff	(400 MeV)	15	3.4e12	in	f2,f4,f8	1.25	17
homii	(400 MeV)	16	3.0e12	in	f2,f4,f8	1	17

* Experimental data runs are defined in Chapter 5, Table 5.1

** Mode designations are defined in Table 4.1

*** Scaling of net sum impedance from Tables B.7 and B.8

by f6 only (220 MHz, n=16) shows a blowup soon after transition and saturation until the final msec. In (a), excitation by f2 only (83 MHz, n=48) is fairly stable, even when scaled by 40%.

In the full simulation (homcc), both HOM impedances f2 and f6 from above, in addition to f4 (169 MHz, n=18) and f8 (345 MHz, n=46) are added, scaled now only to 25%. Now, the mountain range time development compares with observation (Figure 7.4 (c)). Although unfortunately, no mountain range plots were recorded in this data run (R01), we may refer to the coupled-bunch amplitude growth shown in Chapter 5 and comparable mountain range data (not shown). An initial instability (n=16) grows rapidly and saturates without an obvious large dipole coherent ocillation soon after

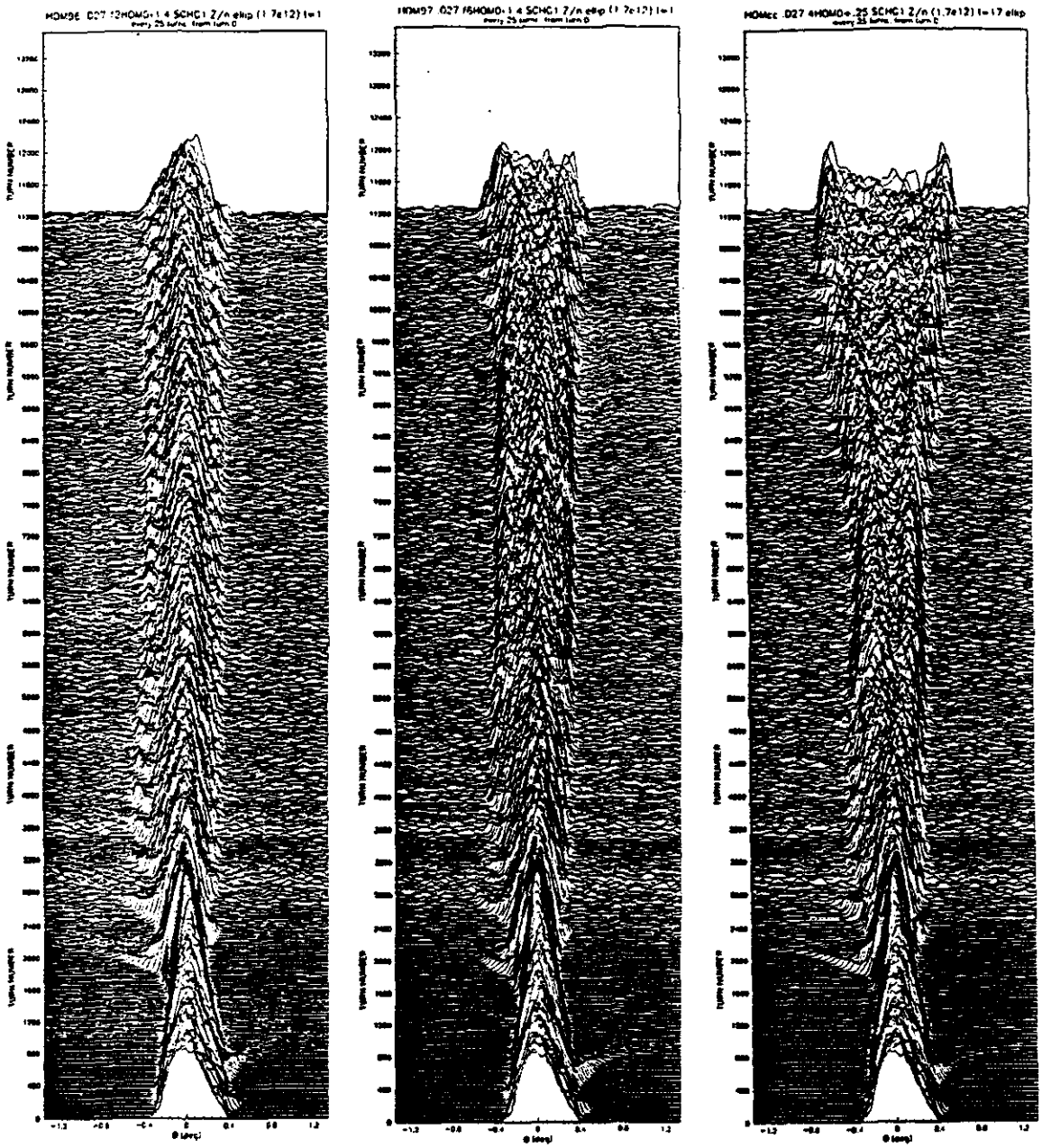

(a) (b) (c)

Figure 7.4 Mountain Range Plots in Simulation, HOM Dampers Out. Shown are the results for (a) f2 RF cavity mode only, (b) f6 only, and (c) all 4 HOMs (f2,f4,f6,f8). In all cases, the impedance has been multiplied by 1.4. The case in (c) corresponds to the simulation of R01. (hom96, hom97, homcc)

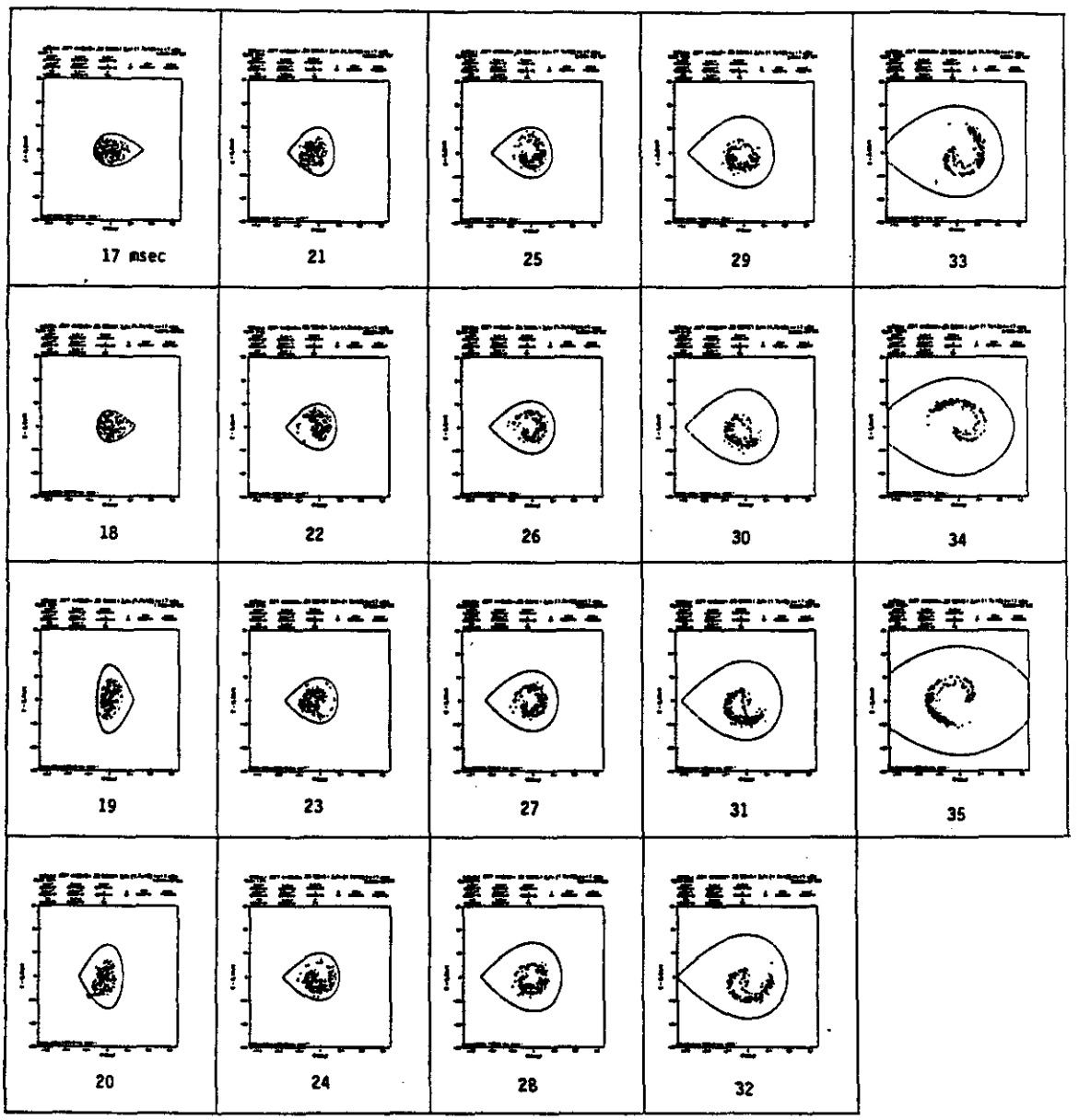

Figure 7.5 ESME Phase Space Plots: HOM Dampers Out. The time starts in the upper left corner at 17 msec in the global cycle and progresses vertically down. The axis scales extrema are $\Delta E = (E - E_s) = \pm 30$ MeV and azimuth $\Theta = \pm 1.3$ deg. This case (15 cavities, 1.7e12 ppp) is used to simulate R01. (homcc)

(a)

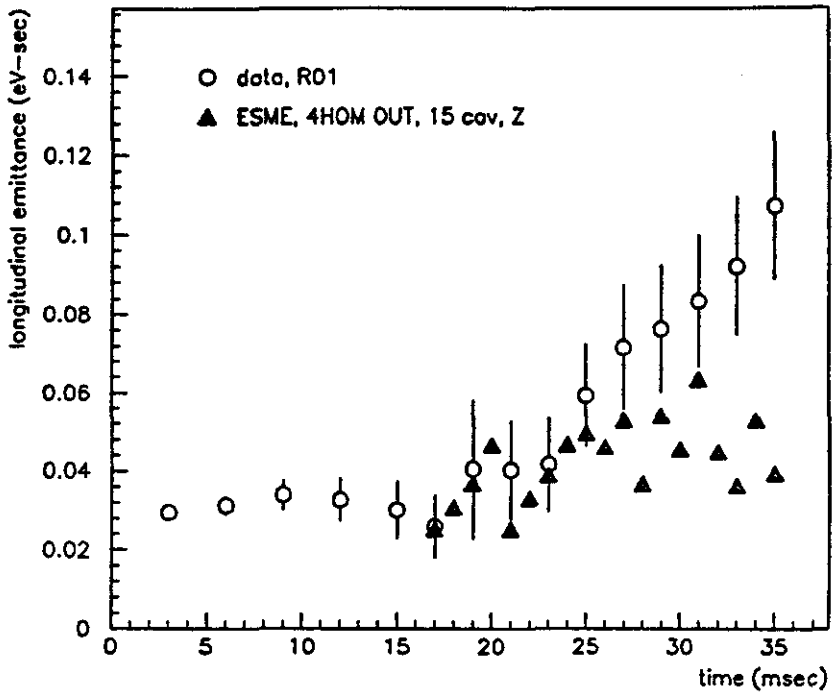

(b)

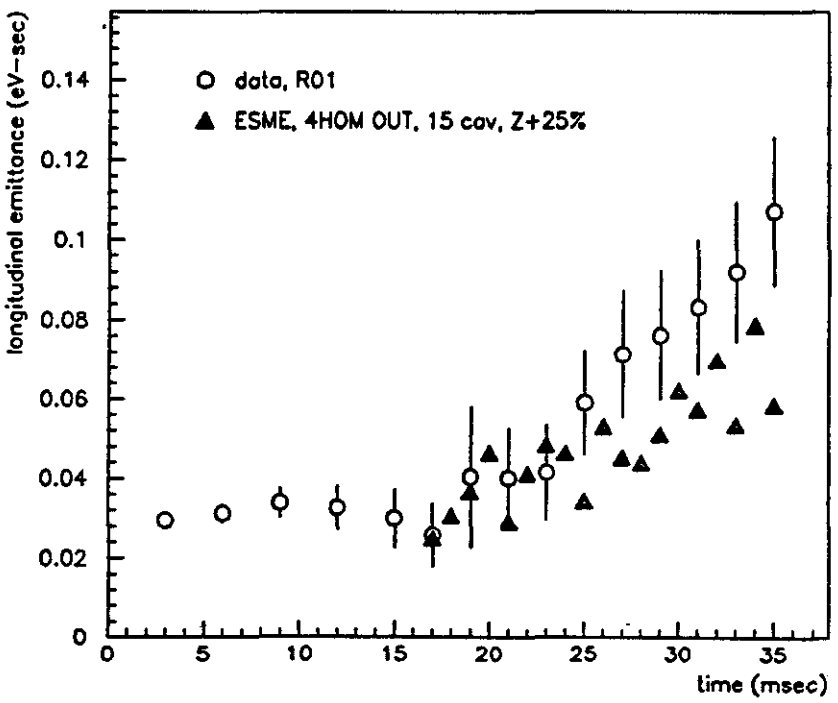

Figure 7.6 Emittance Growth in Simulation Compared with Data, HOM Dampers Out. The ESME simulation results are for 4 HOMs (f2,f4,f6,f8) for (a) 15 cavity net impedance and (b) 15 cavity net impedance multiplied by 1.25. The increased impedance better matches the data. (R01)

transition, and a new dipole oscillation (n=48) begins to grow around 29 msec. Clearly, the influence of the n=16 coupled-bunch mode earlier in the cycle cannot be neglected in the development of the n=48 mode.

The details of the time development in phase space may be seen in Figure 7.5. The phase space plots are at one-msec intervals, starting at 17 msec. One can clearly see the decoherence of n=16 by 27 msec, and a more coherent mode growing afterwards. Note that the particle distribution becomes quite distorted at the end. The projected charge density is double-peaked, sometimes but not necessarily always observed in the beam with these conditions (see example in Figure 1.1). Also, such fine structure in the bunch profile would be smoothed in our averaging process. However, such distortion is plausible, with the effect that the calculation of the emittance overestimates the true beam area. Recall that the emittance calculation using eqn. (3.1.33) assumes a matched beam in the RF bucket. If such a beam is extracted, it will decohere and fill the area bounded by the largest amplitude particles. One simply needs to take care when discussing or interpreting the data.

The emittance for the ESME results for HOM dampers out is plotted in Figure 7.6 compared with data run R01. Again, scaling the impedance by 25% compares more closely with the data. The estimated coupled-bunch mode amplitudes in ESME (from Figure 7.4 (c)) are comparable to R01, but the emittance in somewhat smaller. Also, the bunch length in ESME is seen to oscillate, hence the oscillation in the emittance, which is not observed in reality. One possible explanation is the fact that we cannot average over pulse-to-pulse variations in ESME unless perhaps the initial conditions are varied. Another possibility is that RF phase noise tends to "smear" the fine structure as the beam instability develops, leading to greater spreading.

In the case of HOM dampers in, the ESME result without scaling compares best with the data in R36. Figure 7.7 shows the mountain range plots for the data compared with the simulation. The final coupled-bunch mode amplitude compares well. The phase space plots in Figure 7.8 show a single mode. The emittance is plotted in Figure 7.9. Although three resonances are driving the beam in the simulation, only f2 (84 MHz, n=50) corresponds to a mode observed in the beam spectrum (see Chapter 5). The other cavity modes are include for completeness in the event that they become

important with, for example, higher intensity. The simulation indicates essentially a single mode developing in the beam.

As a final study, the parameters of the main ESME input data files are scaled to the goals of the Linac upgrade; namely, increase the injection energy to 400 MeV and increase the intensity by about a factor of two. Two cases are compared, 16 cavities and no scaling of the impedance and 15 cavities with scaling. The result for 16 cavities, with intensity scaled 40% to 3.0e12 ppp, is shown as a mountain range plot in Figure 7.10 (a) and phase space plots in Figure 7.11. The results indicate a very unstable beam with emittance growth, shown in Figure 7.12, comparable to the pre-HOM dampers levels.

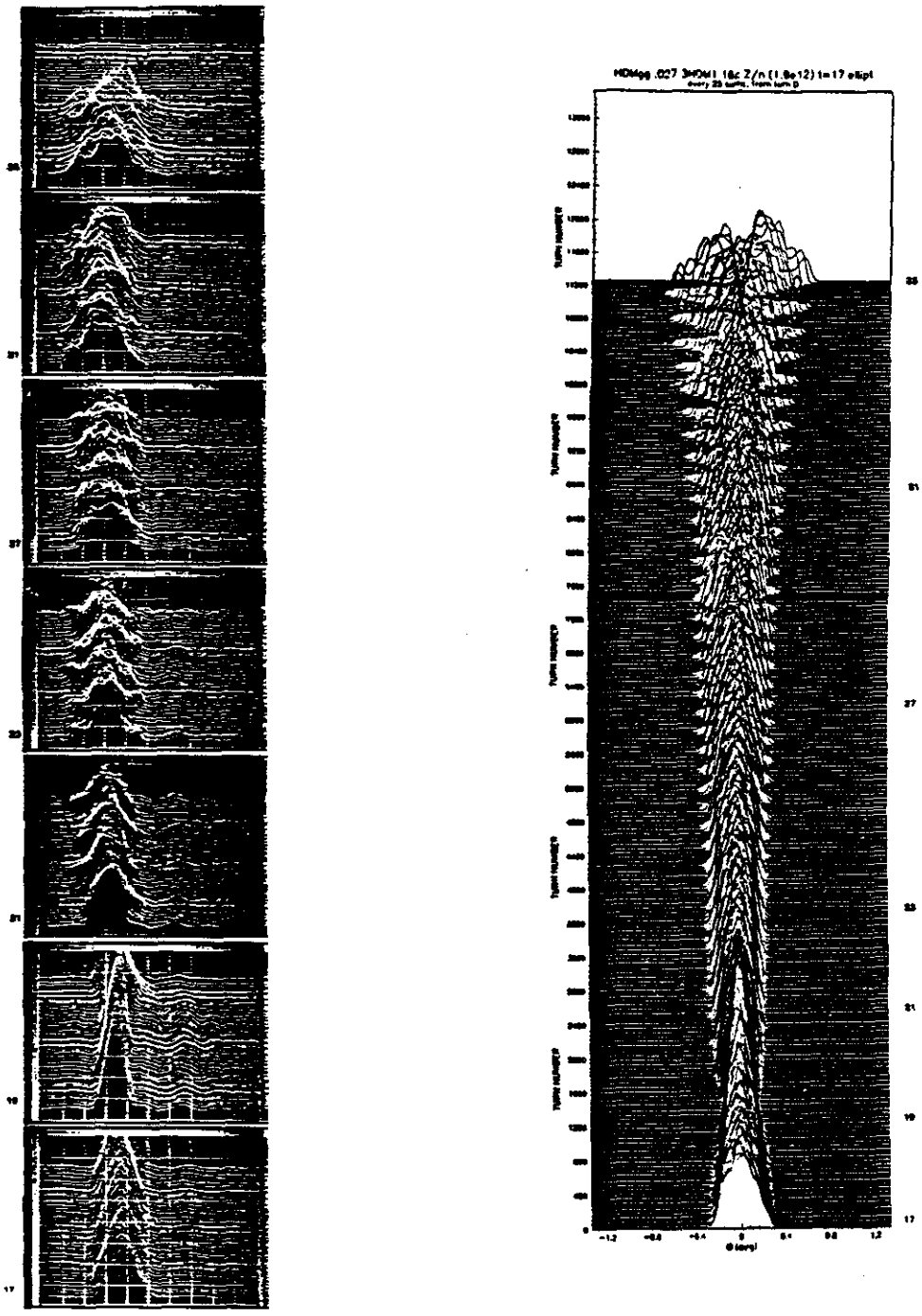

(a) (b)

Figure 7.7 Mountain Range Plots in Simulation Compared with Data, HOM Dampers In. The case of study is data run R36, in which the beam intensity is 1.9e12 ppp, HOM dampers in, 16 cavities. The data (a) mountain range sequence is partial, one msec per plot, one nsec per division, at times in cycle shown. The (b) ESME simulation results are for 3 HOMs (f2,f6,f8) for 16 cavity net impedance. The time development and final coupled-bunch mode amplitude in the simulation matches the data. (homgg)

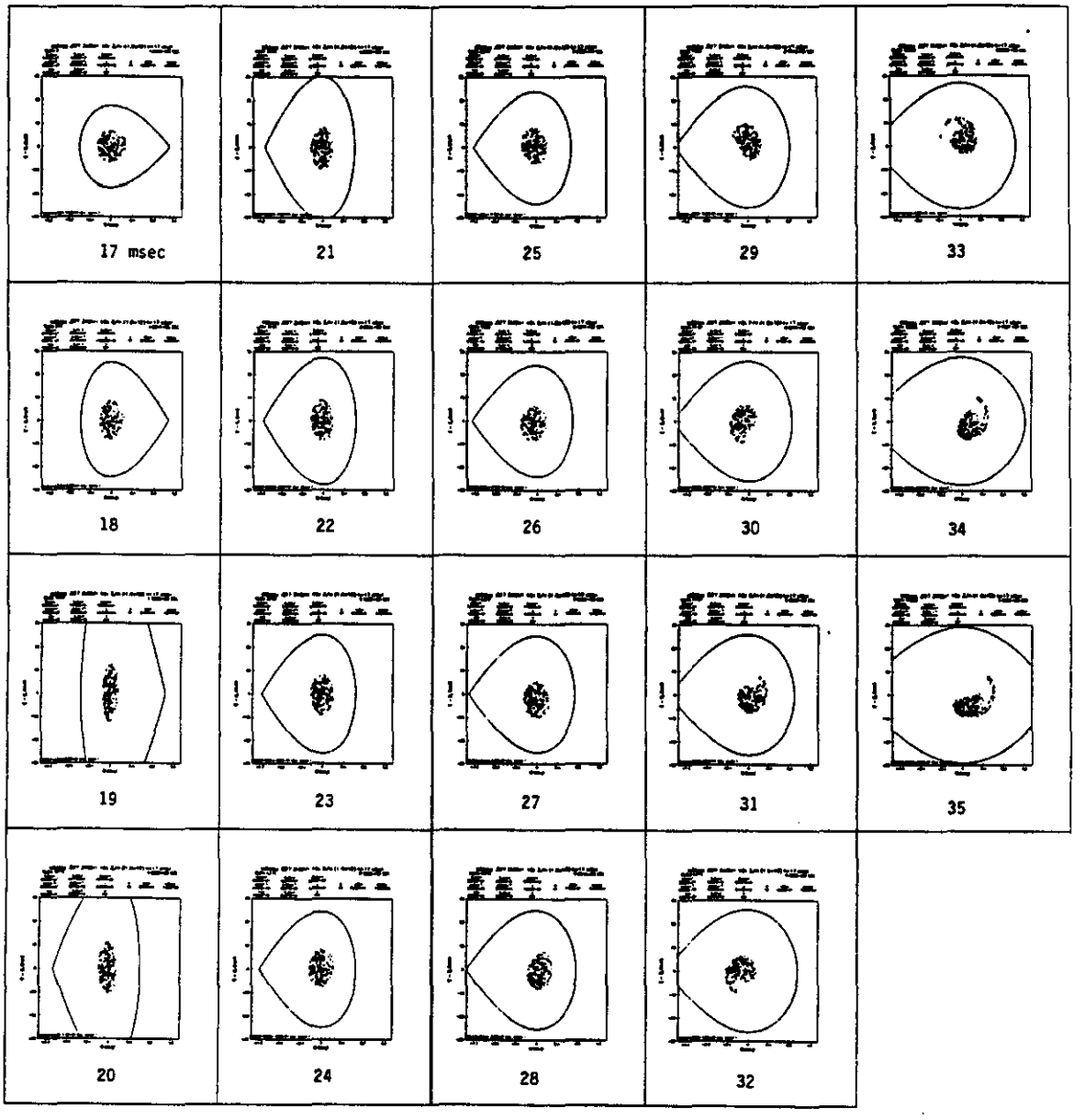

Figure 7.8 ESME Phase Space Plots: HOM Dampers In. The time starts in the upper left corner at 17 msec in the global cycle and progresses vertically down. The axis scales extrema are $\Delta E = (E - E_s) = \pm 30$ MeV and azimuth $\Theta = \pm 1.3$ deg. This case (16 cavities, 1.9e12 ppp) is used to simulate R36. (homgg)

(a)

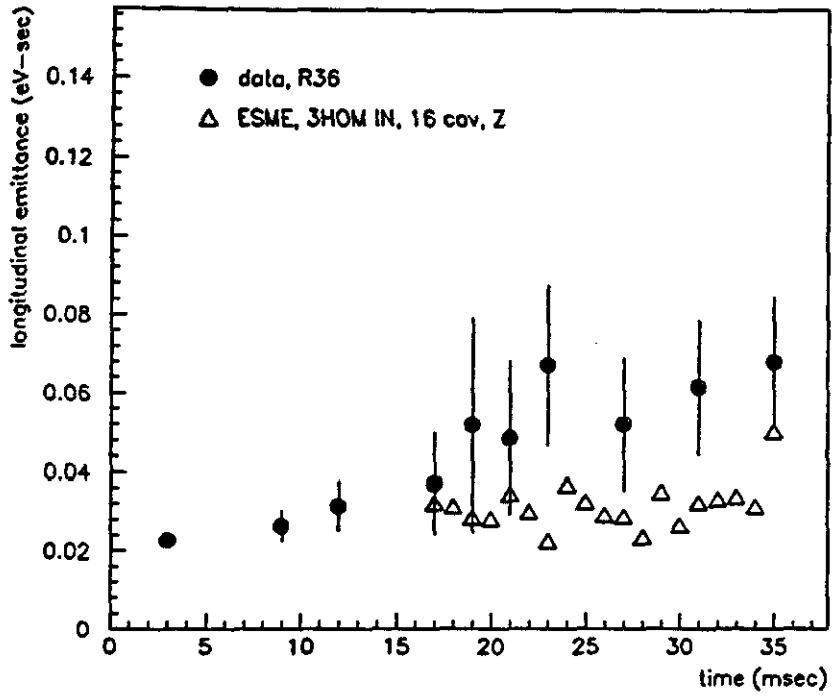

(b)

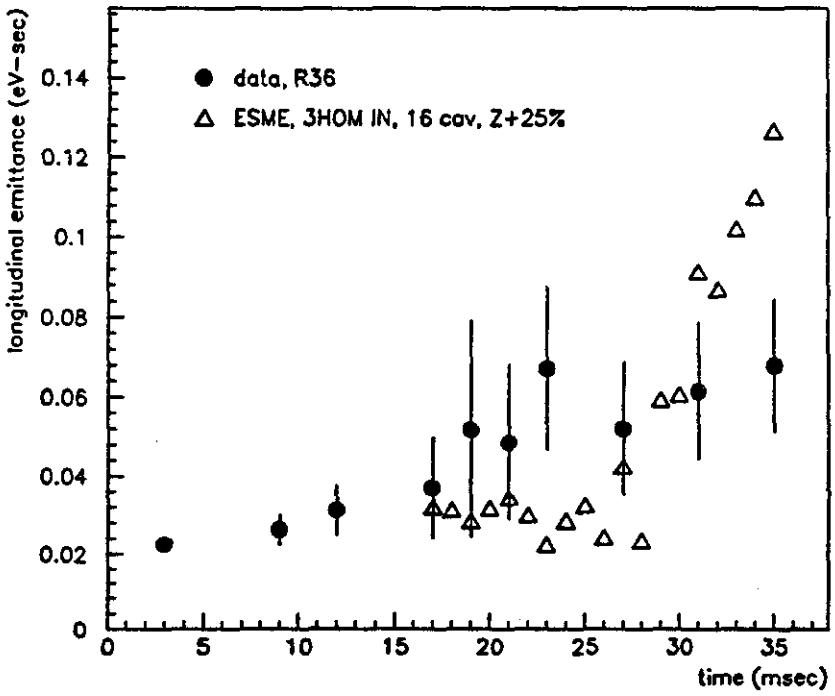

Figure 7.9 Emittance Growth in Simulation Compared with Data, HOM Dampers In. The ESME simulation results are for 3 HOMs (f2,f6,f8) for (a) 16 cavity net impedance and (b) 16 cavity net impedance multiplied by 1.25. Now, the original impedance matches the data. (R36)

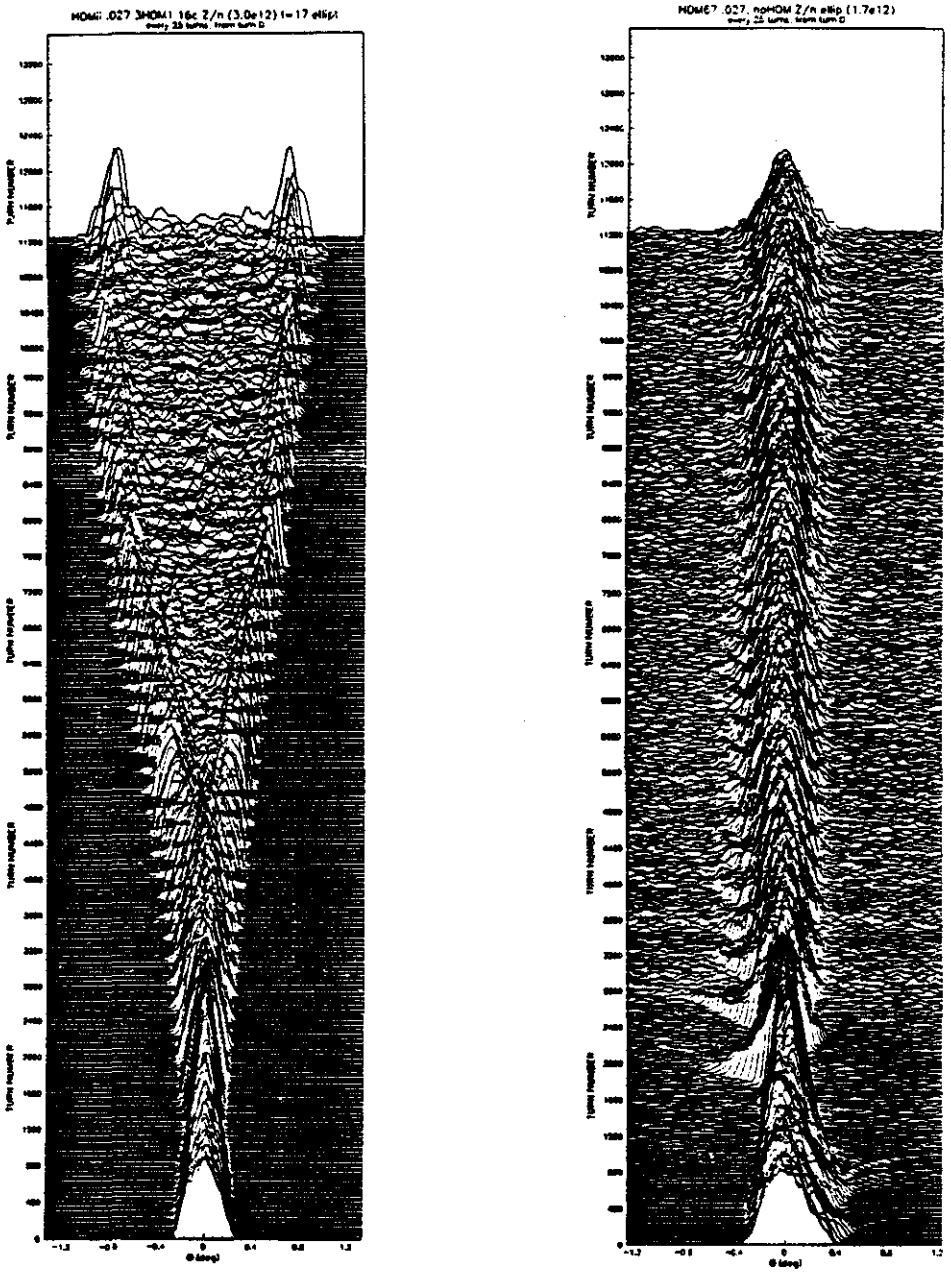

(a) (b)

Figure 7.10 Mountain Range Plots in Simulation for Both 400 MeV Upgrade and no HOM Impedance. In (a), the beam intensity is 3.0e12 ppp with 16 cavities, HOM dampers in. (homii) As a baseline, (b) shows the result for 15 cavity RF voltage including the magnet broadband impedance and space charge but no RF cavity HOM impedance.

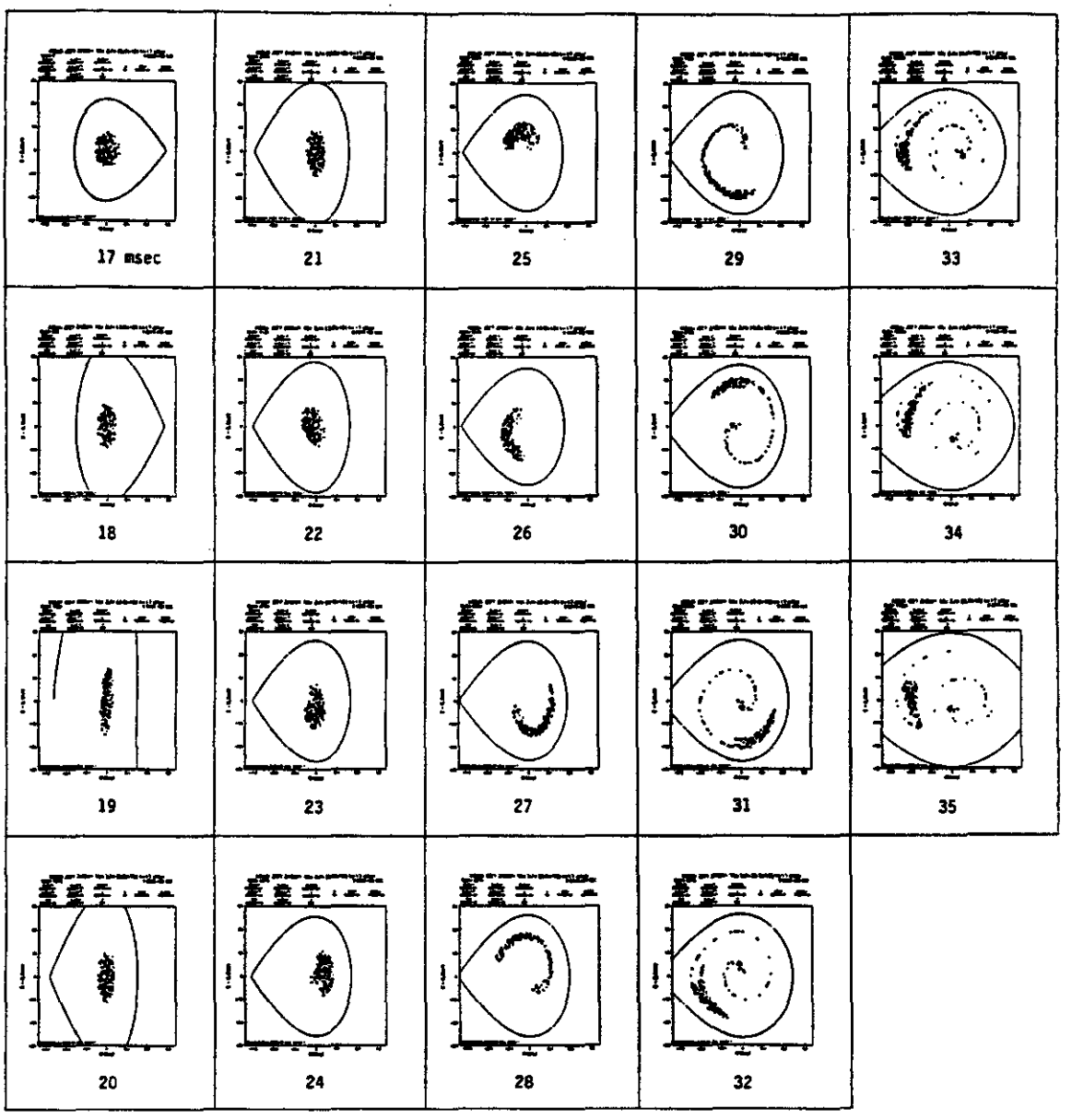

Figure 7.11 ESME Phase Space Plots: HOM Dampers In, 400 MeV Upgrade. The time starts in the upper left corner at 17 msec in the global cycle and progresses vertically down. The axis scales extrema are $\Delta E = (E - E_s) = \pm 30$ MeV and azimuth $\Theta = \pm 1.3$ deg. This case predicts the beam conditions after the Linac upgrade, simulating the nominal 16 cavities and 40% increased intensity: 3.0e12 ppp. (homii)

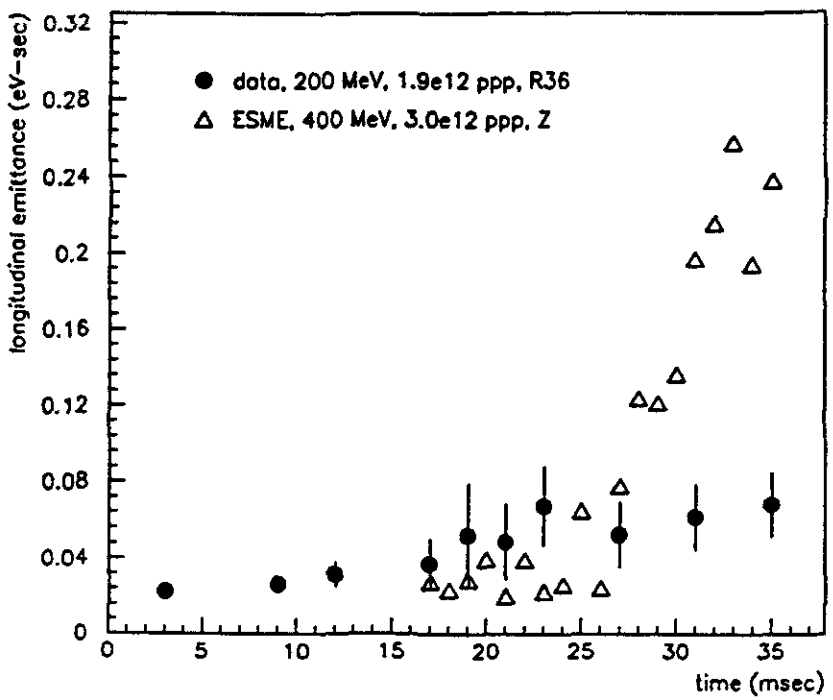

Figure 7.12 Emittance Growth Predicted by Simulation for 400-MeV Linac Upgrade. The ESME simulation results correspond to a beam intensity of 3.0e12 ppp, HOM dampers in, 3 HOMs (f2,f6,f8) for16 cavity net impedance . For comparison, the data for R36 (1.9e12 ppp) is superimposed.

8. CONCLUSIONS

In this thesis, we studied the long-observed longitudinal coupled-bunch instability in the Fermilab Booster, a rapidly-cycling proton synchrotron. Following careful measurements and analysis, several RF cavity parasitic higher-order modes were found to drive the unstable modes. Installation of passive RF cavity HOM dampers proved to strongly suppress the instability. The well-known longitudinal coupled-bunch mode theory was reviewed and evaluated including finite bunch length effects and Landau damping for the parameters of the Booster. Predictions of mode growth rates were found to be in general good agreement with experimental observations, both temporally and in frequency space. With the inclusion of Landau damping, the stability analysis is in overall agreement with the observed unstable mode spectrum. Particle simulation using the ESME code were carried out to describe observations of large amplitude oscillations and saturation effects leading to emittance growth in the latter part of the acceleration cycle. These efforts represent the most comprehensive study to date of this instability in the Booster.

8.1 Conclusions

In hindsight, the identification of the offensive RF cavity parasitic higher-order modes appears to be straightforward. The data presented actually follow a long series of studies in which we systematically overcame the difficulties and limitations of such measurements in a rapidly-cycling machine such as the Booster. In the final analysis, a multiple-step approach combining experiment and theory was required to study the problem from all angles: the beam, the RF cavities, and analysis. Even after installation of RF cavity mode dampers suppressed the long-observed longitudinal coupled-bunch instability, questions remained as to whether the behavior scaled as predicted by the theory. Also, the details of the longitudinal emittance growth were unclear.

First, we compared observations in the Booster data with the predictions of the linear coupled-bunch mode theory. While there is strong evidence that nonlinear

effects are important, we wished to study the unstable mode growth data quantitatively at least to determine the regime for which the linear theory is valid. A rigorous test of and modification of some of the assumptions used in the literature is required for proper application to the Booster. Solutions were found numerically using standard algorithms. It was found that including self-consistently the effects of the beam momentum spread in the nonlinear RF potential (Landau damping) is essential to accurately describe the unstable beam behavior.

The linear theory is completely inadequate in explaining the emittance growth resulting from the instability. Instead, a fully nonlinear simulation was invoked using the longitudinal particle tracking code ESME developed at Fermilab to study the response of the beam in the presence of a high-Q driving impedance. Subsequent analyses of the results indicate that the emittance growth may be explained by the filamentation of the bunch in the nonlinear RF potential. There is a complex interaction between the two unstable modes (before HOM damping) which is not obvious when studying the effect of each driving coupling impedance individually. The coupled-bunch instability cannot be studied adequately by simulating only a single bunch; although the impedance may be scaled, the interbunch phase cannot be properly modeled in a code such as ESME. While some details may not correspond exactly to observations of the beam, the general characteristics of the results compare well with the data and thus, we have some confidence in exploring the parameter space. For example, parameters such as the RF voltage have not been optimized for the simulation of the 400 MeV upgrade; however, the simulation results predict that for increased intensities, the coupled-bunch instability continues to present the problem of emittance growth. The simulation has led to a deepened understanding of the subtleties and sensitivities of the instability on various parameters.

The main lesson learned from these efforts is that while analytical means can be used to predict general instability characteristics for an accelerator, at best it can be used as a tool to determine possible worst-case scenarios. Limits on the maximum allowable coupling impedance given by these worst-case instability thresholds may prove to be over-restrictive. The damping mechanism provided by the momentum spread in the beam can significantly alter the threshold. While the importance of this effect can perhaps be predicted qualitatively, the exact time development of the instability behavior, including emittance growth, most probably cannot be

predetermined without experiment or further study. The quantitative analysis of the data was an iterative process, and supporting data from the beam and bench measurements were essential in the success of the effort to suppress this particular instability for this machine.

8.2 Recommendations

An analytical model of the emittance growth, which is valid for growth rates slow with respect to mode frequencies, should be explored. In this model, the stationary distribution in the Vlasov equation is allowed to evolve in time. This corresponds to an emittance growth which may be described as a radial diffusion. This can be expected to be valid in the case that the decoherence time is of the order of the instability growth rate. The simulation results suggest that under certain conditions, this quasilinear theory may be applicable. A natural extension may be made to use the measured particle distribution rather than a gaussian in the numerical analysis.

Further studies would be fruitful with a tracking code such as ESME. It would be useful to modify the code to produce spectral output such as the FFTs measured for the beam. Given a set of data files which compare well with observations, a more extensive study of the sensitivity and scaling of parameters such as intensity and impedance could be performed. A comparison of the scaling between the present case after HOM dampers installed, with one coupled-bunch mode, could be made to that previously, with two modes.

Finally, the details of the space charge and microwave instabilities should be studied in a self-consistent matter in a way similar to the procedure for the coupled-bunch instability. The properties and conditions of thresholds need to be better understood in the dynamic case of slewing frequencies in a rapidly-cycling synchrotron such as the Booster. The specific influence of crossing transition energy as it relates to altering the particle distribution should be explored to better characterize the effect on the coupled-bunch instability. It should be studied as to whether the higher charge densities and peak current or the whether the presence of higher-order synchrotron mode components is the dominant effect.

LIST OF REFERENCES

LIST OF REFERENCES

1. Accelerator Division, "The Fermilab Upgrade – An Overview," FNAL internal report, Jan 1989.

2. G. Guignard, "Selection of Formulae Concerning Proton Storage Rings," CERN report, ISR/77-10, 1977.

3. S. Peggs and M. Harvey, ed, Proc. of Fermilab III Instabilities Workshop, FNAL, Jun 1990.

4. F. Sacherer, "Methods for Computing Bunched-Beam Instabilities," CERN report, /SI-BR/72-5, 1972.

5. Booster staff and E. L. Hubbard, ed, "Booster Synchrotron," FNAL report TM 405, 1973.

6. J. Crawford, "Booster Rookie Book," FNAL internal report, Nov 1980.

7. M. Conte and W. W. MacKay, An Introduction to the Physics of Particle Accelerators, World Scientific, 1991.

8. D. A. Edwards and M. J. Syphers, An Introduction to the Physics of Particle Accelerators, John Wiley & Sons, Inc, 1993.

9. R. Baartman and S. Koscielniak, "Introduction to RF Systems in Accelerators," course notes, US Particle Accelerator School, Florida State University, Jan 1993.

10. W. Merz, "Main Ring & Booster RF," FNAL internal report, Sep 1980.

11. H. Bruck, *Accélérateurs Circulaires de Particules*, Presses Universitaires de France, Paris, 1966, p 159f.

12. E. J. N. Wilson, "Proton Synchrotron Accelerator Theory," CERN report, 77-07, Mar 1977.11.

13. S. Ohnuma, "The Beam and the Bucket," FNAL report, TM-1381, Jan 1986.

14. C. Bovet, R. Gouiran, I. Gumowshi, and K. H. Reich, "A Selection of Formulae and Data Useful for the Design of A. G. Synchrotrons," CERN report, /MPS-SI/Int. DL/70/4, Apr 1970.

15. R. H. Siemann, "Bunched Beam Diagnostics," US Particle Accelerator School, Cornell University, AIP Proc. 184, 1988.

16. B. Zotter, "Longitudinal Stability of Bunched Beams, Part II: Synchrotron Frequency Spread," CERN report, SPS/81-19 (DI), 1981.

17. J. L. Laclare, "Bunched Beam Coherent Instabilities," Proc. CERN Accelerator School, Sep 1985, CERN 87-03, 1987.

18. G. Arfken, Mathematical Methods for Physicists, Academic Press, Inc, 1970, p 670.

19. J. A. MacLachlan, "Fundamentals of Particle Tracking for the Longitudinal Projection of Beam Phasespace in Synchrotrons," FNAL report, FN-481, Apr 1988.

20. G. Hok, "Response of a Linear Resonant System to Excitation of a Frequency Varying Linearly with Time", Journal of Applied Physics, 19, Mar 1948, p 242.

21. F. Reif, Fundamentals of Statistical and Thermal Physics, McGraw-Hill Book Company, 1965.

22. C. Pellegrini, "Single Beam Coherent Instabilities in Circular Accelerators and Storage Rings," 1981 Summer School on High Energy Particle Accelerators, AIP Proc. 87, 1982.

23. J. M. Wang, "Longitudinal Symmetric Coupled Bunch Modes," BNL report, BNL 51302, Dec 1980.

24. S. Krinsky and J. M. Wang, "Longitudinal Instabilities of Bunched Beams Subject to a Non-Harmonic RF Potential," Journal Particle Accelerators, 17, 1985.

25. F. Caspers, "Bench Methods for Beam Coupling Impedance Measurements," CERN report, PS/91-36 (AR), Jun 1991.

26. G. P. Jackson, "Review of Impedance Measurements at Fermilab," Proc. of Fermilab III Workshop on Instabilities, Batavia, FNAL, Jun 1990.

27. F. Caspers, "Beam Impedance Measurements Using the Coaxial Wire Method," CERN report, PS/88-59 (AR/OP), Oct 1988.

28. R. E. Collin, Field Theory of Guided Waves, 2nd ed, IEEE Press, 1991, pp 191-2.

29. "S-Parameter Design," Hewlett Packard Application Note 154.

30. P. L. Colestock, P. J. Chou, B. Fellenz, M. Foley, F. Harfoush, K. Harkay, G. Jackson, Q. Kerns, D. McConnell, and K. Y. Ng, "A Critical Survey of Stretched-Wire Impedance Measurements at Fermilab," Proc. of 14th IEEE Particle Accelerator Conference, San Francisco, May 1991.

31. Booster drawing # 0334.02-ME-5373

32. L. C. Maier, Jr. and J. C. Slater, "Field Strength Measurements in Resonant Cavities," Journal of Applied Physics, 23,1, Jan 1952.

33. L. B. Mullett, "Perturbations of a Resonator," Atomic Energy Research Establishment, G/R.853, Feb 1952.

34. L. C. Maier, Jr., "Field Strength Measurements in Resonant Cavities," MIT Research Laboratory of Electronics, Technical Report No. 143, Nov 1949.

35. Vector Fields, Inc, CA.

36. D. Wildman, FNAL, private communication.

37. H. H. Umstatter, "On the Measurement and Interpretation of Coupling Impedance Data in the Frequency and Time Domain, Proc. of 6th IEEE Particle Accelerator Conference, Washington, DC, Jun 1975.

38. S. C. Snowdon, "Wave Propagation Between Booster Laminations Induced by Longitudinal Motion of Beam," FNAL report TM-277, Nov 1970.

39. R. Gluckstern, "Coupling Impedance and Energy Loss with Magnet Laminations," FNAL report TM-1374, Nov 1985.

40. A. G. Ruggiero, "Energy Loss due to the Resistive Magnet Laminations in the NAL Booster," FNAL report FN-230, May 1971.

41. R. E. Shafer, "Coupling Impedance of Laminated Magnets in the Booster," FNAL report TM-1408, Jul 1986.

42. B. Zotter, "Longitudinal Stability of Bunched Beams, Part III: Mode Coupling and the Microwave Instability," CERN report, SPS/81-20 (DI), 1981.

43. J. Crisp, FNAL, private communication.

44. M. Month and R. Peierls, "Coupling Impedance Structure Above the Cutoff Frequency," Nucl. Inst. Meth. 137 (1976), p 299.

45. C. D. Moore, et al, "Single Bunch Intensity Monitoring System Using an Improved Wall Current Monitor," Proc. of 13th IEEE Particle Accelerator Conference, Chicago, Mar 1989.

46. J. Borer and R. Jung, "Diagnostics," Proc. CERN Accelerator School on Antiprotons for Colliding Beam Facilities, Oct 1984, CERN report, /LEP-BI/84-14, Oct 1984.

47. R. Webber, "Longitudinal Emittance, An Introduction to the Concept and Survey of Measurements Techniques Including Design of a Wall Current Monitor," FNAL report, TM-1655, 1990. (Also published in the Proc. of Workshop on Accelerator Instrumentation, Upton, NY, Oct 1989.)

48. Various published papers, such as:

C. M. Ankenbrandt, J. E. Griffin, R. P. Johnson, J. Lackey, K. Meisner, "Longitudinal Motion of the Beam in the Fermilab Booster," IEEE Trans. Nuclear Science, NS-24, vol. 3, Jun 1977.

K.-Y. Ng, "Longitudinal Coupled-Bunch Instability in the Fermilab Booster," FNAL report, FN-464, Sep 1987.

M. Cornacchia, "Observations and Computations of Higher Energy Collective Effects in the Fermilab Booster, FNAL report, TM-1442, Feb 1987.

Y.-C. Chao and K.-Y. Ng, "Analytical and Numerical Studies of the Landau Cavity," FNAL report, FN-470, Apr 1988.

In addition, references are made in various unpublished internal FNAL Accelerator Division experimental notes (eg. EXP-80, 81) and logbook entries.

49. Y. C. Chao and K.-Y. Ng, "Analytical and Numerical Studies of the Landau Cavity," FNAL report, FN-470, Apr 1988.

50. K.-Y. Ng, "Longitudinal Coupled-Bunch Instability in the Fermilab Booster," FNAL report, FN-464, Sep 1987.

51. D. Wildman and K. Harkay, "HOM RF Cavity Dampers for Supressing Coupled Bunch Instabilities in the Fermilab Booster," Proc. of 15th IEEE Particle Accelerator Conference, Washington, D.C., May 1993.

52. S. Stahl and J. MacLachlan, "User's Guide to ESME v. 7.1," FNAL report, TM-1650, Feb 1990.

53. J. A. MacLachlan, "An ESME Update (v.7.2)," Feb 1991. (unpublished)

54. J. A. MacLachlan, "Differential Equations for Longitudinal Motion in a Synchrotron," FNAL report, FN-532, Jan 1990.

55. S. Stahl and S. A. Bogacz, "Simulation of Coupled Bunch Mode Growth Driven by a High-Q Resonator: A Transient Response Approach," Proc. of 13th IEEE Particle Accelerator Conference, Chicago, Mar 1989.

56. V. Bharadwaj, J. Crisp, K. Harkay, J. Lackey, W. Merz, S. Stahl, "Coupled-Bunch Instability and Longitudinal Emittance Growth in the Fermilab Booster," Proc. of 14th International Conference on High Energy Accelerators, Tsukuba, Japan, Aug 1989.

57. G. N. Watson, Theory of Bessel Functions, Cambridge University Press, 1966, p 395.

58. M. Abramowitz and I. Stegun, ed, Handbook of Mathematical Functions, Dover Publ., 1972.

Appendix A: Booster Kinematic and Operational Tables and Curves

Tables and plots of important Booster parameters are assembled in this Appendix. Included are kinematic parameters of the beam as well as operational parameters of the RF system.

APPENDICES

Table A.1 Standard Booster Kinematic Parameters: 200 MeV to 8 GeV. (17 cavities)

TIME (ms)	BETA	ETA	CP (GeV)	K (GeV)	FREQRF (MHz)	VOLTA (kV)	VOLTRF (kV)	PHIS (deg)	FREQS (kHz)	BKTA (eV-s)
0.0	No beam									
1.0	No beam									
2.0	0.5709	-0.6404	0.6524	0.2045	30.3178	0.0000	15.5974	0.0000	6.8339	0.0110
3.0	0.5815	-0.6281	0.6707	0.2151	30.8825	57.7755	257.1310	12.9848	27.0025	0.0285
4.0	0.6116	-0.5922	0.7254	0.2477	32.4809	115.0382	436.1577	15.2929	33.5045	0.0359
5.0	0.6562	-0.5357	0.8160	0.3052	34.8482	171.2798	536.4191	18.6207	34.2085	0.0381
6.0	0.7084	-0.4645	0.9416	0.3910	37.6183	228.0010	588.3536	22.5894	31.8484	0.0383
7.0	0.7612	-0.3869	1.1013	0.5085	40.4239	278.7163	685.4484	23.9926	29.9131	0.0448
8.0	0.8095	-0.3111	1.2935	0.6597	42.9876	328.9577	792.0110	24.5410	27.3747	0.0553
9.0	0.8504	-0.2431	1.5166	0.8451	45.1619	376.2792	763.7298	29.5173	22.0018	0.0531
10.0	0.8834	-0.1859	1.7686	1.0638	46.9129	420.2609	794.6964	31.9266	18.2948	0.0592
11.0	0.9091	-0.1399	2.0472	1.3137	48.2772	460.5123	801.9977	35.0441	14.7625	0.0633
12.0	0.9287	-0.1038	2.3500	1.5921	49.3203	496.6761	798.9866	38.4355	11.7116	0.0684
13.0	0.9436	-0.0759	2.6743	1.8958	50.1114	528.4315	779.3379	42.6916	9.0534	0.0656
14.0	0.9549	-0.0545	3.0172	2.2214	50.7107	555.4964	785.1463	45.0324	7.1490	0.0725
15.0	0.9635	-0.0380	3.3757	2.5653	51.1664	577.6307	803.5376	45.9604	5.6900	0.0878
16.0	0.9700	-0.0253	3.7465	2.9239	51.5152	594.6379	799.9606	48.0162	4.3283	0.1001
17.0	0.9751	-0.0154	4.1264	3.2935	51.7844	606.3671	795.5520	49.6582	3.1694	0.1211
18.0	0.9791	-0.0077	4.5121	3.6703	51.9939	612.7141	769.3500	52.7881	2.0428	0.1438
19.0	0.9822	-0.0017	4.9000	4.0508	52.1586	613.6225	763.8170	53.4525	0.8977	0.3076
20.0	0.9846	0.0032	5.2868	4.4311	52.2891	609.0845	779.1933	51.4152	1.2401	0.2664
21.0	0.9866	0.0071	5.6690	4.8079	52.3935	599.1402	765.9925	51.4602	1.7692	0.1829
22.0	0.9882	0.0102	6.0433	5.1774	52.4775	583.8778	766.7710	49.5945	2.1023	0.1768
23.0	0.9894	0.0127	6.4062	5.5363	52.5456	563.4329	746.0853	49.0416	2.2654	0.1661
24.0	0.9905	0.0148	6.7546	5.8812	52.6012	537.9870	725.2546	47.8842	2.3738	0.1670
25.0	0.9913	0.0165	7.0855	6.2090	52.6467	507.7659	697.1954	46.7439	2.4264	0.1696
26.0	0.9920	0.0179	7.3957	6.5167	52.6840	473.0377	676.1566	44.3947	2.4880	0.1866
27.0	0.9926	0.0190	7.6827	6.8015	52.7146	434.1109	647.9259	42.0671	2.5132	0.2040
28.0	0.9931	0.0200	7.9438	7.0607	52.7396	391.3308	612.5104	39.7096	2.5064	0.2216
29.0	0.9935	0.0207	8.1768	7.2921	52.7600	345.0772	577.0410	36.7276	2.4943	0.2470
30.0	0.9938	0.0213	8.3795	7.4936	52.7764	295.7609	534.4027	33.6035	2.4531	0.2733
31.0	0.9940	0.0218	8.5502	7.6632	52.7894	243.8192	477.4740	30.7067	2.3588	0.2926
32.0	0.9942	0.0222	8.6873	7.7996	52.7992	189.7134	420.5120	26.8174	2.2565	0.3223
33.0	0.9944	0.0224	8.7897	7.9014	52.8062	133.9237	377.7801	20.7629	2.1895	0.3856
34.0	0.9944	0.0226	8.8564	7.9677	52.8107	76.9453	306.5173	14.5385	2.0066	0.4328
35.0	0.9945	0.0227	8.8869	7.9980	52.8127	19.2838	256.6253	4.3095	1.8634	0.5608
36.0	No beam									

Table A.2 Variation on Booster Kinematic Parameters: 200 MeV to 4 GeV

TIME (ms)	BETA	GAMMA	ETA	CP (GeV)	K (GeV)	FREQA (MHz)	TREV (us)	VOLTA (kV)
0.0	*** no beam ***							
1.0	*** no beam ***							
2.0	0.5703	1.2174	-0.6410	0.6515	0.2040	30.2883	2.7733	0.0000
3.0	0.5758	1.2231	-0.6347	0.6608	0.2093	30.5784	2.7470	29.4392
4.0	0.5917	1.2404	-0.6162	0.6887	0.2256	31.4222	2.6733	58.6171
5.0	0.6166	1.2702	-0.5861	0.7348	0.2535	32.7434	2.5654	87.2747
6.0	0.6483	1.3133	-0.5460	0.7989	0.2940	34.4266	2.4400	115.1576
7.0	0.6842	1.3711	-0.4982	0.8802	0.3482	36.3337	2.3119	142.0184
8.0	0.7217	1.4446	-0.4455	0.9782	0.4171	38.3245	2.1918	167.6186
9.0	0.7584	1.5343	-0.3911	1.0918	0.5013	40.2768	2.0856	191.7310
10.0	0.7927	1.6405	-0.3379	1.2202	0.6010	42.0990	1.9953	214.1416
11.0	0.8235	1.7629	-0.2881	1.3622	0.7156	43.7350	1.9207	234.8515
12.0	0.8504	1.9006	-0.2431	1.5165	0.8450	45.1608	1.8600	253.0786
13.0	0.8733	2.0524	-0.2037	1.6817	0.9875	46.3763	1.8113	269.2593
14.0	0.8925	2.2169	-0.1698	1.8565	1.1416	47.3964	1.7723	283.0501
15.0	0.9084	2.3922	-0.1410	2.0391	1.3063	48.2437	1.7412	294.3285
16.0	0.9216	2.5765	-0.1169	2.2281	1.4793	48.9433	1.7163	302.9945
17.0	0.9325	2.7679	-0.0968	2.4217	1.6588	49.5191	1.6963	308.9710
18.0	0.9414	2.9641	-0.0801	2.6182	1.8429	49.9928	1.6802	312.2050
19.0	0.9487	3.1632	-0.0662	2.8158	2.0297	50.3927	1.6672	312.6680
20.0	0.9548	3.3632	-0.0547	3.0129	2.2173	50.7044	1.6567	310.3558
21.0	0.9598	3.5619	-0.0451	3.2077	2.4038	50.9703	1.6480	305.2886
22.0	0.9639	3.7573	-0.0371	3.3984	2.5872	51.1909	1.6409	297.5117
23.0	0.9674	3.9477	-0.0305	3.5833	2.7658	51.3742	1.6351	287.0941
24.0	0.9703	4.1310	-0.0249	3.7608	2.9378	51.5268	1.6302	274.1283
25.0	0.9727	4.3055	-0.0202	3.9294	3.1016	51.6540	1.6262	258.7293
26.0	0.9747	4.4696	-0.0163	4.0875	3.2555	51.7600	1.6229	241.0338
27.0	0.9763	4.6216	-0.0131	4.2337	3.3982	51.8482	1.6201	221.1988
28.0	0.9777	4.7602	-0.0104	4.3668	3.5281	51.9212	1.6178	199.4004
29.0	0.9788	4.8839	-0.0082	4.4855	3.6443	51.9811	1.6160	175.8323
30.0	0.9797	4.9917	-0.0064	4.5888	3.7454	52.0297	1.6145	150.7033
31.0	0.9805	5.0826	-0.0050	4.6758	3.8307	52.0682	1.6133	124.2368
32.0	0.9810	5.1556	-0.0039	4.7456	3.8992	52.0977	1.6124	96.6674
33.0	0.9814	5.2102	-0.0031	4.7978	3.9504	52.1189	1.6117	68.2401
34.0	0.9817	5.2457	-0.0026	4.8318	3.9838	52.1324	1.6113	39.2070
35.0	0.9818	5.2619	-0.0024	4.8473	3.9990	52.1384	1.6111	9.8260
36.0	*** no beam ***							

Table A.3 Booster Kinematic Parameters after Linac Upgrade: 400 MeV to 8 GeV

TIME (ms)	BETA	GAMMA	ETA	CP (GeV)	K (GeV)	FREQA (MHz)	TREV (us)	VOLTA (kV)
0.0	*** no beam ***							
1.0	*** no beam ***							
2.0	0.7130	1.4263	-0.4578	0.9543	0.4000	37.9674	2.2183	0.0000
3.0	0.7194	1.4397	-0.4487	0.9719	0.4126	38.2061	2.1986	55.6583
4.0	0.7375	1.4806	-0.4224	1.0245	0.4510	39.1640	2.1448	110.8225
5.0	0.7642	1.5505	-0.3823	1.1118	0.5165	40.5848	2.0697	165.0031
6.0	0.7958	1.6512	-0.3331	1.2329	0.6110	42.2595	1.9877	217.7191
7.0	0.8282	1.7844	-0.2803	1.3867	0.7360	43.9834	1.9098	268.5026
8.0	0.8587	1.9510	-0.2290	1.5719	0.8923	45.5999	1.8421	316.9029
9.0	0.8854	2.1509	-0.1824	1.7868	1.0799	47.0177	1.7866	362.4903
10.0	0.9077	2.3830	-0.1424	2.0295	1.2976	48.2040	1.7426	404.8603
11.0	0.9258	2.6454	-0.1092	2.2980	1.5438	49.1656	1.7085	443.6366
12.0	0.9402	2.9355	-0.0823	2.5897	1.8161	49.9299	1.6824	478.4752
13.0	0.9515	3.2505	-0.0609	2.9021	2.1117	50.5307	1.6624	509.0668
14.0	0.9604	3.5871	-0.0440	3.2324	2.4275	51.0010	1.6470	535.1400
15.0	0.9673	3.9419	-0.0306	3.5777	2.7604	51.3690	1.6352	556.4631
16.0	0.9727	4.3113	-0.0201	3.9350	3.1070	51.6580	1.6261	572.8471
17.0	0.9770	4.6916	-0.0117	4.3010	3.4638	51.8859	1.6189	584.1464
18.0	0.9804	5.0791	-0.0050	4.6725	3.8275	52.0668	1.6133	590.2608
19.0	0.9831	5.4702	0.0003	5.0462	4.1944	52.2114	1.6088	591.1359
20.0	0.9853	5.8611	0.0046	5.4188	4.5612	52.3276	1.6053	586.7642
21.0	0.9871	6.2481	0.0081	5.7870	4.9243	52.4217	1.6024	577.1843
22.0	0.9886	6.6277	0.0110	6.1476	5.2805	52.4983	1.6001	562.4813
23.0	0.9897	6.9963	0.0133	6.4972	5.6263	52.5610	1.5981	542.7856
24.0	0.9907	7.3505	0.0152	6.8329	5.9587	52.6125	1.5966	518.2722
25.0	0.9915	7.6871	0.0168	7.1516	6.2745	52.6550	1.5953	489.1585
26.0	0.9922	8.0031	0.0181	7.4505	6.5710	52.6901	1.5942	455.7030
27.0	0.9927	8.2955	0.0192	7.7269	6.8454	52.7190	1.5934	418.2026
28.0	0.9932	8.5617	0.0201	7.9785	7.0952	52.7428	1.5926	376.9903
29.0	0.9935	8.7993	0.0208	8.2029	7.3181	52.7622	1.5920	332.4318
30.0	0.9938	9.0061	0.0214	8.3982	7.5121	52.7779	1.5916	284.9226
31.0	0.9940	9.1803	0.0219	8.5626	7.6756	52.7903	1.5912	234.8843
32.0	0.9942	9.3203	0.0222	8.6947	7.8069	52.7997	1.5909	182.7613
33.0	0.9944	9.4248	0.0225	8.7934	7.9050	52.8065	1.5907	129.0160
34.0	0.9944	9.4929	0.0226	8.8576	7.9689	52.8108	1.5906	74.1255
35.0	0.9945	9.5240	0.0227	8.8870	7.9981	52.8127	1.5905	18.5772
36.0	*** no beam ***							

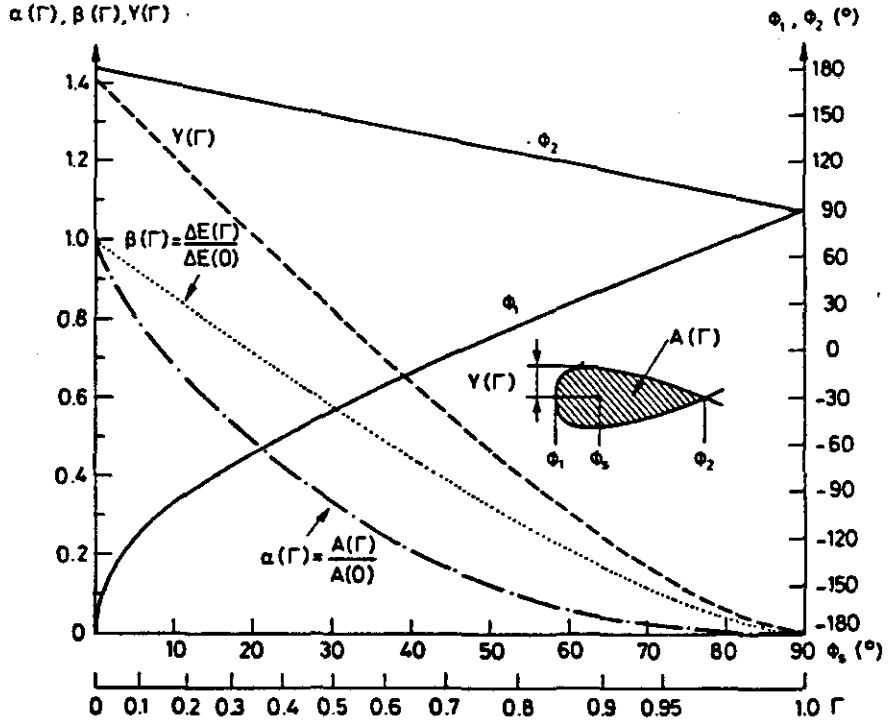

Figure A.1 Moving RF Bucket Parameters. The RF bucket area, height, and length may be determined from the plot given the shynchronous phase angle. (Ref. 14)

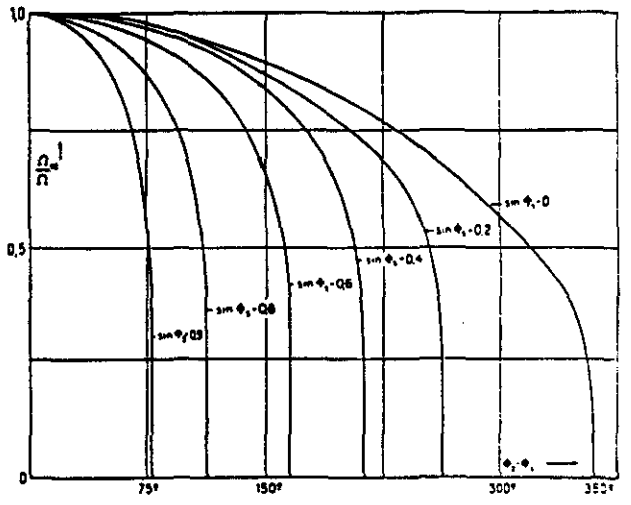

Figure A.2 Amplitude Dependence of Synchrotron Frequency. The vertical scale is $\omega_s(\phi)/\omega_s(0)$ and the horizontal is $(\phi_s-\phi_1)$. The synchrotron frequency is fairly constant for small ϕ_s and bunch lengths small compared to the bucket length, and falls rapidly to zero at the separatrix. (Ref. 11)

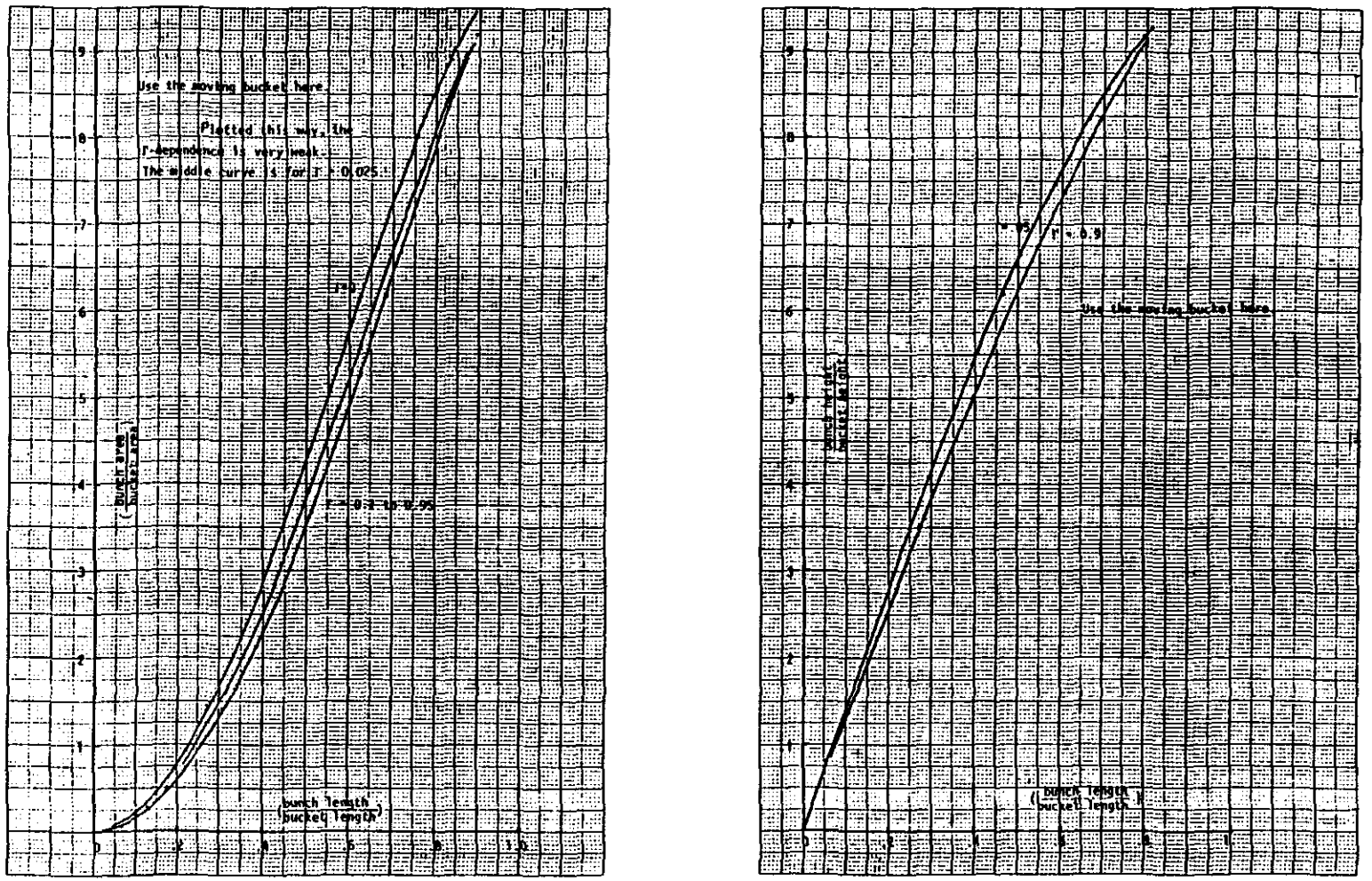

Figure A.3 Beam Scaling Parameters. Curves give ratio of bunch to bucket area (left) and height (right) for varying synchrotron phase angle ϕ_s. (Ref. 13)

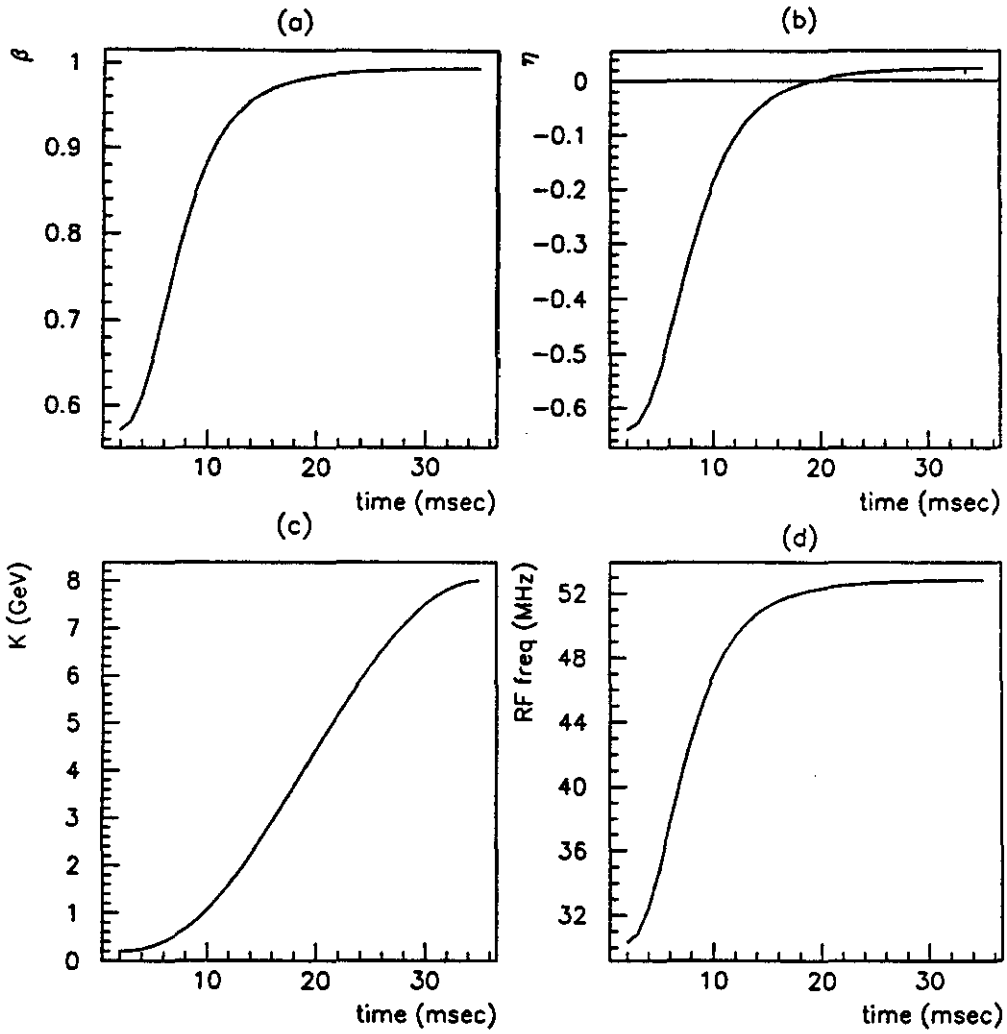

Figure A.4 Standard Booster Kinematic Parameters. Shown is the variation with time in the acceleration cycle for (a) relativistic β, (b) slip factor η, (c) kinetic energy K, and (d) RF frequency.

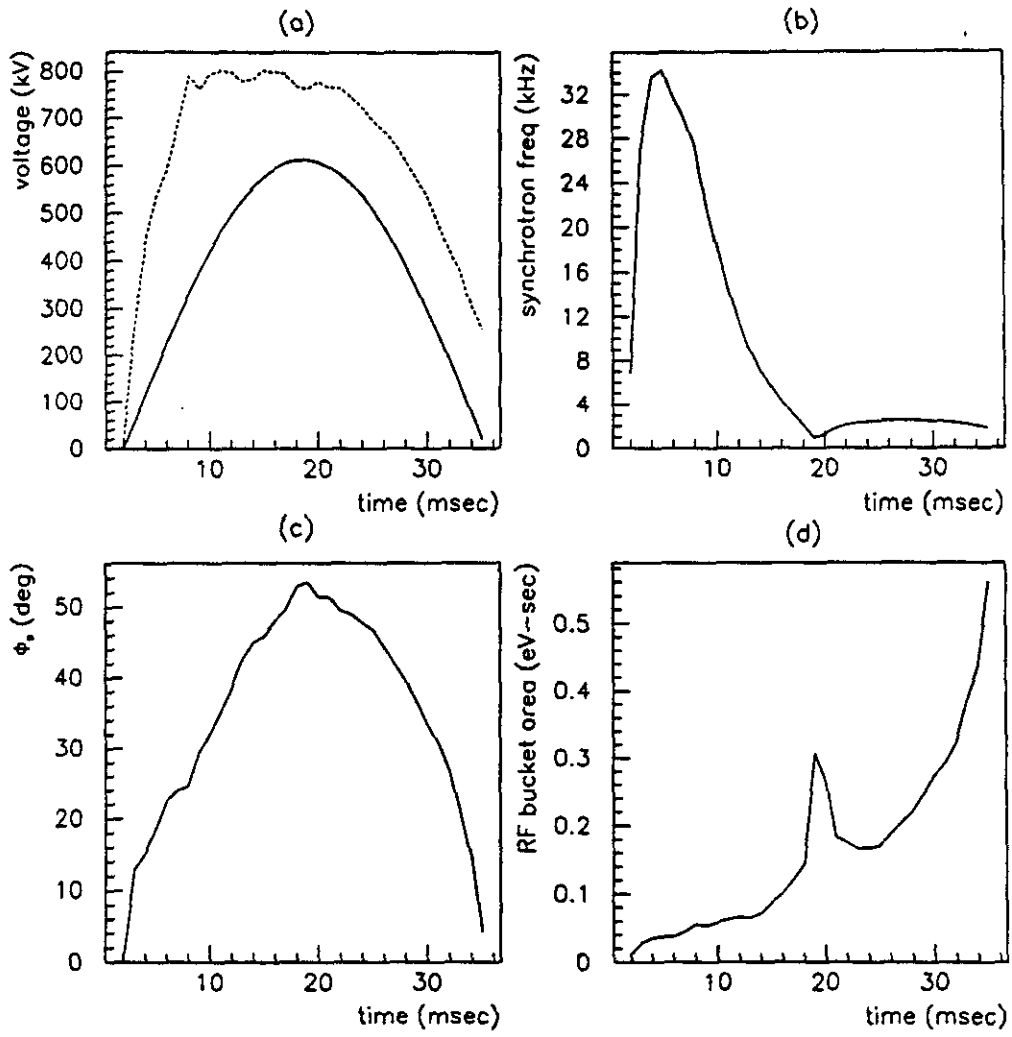

Figure A.5 Standard Booster Acceleration Parameters. Shown in (a) is the variation with time in the acceleration cycle for the theoretical accelerating voltage (solid) and measured RF voltage for 17 cavities (dashed). Corresponding to this example is the (b) synchrotron frequency, (c) synchronous phase angle , and (d) RF bucket area. The peak in the bucket area at transition is empirically found to be important for a stable beam.

Appendix B: RF Cavity Impedance Tables

Tables of Booster RF cavity impedance data and calculations are assembled in this Appendix. Included are records of the single-gap stretched-wire, bead-pull and double-gap stretched wire measurement results. The equivalent model resonator R and Q are calculated and tabulated for the single cavity and net sum impedance based on the single-gap stretched-wire data.

Table B.1 Single-Gap Stretched Wire Datasets

SGSWnn *	t_{cycle} (msec)	f_{RF} calc (MHz)	f_{RF} msrd (MHz)	Q **	V_{pgm} *** (V)	archive no.	date
01	3	30.8822	30.87	191	0.277	1657	91/6/19
02	6	37.6181	37.715	324	0.968	1688	"
03	9	45.1619	45.28	602	2.621	1719	"
04	12	49.3203	49.16	804	4.48	1750	"
05	15	51.1665	51.025	829	6.04	1781	"
06	17	51.7844	51.70	896	6.83	1812	"
08	18	51.9940	52.00	799	7.22	1874	"
09	19	52.1586	52.122	898	7.41	1967	91/6/20
10	20	52.2891	52.251	902	7.61	1998	"
11	21	52.3935	52.378	898	7.81	2029	"
12	23	52.5457	52.543	881	8.10	2060	"
13	25	52.6467	52.647	970	8.29	125	"
14	29	52.7600	52.7575	969	8.49	156	"
15	short out (HOM dampers OUT)				0	1905	91/6/19
16	short in, unshorted gap				0	1936	"
17	short in, shorted gap				0	187	91/6/21
	reference pipe					1626	91/6/19
	cable calibration					1595	"
28	3	30.8822	30.84	187	0.254	716	91/6/28
29	6	37.6181	37.65	327	0.897	842	"
30	9	45.1619	45.197	583	2.489	1030	"
21	12	49.3203	49.397	942	4.48	468	91/6/26
31	15	51.1665	51.166	1100	5.90	999	91/6/28
32	17	51.7844	51.792	1112	6.57	968	"
23	18	51.9940	51.992	1156	6.83	530	91/6/26
33	19	52.1586	52.161	1140	7.04	906	91/6/28
24	20	52.2891	52.291	1129	7.22	561	91/6/26
34	21	52.3935	52.364	1160	7.30	875	91/6/28
26	23	52.5457	52.561	1148	7.61	654	91/6/27
35	25	52.6467	52.623	1175	7.72	811	91/6/28
36	29	52.7600	52.746	1190	7.90	780	"
37	35	52.8127	52.813	1355	8.02	749	"
38	short out (HOM dampers IN)				0	937	"
39	short in, unshorted gap				0	1063	"
40	short in, shorted gap				0	1162	"
	reference pipe					344	91/6/26
	cable calibration					592	91/6/27

* HOM dampers OUT for nn=1-17; HOM dampers IN for nn=21-40

** Via transmission measurement through gap monitors

*** Bias current program voltage scaling: 250 A/V

Table B.2 Single-Gap Impedance, Single-Gap Stretched Wire, HOM Dampers Out

t (ms)	f_{RF} (MHz)	R (kΩ)	Q	f1	R	Q	f2	R	Q
3		--	191	79.91	8.2	127	82.71	6.0	182
6	37.72	--	324	79.93	7.95	174	82.08	3.9	342
9	45.3	8.4	566	79.9	7.9	182	82.6	5.75	217
12	49.2	11.3	703	79.9	7.9	182	82.6	5.8	212
15	51.04	13.3	850	79.93	7.95	170	82.65	5.9	210
17	51.7	14.7	862	79.93	8.1	182	82.65	6.05	202
18	52.01	15.0	867	79.93	8.1	182	82.67	6.15	223
19	52.14	14.7	869	79.93	7.8	174	82.67	5.85	212
20	52.26	14.5	871	79.93	7.85	174	82.67	5.85	212
21	52.39	14.8	873	79.93	7.95	182	82.65	5.9	212
23	52.56	14.8	876	79.93	7.75	174	82.67	5.9	212
25	52.66	14.7	752	79.91	7.9	182	82.65	6.0	212
29	52.76	*	969	79.93	7.7	174	82.65	5.85	212

t	f3	R	Q	f4	R	Q	f5	R	Q
3	73.8	1.04	207	108.9	1.67	156	195.9	28.4	1120
6	84.0	3.51	247	124.9	1.26	178	196	27.3	1120
9	93.8	4.25	335	147.1	1.65	245	195.9	33.0	1570
12	99.5	4.32	369	158.8	2.71	318	196	30.8	1310
15	102.8	4.45	340	164.2	3.2	330	196	31.9	1310
17	104.0	4.58	347	166.2	3.3	416	196	36.2	1570
18	104.6	4.52	349	167	3.4	334	196	36.8	1960
19	104.9	4.45	466	167.4	3.16	419	196	31	1570
20	105.1	4.46	350	167.8	3.24	336	196	32.3	1570
21	105.4	4.45	420	168.1	3.3	336	196	36.9	1960
23	105.8	4.51	353	168.6	3.27	422	196	31.6	1307
25	106	4.44	471	168.9	3.28	338	196	34	1307
29	106.2	4.4 3	531	169.2	3.2	423	196	27.9	1120

t	f6	R	Q	f7	R	Q	f8	R	Q
3	160	0	0	326.5	3.5	93.3	341.9	5.3	58.9
6	170.3	0.32	68.1	326.3	3	58.3	342.2	3.55	81.5
9	198.7	2.71	284	326.6	3.9	85.9	344.6	6.3	49.9
12	209	5.12	523	326.1	1.24	81.5	349.9	1.27	72.9
15	214.8	6.2	430	326.5	1.57	110	341.6	2.94	120
17	217	6.15	434	326.6	1.5	102	343	3.4	137
18	217.9	5.65	436	326.6	1.67	109	343.5	3.7	143
19	218.3	5.05	364	326.8	1.62	113	343.8	3.53	149
20	218.7	5.05	365	326.8	1.64	109	344	3.54	150
21	219	4.88	313	326.8	1.67	109	344.3	3.69	157
23	219.5	4.71	314	327	1.71	105	344.7	3.69	157
25	219.9	4.58	314	326.9	1.75	109	344.9	3.76	157
29	220.2	4.24	315	326.9	1.68	105	345.2	3.60	164

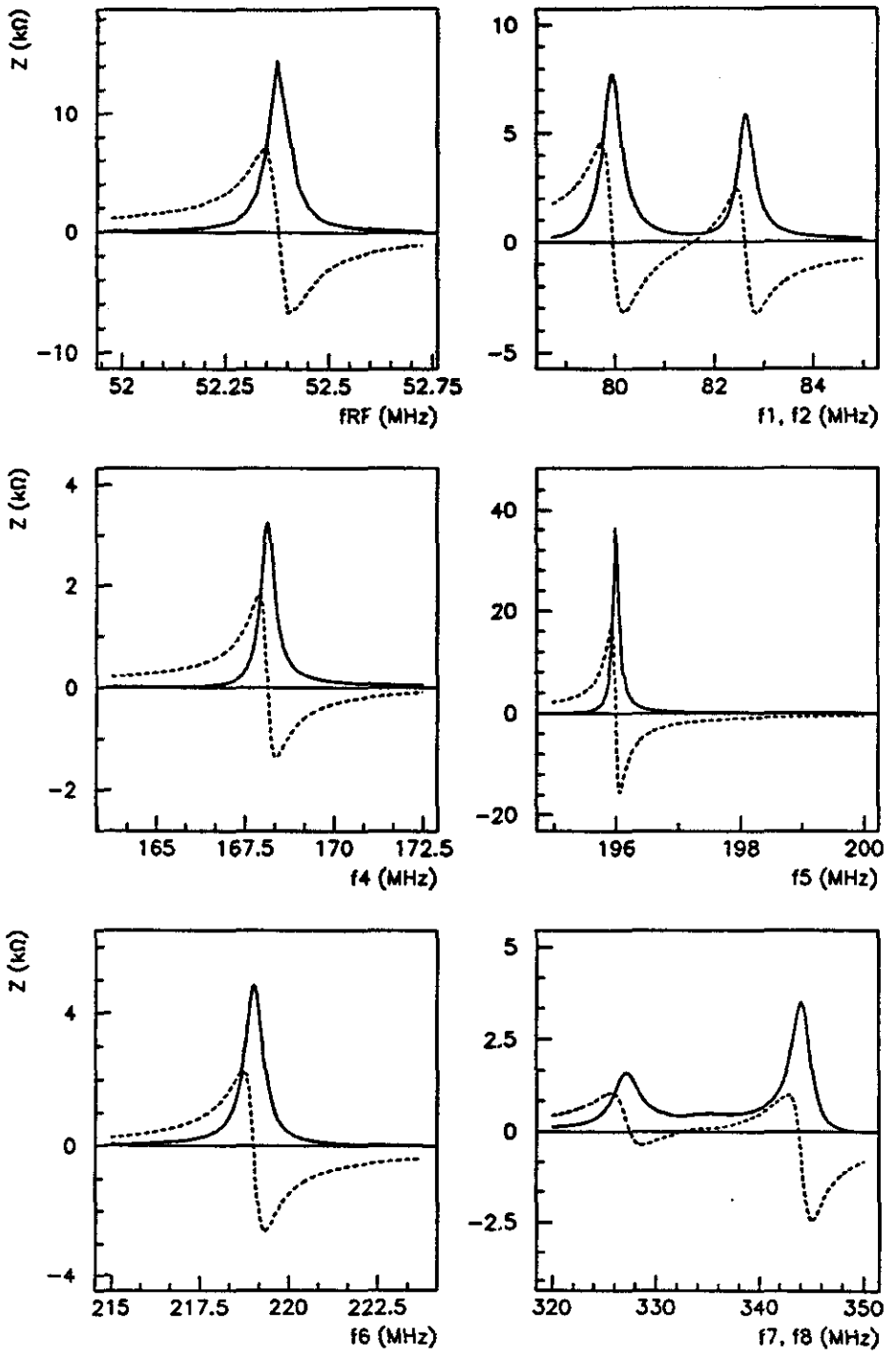

Figure B.1 Single-Gap Impedance (ReZ, ImZ) De-embedded, HOM Dampers Out, Showing Detail (t=21 msec).

Table B.3 Single-Gap Impedance, Single-Gap Stretched Wire, HOM Dampers In

t (ms)	f_{RF} (MHz)	R (kΩ)	Q	f1	R	Q	f2	R	Q	f3
3	30.87									
6	37.72			(raw	data	recorded	but	not	analyzed)	
9	45.3	9.0	560							
12	49.2	11.5	700							
15	51.18	16.1	850	82.12	2.11	31	84.7	2.51	55	103.1
17	51.78	18.2	1000	82.15	2.12	31	84.71	2.53	56	104.1
18	52.00	16.8	1300	82.12	1.82	31	84.71	2.17	43	104.5
19	52.16	17.6	870	82.14	2.11	30	84.7	2.5	53	104.8
20	52.29	15.6	870	82.09	1.88	31	84.69	2.21	56	105.1
21	52.34	18.3	870	82.12	2.11	32	84.71	2.52	56	105.2
23	52.56	18.8	876	82.15	2.22	30	84.71	2.66	54	105.6
25	52.63	18.2	1053	82.12	2.08	30	84.7	2.5	54	105.7
29	52.76	18.0	959	82.1	2.08	30	84.7	2.5	56	106.0
35	52.8	20.1	1056	82.1	2.08	32	84.7	2.5	56	106.1

t	R	Q	f4	R	Q	f5	R	Q	f9	R
3										
6										
9										
12										
15	5.55	450	162.0	2.47	220	196.8	2.14	120	262.1	1.73
17	5.75	450	163.6	2.13	220	196.8	2.15	120	262.7	2.12
18	5.13	450	164.1	1.81	220	196.8	1.99	120	263.0	2.10
19	5.93	450	164.5	1.89	206	196.8	2.15	109	263.4	2.2
20	5.42	460	164.8	1.75	180	196.7	2.15	120	263.5	2.44
21	5.95	470	164.9	1.72	165	196.8	2.13	123	263.7	2.2
23	6.35	459	165.4	1.63	165	196.8	2.26	123	264.1	2.32
25	6.0	470	165.6	1.5	153	196.8	2.12	123	264.2	2.2
29	6.0	461	165.8	1.37	144	196.8	2.09	116	264.4	2.18
35	6.0	530	166.0	1.27	138	196.8	2.10	116	264.6	2.17

t	Q	f10	R	Q	f11	R	Q	f8	R	Q
3										
6										
9										
12										
15	130	--	--	--	302.8	0.96	63	338.2	2.9	210
17	220	--	--	--	302.9	1.05	63	339.5	3.17	230
18	240	--	--	--	302.9	1.1	89	340.0	3.2	240
19	220	--	--	--	304.0	1.16	101	340.4	3.18	243
20	240	301.7	0.9	140	304.8	1.25	140	340.7	3.85	240
21	240	302.1	0.77	82	305.4	1.11	133	340.9	3.25	244
23	240	302.3	0.85	70	306.9	1.15	162	341.5	3.37	244
25	240	302.4	0.81	69	307.5	1.12	162	341.7	3.24	263
29	259	302.5	0.82	69	308.2	1.14	181	342.0	3.28	263
35	265	302.6	0.82	70	308.8	1.17	193	342.2	3.29	263

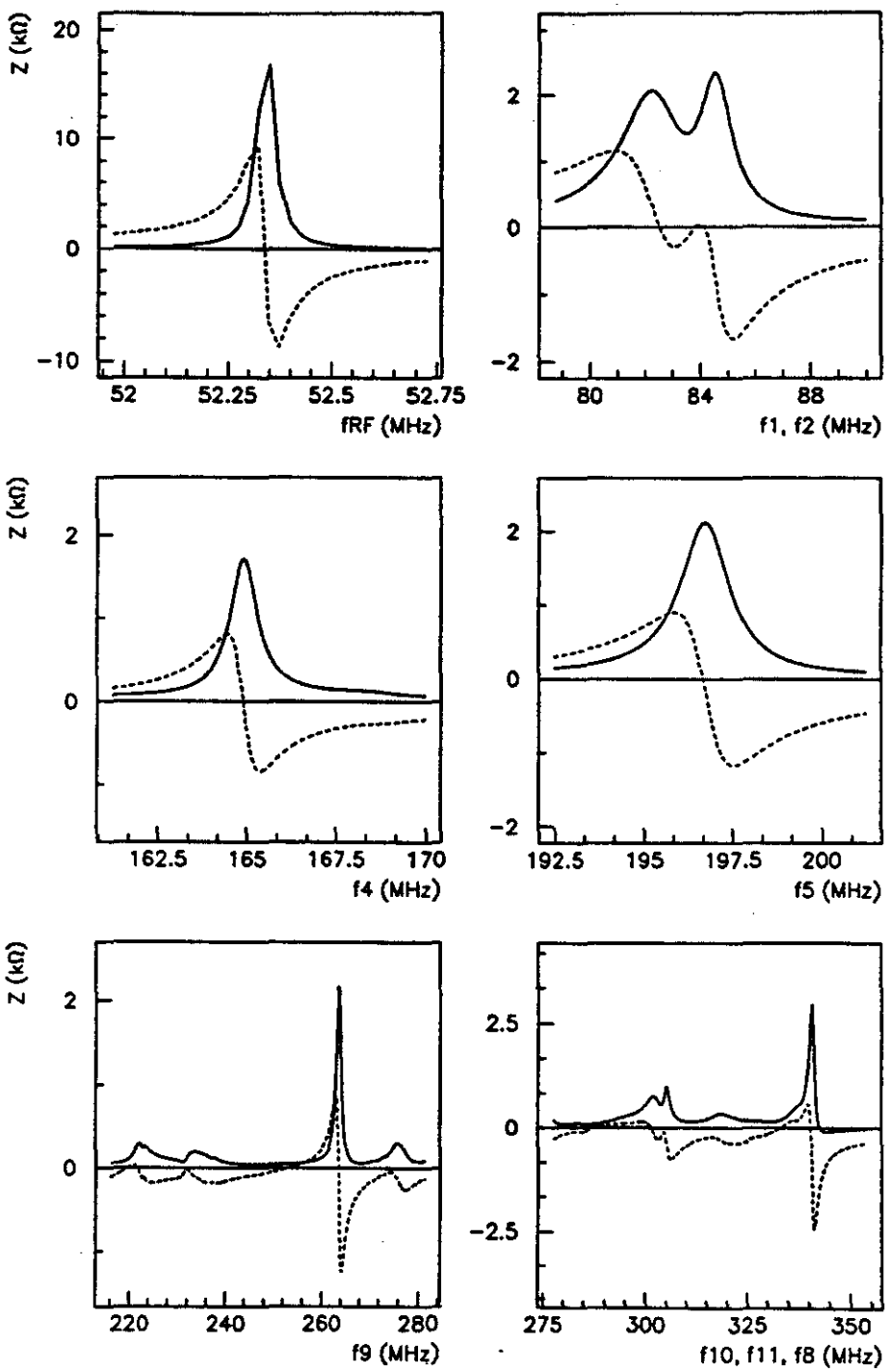

Figure B.2 Single-Gap Impedance (ReZ, ImZ) De-embedded, HOM Dampers In, Showing Detail (t=21 msec).

Table B.4 Phase Shift Results from Bead-Pull Method.

	V_{pgm}=6.0 V * (t=15 msec)			V_{pgm}=7.2 V (t=21 msec)			V_{pgm}=8.5 V (t>35 msec)		
	freq (MHz)	phase shift (deg)	phase slope deg/Hz ($\times 10^{-4}$)	freq (MHz)	phase shift (deg)	phase slope deg/Hz ($\times 10^{-4}$)	freq (MHz)	phase shift (deg)	phase slope deg/Hz ($\times 10^{-4}$)
f_{RF}	51.429	0.3	16	52.431	0.20	16	53.231	0.4	16
f1	79.821	0.3	2.3	79.853	0.28	0.6	79.856	0.26	2.4
f2	83.699	0.16	2.5	83.755	0.16	2.4	83.703	0.2	2.3
f3	103.109	0.17	4.5	104.950	0.2	3.5	106.581	0.16	4
f4	164.404	0.2	2.5	167.312	0.2	2.0	169.517	0.2	2.2
f5	196.178	2.70	10	196.761	2.8	10	196.168	2.7	10
f6	214.848	0.5	2.7	219.988	--	0.1	220.372	0.48	2.5
	393.199	0.25	1.2	392.988	0.2	1.0	393.089	0.26	1.2
	444.802	0.30	0.95	444.909	0.32	1.0	445.109	0.22	0.8

* Bias current program voltage scaling: 250 A/V

Table B.5 Comparison of Single-Gap Impedance Calculation Between Bead-Pull and Stretched-Wire Methods. (HOM Dampers Out, t=15 msec)

	Bead-Pull				Stretched-Wire		
	f (MHz)	R (kΩ)	Q	ΔR/<R> (%)	f (MHz)	R (kΩ)	Q
f_{RF}	51.429	15	720	12	51.04	13.3	850
f1	79.821	9.8	160	21	79.93	7.95	170
f2	83.699	5.0	180	16	82.65	5.9	210
f3	103.109	4.3	400	3	102.8	4.45	340
f4	164.404	3.2	360	0	164.2	3.2	330
f5	196.178	36	1710	12	196.0	31.9	1310
f6	214.848	6.0	510	3	214.8	6.2	430

Table B.6 Frequency Spread in HOMs Among Booster RF Cavities.

cavity no.	position in ring rel. to cav. no. 1 (deg)	f1 (MHz)	f2 (MHz) (a)	(b)	(ave.)	f4 (MHz)	f5 (MHz)	f6 (MHz)
1	0.0	79.95		82.67	82.67			
2	2.38	79.90	82.39	82.62	82.51			
3	19.77	79.88	82.80	82.79	82.80			
4	22.15	79.91	82.72	82.93	82.83			
5	39.54	79.82	82.37	82.83	82.60			
6	41.92	79.84	82.02	82.79	82.40			
7	59.31	79.86	82.66	82.89	82.78			
8	61.69	79.93		82.65	82.65	169.2	196.0	220.2
9	138.39	81.83	82.40	83.56	82.40	168.0	196.3	220.4
10	140.77	81.71	82.83	83.33	82.83	169.6	197.3	220.8
11	158.16	81.56	82.40	83.86	82.40		198.4	221.2
12	160.54		82.40		82.40		196.1	220.4
13	177.93	80.12	82.20	82.72	82.46			222.4
14	180.31	79.84	82.90	82.66	82.78			
15	197.70	79.64	82.40	82.46	82.43	168.4		220.0
16	200.08	80.00	82.40	82.66	82.53	168.8		220.4
17	98.85	79.99	82.53	82.90	82.72			
18	101.23	79.94	82.00	82.94	82.47	168.8		220.8

* After HOM dampers installed, terminated in cantenna only (not included in average).

Table B.7 Equivalent R, Q for Single-Cavity and Net Sum Impedance, HOM Dampers Out.

Single-Cavity Z				
	f_{RF} (MHz)	R (kΩ)	Q	R/Q (Ω)
17	51.71	50.5	1030	49
19	52.14	41.8	870	48
21	52.40	43.4	870	50
23	52.57	43.1	750	57
25	52.66	44.0	880	50
29	--	--	--	--
	f2	R	Q	R/Q
17	82.61	21.8	300	73
19	82.61	21.6	280	77
21	82.61	21.8	290	75
23	82.61	22.2	290	76
25	82.61	21.6	280	77
29	82.61	21.5	290	74
	f4	R	Q	R/Q
17	166.3	7.2	420	17
19	167.5	7.35	420	17
21	168.2	7.3	420	17
23	168.8	7.6	420	18
25	169.1	7.1	440	16
29	169.4	7.3	420	17
	f6	R	Q	R/Q
17	216.9	23.3	540	43
19	218.2	18.7	550	34
21	219.0	17.5	440	40
23	219.5	17.1	440	39
25	219.8	17.1	440	39
29	220.1	15.9	550	29
	f8	R	Q	R/Q
17	343.0	11.7	180	65
19	343.8	12.2	200	61
21	344.3	12.8	200	64
23	344.7	12.8	220	58
25	345.0	13.0	200	65
29	345.2	12.6	220	57

Net Sum Z (15 cavities)				
	f_{RF} (MHz)	R (kΩ)	Q	R/Q (Ω)
17	51.71	755	1030	730
19	52.14	630	870	720
21	52.40	650	870	750
23	52.57	645	750	860
25	52.66	660	880	750
29	--	--	--	--
	f2	R	Q	R/Q
17	82.58	195	190	1000
19	82.59	192	190	1000
21	82.57	193	190	1000
23	82.59	197	180	1100
25	82.58	195	180	1100
29	82.59	192	180	1100
	f4	R	Q	R/Q
17	166.4	51.5	200	260
19	167.6	52	200	260
21	168.3	52	190	270
23	168.8	54	190	280
25	169.1	51	190	270
29	169.2	52	190	270
	f6	R	Q	R/Q
17	217.0	169	300	560
19	218.4	146	280	520
21	219.1	144	280	510
23	219.6	142	260	550
25	219.9	142	260	550
29	220.2	134	260	510
	f8	R	Q	R/Q
17	343.2	147	190	770
19	344.0	151	190	790
21	344.6	157	190	830
23	345.0	157	190	830
25	345.2	159	190	840
29	345.5	154	190	810

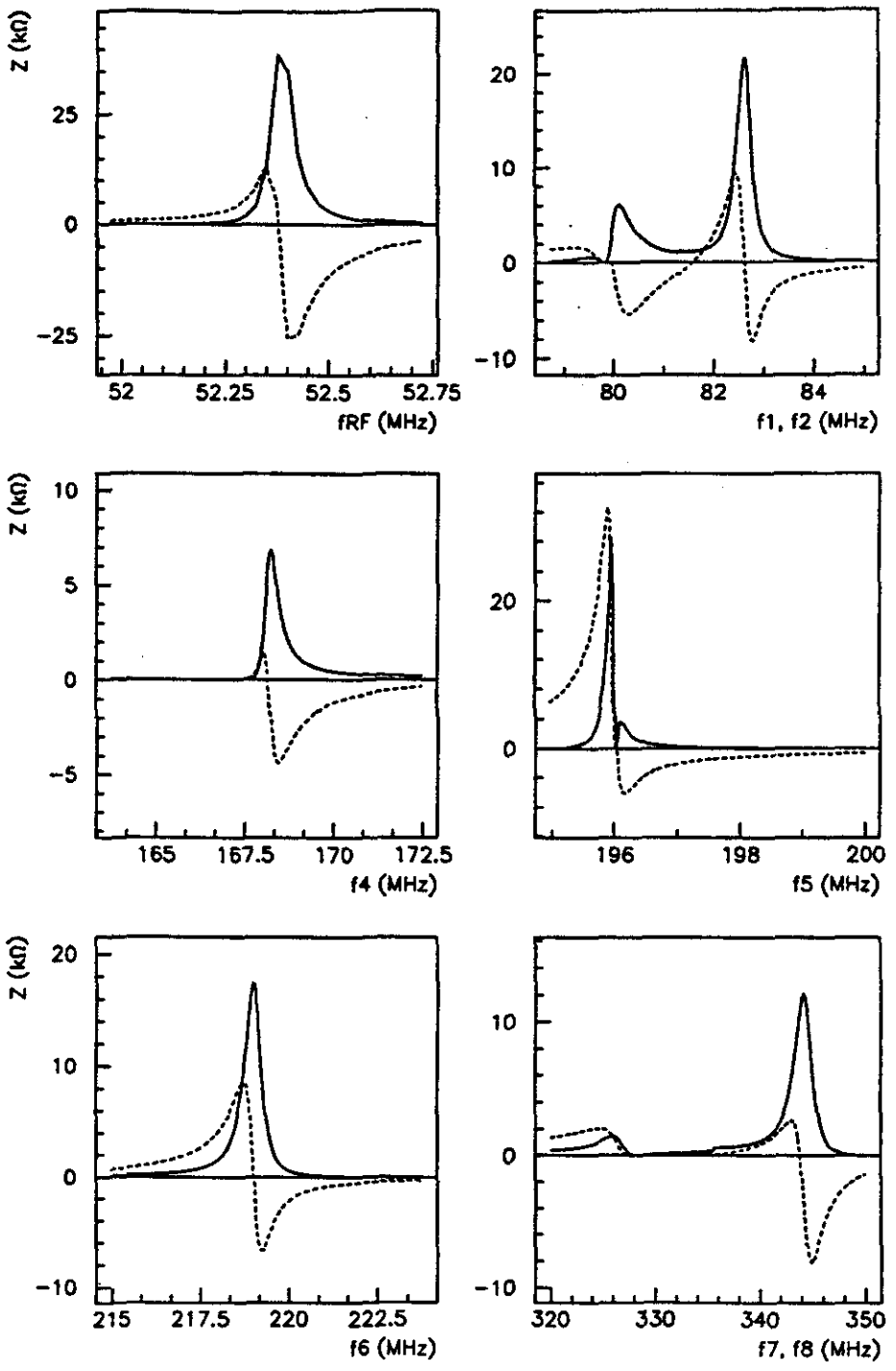

Figure B.3 Single Cavity Impedance (ReZ, ImZ) Calculated, HOM Dampers Out, Showing Detail (t=21 msec).

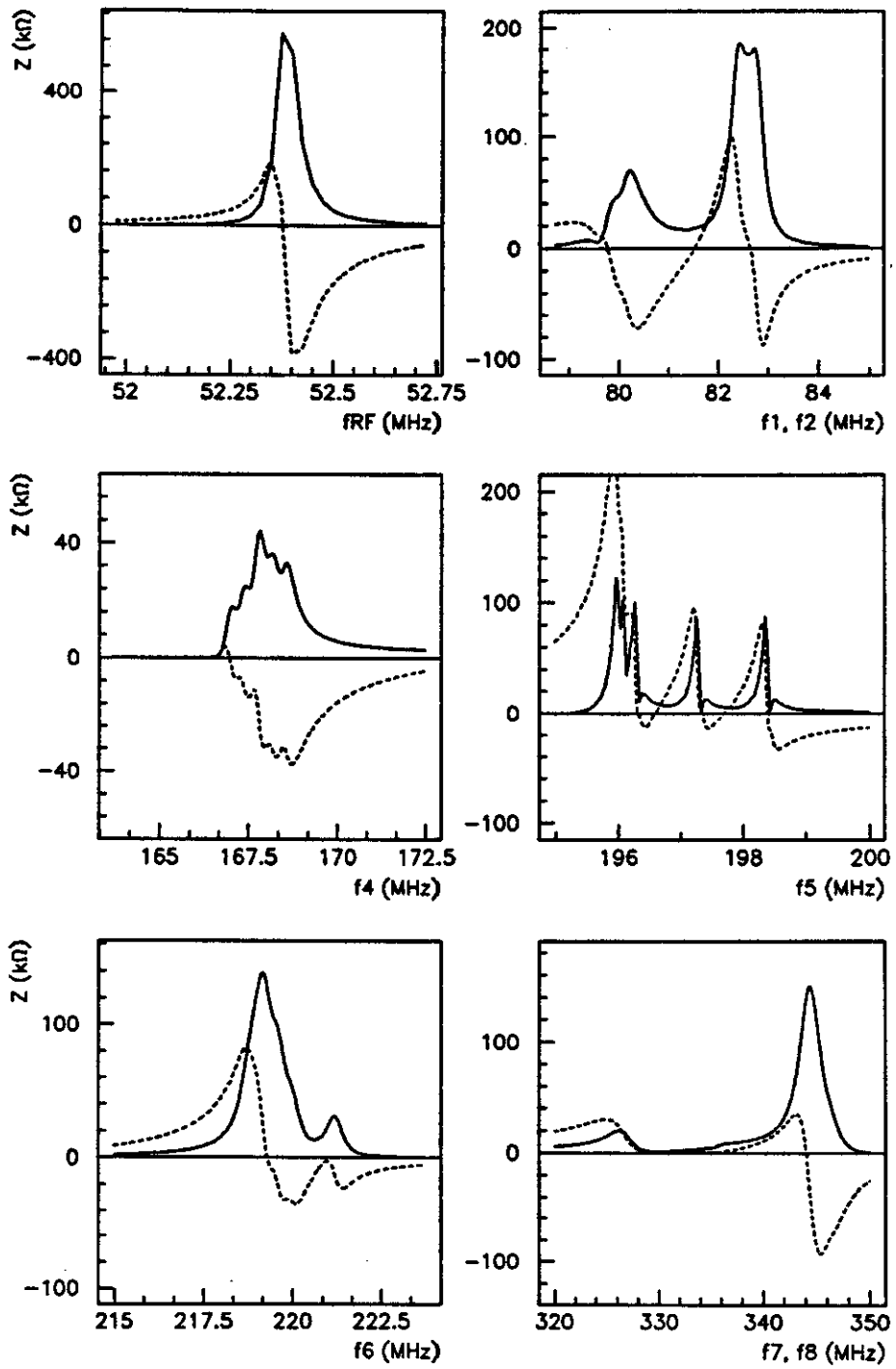

Figure B.4 Net Impedance (ReZ, ImZ) Calculated, 15 Cavities, HOM Dampers Out, Showing Detail (t=21 msec).

Table B.8 Equivalent R, Q for Single-Cavity and Net Sum Impedance, HOM Damper In.

Single-Cavity Z				
	f_{RF} (MHz)	R (kΩ)	Q	R/Q (Ω)
17	51.79	60	860	70
19	52.18	68	1300	52
21	52.35	68	1300	52
23	52.57	65	1100	59
25	52.64	61	1100	55
29	52.75	51	1100	46
	f2	R	Q	R/Q
17	84.61	7.25	110	66
19	84.63	7.25	68	110
21	84.63	7.4	68	110
23	84.63	7.65	66	110
25	84.63	7.15	68	100
29	84.63	7.2	70	100
	f4	R	Q	R/Q
17	163.9	4.09	200	20
19	164.8	3.81	170	22
21	165.3	3.34	150	22
23	165.8	3.28	150	22
25	166.0	2.85	140	20
29	166.2	2.70	130	21
	f8	R	Q	R/Q
17	339.6	11.5	310	37
19	340.5	11.7	310	38
21	341.0	11.8	280	42
23	341.6	12.2	310	39
25	341.7	11.9	340	35
29	342.1	12.0	310	39

Net Sum Z (15 cavities)				
	f_{RF} (MHz)	R (kΩ)	Q	R/Q (Ω)
17	51.79	900	860	1000
19	52.18	1020	1300	780
21	52.35	1030	1300	790
23	52.57	975	1100	890
25	52.64	915	1100	830
29	52.75	765	1100	690
	f2	R	Q	R/Q
17	84.56	104	60	1700
19	84.56	103	60	1700
21	84.56	105	62	1700
23	84.56	110	60	1800
25	84.56	100	62	1600
29	84.56	100	62	1600
	f4	R	Q	R/Q
17	164.1	39.9	120	330
19	165.0	38.4	110	350
21	165.5	35.7	100	360
23	165.9	36.3	100	360
25	166.1	32.5	100	320
29	166.3	31.4	100	310
	f8	R	Q	R/Q
17	339.8	128	220	580
19	340.8	128	210	610
21	341.2	127	220	580
23	341.9	132	230	570
25	342.1	126	220	570
29	342.4	127	220	580

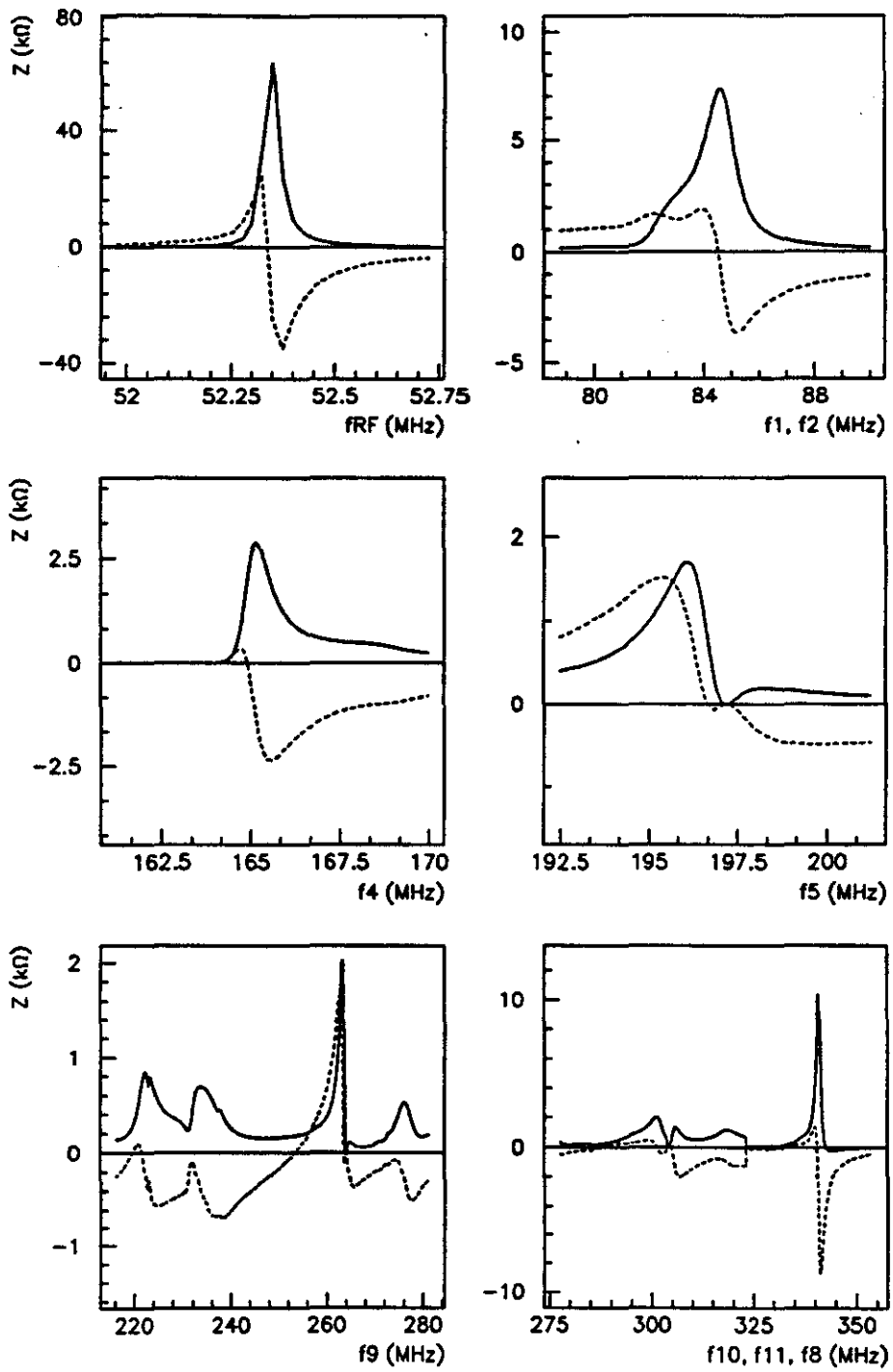

Figure B.5 Single Cavity Impedance (ReZ, ImZ) Calculated, HOM Dampers In, Showing Detail (t=21 msec).

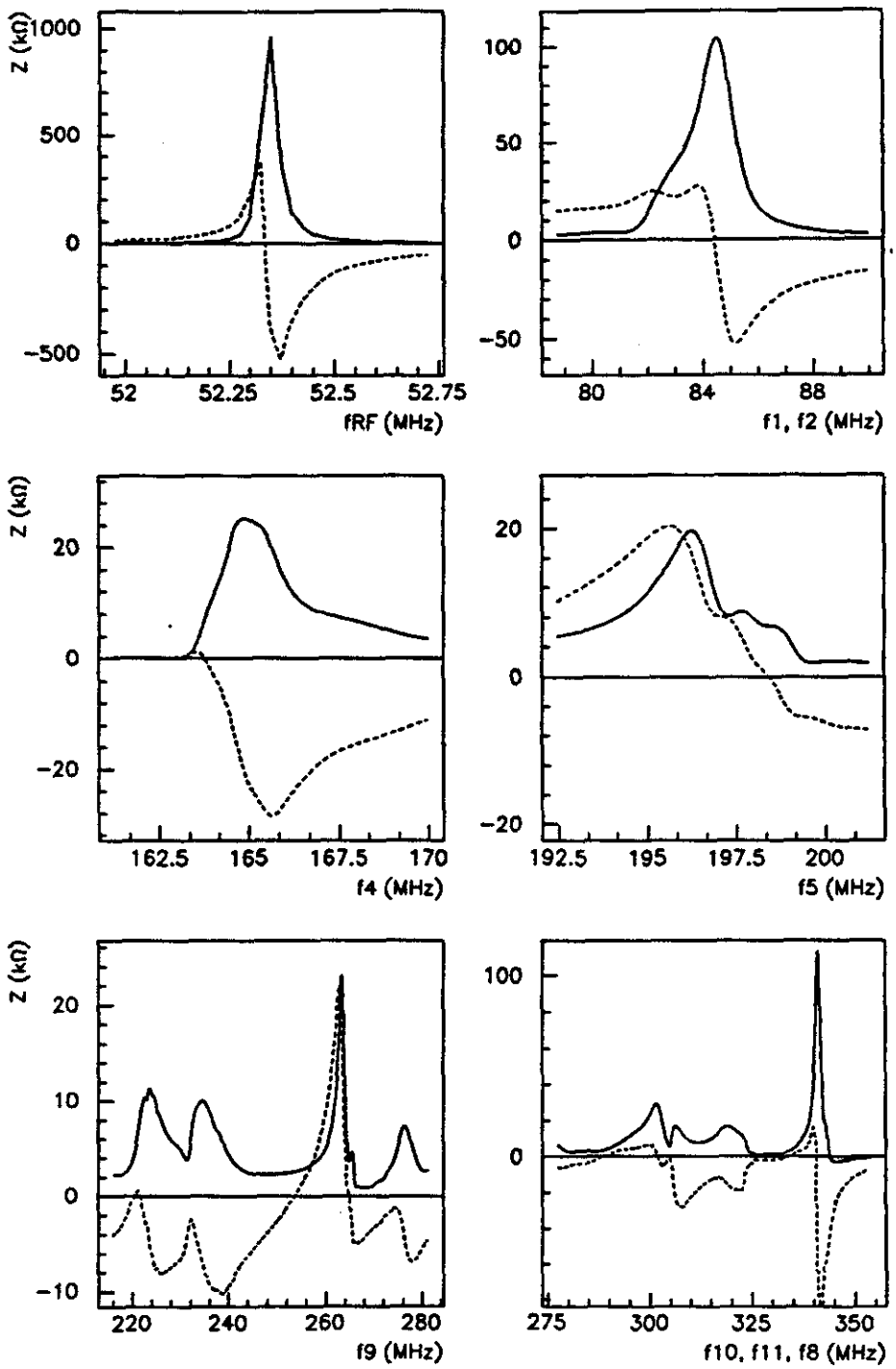

Figure B.6 Net Impedance (ReZ, ImZ) Calculated, 15 Cavities, HOM Dampers In, Showing Detail (t=21 msec).

Table B.9 Comparison of Single-Gap Impedance due to Resonant Modes for Nominal and Damped RF Cavity at t=21 msec.

frequency nominal (MHz)		Δf damped (MHz)	R nominal (kΩ)	R damped (kΩ)	ratio R damp/nom	R/Q nominal (Ω)	R/Q damped (Ω)
f_{RF}	52.4	-(0.1) *	14.8	18.3	1.2	17	21
f1	79.9	+2.2	7.95	2.11	0.3	44	66
f2	82.7	+2.0	5.9	2.52	0.4	27	45
f3	105.4	-0.2	4.45	5.95	1.3	10	13
f4	168.1	-3.2	3.3	1.72	0.5	10	10
f5	196.0	+0.8	36.9	2.13	0.06	19	17
f6	219.0	+4.1 **	4.88	0.35 **	0.07	16	**
f7	326.8	--	1.67	--	--	15	--
f8	344.3	-3.4	3.69	3.25	0.9	23	13
f9	--	(263.7)	--	2.2	--	--	9.2
f10	--	(302.1)	--	0.77	--	--	9.4
f11	--	(305.4)	--	1.11	--	--	8.3

* Comparison between nominal and damped fundamental frequency inexact because bias current chosen by hand. In operation, values are equal for a particular time in the cycle.
* Damped f6 no longer a real mode

Table B.10 Effect of Cavity Shorts on Impedance vs. HOM Dampers (bias I_b=0).

		f (MHz)	R (kΩ)	R/Q (Ω)
nominal cavity	no short	79.89	8.05	51
		82.61	5.95	28
		195.9	26.4	24
	unshorted gap	81.57	10.5	70
		195.3	2.71	26
	shorted gap	86.49	5.7	47
		195.2	2.12	26
damped cavity	no short	82.06	2.11	68
		84.57	2.45	45
		196.7	1.91	21
	unshorted gap	83.82	3.34	86
		196.2	1.54	20
	shorted gap	88.32	2.64	55
		196.2	1.14	17

Appendix C: ESME Input Data Files for Simulation of Booster

Sample input files used in the Booster ESME simulation of coupled-bunch instability are reproduced here, corresponds to the nominal conditions: 1.7e12 ppp, nominal 15 cavities, no HOM dampers. The main input file HOMBB.DAT gives the tracking and RF voltage data. The simulation is begun at 17 msec in the global cycle. Note that there is a 2 msec lag between the time in the cycle and actual time on the sinusoidal acceleration curve. The space charge calculation is turned off, but the effect of the broadband and high-Q resonant impedances are included. The file DMAGNET.DAT (broadband) gives the coefficients for the real and imaginary impedance over five frequency ranges. The files RBttH0.DAT (HOM resonances, dampers out) give frequency, R, multiplier and Q. These were created from the calculated net impedance of Table B.7, interpolating between measured values for a smooth variation in frequency and R over the simulation. Also given are the files RBttH1.DAT (dampers in) from Table B.8. The impedance files are called at appropriate times tt during tracking.

Main input file: HOMBB.DAT

```
W   HOMbb Booster cbm 4 HOM thru cyle. HOM OUT. 15 cav
W      mistake in homaa: forgot to set nr=4
W      Scale Z=Z*1 stretched wire: rbxxh0.dat
W      Interpolate HOM Z and VRF between msee data t=17.18.19.20
W      Turn SCON on. set b=0.606530659*a (problems with space charge calc)
W      npoint=800. HOM sumZ (15). npjmp=4. emit=0.027
W      dmagnet Z/n. beampipe radius=3 cm. elliptic. track t=17 to t=35
W      VRF from R07 data (see [.BBKT]VRF_R07.DAT)
W      ESME v7.2. QREZON for HOM. magnet
W
R   FERMILAB BOOSTER
 $RING REQ=75.47. GAMMAT=5.446. ALPHA1=0.0. EK0I=203.. EK0F=8000..
     TI=0.0. TF=0.033333333. TSTART=0.015. KURVEB=3. FRAC=1 $END
A   53 MHZ RF SYSTEM (t=17-17.5 in cycle)
 $RF H=84. VI=.678. VF=.667. KURVE=1. TVBEG=0.0150. TVEND=0.0155.
     ISYNC=1 $END
P   PUT IN 84 BUNCHES (1)
 $POPL8 KIND=14. SBNCH=.027. NPOINT=800. THOFF=-180. $END
P   PUT IN 84 BUNCHES (2)
 $POPL8 THTRAN=4.285714286. ETRAN=0. $END

          (... repeat for bunches (3) through (83) ...)

P   PUT IN 84 BUNCHES (84)
 $POPL8 THTRAN=4.285714286. ETRAN=0. $END
W   Force (1+2*ln(b/a)=0 by letting b=0.606530659*a. where a=0.002 default
B   SET UP THE SPACE CHARGE CALCULATION (note ENQ is ppp)
 $SCHG NBRES=5000. NZ=5. NR=4. ENQ=1.7e12. QREZON=T.
  SCON=T. A=0.002. B=0.0012130613 $END
dmagnet.dat
rb17h0.dat
O   Graphic format.
 $GRAPH MPLOT=625. IOPT=1. THPMIN=-1.35. THPMAX=1.35. DEPMIN=-30..
  DEPMAX=30.. TITLE=T. IDEV=1. PLTSW(5)=F. PLTSW(8)=T. PLTSW(10)=T.
  PLTSW(12)=F. PLTSW(16)=T. RBMIN=-1.35. RBMAX=1.35. NPJMP=4 $END
HOMbb .027 4HOM0*1 SCHG1 Z/n ellip (1.7e12) t=17
D   Display starting conditions.
M   Save histograms for mountain range
 $MRANGE MRTHBMIN=-1.35. MRTHBMAX=1.35. MRMPLOT=25 $END
W4   Calculate moments for n=42 bunch
W $TAKEMOM IBOUND=1. THRMIN=-3.0. THRMAX=3.0 $END
T   Now track (0.5 msec)
 $CYCLE TTRACK=.0005. HISTRY=.T.. MOMNTS=.T. $END
B   SET UP THE SPACE CHARGE CALCULATION (note ENQ is ppp)
 $SCHG NBRES=5000. NZ=5. NR=4. ENQ=1.7e12. QREZON=T.
  SCON=T. A=0.002. B=0.0012130613 $END
dmagnet.dat
rb175h0.dat
A   53 MHZ RF SYSTEM (t=17.5-18 in cycle)
 $RF H=84. VI=.667. VF=.655. KURVE=1. TVBEG=0.0155. TVEND=0.0160.
     ISYNC=1 $END
T   Now track (0.5 msec)
 $CYCLE TTRACK=.0005. HISTRY=.T.. MOMNTS=.T. $END
B   SET UP THE SPACE CHARGE CALCULATION (note ENQ is ppp)
 $SCHG NBRES=5000. NZ=5. NR=4. ENQ=1.7e12. QREZON=T.
  SCON=T. A=0.002. B=0.0012130613 $END
dmagnet.dat
rb18h0.dat
A   53 MHZ RF SYSTEM (t=18-18.5 in cycle)
 $RF H=84. VI=.655. VF=.654. KURVE=1. TVBEG=0.0160. TVEND=0.0165.
     ISYNC=1 $END
T   Now track (0.5 msec)
 $CYCLE TTRACK=.0005. HISTRY=.T.. MOMNTS=.T. $END
B   SET UP THE SPACE CHARGE CALCULATION (note ENQ is ppp)
 $SCHG NBRES=5000. NZ=5. NR=4. ENQ=1.7e12. QREZON=T.
  SCON=T. A=0.002. B=0.0012130613 $END
dmagnet.dat
rb185h0.dat
A   53 MHZ RF SYSTEM (t=18.5-19 in cycle)
 $RF H=84. VI=.654. VF=.652. KURVE=1. TVBEG=0.0165. TVEND=0.0170.
     ISYNC=1 $END
T   Now track
 $CYCLE TTRACK=.0005. HISTRY=.T.. MOMNTS=.T. $END
B   SET UP THE SPACE CHARGE CALCULATION (note ENQ is ppp)
 $SCHG NBRES=5000. NZ=5. NR=4. ENQ=1.7e12. QREZON=T.
  SCON=T. A=0.002. B=0.0012130613 $END
```

```
dmagnet.dat
rb19h0.dat
A   53 MHZ RF SYSTEM (t=19-19.5 in cycle)
 $RF H=84. VI=.652. VF=.658. KURVE=1. TVBEG=0.0170. TVEND=0.0175.
     ISYNC=1 $END
T   Now track (0.5 msec)
 $CYCLE TTRACK=.0005. HISTRY=.T.. MOMNTS=.T. $END
B   SET UP THE SPACE CHARGE CALCULATION (note ENQ is ppp)
 $SCHG NBRES=5000. NZ=5. NR=4. ENQ=1.7e12. QREZON=T.
  SCON=T. A=0.002. B=0.0012130613 $END
dmagnet.dat
rb195h0.dat
A   53 MHZ RF SYSTEM (t=19.5-20 in cycle)
 $RF H=84. VI=.658. VF=.664. KURVE=1. TVBEG=0.0175. TVEND=0.0180.
     ISYNC=1 $END
T   Now track (0.5 msec)
 $CYCLE TTRACK=.0005. HISTRY=.T.. MOMNTS=.T. $END
B   SET UP THE SPACE CHARGE CALCULATION (note ENQ is ppp)
 $SCHG NBRES=5000. NZ=5. NR=4. ENQ=1.7e12. QREZON=T.
  SCON=T. A=0.002. B=0.0012130613 $END
dmagnet.dat
rb20h0.dat
A   53 MHZ RF SYSTEM (t=20-20.5 in cycle)
 $RF H=84. VI=.664. VF=.661. KURVE=1. TVBEG=0.0180. TVEND=0.0185.
     ISYNC=1 $END
T   Now track (0.5 msec)
 $CYCLE TTRACK=.0005. HISTRY=.T.. MOMNTS=.T. $END
B   SET UP THE SPACE CHARGE CALCULATION (note ENQ is ppp)
 $SCHG NBRES=5000. NZ=5. NR=4. ENQ=1.7e12. QREZON=T.
  SCON=T. A=0.002. B=0.0012130613 $END
dmagnet.dat
rb205h0.dat
A   53 MHZ RF SYSTEM (t=20.5-21 in cycle)
 $RF H=84. VI=.661. VF=.658. KURVE=1. TVBEG=0.0185. TVEND=0.0190.
     ISYNC=1 $END
T   Now track (0.5 msec)
 $CYCLE TTRACK=.0005. HISTRY=.T.. MOMNTS=.T. $END
B   SET UP THE SPACE CHARGE CALCULATION (note ENQ is ppp)
 $SCHG NBRES=5000. NZ=5. NR=4. ENQ=1.7e12. QREZON=T.
  SCON=T. A=0.002. B=0.0012130613 $END
dmagnet.dat
rb21h0.dat
A   53 MHZ RF SYSTEM (t=21-22 in cycle)
 $RF H=84. VI=.658. VF=.655. KURVE=1. TVBEG=0.0190. TVEND=0.0200.
     ISYNC=1 $END
T   Now track
 $CYCLE TTRACK=.001. HISTRY=.T.. MOMNTS=.T. $END
W   INTERPOLATED
B   SET UP THE SPACE CHARGE CALCULATION (note ENQ is ppp)
 $SCHG NBRES=5000. NZ=5. NR=4. ENQ=1.7e12. QREZON=T.
  SCON=T. A=0.002. B=0.0012130613 $END
dmagnet.dat
rb22h0.dat
A   53 MHZ RF SYSTEM (t=22-23 in cycle)
 $RF H=84. VI=.655. VF=.638. KURVE=1. TVBEG=0.0200. TVEND=0.0210.
     ISYNC=1 $END
T   Now track
 $CYCLE TTRACK=.001. HISTRY=.T.. MOMNTS=.T. $END
B   SET UP THE SPACE CHARGE CALCULATION (note ENQ is ppp)
 $SCHG NBRES=5000. NZ=5. NR=4. ENQ=1.7e12. QREZON=T.
  SCON=T. A=0.002. B=0.0012130613 $END
dmagnet.dat
rb23h0.dat
A   53 MHZ RF SYSTEM (t=23-24 in cycle)
 $RF H=84. VI=.638. VF=.620. KURVE=1. TVBEG=0.0210. TVEND=0.0220.
     ISYNC=1 $END
T   Now track
 $CYCLE TTRACK=.001. HISTRY=.T.. MOMNTS=.T. $END.
W   INTERPOLATED
B   SET UP THE SPACE CHARGE CALCULATION (note ENQ is ppp)
 $SCHG NBRES=5000. NZ=5. NR=4. ENQ=1.7e12. QREZON=T.
  SCON=T. A=0.002. B=0.0012130613 $END
dmagnet.dat
rb24h0.dat
A   53 MHZ RF SYSTEM (t=24-25 in cycle)
 $RF H=84. VI=.620. VF=.599. KURVE=1. TVBEG=0.0220. TVEND=0.0230.
     ISYNC=1 $END
```

```
T   Now track
$CYCLE TTRACK=.001, HISTRY=.T., MOMNTS=.T. $END
B   SET UP THE SPACE CHARGE CALCULATION (note ENQ is ppp)
 $SCHG NBRES=5000, NZ=5, NR=4, ENQ=1.7e12, QREZON=T,
  SCON=T, A=0.002, B=0.0012130613 $END
dmagnet.dat
rb25h0.dat
A   53 MHZ RF SYSTEM (t=25-26 in cycle)
 $RF H=84, VI=.599, VF=.575, KURVE=1, TVBEG=0.0230, TVEND=0.0240,
     ISYNC=1 $END
T   Now track
 $CYCLE TTRACK=.001, HISTRY=.T., MOMNTS=.T. $END
A   53 MHZ RF SYSTEM (t=26-27 in cycle)
 $RF H=84, VI=.575, VF=.554, KURVE=1, TVBEG=0.0240, TVEND=0.0250,
     ISYNC=1 $END
T   Now track
 $CYCLE TTRACK=.001, HISTRY=.T., MOMNTS=.T. $END
W   INTERPOLATED
B   SET UP THE SPACE CHARGE CALCULATION (note ENQ is ppp)
 $SCHG NBRES=5000, NZ=5, NR=4, ENQ=1.7e12, QREZON=T,
  SCON=T, A=0.002, B=0.0012130613 $END
dmagnet.dat
rb27h0.dat
A   53 MHZ RF SYSTEM (t=27-28 in cycle)
 $RF H=84, VI=.554, VF=.532, KURVE=1, TVBEG=0.0250, TVEND=0.0260,
     ISYNC=1 $END
T   Now track
 $CYCLE TTRACK=.001, HISTRY=.T., MOMNTS=.T. $END
A   53 MHZ RF SYSTEM (t=28-29 in cycle)
 $RF H=84, VI=.532, VF=.490, KURVE=1, TVBEG=0.0260, TVEND=0.0270,
     ISYNC=1 $END
T   Now track
 $CYCLE TTRACK=.001, HISTRY=.T., MOMNTS=.T. $END
B   SET UP THE SPACE CHARGE CALCULATION (note ENQ is ppp)
 $SCHG NBRES=5000, NZ=5, NR=4, ENQ=1.7e12, QREZON=T,
  SCON=T, A=0.002, B=0.0012130613 $END
dmagnet.dat
rb29h0.dat
A   53 MHZ RF SYSTEM (t=29-30 in cycle)
 $RF H=84, VI=.490, VF=.451, KURVE=1, TVBEG=0.0270, TVEND=0.0280,
     ISYNC=1 $END
T   Now track
 $CYCLE TTRACK=.001, HISTRY=.T., MOMNTS=.T. $END
A   53 MHZ RF SYSTEM (t=30-31 in cycle)
 $RF H=84, VI=.451, VF=.401, KURVE=1, TVBEG=0.0280, TVEND=0.0290,
     ISYNC=1 $END
T   Now track
 $CYCLE TTRACK=.001, HISTRY=.T., MOMNTS=.T. $END
A   53 MHZ RF SYSTEM (t=31-32 in cycle)
 $RF H=84, VI=.401, VF=.351, KURVE=1, TVBEG=0.0290, TVEND=0.0300,
     ISYNC=1 $END
T   Now track
 $CYCLE TTRACK=.001, HISTRY=.T., MOMNTS=.T. $END
A   53 MHZ RF SYSTEM (t=32-33 in cycle)
 $RF H=84, VI=.351, VF=.308, KURVE=1, TVBEG=0.0300, TVEND=0.0310,
     ISYNC=1 $END
T   Now track
 $CYCLE TTRACK=.001, HISTRY=.T., MOMNTS=.T. $END
A   53 MHZ RF SYSTEM (t=33-34 in cycle)
 $RF H=84, VI=.308, VF=.258, KURVE=1, TVBEG=0.0310, TVEND=0.0320,
     ISYNC=1 $END
T   Now track
 $CYCLE TTRACK=.001, HISTRY=.T., MOMNTS=.T. $END
A   53 MHZ RF SYSTEM (t=34-35 in cycle)
 $RF H=84, VI=.258, VF=.212, KURVE=1, TVBEG=0.0320, TVEND=0.0330,
     ISYNC=1 $END
T   Now track
 $CYCLE TTRACK=.001, HISTRY=.T. MOMNTS=.T. $END
H   Plot parameter histories
 $HISTRY NPLT=1,13,1,4,1,6,1,5,1,7 $END
N   Now plot mountain ranges
 $MRPLOT SCALE=.25, SMOOTH=.T. $END
Q   Stop
```

Broadband impedance file: DMAGNET.DAT

```
0
0.9048e-1,0.1918,0.2024e-2,-0.25e-4
-0.7144e-2,0.6524e-1,0.45e-2,-0.6667e-4
60
19.21,-0.4743,0.8746e-2,-0.4074e-4
-13.91,0.8243,-0.1075e-1,0.4074e-4
110
-3.957,0.5551,-0.4405e-2,0.1111e-4
35.97,-0.661,0.4036e-2,-0.8333e-5
170
3.561,0.1677,-0.6228e-3,0.7275e-8
-9.425,0.124,-0.5578e-3,0.7630e-6
350
-1.7,0.0,0
17.0,0.0,0
```

Resonance Data Files,
HOM damper IN:

```
::::::::::::
rb17h1.dat
::::::::::::
 84.56  104000.0  1  60.0
 164.1    40000.0  1  120.0
 339.8   120000.0  1  220.0
::::::::::::
rb175h1.dat
::::::::::::
 84.56  104000.0  1  60.0
 164.3    40000.0  1  120.0
 340.05  120000.0  1  220.0
::::::::::::
rb18h1.dat
::::::::::::
 84.56  104000.0  1  60.0
 164.55   40000.0  1  120.0
 340.3   120000.0  1  215.0
::::::::::::
rb185h1.dat
::::::::::::
 84.56  104000.0  1  60.0
 164.8    30000.0  1  115.0
 340.55  128000.0  1  210.0
::::::::::::
rb19h1.dat
::::::::::::
 84.56  104000.0  1  60.0
 165.0    30000.0  1  110.0
 340.8   128000.0  1  210.0
::::::::::::
rb195h1.dat
::::::::::::
 84.56  104000.0  1  60.0
 165.1    38000.0  1  110.0
 340.9   128000.0  1  210.0
::::::::::::
rb20h1.dat
::::::::::::
 84.56  105000.0  1  60.0
 165.25  37000.0  1  105.0
 341.0   128000.0  1  215.0
::::::::::::
rb205h1.dat
::::::::::::
 84.56  105000.0  1  60.0
 165.4    37000.0  1  100.0
 341.1   124000.0  1  220.0
::::::::::::
rb21h1.dat
::::::::::::
 84.56  105000.0  1  62.0
 165.5    36000.0  1  100.0
 341.2   128000.0  1  220.0
::::::::::::
rb22h1.dat
::::::::::::
 84.56  107000.0  1  62.0
 165.7    36000.0  1  100.0
 341.55  130000.0  1  225.0
::::::::::::
rb23h1.dat
::::::::::::
 84.56  109000.0  1  60.0
 165.9    37000.0  1  100.0
 341.9   132000.0  1  230.0
::::::::::::
rb24h1.dat
::::::::::::
 84.56  106000.0  1  60.0
 166.0    35000.0  1  100.0
 342.0   130000.0  1  225.0
::::::::::::
rb25h1.dat
::::::::::::
 84.56  102000.0  1  62.0
 166.1    33000.0  1  100.0
 342.1   127000.0  1  220.0
::::::::::::
rb27h1.dat
::::::::::::
 84.56  102000.0  1  62.0
 166.2    32000.0  1  100.0
 342.25  127000.0  1  220.0
::::::::::::
rb29h1.dat
::::::::::::
 84.56  102000.0  1  62.0
 166.3    32000.0  1  100.0
 342.4   127000.0  1  220.0
```

Resonance Data Files,
HOM damper OUT:

```
::::::::::::::
rb17h0.dat
::::::::::::::
 82.58  196000.0  1  190.0
 166.4   52000.0  1  200.0
 217.1  169000.0  1  300.0
 343.2  148000.0  1  190.0
::::::::::::::
rb175h0.dat
::::::::::::::
 82.57  198000.0  1  190.0
 166.75  53000.0  1  200.0
 217.8  169000.0  1  290.0
 343.5  153000.0  1  190.0
::::::::::::::
rb18h0.dat
::::::::::::::
 82.55  200000.0  1  190.0
 167.1   54000.0  1  200.0
 218.0  162000.0  1  290.0
 343.8  154000.0  1  190.0
::::::::::::::
rb185h0.dat
::::::::::::::
 82.57  196000.0  1  190.0
 167.35  53000.0  1  200.0
 218.2  155000.0  1  290.0
 343.9  155000.0  1  190.0
::::::::::::::
rb19h0.dat
::::::::::::::
 82.59  192000.0  1  190.0
 167.6   52000.0  1  200.0
 218.4  147000.0  1  280.0
 344.0  152000.0  1  190.0
::::::::::::::
rb195h0.dat
::::::::::::::
 82.59  193000.0  1  190.0
 167.75  50000.0  1  195.0
 218.6  149000.0  1  280.0
 344.15 152000.0  1  190.0
::::::::::::::
rb20h0.dat
::::::::::::::
 82.58  194000.0  1  190.0
 167.9   47000.0  1  190.0
 218.8  151000.0  1  280.0
 344.3  152000.0  1  190.0
::::::::::::::
rb205h0.dat
::::::::::::::
 82.58  194000.0  1  190.0
 168.1   50000.0  1  190.0
 218.95 148000.0  1  280.0
 344.45 155000.0  1  190.0
::::::::::::::
rb21h0.dat
::::::::::::::
 82.57  193000.0  1  190.0
 168.3   52000.0  1  190.0
 219.1  144000.0  1  280.0
 344.6  157000.0  1  190.0
::::::::::::::
rb22h0.dat
::::::::::::::
 82.58  195000.0  1  185.0
 168.55  53000.0  1  190.0
 219.35 143000.0  1  270.0
 344.8  158000.0  1  190.0
::::::::::::::
rb23h0.dat
::::::::::::::
 82.59  197000.0  1  180.0
 168.8   54000.0  1  190.0
 219.6  142000.0  1  260.0
 345.0  158000.0  1  190.0
::::::::::::::
rb24h0.dat
::::::::::::::
 82.59  196000.0  1  180.0
 168.95  53000.0  1  190.0
 219.75 142000.0  1  260.0
 345.1  159000.0  1  190.0
::::::::::::::
rb25h0.dat
::::::::::::::
 82.58  195000.0  1  180.0
 169.1   51000.0  1  190.0
 219.9  142000.0  1  260.0
 345.2  159000.0  1  190.0
::::::::::::::
rb27h0.dat
::::::::::::::
 82.59  194000.0  1  180.0
 169.15  52000.0  1  190.0
 220.05 138000.0  1  260.0
 345.35 157000.0  1  190.0
::::::::::::::
rb29h0.dat
::::::::::::::
 82.59  192000.0  1  180.0
 169.2   52000.0  1  190.0
 220.2  134000.0  1  260.0
 345.5  154000.0  1  190.0
```

VITA

Katherine C. Harkay received her Bachelor of Science degree in physics in 1982 from St. John's University in Queens, New York. She received her Master of Science degree in 1984, also in physics, from Purdue University in West Lafayette, Indiana. For a period of five years, she worked at ANSER, Inc., a technical consulting company in Arlington, Virginia, where she was responsible for providing analytic support in the area of space systems technologies on contract with the United States Air Force. In 1989, she returned to academia to pursue her Doctor of Philosophy degree in physics at Purdue. She was accepted into the Joint University-Fermilab Doctoral Research Program in Accelerator Physics, and conducted her research efforts at Fermi National Accelerator Laboratory under the guidance of the Accelerator Division. Upon completion of all requirements for the PhD, she accepted a position at Argonne National Laboratory in the Accelerator Systems Division of the Advanced Photon Source. Katherine was born on March 25, 1961 in New York to Robert L. and Josephine Somkuthy Harkay. In the proud tradition of her family, she has been an active leader in the American-Hungarian community for fifteen years.

VITA